12-2003

Numerical Simulation of Separating Flows Using Computational Models Based on the Vorticity Confinement Method

Lesong Wang
University of Tennessee - Knoxville

To the Graduate Council:

I am submitting herewith a dissertation written by Lesong Wang entitled "Numerical Simulation of Separating Flows Using Computational Models Based on the Vorticity Confinement Method." I have examined the final electronic copy of this dissertation for form and content and recommend that it be accepted in partial fulfillment of the requirements for the degree of Doctor of Philosophy, with a major in Engineering Science.

John S. Steinhoff, Major Professor

We have read this dissertation and recommend its acceptance:

K. C. Reddy, Charles L. Merkle, John E. Caruthers

Accepted for the Council:
Carolyn R. Hodges

Vice Provost and Dean of the Graduate School

(Original signatures are on file with official student records.)

To the Graduate Council:

I am submitting herewith a dissertation written by Lesong Wang entitled "Numerical Simulation of Separating Flows Using Computational Models Based on the Vorticity Confinement Method." I have examined the final electronic copy of this dissertation for form and content and recommend that it be accepted in partial fulfillment of the requirements for the degree of Doctor of Philosophy, with a major in Engineering Science.

John S. Steinhoff

Major Professor

We have read this dissertation
and recommend its acceptance:

K. C. Reddy

Charles L. Merkle

John E. Caruthers

Acceptance for the Council:

Anne Mayhew

Vice Provost and Dean of
Graduate Studies

(Original Signatures are on file with official student records.)

NUMERICAL SIMULATION OF SEPARATING FLOWS USING COMPUTAIONAL MODELS BASED ON THE VORTICITY CONFINEMENT METHOD

A Dissertation
Presented for the
Doctor of Philosophy
Degree
The University of Tennessee, Knoxville

Lesong Wang
December 2003

Dedication

This dissertation is dedicated to my wife, Constance Wang, and my child, Steven Wang, and my parents, Guangyan Wang and Yaoxin Lu, and my brothers and sisters, Shengchao Wang, Dongmei Wang, Qiuju Wang, Namei Wang and Shenghai Wang, and my sister-in-law, Baozhen Liao, and the rest of the family, for always supporting me, inspiring me, and encouraging me to pursue a dream that rooted in the heart of a Chinese farmer's child from the beginning of his life.

Acknowledgement

I would like to express my deepest gratitude to my advisor, Professor John Steinhoff, for his continuous instruction, education, inspiration and technical guidance throughout my graduate studies. Sincere thanks are extended to other committee members: Dr. K.C. Reddy, Dr. John Caruthers, Dr. Charles Merkle, for their knowledgeable comments and advice. I also want to express my special appreciation to Dr. Boris Kupershmidt for his assistance in mathematics.

Recognition is given to my colleagues in UTSI and Flow Analysis, Inc. for the valuable discussions. I also would like to express my appreciation to the library staffs for their assistance.

I want to thank my parents, my child, my other relatives and all my friends in China and in US, for their continuous supports.

Finally, I would like to thank my wife. This work would not have been possible without her patience, understanding and encouragement.

This work was partially supported by the Army Research Office and the University of Tennessee Space Institute.

Abstract

The objective of the present research is to investigate the recent development of the vorticity confinement method. First, a new formulation of the vorticity confinement term is studied. Advantages of the new formulation over the original one include the ability to conserve the momentum, and the ability to preserve the centroid motion of some flow properties such as the vorticity magnitude. Next, new difference schemes, which are simpler and more efficient than the old schemes, are discussed. At last, two computational models based on the vorticity confinement method are investigated. One of the models is devised to simulate inviscid flows over bodies with surfaces not aligned with the grid. The other is a surface boundary layer model, which is intended for efficiently simulating viscous flows with separations from the body surfaces.

To validate the computational models, numerical simulations of three-dimensional flows over a 6:1 ellipsoid at incidence are performed. Comparisons have been made with exact solutions for inviscid simulations or experimental data for viscous simulations, and data obtained with conventional CFD methods. It is observed that both the inviscid and the viscous solutions with the new models exhibit good agreement with the exact solutions or the experiment data. The new models can have much higher efficiency than conventional CFD methods, and are able to obtain solutions with comparable accuracy.

Table of Contents

List of Figures

Nomenclature

a	Vorticity confinement length scale
CFL	Courant-Friedriches-Lewy number
C_p	Pressure coefficient
$\vec{E}, \vec{F}, \vec{G}$	Flux vectors
h	Distance to the surface
i,j,k	Indices of inner grid
I,J,K	Indices of outer grid
$\vec{n}$	Unit vector
N	Total number of surrounding grid points
P	Pressure
P_∞	Pressure at infinity
$\vec{q}$	Velocity vector
$\vec{q}_\infty$	Free stream velocity
$\vec{Q}$	Primary transport variable
$< Q >$	Centroid of velocity
$\vec{s}$	Confinement vector
s	Confinement scalar
t	Time
u	Velocity component in x direction
v	Velocity component in y direction
w	Velocity component in z direction
$\vec{W}$	Harmonic mean of the vorticity
x,y,z	Coordinates of a Cartesian grid
ξ, η, ζ	Coordinates of a curvilinear grid

$\hat{x}$	Coordinate of a grid point
$< \hat{X} >$	Centroid of variables
X/L	Position of a cross plane
ε	Confinement coefficient
μ	Artificial diffusion coefficient
ϕ	Scalar field
$< \psi >$	Total scalar value
Φ	Harmonic mean of a scalar variable
φ	Pressure variable
φ_∞	Pressure value at infinity
ρ	Density
Γ	Circulation
λ	Aspect ratio of an ellipsoid
Δt	Time step
$\vec{\omega}$	Vorticity vector
$\Delta x, \Delta y, \Delta z$	Grid spacing for Cartesian grid
∇	Gradient operator

1. Introduction

1.1 Background

Over the last forty years, Computational Fluid Dynamics (CFD) has evolved from the specialty of a small band of enthusiasts into a vast and industrially oriented enterprise. Resources committed to CFD research are increasing rapidly, at the same time new areas of application continue to open up. The applications of CFD nowadays have already spread over a considerable variety of disciplines and specializations, ranging from aerodynamics to environmental preservation and from shore protection to biological science [22]. Regarding the state of diversity and the fragmentation CFD currently carries, it is very important to develop methods that are cost effective and easy to adapt for various problems across different areas. Unfortunately, this is not always the case for most of the modern CFD methods. The situation is almost opposite to what is hoped. These methods normally are highly customized and awkward to adapt to new configurations, not to mention the usability for areas outside the one they are originally designed for. Further more, most of the existing methods are resource intensive for complicated modern flow problems such as flow over a whole aircraft body, flow over a block of buildings, etc.

Most high Reynolds number separated flows are turbulent. In the area of mathematics, tools for non-linear types of problems are still very limited. Unfortunately, being one of the most challenging subjects of modern science, turbulence is a phenomena caused by the non-linear characteristics intrinsic to the dynamics of fluid flows. Due to the lack of mathematical tools, turbulence presents difficult challenges for CFD

applications. The well-known Navier-Stokes equations are able to describe the dynamics of fluid flows under most conditions. The simulation of fluid flows thus becomes mainly a task of numerically solving or modeling the Navier-Stokes equations. The existence of a wide range of length scales makes Direct Numerical Simulation (DNS) of turbulence flow extremely resource demanding, and unrealistic for most real world applications [30]. In most of the existing methods dealing with turbulent flows, turbulence is modeled by solving model equations rather than simulated by solving the exact Navier-Stokes equations [3][22][39].

A large number of approaches have been proposed during the last 30 years. These methods can be roughly categorized into two major methodologies: time-averaging and space-averaging methods [21][22][47]. The time averaging methods are based on the Reynolds averaged Navier-Stokes (RANS) equations. Since the Navier-Stokes equations are nonlinear, this leads to a situation in which there are more unknowns than equations, which is the so-called "closure" problem of turbulence modeling [39]. Constraints must be devised to make the number of independent equations equal the number of unknown variables. The time-averaged model thus can be classified by the number of constraints used for turbulence quantities, ranging from the zero equation model (better known as the mixing length model) to stress-flux models with as many as six constraints [21][22][47]. Among all these models, the two equation k-ε and k-ω models [47][48] seem to be the most popular, where two constraint equations are devised to solve for the turbulence quantities introduced in the Reynolds averaged equation: the turbulence kinetic energy and turbulent energy dissipation [22]. Space averaged methods, mainly the Large Eddy Simulation (LES) method, simulate the larger scales of motion while accepting that the smaller scales will not be properly represented [21]. Larger scales are solved directly without modeling and the smaller scales are filtered out and need to be modeled. There certainly are crossovers between these two types of methods. RANS methods are also "space-averaged" over small eddies, while the LES methods typically require time-averaging turbulence models for solving sub-scale eddies [28][47]. There are also hybrid methods such as Detached Eddy Simulations (DES), which attempt to use RANS models

in predicating boundary layer growth and separation, and to use LES away from solid surfaces to model the typically geometry-dependent and unsteady scale of motion in separated regions [26][27][36][45].

For both of these approaches, higher order methods are necessary to minimize the amount of artificial diffusion introduced by discretization [3][16][35][37]. The grid normally must be very fine for regions around the surface, to minimize the numerical dissipation introduced by the turbulence model [3][18][35]. For unsteady flows with large regions of vortical features, to successfully capture the flow properties, the grid may need to be updated according to the flow situations. Otherwise the vortical features will disappear rapidly due to the numerical diffusion, since the grid away from the surface in most cases is very coarse. To deal with this situation, adaptive grids are used in many applications [16][28][37]. As a result, although conventional methods may be efficient for some flows with relatively low Reynolds numbers or simple body geometries, they are inefficient and sometimes not even feasible for flows with multiple thin vortices convecting over long distances and high Reynolds number flows over complicated bodies [1][3][35][22].

The vorticity confinement Method, originally developed in early 1990s [50][51], introduces a very different way to simulate vortical features in fluid flows. This new method is based on a set of new model equations. The discretized model equations generate solutions that can represent a vortical feature with very few grid points. The grid for the computation thus can be made coarser compared to conventional methods, for which sufficient number of grid points are needed across vortical features in order to approximately solve the conventional model equations.

One of the salient features of the new models is the introduction of a nonlinear negative diffusion term, which plays a critical role in areas with concentrated vorticity. These new difference equations can capture a vortical feature with only two to three grid cells and the resulting vortical structure behaves like a solitary wave, which can convect

with the main flow for indefinite durations without spreading or changing its main features.

The solutions of the new models approximate those of the Navier-Stokes equations in most parts of the flow field, where the flow is nearly irrotational. In the vortical regions, the solutions are not good approximation but preserve many of the integral properties of the flows [2][3]. In many practical flow problems, such as flows with very thin vortex features, only these integral properties are important. Thus the solutions can be very accurate globally even if the internal structures of the vortical regions are not exactly solved [1][3].

The advantage of the method is that computational schemes can be devised based on the confinement method that require orders of magnitude smaller computational resources and simpler numerical procedures than typical conventional methods while achieving comparable accuracy. The usefulness of the confinement method is not limited to fluid dynamics applications. It can be applied to a large range of scientific problems where the numerical spreading of flow features is one of the major concerns. It is not surprising that the confinement method has already been applied to many other areas such as computational acoustics and even some graphics applications in the movie industry, etc [2][12][15][58].

1.2 Objectives and Structure

1.2.1 Study of the new confinement formulation and new computational schemes

In the past, most of the confinement methods have used a non-conservative formulation for the confinement terms [1][13][14][16-20][38][49-58]. Recently, a new conservative confinement formulation has been developed [2]. The new confinement

formulation has many advantages over the old one, such as it explicitly conserves the momentum and preserves the centroid motion of vortical features, etc. The new confinement is one of the main topics of this dissertation.

The numerical schemes are also revised in this thesis, both for the conservative and non-conservative confinement formulations. These new schemes are simpler than those used in the past applications of the confinement methods, and at the same time, are able to achieve higher efficiency and better accuracy.

1.2.2 The surface boundary layer model

Using vorticity confinement as a rough boundary layer model on non-body conforming grids can yield good results for massively separated flows [1][14][17][18][20]. However, for flows where the internal structures of the boundary layer are very important in determining the separation point, the thick artificial boundary layer obtained from this model may prevent it from being able to accurately model the dynamics of the separation process [3].

A new boundary layer model is developed and studied in this dissertation. In addition to the existing vorticity confinement method, the surface boundary layer model is able to

1) use a body-conforming grid to explicitly define the surface,
2) treat small features that have less thickness,
3) provide better capability to predict the separation process,
4) provide better resolution.

1.2.3 The structure of the dissertation

The dissertation is organized into three main parts. The first main part is dedicated to the study of the vorticity confinement method. Many new developments of the method

that have not been previously covered in the literature are discussed, followed by the newly revised numerical scheme. After that, some simple test cases are performed using the newly described methods. The last part of this section summarizes some of the main features of the vorticity confinement methods.

The second main part is concentrated on discussing newly designed surface boundary models. An inviscid surface model and a viscous surface boundary layer model are presented, followed by some simple numerical demonstrations.

In the last main part, full three-dimensional flows are computed to demonstrate the capability of the discussed models. Flows over a 6:1 ellipsoid with various incidence angles are simulated, first using the inviscid model, next using the conservative confinement on a uniform Cartesian grid without the surface model, and last, using the viscous surface boundary layer model coupled with the conservative confinement method. The results are presented and discussed in detail.

A brief conclusion and recommendations for future studies conclude the dissertation.

2. The Vorticity Confinement Method

In this chapter, the theory of vorticity confinement is presented. There is a lot of existing literature dedicated to vorticity confinement [1][2][13][14][16-20][38][49-58], in which one can find many successful applications of the methods. However, an organized presentation of the theory still needs to be created, especially the inclusion of some of the important developments in recent studies. The theory and numerical scheme presented in this context is in many parts different from those involving the original confinement method, and includes the descriptions of the new confinement method that have not been fully described in previous studies [2]. The new method involves a better-founded mathematical and physical basis, using simpler but more accurate numerical schemes. The context in this section is set with the intention of documenting the most classical aspects as well as the newest developments of the vorticity confinement theory. It is hoped that this thesis can provide some useful information for people who are interested in utilizing the method.

The mathematical models are presented first, followed by detailed studies of the mathematical and physical properties of the model equations. Due to the vast possible variation of the vorticity confinement formulation, many of the results may vary from the existing literature. The formulations described here are the ones used to obtain results presented in the thesis and are proved to be successful. Following the discussion of the theory are the computational schemes for adapting the method to numerical computations. Compared to past studies, major changes are made to the numerical schemes, especially the numerical formulation of the vorticity confinement term. Next some classic simple flows are studied to illustrate some important features of the newly presented methods. The final section is dedicated to the discussion of the salient features

of the vorticity confinement method. This section serves to summarize the topics and problems raised in the previous three sections.

2.1 The Theory of the Vorticity Confinement Method

2.1.1 The vorticity confinement method

The governing equations for vorticity confinement methods are based on the continuity equation and the momentum equations for unsteady inviscid incompressible flow, with two added terms

$$\nabla \cdot \vec{q} = 0 \tag{2.1}$$

$$\partial_t \vec{q} = -(\vec{q} \cdot \nabla)\vec{q} - \frac{1}{\rho}\nabla p + \mu \nabla^2 \vec{q} + \varepsilon \vec{s} \tag{2.2}$$

where $\vec{q}$, p and ρ are the velocity vector, the pressure and the density, respectively [2][50].

The third term on the right hand side of equation (2.2) is a diffusion term, in which μ is a diffusion coefficient. The last term on the right hand side of equation (2.2) is the confinement term, in which ε is the confinement coefficient. The confinement term can take different forms according to the specific set up of a flow problem. The confinement term can confine the vortical region and keep it from numerical spreading, which is the reason why it is referred to as "vorticity confinement".

2.1.2 The non-conservative vorticity confinement formulation

In the early applications of the vorticity confinement method, a non-conservative confinement formulation was developed [50][51]. The formulation for this non-conservative confinement term is

$$\vec{s} = \vec{n} \times \vec{\omega} \tag{2.3}$$

where

$$\vec{\omega} = \nabla \times \vec{q} \tag{2.4}$$

$$\vec{n} = \nabla |\vec{\omega}| / \left| \nabla |\vec{\omega}| \right| \tag{2.5}$$

from which it can be observed that $\vec{n}$ is a unit vector pointing towards the local maximum of the vorticity magnitude.

This confinement term alters the total momentum of the flow field, thus it is called "non-conservative vorticity confinement".

An alternative way to look at the non-conservative confinement term is to look at the corresponding vorticity equation. By taking the curl of both sides of equation (2.2), assuming ε is constant and using equation (2.3), it yields

$$\left(\frac{\partial \vec{\omega}}{\partial t} + \vec{q} \cdot \nabla \vec{\omega} - \vec{\omega} \cdot \nabla \vec{q} - \mu \nabla^2 \vec{\omega} \right) = \varepsilon \nabla \times (\vec{n} \times \vec{\omega}) \tag{2.6}$$

in which the confinement term is isolated to the right hand side for easier identification. Notice that the pressure term disappears due to the nature of the pressure field, i.e., it acts on the centroid of a mass without generating rotation, thus does not contribute directly to the vorticity dynamics.

Equation (2.6) illustrates a very important property: Although the non-conservative vorticity confinement term does not conserve the total momentum, it conserves the total vorticity.

The confinement term can be split in the following way:

$$\nabla \times \vec{n} \times \vec{\omega} = -\vec{n} \cdot \nabla \vec{\omega} + \hat{n}\left(\nabla \cdot \vec{\omega}\right) + \vec{\omega} \cdot \nabla \vec{n} - \vec{\omega}\left(\nabla \cdot \vec{n}\right) \tag{2.7}$$

The first term convects the vorticity towards the centroid of the vorticity field. The second term vanishes since all curls are solenoidal.

The physical meaning of the remaining two terms are not as clear as the first two. The third term, which is zero for two-dimensional flows, resembles a stretching effect if the $\vec{n}$ vector and the vorticity vector are not perpendicular. As to the last term, since

$$\vec{n} \to \nabla \left| \vec{\omega} \right| \tag{2.8}$$

where "$\to$" means "relate to", it can have

$$\nabla \cdot \vec{n} \to \nabla^2 \left| \vec{\omega} \right| \tag{2.9}$$

which is related to the Laplacian of $\left| \vec{\omega} \right|$ or the smoothness level of the vorticity magnitude field. It can be expected the last two terms to have some effect on the shape of the resulting vortical region.

2.1.3 The conservative vorticity confinement formulation

The most recent development of vorticity confinement method highlights a new conservative formulation [2]. The introduction of the new confinement formulation is based on a mathematical concept called " harmonic mean", on discrete lattices.

The harmonic mean

For a scalar ϕ, the function on a discrete lattice

$$H = \left[\frac{\sum_l C_l (\phi)^{-1}}{\sum_l C_l} \right]^{-1} \tag{2.10}$$

where $\sum_l (\cdot)$ represents the sum over the lattice nodes surrounding a given lattice nodes and C_l is a weight factor, is called the **harmonic mean of** ϕ [2].

For a scalar field on a computational grid, the conservative confinement term can be formed based on the harmonic mean of the scalar field

$$\varepsilon S = -\varepsilon \nabla_d{}^2 \Phi \tag{2.11}$$

where the subscript d means the corresponding difference form to a continuous spatial derivative and

$$\Phi = \left[\frac{\sum_{l=1}^{N} \left(d_l \phi_l \right)^{-1}}{\sum_{l=1}^{N} \left(d_l \right)^{-1}} \right]^{-1} \tag{2.12}$$

in which d_l is the distance from a grid node to its *lth* surrounding node (figure 2-1), which has a scalar value ϕ_l. N is the total number of surrounding nodes. For a uniform Cartesian grid, d_l is set the same for all surrounding nodes (ignoring the corner nodes), thus equation (2.12) can be simplified as

$$\Phi = \left[\frac{\sum_{l=1}^{N} \left(\phi_l \right)^{-1}}{N} \right]^{-1} \tag{2.13}$$

in which N can be set as six for three-dimensional grid and four for two-dimensional grid, resulting in the following index form:

$$\Phi_{i,j,k} = \left[\frac{\left(\phi_{i+1,j,k} \right)^{-1} + \left(\phi_{i-1,j,k} \right)^{-1} + \left(\phi_{i,j+1,k} \right)^{-1}}{6} + \frac{\left(\phi_{i,j-1,k} \right)^{-1} + \left(\phi_{i,j,k+1} \right)^{-1} + \left(\phi_{i,j,k-1} \right)^{-1}}{6} \right] \tag{2.14}$$

for a three dimensional uniform Cartesian grid, and

$$\Phi_{i,j} = \left[\frac{\left(\phi_{i+1,j} \right)^{-1} + \left(\phi_{i-1,j} \right)^{-1} + \left(\phi_{i,j+1} \right)^{-1} + \left(\phi_{i,j-1} \right)^{-1}}{4} \right]^{-1} \tag{2.15}$$

for a two-dimensional uniform Cartesian grid.

Start with the convection equation for a scalar field in difference form

$$\frac{\partial \phi}{\partial t} = -\nabla_d \cdot \left(\vec{q} \phi \right) \tag{2.16}$$

Adding the conservative confinement term and a numerical diffusion term to equation (2.16) yields

$$\frac{\partial \phi}{\partial t} = -\nabla_d \cdot (\vec{q}\phi) + \mu \nabla_d{}^2 \phi - \varepsilon \nabla_d{}^2 \Phi \tag{2.17}$$

where μ and ε are two numerical coefficients for the diffusion term and the confinement term, respectively. Next a similar idea is extended to the vorticity vector field. First apply the harmonic mean to the magnitude of the vorticity field $|\vec{\omega}|$

$$\left|\vec{W}\right| = \left[\frac{\sum_{l=1}^{N} \left(d_l \left| \vec{\omega}_l \right| \right)^{-1}}{\sum_{l=1}^{N} \left(d_l \right)^{-1}} \right]^{-1} \tag{2.18}$$

next the computed mean magnitude is vectorized by

$$\vec{W} = \frac{\vec{\omega}}{\left|\vec{\omega}\right|} \left|\vec{W}\right| \tag{2.19}$$

next a vorticity confinement term is defined as

$$\vec{s} = \nabla_d \times \vec{W} \tag{2.20}$$

substituting into equation (2.17) and transforming it into difference form yields

$$\partial_t \vec{q} = -(\vec{q} \cdot \nabla_d)\vec{q} - \frac{1}{\rho} \nabla_d p + \mu \nabla_d{}^2 \vec{q} + \varepsilon \nabla_d \times \vec{W} \tag{2.21}$$

It can be observed from equations (2.17) and (2.21) that the conservative confinement term does not alter the total momentum (or total magnitude for scalar field). Later in this section, it is proved that the conservative confinement term also preserves the motion of the centroids of several important flow features such as mass and vorticity magnitude.

2.1.4 Analytical solutions of zero convection formulations

Analytical solution for the non-conservative vorticity confinement equation

Analytical solution of the non-conservative vorticity confinement equation for a two dimensional axisymmetric vortex (figure 2-2) in uniform free steam is derived below. Brief derivation can also be found in [51].

Using polar coordinates, the momentum equations for inviscid incompressible flow with added numerical diffusion terms can be written as

$$\begin{aligned}\rho\left(\frac{\partial q_r}{\partial t}+q_r\frac{\partial q_r}{\partial r}+\frac{q_\theta}{r}\frac{\partial q_r}{\partial \theta}-\frac{{q_\theta}^2}{r}\right)&=\mu\left[\frac{\partial}{\partial r}\left(\frac{1}{r}\frac{\partial}{\partial r}\left(rq_r\right)\right)+\frac{1}{r^2}\frac{\partial^2 q_r}{\partial \theta^2}-\frac{2}{r^2}\frac{\partial^2 q_\theta}{\partial \theta}\right]-\frac{\partial p}{\partial r}\\ \rho\left(\frac{\partial q_\theta}{\partial t}+q_r\frac{\partial q_\theta}{\partial r}+\frac{q_\theta}{r}\frac{\partial q_\theta}{\partial \theta}-\frac{q_\theta q_r}{r}\right)&=\mu\left[\frac{\partial}{\partial r}\left(\frac{1}{r}\frac{\partial}{\partial r}\left(rq_\theta\right)\right)+\frac{1}{r^2}\frac{\partial^2 q_\theta}{\partial \theta^2}+\frac{2}{r^2}\frac{\partial^2 q_r}{\partial \theta}\right]-\frac{1}{r}\frac{\partial p}{\partial \theta}\end{aligned} \tag{2.22}$$

Selecting a reference frame moving with the uniform free stream speed, for a two-dimensional axisymmetric concentrated vortex, the following conditions can be imposed

$$\begin{aligned}q_r&=0\\ \frac{\partial q_\theta}{\partial \theta}&=0\\ \frac{\partial p}{\partial \theta}&=0\end{aligned} \tag{2.23}$$

substituting into (2.22), it yields

$$\begin{aligned}-\rho\frac{{q_\theta}^2}{r}&=-\frac{\partial p}{\partial r}\\ \rho\frac{\partial q_\theta}{\partial t}&=\mu\frac{\partial}{\partial r}\left(\frac{1}{r}\frac{\partial}{\partial r}\left(rq_\theta\right)\right)\end{aligned} \tag{2.24}$$

The solution of the second equation of can be easily derived to be

$$q_\theta=\frac{\Gamma}{2\pi r}\left(1-e^{-r^2/4\mu t}\right) \tag{2.25}$$

where Γ is the circulation of the vortex flow. The only possible steady solution is

$$q_\theta=0$$

thus there is no non-trivial steady solution for equation (2.24). Next add in the non-conservative vorticity confinement term. Since

$$\begin{aligned} \hat{n} &= \{n_r, n_\theta\} = \{1, 0\} \\ \hat{n} \times \bar{\omega} &= \{n_\theta \omega_z, -n_r \omega_z\} = \{0, -\omega_z\} \end{aligned} \tag{2.26}$$

substituting into equation (2.24) yields the momentum equation with the non-conservative confinement term added:

$$\begin{aligned} -\rho \frac{{q_\theta}^2}{r} &= -\frac{\partial p}{\partial r} \\ \rho \frac{\partial q_\theta}{\partial t} &= \mu \frac{\partial}{\partial r}\left(\frac{1}{r}\frac{\partial}{\partial r}(r q_\theta)\right) + \varepsilon \frac{1}{r}\frac{\partial}{\partial r}(r q_\theta) \end{aligned} \tag{2.27}$$

Since the pressure is decoupled from the second equation, it enables us to solve for the velocity independently from it. The solution for pressure thus can be derived by substituting the velocity into the first equation. If one is seeking for steady solution, i.e.

$$\frac{\partial q_\theta}{\partial t} = 0 \tag{2.28}$$

The steady solution for the velocity, if exists, should satisfy the following equation

$$\mu \frac{\partial}{\partial r}\left(\frac{1}{r}\frac{\partial}{\partial r}(r q_\theta)\right) + \varepsilon \frac{1}{r}\frac{\partial}{\partial r}(r q_\theta) = 0 \tag{2.29}$$

The solution of equation (2.29) can be obtained by solving the following equations

$$\begin{aligned} \mu \frac{\partial Q}{\partial r} &= -\varepsilon Q \\ Q &= \frac{1}{r}\frac{\partial}{\partial r}(r q_\theta) \end{aligned} \tag{2.30}$$

The first equation has a solution of the form

$$Q = Q_0 e^{-r\varepsilon/\mu} \tag{2.31}$$

where Q_0 is an arbitrary constant. Substituting into the second equation of (2.30) yields

$$Q_0 e^{-r\varepsilon/\mu} = \frac{1}{r}\frac{\partial}{\partial r}(r q_\theta) \tag{2.32}$$

which has the general solution

$$q_\theta = \frac{-a^2 Q_0}{r}(r/a + 1)e^{-r/a} + \frac{a}{r}Q_1 \tag{2.33}$$

where Q_1 is another arbitrary constant that needs to be determined by boundary conditions, and

$$a = \mu / \varepsilon \tag{2.34}$$

The solution can be simplified further as

$$q_\theta = \frac{C_1}{r}\left(1 - C_2\left(1 + r/a\right)e^{-r/a}\right) \tag{2.35}$$

where C_1 and C_2 are constants to be determined by the flow conditions. For flow induced by a concentrated vortex with circulation Γ

$$\oint_{r\to\infty} q_\theta dr = \Gamma \tag{2.36}$$

substituting into equation (2.35) gives

$$C_1 = \frac{\Gamma}{2\pi} \tag{2.37}$$

Also it requires the vorticity magnitude be finite when $r \to 0$, which gives

$$C_2 = 1 \tag{2.38}$$

Finally the exact solution can be written as

$$q_\theta = \frac{\Gamma}{2\pi r}\left(1 - \left(1 + r/a\right)e^{-r/a}\right) \tag{2.39}$$

which defines an axisymmetric vortex, whose core size is determined by the ratio

$$a = \mu / \varepsilon \tag{2.40}$$

Non-convection solution for the conservative vorticity confinement equation

As a simple first step, the diffusion term and confinement term are isolated from equation (2.17) and a solution of the following equation

$$\nabla_d{}^2(\mu\phi - \varepsilon\Phi) = 0 \tag{2.41}$$

is derived in a uniform Cartesian grid. It is assumed that μ and ε are constant.

At the end of this chapter, the topic of fast and slow varying variables is addressed. Equation (2.41) describes the dynamics of variables whose convergence rate is

much faster than other variables in the momentum equation, thus the solution derived here can represent the solution of the dynamical behavior of the fast variables. This argument follows that of reference [2].

For Laplace equation

$$\nabla^2 \phi = 0 \tag{2.42}$$

the maximum principle implies:

If the Laplacian of a function vanishes everywhere in a region and the function is zero on the boundary, then it is zero everywhere.

Approximating this property in a discretized way, if one has

$$\nabla_d^{\,2}(\mu\phi - \varepsilon\Phi) = 0 \tag{2.43}$$

and

$$\mu\phi - \varepsilon\Phi = 0 \tag{2.44}$$

on the boundary, it gives

$$\mu\phi - \varepsilon\Phi = 0 \tag{2.45}$$

everywhere.

Assuming the boundary conditions stated in equation (2.44), and one can seek for the solution of

$$\mu\phi - \varepsilon\Phi = 0 \tag{2.46}$$

as a valid solution for equation (2.41).

The simplest solution would be a 1-D solution for a pulse, for which

$$\Phi_i = 2\left(\frac{1}{\phi_{i-1}} + \frac{1}{\phi_{i+1}}\right)^{-1} \tag{2.47}$$

substituting this into equation (2.46) and after some rearrangement of terms, it yields

$$\frac{1}{\phi_i} = \frac{a}{2}\left(\frac{1}{\phi_{i-1}} + \frac{1}{\phi_{i+1}}\right)$$
$$a = \frac{\mu}{\varepsilon} \tag{2.48}$$

Defining

$$f(x_i) = \frac{1}{\phi_i} \tag{2.49}$$

where x_i is the coordinate of the grid point with index number *i*. Substituting equation (2.49) into equation (2.48) gives

$$f(x_i) = \frac{a}{2}\left(f(x_{i+1}) + f(x_{i-1})\right) \tag{2.50}$$

Denote the grid spacing as Δx, the coordinate can be written as

$$x_i = x_0 + (i-1)\Delta x \tag{2.51}$$

where x_0 is the coordinate for the grid node with index 1. To make it simple, it is supposed that

$$x_0 = 0 \tag{2.52}$$

The following function satisfies equation (2.50):

$$f(x_i) = c_1 e^{-\beta i \Delta x} + c_2 e^{\beta i \Delta x} \tag{2.53}$$

where β must satisfy the following relation

$$\beta = \sec h^{-1}(a) \tag{2.54}$$

and c1 and c2 are constants to be determined by the boundary conditions. Finally the general solution for equation (2.48) is

$$\phi_i = \left(c_1 e^{-\beta i \Delta x} + c_2 e^{\beta i \Delta x}\right)^{-1} \tag{2.55}$$

For a one-dimensional pulse with a maximum scalar value of 1 with symmetric boundary conditions (figure 2-3), one has

$$C_1 = C_2 \tag{2.56}$$

and

$$\phi_i = \frac{1}{c_1}\left(e^{-\beta i\Delta x} + e^{\beta i\Delta x}\right)^{-1} = \sec h\left(\beta i\Delta x - \beta_0\right) \tag{2.57}$$

where β_0 is the centroid of the pulse. Look back to equation (2.54), which can be rewritten as

$$\sec h\beta = a$$

So the solution of the form (2.57) exists for

$$a \le 1$$

which requires

$$\varepsilon \ge \mu$$

For

$$\varepsilon = \mu$$

the solution degenerates into a constant, which is trivial, thus the condition for nontrivial solution of equation (2.46) is

$$\varepsilon > \mu$$

Again, similar to the solution for concentrated vortex, the width of the resulting pulse is determined by the ratio of

$$a = \mu / \varepsilon \tag{2.58}$$

Unlike the previously discussed analytical solution for the non-conservative formulation, other than being an analytical solution to a continuous equation, this solution is an exact solution to the difference equation (2.41).

2.1.5 Properties with convection, preservation of centroid

It can be proved that for the conservative confinement formulation, the motion of the centroids of many flow properties is preserved. In reference [2], the preservation of the centroid of a convecting scalar field is discussed, although a detailed derivation is not presented.

For a difference equation

$$\frac{\partial \phi}{\partial t} = L_d(\phi) + \delta_d{}^2 A \tag{2.59}$$

where $\delta_d{}^2$ represent second derivative difference operator in space. ϕ can be a scalar or a component of a vector. A is an arbitrary scalar. L_d is a function that can take both derivatives and vectors as operators. For example, for the a scalar convection equation (2.17)

$$L_d(\phi) = \nabla_d \cdot (\vec{q}\phi) \tag{2.60}$$

Define L_c and $\delta_c{}^2$ to be central difference formulae for L_d and $\delta_d{}^2$, respectively. Equation (2.59) can be written in central difference form as

$$\frac{\partial \phi}{\partial t} = L_c(\phi^n) + \delta_c{}^2 A^n \tag{2.61}$$

Define

$$<\psi> \equiv \sum_{\Omega} \phi \tag{2.62}$$

and

$$<\hat{X}>^n \equiv \sum_{\Omega} (\hat{x}\phi^n) / <\psi> \tag{2.63}$$

where $\sum_{\Omega}$ represents the sum over all the grid nodes of a computational grid, and $\hat{x}$ is the physical coordinate of a given node. Multiplying both sides of (2.61) by $\frac{\hat{x}}{<\psi>}$ and taking the sum over the whole field gives

$$\frac{1}{<\psi>}\sum_{\Omega} \hat{x}\frac{\partial}{\partial t}\phi = \frac{1}{<\psi>}\sum_{\Omega} \hat{x}L_c(\phi) + \frac{1}{<\psi>}\sum_{\Omega} \hat{x}\delta_c{}^2 A \tag{2.64}$$

The following property can be proved:

$$\sum_{\Omega} \hat{x}\delta_c{}^2 A = 0 \tag{2.65}$$

The detailed derivation of this property is placed in appendix II. The last term in equation

(2.64) is zero according to the property (2.65).

For a conservative variable ϕ, the following property can be assumed:

$$< \psi >= const \tag{2.66}$$

Using (2.65) and (2.66), equation (2.64) is simplified into

$$\frac{\partial}{\partial t}\sum_{\Omega}\frac{\hat{x}}{< \psi >}\phi = \sum_{\Omega}\frac{\hat{x}}{< \psi >}L_c(\phi) \tag{2.67}$$

or

$$\frac{\partial}{\partial t} < \hat{X} >= \sum_{\Omega}\frac{\hat{x}}{< \psi >}L_c(\phi) \tag{2.68}$$

The left hand side of equation (2.68) represents the evolution of the centroid. It can be observed that adding a second spatial derivative in central difference form does not change the centroid motion of a scalar or a vector component. The scalar confinement equation (2.17) and the vorticity confinement equation (2.18) in component forms belong to the class of equations represented by equation (2.59). Since the confinement terms are all second spatial derivatives, the centroid motion of a scalar field or a velocity field is not altered by adding either the scalar confinement term or the vorticity confinement term.

Define the weighted mean velocity as

$$< Q >^n = \frac{\sum_{\Omega}\left(\vec{q}^n\phi^n\right)\cdot\vec{I}}{< \psi >} \tag{2.69}$$

The centroid motion of the scalar confinement equation (2.17) can be derived to be

$$\left\langle \hat{X} \right\rangle^{n+1} = \left\langle \hat{X} \right\rangle^{n} + \Delta t \left\langle Q \right\rangle^{n} \tag{2.70}$$

where $\vec{I} = (1,1,1)$ is an identity vector. Detailed derivation of equation (2.70) can be found in appendix II.

2.1.6 Fast and slow variables

There is a very important property associated with the confinement terms. The two confinement parameters, ε and μ, are determined by the two small scales of the computation, the cell size and the time step. The flow can relax to a converged vortical structure in a small number of time steps and involve only a small number of grid cells surrounding the vortical region [2]. The time scale and the length scale thus are of a "computational" type, which is much smaller than the real corresponding physical time and length scales in most numerical simulations. The variation rate of the "outer" irrotational flow field by contrast is in accordance with the much larger physical scales. This forms a two-scale problem: a fast dynamical process for the internal structure of the convecting vortical region, which is governed by the following dynamical equation:

$$\mu\nabla^2\vec{q} + \varepsilon\vec{s} \approx 0 \tag{2.71}$$

and a slower dynamical system that can be approximated by the inviscid Euler Equation

$$\partial_t\vec{q} = -(\vec{q}\cdot\nabla)\vec{q} - \frac{1}{\rho}\nabla p \tag{2.72}$$

2.2 Discretization of the Confinement Formulation and the Fractional Step Method

To make the description concise, a list of difference operators is defined here first. In this section, only uniform Cartesian grid is considered. Unless specified otherwise, all the discussion in this section is subject to computations on uniform Cartesian grid.

1) First order forward difference operator for time derivative:

$$\delta_t(\cdot) = \frac{(\cdot)^{n+1} - (\cdot)^n}{\Delta t} \tag{2.73}$$

2) Central difference formulae for first order spatial derivatives:

$$\begin{aligned}\delta_i(\cdot) &= \frac{(\cdot)_{i+1,j,k} - (\cdot)_{i-1,j,k}}{2\Delta x} \\ \delta_j(\cdot) &= \frac{(\cdot)_{i,j+1,k} - (\cdot)_{i,j-1,k}}{2\Delta y} \\ \delta_k(\cdot) &= \frac{(\cdot)_{i,j,k+1} - (\cdot)_{i,j,k-1}}{2\Delta y}\end{aligned} \tag{2.74}$$

3) Central difference formulae for second order spatial derivatives:

$$\begin{aligned}\delta_i^2(\cdot) &= \frac{(\cdot)_{i+1,j,k} - 2(\cdot)_{i,j,k} + (\cdot)_{i-1,j,k}}{\Delta x^2} \\ \delta_j^2(\cdot) &= \frac{(\cdot)_{i,j+1,k} - 2(\cdot)_{i,j,k} + (\cdot)_{i,j-1,k}}{\Delta y^2} \\ \delta_k^2(\cdot) &= \frac{(\cdot)_{i,j,k+1} - 2(\cdot)_{i,j,k} + (\cdot)_{i,j,k-1}}{\Delta z^2}\end{aligned} \tag{2.75}$$

which apply to both scalar and vector variables.

2.2.1 The fractional step method

Typical applications of Confinement method to incompressible flow on uniform Cartesian grid have been solved with a completely explicit fractional-step scheme [18][32], which is described below.

Starting with the governing confinement model equation

$$\partial_t \vec{q} = -(\vec{q} \cdot \nabla)\vec{q} - \frac{1}{\rho}\nabla p + [\mu \nabla^2 \vec{q} + \varepsilon \vec{s}] \tag{2.76}$$

The first order forward difference operator for time derivative is used for time discretization.

$$\delta_t \vec{q} = \frac{\vec{q}^{n+1} - \vec{q}^{n}}{\Delta t} \tag{2.77}$$

substituting this into equation (2.76) leads to

$$\vec{q}^{n+1} = \vec{q}^{n} - \Delta t\left(\vec{q}^{n} \cdot \nabla\right)\vec{q}^{n} - \frac{\nabla t}{\rho}\nabla p^{n} + \nabla t\mu\nabla^2\vec{q}^{n} + \Delta t\varepsilon\vec{s}^{n} \tag{2.78}$$

To eliminate pressure and density from the equation (2.78), a pressure function is introduced as

$$\varphi = -\frac{\left(p - p_{\infty}\right)}{\rho} \tag{2.79}$$

so that p and ρ do not occur explicitly. It follows that

$$\nabla\varphi = -\frac{1}{\rho}\nabla p \tag{2.80}$$

Thus the final equation to perform the fractional step scheme is

$$\vec{q}^{n+1} = \vec{q}^{n} - \Delta t\left(\vec{q}^{n} \cdot \nabla\right)\vec{q}^{n} + \Delta t\nabla\varphi^{n} + \Delta t\mu\nabla^2\vec{q}^{n} + \Delta t\varepsilon\vec{s}^{n} \tag{2.81}$$

A fractional step method which approximately solves the above equation can be described as a five-step scheme as below [18][32].

Convection step

The computation based on the following space discretized formulation is performed to simulate the convection step

$$\vec{q}\,' = \vec{q}^{n} - \Delta t\left(\vec{q}^{n} \cdot \nabla\right)\vec{q}^{n} \tag{2.82}$$

Artificial diffusion step

$$\vec{q}\,'' = \vec{q}\,' + \Delta t\mu\nabla^2\vec{q}\,' \tag{2.83}$$

Normally maximum diffusion allowed by instability limit can be added in this step. This is very different from traditional methods, where excessive artificial diffusion should be avoided by all means.

Confinement step

$$\vec{q}''' = \vec{q}'' + \Delta t \varepsilon \vec{s}'' \tag{2.84}$$

where $\vec{s}^{*}$ is the confinement term calculated based on $\vec{q}^{*}$. This is the heart of the confinement method. A nonlinear confinement term is added to keep the vortical region from spreading due to the artificial diffusion introduced by the previous step, while at the same time trying to simulate the dynamics of the vortical region.

Poisson solver for the pressure

Next step is to solve for the pressure function φ. The conservation of mass requires

$$\nabla \cdot \vec{q}^{\,n+1} = 0 \tag{2.85}$$

thus φ must be computed such that

$$\nabla \cdot \vec{q}^{\,n+1} = \nabla \cdot \left(\vec{q}''' + \Delta t \nabla \varphi''' \right) = 0 \tag{2.86}$$

which yields the Poisson equation

$$\nabla^2 \varphi''' = -\frac{1}{\Delta t} \nabla \cdot \vec{q}''' \tag{2.87}$$

Any properly selected Poisson solver can be used to derive the pressure from equation (2.87). In most of the past applications of the confinement method on uniform Cartesian grids [1][2][13][14][17][18][19][54], a direct Cartesian grid Poisson solver, FORTRAN subprograms HW3CRT and HWSCRT of "FISHPACK" [59], is used for three-dimensional and two-dimensional Poisson equation solutions respectively. This fast direct solver is also used in present study. Since it requires that both the equation and the boundary conditions be separable, this solver may not apply to complex geometries or to complicated boundary conditions that lead to non-separable equations. More information about "FISHPACK" can be found in reference [59].

Mass and momentum conservation step

$$\vec{q}^{n+1} = \vec{q}''' + \Delta t \nabla \varphi''' \tag{2.88}$$

The gradient of the pressure derived from the last step is added to the velocity field. This step completes the momentum equation. Mass conservation is also enforced, since

$$\nabla \cdot \vec{q}^{n+1} = \nabla \cdot \left(\vec{q}''' + \Delta t \nabla \varphi''' \right) = \Delta t \nabla^2 \phi''' + \nabla \cdot \vec{q}''' = 0 \tag{2.89}$$

2.2.2 New formulations for the vorticity confinement method

In the existing literature [1][2][13][14][17][18][19], a large part of the difference scheme is based on staggered grids, where two types of grids are used for different parts of the fractional step scheme: a velocity grid and a pressure grid. Typically the velocity grid is based on grid nodes, while the pressure grid uses grid centers. The "FISHPACK" Poisson solver is performed on the pressure grid. The vorticity confinement term requires the use of both grids. Other parts of the computation are based solely on the velocity grid. One can refer to the literature for more details.

In the new scheme described in this context, only the grid nodes are used for all parts of the computation. By eliminating the usage of a staggered grid, the numerical scheme can be greatly simplified. The complex algorithms for calculating the confinement term are avoided in the new scheme.

Convection step

Central difference and conservative forms should be used for the convection step. This addresses two problems. First it is important to have full control over when and how to add the artificial diffusion, so central difference scheme is used to avoid introducing the non-homogenous diffusion by a biased convection scheme. Second, the conservation of momentum and the preservation of the centroids of many flow properties are essential

for accurately simulating the dynamics of the vortical features.

The momentum equation for 3-D incompressible flow can be written in conservative forms as

$$\begin{aligned}
&\frac{\partial u}{\partial t}+\frac{\partial uu}{\partial x}+\frac{\partial uv}{\partial y}+\frac{\partial uw}{\partial z}=-\frac{1}{\rho}\frac{\partial p}{\partial x}+\mu\left(\frac{\partial^2 u}{\partial x^2}+\frac{\partial^2 u}{\partial y^2}+\frac{\partial^2 u}{\partial z^2}\right)\\
&\frac{\partial v}{\partial t}+\frac{\partial uv}{\partial x}+\frac{\partial vv}{\partial y}+\frac{\partial vw}{\partial z}=-\frac{1}{\rho}\frac{\partial p}{\partial y}+\mu\left(\frac{\partial^2 v}{\partial x^2}+\frac{\partial^2 v}{\partial y^2}+\frac{\partial^2 v}{\partial z^2}\right)\\
&\frac{\partial w}{\partial t}+\frac{\partial uw}{\partial x}+\frac{\partial vw}{\partial y}+\frac{\partial ww}{\partial z}=-\frac{1}{\rho}\frac{\partial p}{\partial z}+\mu\left(\frac{\partial^2 w}{\partial x^2}+\frac{\partial^2 w}{\partial y^2}+\frac{\partial^2 w}{\partial z^2}\right)
\end{aligned} \tag{2.90}$$

in which constant μ is assumed. For the convection step, the following difference equations are used

$$\begin{aligned}
u' &= u^n-\Delta t\left(\delta_i\left(u^n u^n\right)+\delta_j\left(u^n v^n\right)+\delta_k\left(u^n w^n\right)\right)\\
v' &= v^n-\Delta t\left(\delta_i\left(u^n v^n\right)+\delta_j\left(v^n v^n\right)+\delta_k\left(v^n w^n\right)\right)\\
w' &= w^n-\Delta t\left(\delta_i\left(u^n w^n\right)+\delta_j\left(v^n w^n\right)+\delta_k\left(w^n w^n\right)\right)
\end{aligned} \tag{2.91}$$

where the difference operators are the central difference operators defined earlier in formulae (2.74).

Diffusion step

A standard central difference scheme (2.75) is used for the second spatial derivatives

$$\vec{q}\,'' = \vec{q}\,' + \mu\Delta t\left(\delta_i^2\vec{q}\,' + \delta_j^2\vec{q}\,' + \delta_k^2\vec{q}\,'\right) \tag{2.92}$$

According to the past experience, this type of homogenous diffusion is the optimum type of numerical diffusion for the confinement method. Maximum diffusion could be added as long as it does not exceed the instability limit. But for better accuracy, maximum diffusion is not recommended, which will be discussed later in detail. The detailed stability analysis is also discussed later when selecting the numerical coefficients for the computations.

Vorticity confinement step

a) Non-conservative confinement formulation

Unlike the past applications, the vorticity field is calculated directly at each grid node using the previously defined standard difference operators (2.74) for first order derivatives

$$\begin{aligned}\vec{\omega}'' &= \left(\omega''_x, \omega''_y, \omega''_z\right)^T \\ &= \left(\delta_j\left(w''\right) - \delta_k\left(v''\right), \delta_k\left(u''\right) - \delta_i\left(w''\right), \delta_i\left(v''\right) - \delta_j\left(u''\right)\right)^T\end{aligned} \tag{2.93}$$

The $\hat{n}$ vector is also calculated on the grid nodes, by directly calculating the gradient of the vorticity magnitude

$$\hat{n} = \left(n_x, n_y, n_z\right)^T = \frac{\nabla\left|\vec{\omega}''\right|}{\left|\nabla\left|\vec{\omega}''\right|\right|} \tag{2.94}$$

which is a unit vector pointing towards the local centroid of the vortical region. The difference schemes for calculating the gradient are

$$\begin{aligned}\nabla\left|\vec{\omega}''\right| &= \left(\delta_i\left(\left|\vec{\omega}''\right|\right), \delta_j\left(\left|\vec{\omega}''\right|\right), \delta_k\left(\left|\vec{\omega}''\right|\right)\right)^T \\ \left|\nabla\left|\vec{\omega}''\right|\right| &= \left(\left(\delta_i\left(\left|\vec{\omega}''\right|\right)\right)^2 + \left(\delta_j\left(\left|\vec{\omega}''\right|\right)\right)^2 + \left(\delta_k\left(\left|\vec{\omega}''\right|\right)\right)^2\right)^{1/2}\end{aligned} \tag{2.95}$$

The vorticity confinement term thus can be calculated at each grid node by

$$\delta\vec{q}''' = \varepsilon\vec{s} = \varepsilon\hat{n}\times\vec{\omega}'' = \varepsilon\left(n_y\omega''_z - n_z\omega''_y, n_z\omega''_x - n_x\omega''_z, n_x\omega''_y - n_y\omega''_x\right)^T \tag{2.96}$$

The confinement term is applied directly to the velocity field on the grid nodes by

$$\vec{q}''' = \vec{q}'' + \Delta t\delta\vec{q}''' \tag{2.97}$$

b) Conservative confinement formulation

The same vorticity vector field calculated by equation (2.93) is used for conservative formulation of the vorticity confinement term.

The formula for calculating the harmonic mean is also based purely on grid nodes

$$\vec{W}''_{i,j,k} = \left(W''_x, W''_y, W''_z\right)^T$$
$$= 6\frac{\vec{\omega}''_{i,j,k}}{\left|\vec{\omega}''_{i,j,k}\right|}\left[\left(\left|\vec{\omega}''_{i+1,j,k}\right|\right)^{-1} + \left(\left|\vec{\omega}''_{i-1,j,k}\right|\right)^{-1} + \left(\left|\vec{\omega}''_{i,j+1,k}\right|\right)^{-1}\right. \tag{2.98}$$
$$\left. + \left(\left|\vec{\omega}''_{i,j-1,k}\right|\right)^{-1} + \left(\left|\vec{\omega}''_{i,j,k+1}\right|\right)^{-1} + \left(\left|\vec{\omega}''_{i,j,k-1}\right|\right)^{-1}\right]^{-1}$$

Next the curl of $\vec{W}''$ is computed by using the standard central difference formulae (2.74) for first derivatives

$$\nabla \times \vec{W}'' = \left(\delta_j W''_z - \delta_k W''_y, \delta_k W''_x - \delta_i W''_z, \delta_i W''_y - \delta_i W''_x\right)^T \tag{2.99}$$

The confinement correction to the velocity field is calculated by

$$\delta\vec{q}''' = \varepsilon\nabla \times \vec{W}'' \tag{2.100}$$

which is added to the velocity as

$$\vec{q}''' = \vec{q}'' + \Delta t\delta\vec{q}''' \tag{2.101}$$

In the past, the vorticity vectors are first calculated on grid centers. The harmonic mean is performed purely on grid center and has to use an upwind-weighted averaging to avoid a numerical instability problem named "thin spreading"[2], which features a thin spreading of pulses in the direction normal to their motion (see reference [2] for more details). For a three- dimensional uniform Cartesian grid, the harmonic mean involves 27 grid centers for each calculation [2]. By comparison, the new scheme uses only 6 grid nodes for calculating a harmonic mean. Also because the new scheme does not exhibit the "thin spreading" phenomena, no upwind weighting is needed. The numerical scheme for calculating the vorticity confinement term can be made much simpler than the old scheme.

Both the conservative and non-conservative formulations of the vorticity confinement term require little additional numerical complication over the standard central difference schemes, which make them very easy to be adapted for non-uniform Cartesian grid or curvilinear grid systems.

Mass and Momentum conservation step

First the right hand side of equation (2.87) is calculated using the standard central difference scheme for first order derivatives

$$\nabla \cdot \vec{q}''' = \delta_i u''' + \delta_j v''' + \delta_k w''' \tag{2.102}$$

The "FISHPACK" Poisson solver is used to solve equation (2.87), yielding a pressure field φ'''. The mass correction is calculated as

$$\delta \vec{q}'''' = \Delta t \left(\delta_i \varphi''', \delta_j \varphi''', \delta_k \varphi''' \right)^T \tag{2.103}$$

Finally the velocity field at the next time step is obtained by adding the mass correction to the velocity field

$$\vec{q}^{\,n+1} = \vec{q}''' + \delta \vec{q}'''' \tag{2.104}$$

This finishes the entire process of updating the velocity field for one time step.

2.2.3 Boundary conditions

Definition of the surface, the F function

A level set function F is defined at each grid node, which satisfies the following conditions:

$$\begin{cases} F > 0, \textit{for points outside the body} \\ F = 0, \textit{for points on the surface} \\ F < 0, \textit{for points inside the body} \end{cases} \tag{2.105}$$

And a filter function is defined as

$$\lambda(F) = \begin{cases} 1, & F > 0 \\ 0, & F \le 0 \end{cases} \tag{2.106}$$

Surface boundary conditions

a) No-slip surface boundary conditions for velocity field

The no-slip boundary condition for the velocity field on a stationary surface can be applied using the filter function as

$$\vec{q}_u = \lambda(F)\vec{q} \tag{2.107}$$

in which $\vec{q}_u$ means the updated velocity vector.

b) Surface condition for pressure field

Due to the fact that no body conforming grid is used and the "FISHPACK" Poisson solver does not allow explicitly specified surface conditions, there are no explicit surface boundary conditions specified for the pressure. However, the no-slip velocity boundary condition can be approximately regarded as an implicitly enforced Neumann-type pressure condition [22]. Apply the no-slip condition to the momentum equation without confinement

$$\frac{\partial \vec{q}}{\partial t} + \vec{q} \cdot \nabla \vec{q} = -\frac{1}{\rho}\nabla p + \mu \nabla^2 \vec{q} \tag{2.108}$$

on the wall it gives

$$\frac{1}{\rho}\nabla p = \mu \nabla^2 \vec{q} \tag{2.109}$$

On the wall, all the derivatives of the velocity in the tangential direction disappear due to $\vec{q} \equiv 0$. So in the direction normal to the surface, one has

$$\frac{1}{\rho}\frac{\partial p}{\partial n} = \mu \frac{\partial^2 q_n}{\partial n^2} \tag{2.110}$$

As long as the flow does not separate from the wall, it turns out to be

$$\frac{\partial p}{\partial n} \approx 0 \tag{2.111}$$

However, for surface region where separation presents, additional explicit surface pressure condition may be necessary for reasonably accurate solutions.

Far field boundary conditions

a) Far field pressure condition

On the inlet boundaries, the pressure is specified to be the pressure at the infinity to ensure a correct free stream pressure input:

$$p_{in} = p_{\infty} \tag{2.112}$$

On all other far field boundaries, the following condition is imposed to insure that there is no pressure constraints enforced by the free boundaries:

$$\frac{\partial p}{\partial n} = 0 \tag{2.113}$$

b) Far field velocity condition

On the inlet boundaries, the velocity is specified to be the free stream velocity:

$$\vec{q}_{in} = \vec{q}_{\infty} \tag{2.114}$$

On all other far field boundaries, the velocity is extrapolated from the inner velocity field by specifying

$$\frac{\partial \vec{q}}{\partial n} = 0 \tag{2.115}$$

2.3 Numerical Experiments

Numerical studies using the methods described in the previous sections are presented in this section to test the most basic and most important properties of the vorticity confinement method: to convect concentrated vortices accurately and without spreading of the vortex core. The method is tested for two cases: a single concentrated vortex convecting in a uniform free stream and a pair of concentrated vortices with opposite strengths convecting in their mutually induced velocity field. The translating velocity for both cases is set up to be much smaller than the maximum velocity around the vortex core, which is a strong case for testing the accuracy of the numerical method.

The induced velocity by the vortex is the dominant velocity component for a single convecting vortex, and for the vortex pair, the induced velocity is the only component of the velocity field. So the induced velocity must be accurately computed to ensure the correct trajectory of the vortices.

Unless specified, for both cases, a 128 x 128 cell grid is used, the cell size is normalized to be 1. The circulation of the vortices is specified as $\Gamma = 2\pi$. The initial velocity magnitude induced by each single vortex is specified as

$$\begin{cases} 1/r & for \quad r > 1 \\ r & for \quad r \le 1 \end{cases} \tag{2.116}$$

in which r is the distance from a given grid node to the vortex center. Thus the maximum induced velocity will be 1 for each single vortex.

Assuming constant diffusion coefficient, the necessary and sufficient stability condition for a linearized Euler equation with diffusion term requires [21]

$$\sum_{n=1}^{N} \sigma_m{}^2 \le 2 \max \left\{ \frac{\mu \Delta t}{\Delta x_l{}^2}, l = 1, 2, ..., N \right\} \le \frac{1}{N} \tag{2.117}$$

where N is the dimension of the space and

$$\sigma_l = \frac{q_l \Delta t}{\Delta x_l} \tag{2.118}$$

For the computation in the present study

$$\Delta x_l \equiv 1 \tag{2.119}$$

Substituting (2.118) and (2.119) into (2.117) yields

$$\frac{|\vec{q}|^2 \Delta t}{2} \le \mu \le \frac{1}{2 \Delta t N} \tag{2.120}$$

The maximum velocity magnitude is 1 and N is 2 for the present study, the time step thus must satisfy

$$\Delta t \le (0.5)^{1/2} \approx 0.707$$

For unsteady problems, a smaller time step should give better accuracy. The time step for

the present study is selected as

$$\Delta t = 0.2$$

which results a CFL number of 0.2 based on the maximum induced velocity. The diffusion coefficient is selected as

$$\mu = 0.1$$

which is close to the minimum required by relation (2.120). The confinement coefficient is selected as

$$\varepsilon = 1.4\mu = 0.14$$

According to equation (2.39), it should result in a radius of 2 to 3 cells for the vortex core computed with the non-conservative confinement.

It is observed in the computations that although maximum diffusion coefficient can be used, the accuracy of the solution may be affected by numerical errors. Using the minimum allowed diffusion coefficient seems to give the best results.

Vorticity contours are plotted from one third of the maximum value to the maximum value of the vorticity magnitude. The total number of time steps for each computation is 5000, and the total computation time is about one minute on an AMD 1.7Ghz PC. The vorticity contours are plotted in one single figure for every 1000 time steps. The trajectories computed using an analytical solution are also incorporated using solid lines with markers indicating the exact positions of the vortices. Plots of velocity field around the vortex cores at the time steps 1000 and 5000 are also shown for each case.

2.3.1 A single vortex convecting in a weak free stream

In the first case, a single vortex is convecting in a uniform free stream with $u_\infty = 0.04$ and $v_\infty = 0.03$, which is the velocity in x direction and y direction, respectively. With a time step 0.2, the vortex should have traveled 40 unit cells in the x

direction and 30 unit cells in y direction after 5000 time steps. Figure 2-4 shows the initial velocity field for the computation. Figure 2-5 shows the velocity distribution according to r. The horizontal axis denotes r, and the vertical axis denotes the velocity magnitude, which is normalized by

$$\begin{cases} \left(|\vec{q}| - \vec{q}_\infty\right) r & for \quad r > 1 \\ |\vec{q}| - \vec{q}_\infty & for \quad r \le 1 \end{cases} \tag{2.121}$$

After the normalization, the initial velocity field becomes

$$\begin{cases} 1 & for \quad r > 1 \\ 1/r & for \quad r \le 1 \end{cases} \tag{2.122}$$

The normalized velocities for all the grid points with r less than 40 are plotted as circles within a same plot.

The radius r is obtained by calculating the centroid of the vorticity field:

$$r_{i,j} = \left(\left(x_{i,j} - \frac{\sum_{\Omega} |\vec{\omega}| x}{\sum_{\Omega} |\vec{\omega}|} \right)^2 + \left(y_{i,j} - \frac{\sum_{\Omega} |\vec{\omega}| y}{\sum_{\Omega} |\vec{\omega}|} \right)^2 \right)^{1/2} \tag{2.123}$$

Figures 2-6 and 2-8 show the velocity vector plots for computation without vorticity confinement after 1000 and 5000 time steps, respectively. As expected, the vortex spreads very quickly due to the artificial diffusion. From the normalized velocity distribution plots (figure 2-7 and figure 2-9), if the vortex radius of the vortex core is defined up to the points with normalized velocity value 0.9, it can be observed that the size of the vortex core has spread to a radius bigger than 13 grid cells after 1000 time steps, and bigger than 30 cells after 5000 time steps. The analytical solutions for the velocity distribution computed using equation (2.25) are also plotted in figure 2-7 and figure 2-9. According to equation (2.25), the vortex core should spread to a radius of 13.6 cells after 1000 time steps and 30.3 cells after 5000 time steps. The computation agrees well with this analysis. There is some spreading of the velocity values, especially when

the radii get big, which may be caused by the error generated when calculating the radius using equation (2.123).

Next the non-conservative confinement formulation is used. Since the non-conservative formulation does not preserve the centroid motion, from the contour plot (figure 2-22) it can be observed that the vortex does not move correctly according to the analytical solution. At the time step 5000, the vortex center is off for about 7 cells compared to the analytical solution. The contours also exhibit some distortion of the vortex shape. Figure 2-10 and figure 2-12 show the velocity fields after 1000 time steps and 5000 time steps. Figure 2-11 and figure 2-13 show the corresponding normalized velocity distribution, from which the radius of the vortex core is hard to tell due to the large spreading of the values of grid nodes with similar radius. This spreading may be resulted because of the velocity fields are not very smooth. The other factor that may cause the spreading is the error generated in calculating the radius. Since the non-conservative confinement term needs to calculate the n vector on a very coarse grid, the resulting n vector field may not be very smooth, especially near the vortex core. For the last term of equation (2.7), one can see that the smoothness of the n vector field may have effect on the shape of the vortex.

The results using the conservative formulation are plotted in figure 2-14, figure 2-15, figure 2-16, figure 2-17 and figure 2-23. From figure 2-23, it can be observed that the movement of the vortex is in agreement with the analytical solution. The disparity is less than 1 grid cell, which is the resolution limit of the grid. What can also be observed in the figure 2-23 is that compared to the results from the non-conservative vorticity confinement, the contour of the vortex is more rounded. The vector plot (figure 2-14 and figure 2-16) also shows a smoother vector field obtained by the conservative confinement formulation. The velocity distributions after 1000 time steps and 5000 time steps can be found in figure 2-15 and 2-17, respectively. The radius of the vortex is about 3 cells according these plots. Much less spreading of the normalized velocities can be observed compared to the results from the non-conservative confinement.

Figure 2-24 shows the contour plot for the results obtained by the old numerical scheme using the non-conservative confinement [18][19]. The vortex moves much slower than that according to the exact solution. The velocity vector plots and vorticity contour plots are shown in figure 2-18, figure 2-19, figure 2-20 and figure 2-21. Compared to the results from the new numerical scheme with the non-conservative confinement, one can see some improvement of the new scheme over the old one on resolving the movement of the vortex. The trajectories of the vortex for the various computations are shown together in figure 2-25.

It can be observed from the figures that the non-conservative confinement using the new numerical scheme results more compact vortex cores than those from the conservative confinement and the old confinement scheme. The maximum vorticity magnitude after 1000 time steps is around 0.8 for the former case and only 0.4 for the latter two cases. This is expected since the new scheme for the non-conservative confinement formulation does not involve averaging over the surrounding cells, while the conservative scheme requires calculating the harmonic mean and the old scheme applies several averaging processes to both the vorticity field and the n vector field. The drawback for not applying any averaging processes may be that the resulting velocity fields are not as smooth as those involve some averaging procedures. It should be mentioned that if it is necessary, one could also apply smoothing to the n vector for the new scheme.

2.3.2 A vortex pair convecting in mutually induced velocity field

In the second case, two vortices with opposite strength are set 20 unit cells apart, resulting in an induced convecting velocity $u_\infty = 0.04$ and $v_\infty = 0.03$ at both of the vortex centers. With a time step of 0.2, the expected movement of the vortex pair after 5000 time steps should be 40 unit cells in x direction and 30 unit cells in y direction. The initial velocity field is shown in figure 2-26.

This simple case in fact is very difficult to simulate due to the large cancellation between the velocity fields induced by each individual vortex. For example, near each vortex core, the velocity induced by the vortex itself is much larger than that induced by the other vortex. Even a small error can result in inaccurate movement of the vortex.

In figures 2-27 and 2-28, which are the velocity fields at the 1000 and 5000 time steps, respectively, for computation without vorticity confinement. The two vortices spread very fast due to the numerical diffusion.

The contour plot for the non-conservative confinement computation is shown in figure 2-35. Again, the movement of the vortices is in disagreement with the analytical solution. Because the two vortices get closer as they move on, the induced velocities become bigger, the vortex pair thus moves faster than that expected from the exact solution. Figure 2-29 and 2-30 show the corresponding vector fields after 1000 and 5000 time steps. The resulting vortex cores are more compact but less rounded than other computations because of the reason discussed before.

Figures 2-31, 2-32 and 2-36 show the results obtained by using the conservative vorticity confinement. The disparity between the numerical solution and analytical solution again falls within one grid cell. The shapes of the vortices are more rounded but more spread than those from the non-conservative confinement. The vector plots also show smoother velocity fields around the vortex cores.

The results from the computation by the old non-conservative confinement scheme are shown in figures 2-33, 2-34, and 2-37. The computed movement of the vortex pair is much slower than that of the exact calculation. The vortex pair in fact turns downward, which may be caused by the averaging processes involved in the computation. The averaging process can introduce errors that bias toward either the x direction or the y direction in most cases.

2.3.3 Grid dependence study and variation of parameters

The difference equation for a convecting scalar field in a uniform Cartesian grid with grid spacing Δx can be written in the following way

$$\phi^{n+1} - \phi^{n-1} = \frac{\Delta t}{\Delta x}\left(-\delta \cdot \left(\vec{q}\phi \right) + \frac{\mu}{\Delta x}\delta^2 \left(\phi - \alpha\Phi \right) \right) \tag{2.124}$$

where

$$\begin{aligned} \delta \cdot (\cdot) = \frac{1}{2}\Big(& (\cdot)_{i+1,j,k} - (\cdot)_{i-1,j,k} \\ & + (\cdot)_{i,j+1,k} - (\cdot)_{i,j-1,k} \\ & + (\cdot)_{i,j,k+1} - (\cdot)_{i,j,k-1} \Big) \end{aligned} \tag{2.125}$$

and

$$\begin{aligned} \delta^2 (\cdot) = & (\cdot)_{i+1,j,k} + (\cdot)_{i-1,j,k} + (\cdot)_{i,j+1,k} \\ & + (\cdot)_{i,j-1,k} + (\cdot)_{i,j,k+1} + (\cdot)_{i,j,k-1} \\ & - 6(\cdot)_{i,j,k} \end{aligned} \tag{2.126}$$

and

$$\alpha = \frac{\varepsilon}{\mu} = \frac{1}{a}$$

If the solution converges to a steady state in the moving frame, equation (2.124) degenerates into

$$-\delta \cdot \left(\vec{q}\phi \right) + \frac{\mu}{\Delta x}\delta^2 \left(\phi - \alpha\Phi \right) = 0 \tag{2.127}$$

Equation (2.127) shows that the converged solution should be independent of Δt as long as it satisfies the stability condition (2.117), although the convergence rate is related to $\Delta t/\Delta x$. Also, if one changes μ and Δx simultaneously but does not change the ratio of $\mu/\Delta x$, the solution should be independent of the grid spacing under proper scaling. The scaling problem will be discussed later in this section. Similar analysis can be extended to the vector equation (2.81). Two ratios are defined as

$$c_1 = \frac{\Delta t}{\Delta x}$$

$$c_2 = \frac{\mu}{\Delta x}$$

If the initial condition is properly scaled, these two ratios, together with the previously defined α, will determine the final solution of the difference equation.

The following relation must be satisfied according to the stability condition

$$\frac{|\vec{q}|_{\max}^{\ 2} c_1^{\ 2}}{2} \le c_1 c_2 \le \frac{1}{4}$$

The confinement method also introduces a length scale that is related to Δx and α:

$$L \sim \frac{\Delta x}{\alpha}$$

which is the same order of magnitude as the size of the vortex core. The maximum velocity of the resulting field thus can be estimated as

$$(q_\theta)_{\max} \sim \frac{\alpha \Gamma}{2\pi \Delta x}$$

The CFL number based on this maximum velocity

$$\sigma \sim \frac{\alpha \Gamma \Delta t}{2\pi \Delta x^2}$$

which should be less than 1.0 for the computations.

Unless otherwise specified, for all the following the computations in this section, the three ratios are selected as:

$$\begin{aligned} c_1 &= 0.1 \\ c_2 &= 0.6 \\ \alpha &= 1.4 \end{aligned} \qquad (2.128)$$

The initial conditions are specified according to the following formula:

$$q_\theta = \begin{cases} \dfrac{\Gamma}{2\pi r} & r > r_0 \\ \dfrac{\Gamma r}{2\pi r_0} & r \le r_0 \end{cases}$$

Γ is selected as 2π, so that the maximum velocity is 1.0 for the initial field. r_0 is selected

as 2.0. It can be verified that these parameters satisfy the stability requirement.

For the case of the convecting vortex pair, in addition to the three ratios, the solutions also depend on how many grid cells there are between the two vortices. It is important to understand that disregarding the overall grid dimension and the grid spacing, as long as the effect of the far field boundary is negligible, the final solution of the vortex pair should be determined by the three ratios and the number of cells between the two vortices, subjecting only to the initial scaling. However, for this to be true, it is necessary that the vortex cores remain small compare to the distance between them, which is one of the main point of the confinement method. To study the cases with different number of cells between the two vortices, it thus is sufficient to use only one grid with fixed grid spacing. A 256 x 256 grid with spacing 1.0 is selected. Four cases are studied, with the number of cells between the two vortices to be 5, 10, 20 and 40.

Figures 2-38 to 2-41 are the vorticity contours for the solutions, with comparison to the movement predicted by the exact solutions. For the case that the two vortices are only five cells apart, there are not enough grid cells between the two vortices for the confinement method to accurately solve the flow field. The two vortices keep canceling each other and losing strength, which explains why the movement of the vortices is slower than that predicted by the exact solution. When the distance increases to 10 cells apart, the shapes of the vortices become smooth and round, the movement is already reasonably close to the exact solution. As the distance further increases, the accuracy of the solution enhances more. The evolution of the maximum vorticity magnitude of the flow field is plotted in figure 2-42, which also shows the convergence rate of the different configurations. When the distance between the vortices is only 5 cells apart, the convergence rate is much slower than the other three cases. The other three cases actually show very similar convergence rate and maximum vorticity, which means as long as the space between the two vortices is sufficient for the confinement method to solve the transition area between positive and negative vorticity regions, the resulting shapes of the vortices will have little dependence on the number of cells between the vortices. Also, as

long as the two vortices are far enough from each other, so that the induced convecting speed will be close to what predicted by the exact solutions, the detailed structures of the vortex cores is not important in determining the movement of the vortices.

Some effort is put on studying the effect of varying the three previously defined ratios: C_1, C_2 and α. The grid and the initial configuration used are the same as the previous case with the two vortices 20 cells apart. Figure 2-43 shows the results for computations with different C_1. As predicted, the convergence rate is heavily dependent on this ratio, though the converged solutions show little dependence on it. For the value 0.2, the solution already converges at the time step around 60, while the solution is not converged until 500 time steps for the value 0.025. Figure 2-44 is the plot for computations with different C_2, which shows that C_2 can also affect the convergence rate but has little effect on the converged solution. As discussed before, the converged solution depends mainly on α, as shown in figure 2-45, which is the plot for the solutions with different α. It can be observed from the figure that in order to get a converged solution, only a narrow range of α can be used. The maximum vorticity increases as α increases. As α reaches a certain value, the solution will become unstable and break into separate vortices, although it will not diverge.

However, one needs to find a way to scale the initial configurations corresponding to the real physical configurations. We use the two vortices convecting in mutually induced field as an example. Assume the number of cells between the two vortices to be N, the circulation calculated based on the numerical variables to be Γ_1 and the grid spacing to be Δx. On the other hand, assume that the physical distance between the two vortices is L, and the actual circulation of the vortex is Γ. Two reference value for velocity and distance can be used for scaling: U_0 and L_0. To determine these two reference variable, the following formula should be used:

$$\begin{aligned} L_0 &= \frac{L}{N\Delta x} \\ U_0 &= \frac{\Gamma N \Delta x}{\Gamma_1 L} = \frac{\Gamma}{\Gamma_1 L_0} \end{aligned} \tag{2.129}$$

The following relation can be used to convert between the numerical variables and physical variables:

$$\begin{aligned} \vec{Q} &= U_0 \vec{q} \\ \hat{X} - \hat{X}_0 &= L_0 \hat{x} \\ T &= \frac{L_0}{U_0} t \end{aligned} \tag{2.130}$$

where $\vec{Q}, \hat{X}$ and T are the physical velocity, the physical coordinate and the physical time, respectively. $\vec{q}$ is the numerical velocity, $\hat{x}$ is the numerical coordinate and t is the numerical time. $\hat{X}_0$ is the physical coordinate for the origin of the numerical coordinate. To ensure the same physical time, the total time step for the two computations is 4000 and 1000, respectively. The distance traveled is one quarter of the distance between the two vortices. The two scaled vector fields for N = 40 and N = 20 are shown in figure 2-46, where N is the distance between the two vortices in the unit of the grid spacing. The combined field is plotted in figure 2-47. As predicted, the two resulting physical fields are different because the solution depends on the number of cell between the two vortices used for the computations. However, the vector fields match each other as the distance from the vortex center become sufficient large, which again has proved that the detailed structure is not important on solving the movement of the vortices.

For the problem of the single vortex, the only length scale that can be used is the vortex core r_0. The reference length scale can be defined as

$$L_0 = \frac{r_0}{\Delta x}$$

The other scaling factors are the same as those in (2.129). Three different grids: 128 x 128 with $\Delta x = 1.0$, 256 x 256 with $\Delta x = 0.5$, 512 x 512 with $\Delta x = 0.25$ is used to simulate a stationary single vortex. To satisfy the stability condition for all three case, a smaller $C_1 = 0.01$ is used, other parameters are the same as those in (2.128). The two reference scales are calculated as

$$\begin{cases} L_0 = 1.0, & U_0 = 1.00 \quad for \quad 128 \times 128 \\ L_0 = 2.0, & U_0 = 0.50 \quad for \quad 256 \times 256 \\ L_0 = 4.0, & U_0 = 0.25 \quad for \quad 512 \times 512 \end{cases}$$

The total time step used for the three grids, starting from the coarsest grid, are 2000, 8000 and 32000, which ensures the time consistency. The converged velocity fields and the corresponding vorticity fields are plotted in figure 2-48 to 2-50. Figure 2-51 shows the velocity distribution for the converged solutions, using the same normalization method used in 2.3.1. The three scaled fields and the scaled vorticity contours shown in figure 2-52 to 2-54 are obtained by scaling the three different solutions using the previously calculated factors. The three fields are merged into a single plot that is shown in figure 2-55. It can be observed that the difference among the three fields is small. The scaled velocity distribution can be found in figure 2-56, which again shows very similar distribution of the three differently computed velocity fields.

2.4 Discussion

Some of the important features of the vorticity confinement are studied in this chapter. The discussion below summarizes some of the topics in the previous sections. There are many other features of the method that are not covered previously but are discussed here based mostly on the past experience on using the method. Some of the features are well studied but many of them are not fully understand, such as the calibration of the numerical coefficients according to a given Reynolds number, etc.

The most significant feature of the vorticity confinement method is the ability to capture thin vortical features such as convecting thin vortex sheets or thin boundary layers with a minimal number of grid cells, without numerical spreading. It automatically captures the global vortical features, while at the same time has no effect on flow outside vortical region. It can simulate the dynamics of the vortical features, and the convecting vortices can interact with each other, remerge, etc. The centroid can move with the correct speed and the total magnitude of the vorticity is conserved. Simple and very

coarse inviscid type grids can be used to get reasonably accurate flow solutions.

The ability to confine vorticity towards the vortical core means that at the same time it can prevent the error from spreading outside the vortical region, while inside the vortical region, the solutions are able to preserve most of the important integral properties. The computational scheme thus can be very robust since the outer flow is free of pollution generated from the vortical area. The flow outside the vortical region can be computed accurately due to its ability to conserve the momentum and preserve the integral type of properties inside the vortical region.

The confinement terms can rapidly converge to a solution for the internal structure of the vortical region, known as the previously discussed "fast variable" process, while the main flow is slowly varying compared to the fast relaxation of the vortical structure. In many flows, unsteady vortex shedding and flow separation indeed have much higher update rate than the otherwise slow changing outer irrotational flow. The fast converging rate of the "fast variables" thus can possibly be used to efficiently treat these kinds of unsteady vortical features. Even for steady flow, it will always be beneficial to have a converged vortical structure at minimal number of time steps.

The nonlinear confinement term does not comply with traditional stability analysis, which is typically a linear type methodology. The confinement term introduces strong nonlinear negative diffusion but the numerical scheme is robust according to the past experience. A nonlinear solitary wave like behavior is observed in many applications.

3. The Surface Boundary Layer Model

The initial attempt at capturing a boundary layer in the present study used a simple model without applying a vorticity confinement term. The whole idea can be split into two parts (see figure 3-1): The first part is an inviscid surface model that can be used to develop an inviscid solution for external flow, from which the pressure is extrapolated onto the surface. The second part is a model equation to be solved solely on the surface, using the extrapolated pressure from the outer flow as its pressure input and feeding back a normal velocity to the outer flow. The model equation has a simple friction term that can simulate the wall shear stress, while the extrapolated pressure drives the flow. If there is an adverse pressure gradient near the surface, coupling with the friction term, boundary eruption, i.e., a large velocity normal to the surface, will be generated with subsequent feed-back to the outer flow, which consequently will result in boundary layer separation [3].

This simple model was tried on several two-dimensional flows, and good results were obtained [3]. However, the attempts on three-dimensional flow were not successful. In two-dimensional flow, the point of flow separation from the surface coincides with the point at which the skin friction vanishes. Large regions of reverse flow typically accompany two-dimensional separation. However flow reversal and zero shear stress may not necessarily accompany separation in three-dimensional flows. Three-dimensional separation actually is rarely associated with the vanishing of the wall shear stress except in a few very special cases [6][8]. Also for a two dimensional separation, the separation is generated from a separation point, which would be a separation line for a three dimensional separation. The simple surface model has difficulty in simulating the complicated three-dimensional separation process. However, the first part of the idea, i.e.,

the inviscid model for developing inviscid flow solution, proves to be very successful, for both two-dimensional and three-dimensional flows.

Later, a new surface boundary layer model based on vorticity confinement is developed and is able to produce very good solutions for flow over a 6:1 ellipsoid with various incidence angles. The main idea is to set up a secondary thin body conforming grid surrounding the surface. The main computation (the "outer" computation) is still performed on a uniform Cartesian grid as before, except that non-slip boundary condition is not applied on the surface. Instead, the surface velocity condition is extrapolated from the boundary model. A separate computation (the "inner" computation) is performed on the inner grid, using a boundary model based on the confinement method but on a body-conforming grid. For its outer boundary, the inner computation retrieves boundary conditions from the outer flow, while using the non-slip velocity boundary condition for velocity on the surface. The resulting boundary layer using this later surface model is not as thin as it was hoped when attempting the initial model, but it is thinner than the computation without this model.

3.1 The Inviscid Surface Model

The outer computation is done using the same scheme described in chapter two, i.e., using vorticity confinement on uniform Cartesian grid, except that the non-slip surface condition is not applied. For grid nodes surrounding the surface, the tangential velocities are extrapolated from the outer flow, while the normal velocity is extrapolated from the inviscid surface model.

The continuity equation for 2-D incompressible flow based on local surface coordinates can be written as

$$\partial_s q_s + \partial_n q_n = 0 \tag{3.1}$$

in which n and s refers to normal direction and tangential direction respectively.

Since the normal velocity should be zero on the surface, the equation can be written in integral form as

$$q_n\big|_h = 0 - \int_0^h \frac{\partial q_s}{\partial s} dh \tag{3.2}$$

where h is the distance from a given point to the surface and $\big|_h$ denotes a point with a distance *h* to the surface. Also, for inviscid flow, the vorticity is zero which gives

$$\partial_n q_s - \partial_s q_n = 0 \tag{3.3}$$

which similarly can be written as

$$q_s\big|_0 = q_s\big|_h - \int_0^h \frac{\partial q_n}{\partial s} dh \tag{3.4}$$

where $\big|_0$ denotes a point with a distance zero to the surface, i.e., a point on the surface. Equation (3.2) and (3.4) provide well-posed model equations for all inviscid computations. The tangential velocity which is the only velocity component on the surface is derived according to equation (3.4), while the normal velocity for the outer flow, is computed according to equation (3.2). For first order accuracy, the model equation becomes

$$\begin{aligned} q_n\big|_h &= 0 - h\frac{\partial q_s}{\partial s}\bigg|_0 \\ q_s\big|_0 &= q_s\big|_h - h\frac{\partial q_n}{\partial s}\bigg|_h \end{aligned} \tag{3.5}$$

3.1.1 Extrapolation scheme for the surface model

Equation (3.5) can be used to extrapolate the surface velocity boundary condition. For an outer two-dimensional uniform Cartesian grid, a grid point with the following properties is defined as a "boundary node":

1) It must be outside the body,

2) At least one of its 8 surrounding nodes is inside the body.

Also, a grid point in outer grid is considered as an "outer node" if it satisfies all of the following properties:

1) It must be outside the body,

2) All of its surrounding nodes must be outside the body.

For each point on the surface, a normal direction $\hat{n}$ and a tangential direction $\hat{s}$ can be calculated. For each "boundary node", a line contains this node and perpendicular to the surface can be draw (see figure 3-2). The normal direction $\hat{n}$ is defined as a unit vector on this line and pointing away from the surface. The tangential direction $\hat{s}$ thus can be defined as a unit vector normal to $\hat{n}$.

The tangential velocity of a "boundary node" can be directly extrapolated from its surrounding grid points, using the second equation of equations (3.5). The following formula can be used

$$\left(q_s\right)_{I,J} = \frac{\sum_{l=1}^{N} s_l \left(\left(q_s\right)_l - (h_l - h_{I,J}) \left(\frac{\partial q_n}{\partial s} \right)_l \right)}{\sum_{l=1}^{N} s_l} \tag{3.6}$$

in which s_l is the corresponding weighting factor

$$s_l = f(l) d_l^{-1} \tag{3.7}$$

where d_l is the distance from the *lth* of its *N* surrounding grid points to the given "boundary node". $f\left(l\right)$ is a filter function defined as

$$f\left(I,J\right) = \begin{cases} 1 & if \quad \left(I,J\right) \in "outer \quad nodes" \\ 0 & Otherwise \end{cases} \tag{3.8}$$

For a given point P on the surface (figure 3-2), its surrounding grid points in the Cartesian grid are located first. Then an equation similar to (3.6) can be used to map the tangential velocity:

$$\left(q_s\right)_i = \frac{\sum_{l=1}^{N} S_l \left(\left(q_s\right)_l - h_l \left(\frac{\partial q_n}{\partial s} \right)_l \right)}{\sum_{l=1}^{N} S_l} \tag{3.9}$$

in which the weighting factor S_l is defined as

$$S_l = F(l) d_l^{-1} \tag{3.10}$$

where d_l is the distance from its *lth* surrounding grid point to the point on the surface, and the filter function is defined as

$$F\left(I,J\right) = \begin{cases} 1 & if \quad \left(I,J\right) \in outside \quad the \quad body \\ 0 & if \quad \left(I,J\right) \in inside \quad the \quad body \end{cases} \tag{3.11}$$

Subsequently, the gradient of the tangential velocity can be calculated on the surface as

$$\left(\frac{\partial q_s}{\partial s} \right)_i = \frac{\left(q_s\right)_{i+1} - \left(q_s\right)_{i-1}}{2\Delta s} \tag{3.12}$$

where Δs is distance between two adjacent points on the surface. For a given "boundary node", projecting it onto the surface (figure 3-2), one can find its surrounding surface points. A normal velocity thus can be fed-back to the corresponding "boundary node" according to the first equation in equations (3.5)

$$\left(q_n\right)_{I,J} = \frac{\sum_{l=1}^{N} \left(d_l\right)^{-1} \left((-1) \cdot h_l \left(\frac{\partial q_s}{\partial s} \right)_l \right)}{\sum_{l=1}^{N} \left(d_l\right)^{-1}} \tag{3.13}$$

where l represents the index of the points on the surface, and all other parameters are defined the same as before. The slip surface boundary condition for inviscid flow thus is simulated.

3.1.2 Test case: inviscid flow over a flat plate

To test the model, two-dimensional flows over a flat plate at incidence angles from 0° to 10° are computed (figure 3-3). The grid used in this computation is uniform Cartesian grid. Three different grid dimensions are used: 64 X 64, 128 X 128 and 256 x 256. The "outer" computation uses the method described in chapter 2 of this dissertation. The length of the flat plate in this computation is 6 cells, 12 cells, and 24 cells for the three different grid setups, respectively. The grid spacing and the numerical coefficients are the same for all three cases.

The exact solution for lift coefficient of the flow over a flat plate at incidence is known [41] as

$$C_L = 2\pi \sin\alpha \tag{3.14}$$

where α is the incidence angle. The pressure coefficient on the flat plate is calculated using Bernoulli relation:

$$C_p = 1 - \frac{|\vec{q}|^2}{|\vec{q}_\infty|^2} \tag{3.15}$$

The lift coefficient is obtained by integrating the pressure coefficient over the whole surface of the flat plate. The computed lift coefficient together with the exact solution is plotted in figure 3-4. As one can see from the figures, for angles smaller than 7°, the results for all three grid setups are reasonably accurate. The accuracy of the simulation increases as the grid dimension increases. For angle great than 7°, the accuracy of the method lowers, and refining the grid is not able to enhance the results.

Full three-dimensional flows over a 6:1 ellipsoid with incidence angles ranging from 0 to 90° are computed using the inviscid surface model, which will be presented in chapter 4 of this dissertation.

3.2 The Surface Boundary Layer Model

3.2.1 The body fitted coordinate

The new surface boundary layer model is implemented on a thin layer of body fitted grid. In conventional methods, generating a body fitted coordinate usually requires solving a set of elliptic equations. The complexity of the grid generation depends on the complexity of the body and boundary conditions. For multi-dimensional bodies such as a whole aircraft, the amount of work required to generate the grid system could be prohibitive. However, the new surface boundary layer model does not require a complicated grid, so that some simple algorithm other than a set of complicated elliptic equations can be used to generate the inner body conforming grid.

3.2.2 Inner grid generation

A simple algorithm is used to generating a simple type of body conforming grid near the surface to provide a basis for the proposed surface model.

For a given point on the surface, its position can be represented by a position vector $\vec{r}_0$. Since the surface has a unit normal at each point, one can denote the normal for this point to be $\hat{n}$ (figure 3-5). The starting point of generating the inner grid is to make the direction of the $\hat{n}$ vector the same as the gradient of one of the coordinate variable, i.e.,

$$\frac{\nabla \xi}{|\nabla \xi|} = \hat{n} \tag{3.16}$$

Thus each point on one of the iso-surface of ξ (i.e. surface of constant ξ) will have equal distance to the surface (body conforming).

The grid system thus can be generated using the following algorithm:

$$\vec{r}_i = \vec{r}_0 + (i-1)\,d\vec{r} \tag{3.17}$$

where $d\vec{r}$ is the grid increment in the ξ direction. After applying the same algorithm to all the surface points, the whole inner grid system is generated. The grid generated by this algorithm has the following properties:

1) Inviscid type,

2) Body Conforming.

Application to a 6:1 ellipsoid

An inner grid (figure 3-6) surrounding a 6:1 ellipsoid is generated using the method described above.

Figure 3-8 shows a symmetry plane of the grid. The whole surface can be generated by rotating this symmetry plane along the long axis of the ellipse.

Two cross plane sections are shown in figure 3-9 and 3-10. Notice that the grid is clipped near both ends of the ellipsoid (see figure 3-7), to avoid overly dense grid cells.

3.2.3 Model equations for the surface boundary layer model

Start with the following basic equations:

$$\partial_t \vec{q} = -(\vec{q}\cdot\nabla)\vec{q} - \frac{1}{\rho}\nabla p + [\mu\nabla^2\vec{q} + \varepsilon\vec{s}] \tag{3.18}$$

A similar fractional step method described in Chapter 2 is used here. First a convection step is conducted

$$\vec{q}\,' = \vec{q}^{\,n} - \Delta t\vec{q}^{\,n}\cdot\nabla\vec{q}^{\,n} \tag{3.19}$$

followed by a diffusion step

$$\vec{q}\,'' = \vec{q}\,' + \Delta t\,\mu\nabla^2\vec{q} \tag{3.20}$$

Confinement step is then performed to convect the diffused vorticity back towards the centroid or surface

$$\vec{q}''' = \vec{q}'' + \Delta t \varepsilon \vec{s} \tag{3.21}$$

Last step is the mass conservation step. Unlike what it is done for the outer flow, where a Poisson equation was solved for the pressure function, in the inner grid, an unsteady diffusion equation is solved by "time-marching". The model used to solve for the pressure is

$$\frac{\partial \varphi}{\partial t} = c\left(\nabla^2 \varphi + \frac{1}{\Delta t} \nabla \cdot \vec{q}''' \right) \tag{3.22}$$

A steady state solution of the above equation is sought, so that it will converge to the solution of the same Poisson equation as before, i.e.

$$\nabla^2 \varphi = -\frac{1}{\Delta t} \nabla \cdot \vec{q}''' \tag{3.23}$$

A point relaxation method referred as the "Point Jacobi" iteration [21][22] is used for this computation. This point relaxation method usually is not very effective for a grid with large dimensions. The number of iterations for convergence typically has an order of $O(N^2)$ [2][21], where N is the number of grid points in a grid dimension. The inner grid is very thin and has only 5 grid points in the direction normal to the surface, the iteration thus converges very fast in this direction. The flow varies the most in the thickness direction of the boundary layer, while in the other two directions the flow is relatively smooth. The convergence rate can be very fast as long as the grid is kept very thin. Next the momentum is corrected using the gradient of the pressure field

$$\vec{q}^{\,n+1} = \vec{q}''' + \Delta t \nabla \varphi \tag{3.24}$$

After this step, the continuity equation is satisfied:

$$\nabla \cdot \vec{q}^{\,n+1} = \nabla \cdot \left(\vec{q}''' + \Delta t \nabla \varphi \right) = \Delta t \nabla^2 \phi + \nabla \cdot \vec{q}''' = 0 \tag{3.25}$$

3.2.4 The metrics of the coordinate transformation

The metrics for coordinate transformation in three-dimensional space [37] between two time-independent grid systems (x, y, z) and (ξ, η, ζ) are

$$\begin{aligned}
x_\xi &= (\eta_y \zeta_z - \zeta_y \eta_z)/J \\
x_\eta &= (\zeta_y \xi_z - \xi_y \zeta_z)/J \\
x_\zeta &= (\xi_y \eta_z - \eta_y \xi_z)/J \\
y_\xi &= (\eta_z \zeta_x - \zeta_z \eta_x)/J \\
y_\eta &= (\zeta_z \xi_x - \xi_z \zeta_x)/J \\
y_\zeta &= (\xi_z \eta_x - \eta_z \xi_x)/J \\
z_\xi &= (\eta_x \zeta_y - \zeta_x \eta_y)/J \\
z_\eta &= (\zeta_x \xi_y - \xi_x \zeta_y)/J \\
z_\zeta &= (\xi_x \eta_y - \eta_x \xi_y)/J
\end{aligned} \tag{3.26}$$

where J is the Jacobian given by the determinant

$$J = \frac{\partial(\xi, \eta, \zeta)}{\partial(x, y, z)} = \begin{vmatrix} \xi_x & \xi_y & \xi_z \\ \eta_x & \eta_y & \eta_z \\ \zeta_x & \zeta_y & \zeta_z \end{vmatrix} \tag{3.27}$$

The inverse relations are given by

$$\begin{aligned}
\xi_x &= (y_\eta z_\zeta - z_\eta y_\zeta)J \\
\xi_y &= (z_\eta x_\zeta - x_\eta z_\zeta)J \\
\xi_z &= (x_\eta y_\zeta - y_\eta x_\zeta)J \\
\eta_x &= (y_\zeta z_\xi - z_\zeta y_\xi)J \\
\eta_y &= (z_\zeta x_\xi - x_\zeta z_\xi)J \\
\eta_z &= (x_\zeta y_\xi - y_\zeta x_\xi)J \\
\zeta_x &= (y_\xi z_\eta - z_\xi y_\eta)J \\
\zeta_y &= (z_\xi x_\eta - x_\xi z_\eta)J \\
\zeta_z &= (x_\xi y_\eta - y_\xi x_\eta)J
\end{aligned} \tag{3.28}$$

3.2.5 The transformed equations and numerical implementations

Because the conservative vorticity confinement term for a given grid point requires calculating harmonic mean over its surrounding grid points, which would introduce difficulty for the inner grid since it has only several grid points across the thickness direction, the non-conservative vorticity confinement formulation is used for the inner grid. For simplicity, non-conservative forms are used in all the difference equations on the inner grid.

The momentum equation without confinement term, with constant diffusion coefficient can be written as [37]

$$\frac{\partial}{\partial t}\vec{Q}+\frac{\partial}{\partial x}\vec{E}+\frac{\partial}{\partial y}\vec{F}+\frac{\partial}{\partial z}\vec{G}=\mu\left(\frac{\partial^2\vec{Q}}{\partial x^2}+\frac{\partial^2\vec{Q}}{\partial y^2}+\frac{\partial^2\vec{Q}}{\partial z^2}\right) \tag{3.29}$$

where

$$\begin{aligned}\vec{Q}&=(u,v,w)^T\\ \vec{E}&=(uu,vu,wu)^T\\ \vec{F}&=(uv,vv,wv)^T\\ \vec{G}&=(uw,vw,ww)^T\end{aligned} \tag{3.30}$$

The following difference operators are defined first

$$\begin{aligned}\left(\frac{\partial(.)}{\partial x}\right)_c&=\delta_i(\cdot)(\xi_x)_{i,j,k}+\delta_j(\cdot)(\eta_x)_{i,j,k}+\delta_k(\cdot)(\zeta_x)_{i,j,k}\\ \left(\frac{\partial(.)}{\partial y}\right)_c&=\delta_i(\cdot)(\xi_y)_{i,j,k}+\delta_j(\cdot)(\eta_y)_{i,j,k}+\delta_k(\cdot)(\zeta_y)_{i,j,k}\\ \left(\frac{\partial(.)}{\partial z}\right)_c&=\delta_i(\cdot)(\xi_z)_{i,j,k}+\delta_j(\cdot)(\eta_z)_{i,j,k}+\delta_k(\cdot)(\zeta_z)_{i,j,k}\end{aligned} \tag{3.31}$$

where

$$\delta_i(\cdot) = \frac{(\cdot)_{i+1,j,k} - (\cdot)_{i-1,j,k}}{2}$$
$$\delta_j(\cdot) = \frac{(\cdot)_{i,j+1,k} - (\cdot)_{i,j-1,k}}{2} \tag{3.32}$$
$$\delta_k(\cdot) = \frac{(\cdot)_{i,j,k+1} - (\cdot)_{i,j,k-1}}{2}$$

Also define

$$\begin{aligned}\left(\frac{\partial^2(\cdot)}{\partial x^2}\right)_c &= \left(\delta_{ii}(\cdot) + \delta_{ij}(\cdot) + \delta_{ik}(\cdot)\right)(\xi_x)_{i,j,k} \\ &+ \left(\delta_{ij}(\cdot) + \delta_{jj}(\cdot) + \delta_{jk}(\cdot)\right)(\eta_x)_{i,j,k} \\ &+ \left(\delta_{ik}(\cdot) + \delta_{jk}(\cdot) + \delta_{kk}(\cdot)\right)(\zeta_x)_{i,j,k} \\ &+ \delta_i(\cdot)\left(\delta_i(\xi_x)(\xi_x)_{i,j,k} + \delta_j(\xi_x)(\eta_x)_{i,j,k} + \delta_k(\xi_x)(\zeta_x)_{i,j,k}\right) \\ &+ \delta_j(\cdot)\left(\delta_i(\eta_x)(\xi_x)_{i,j,k} + \delta_j(\eta_x)(\eta_x)_{i,j,k} + \delta_k(\eta_x)(\zeta_x)_{i,j,k}\right) \\ &+ \delta_k(\cdot)\left(\delta_i(\zeta_x)(\xi_x)_{i,j,k} + \delta_j(\zeta_x)(\eta_x)_{i,j,k} + \delta_k(\zeta_x)(\zeta_x)_{i,j,k}\right)\end{aligned} \tag{3.33}$$

$$\begin{aligned}\left(\frac{\partial^2(\cdot)}{\partial y^2}\right)_c &= \left(\delta_{ii}(\cdot) + \delta_{ij}(\cdot) + \delta_{ik}(\cdot)\right)(\xi_y)_{i,j,k} \\ &+ \left(\delta_{ij}(\cdot) + \delta_{jj}(\cdot) + \delta_{jk}(\cdot)\right)(\eta_y)_{i,j,k} \\ &+ \left(\delta_{ik}(\cdot) + \delta_{jk}(\cdot) + \delta_{kk}(\cdot)\right)(\zeta_y)_{i,j,k} \\ &+ \delta_i(\cdot)\left(\delta_i(\xi_y)(\xi_y)_{i,j,k} + \delta_j(\xi_y)(\eta_y)_{i,j,k} + \delta_k(\xi_y)(\zeta_y)_{i,j,k}\right) \\ &+ \delta_j(\cdot)\left(\delta_i(\eta_y)(\xi_y)_{i,j,k} + \delta_j(\eta_y)(\eta_y)_{i,j,k} + \delta_k(\eta_y)(\zeta_y)_{i,j,k}\right) \\ &+ \delta_k(\cdot)\left(\delta_i(\zeta_y)(\xi_y)_{i,j,k} + \delta_j(\zeta_y)(\eta_y)_{i,j,k} + \delta_k(\zeta_y)(\zeta_y)_{i,j,k}\right)\end{aligned} \tag{3.34}$$

$$
\begin{aligned}
\left(\frac{\partial^2(\cdot)}{\partial z^2}\right)_c &= \left(\delta_{ii}(\cdot)+\delta_{ij}(\cdot)+\delta_{ik}(\cdot)\right)(\xi_z)_{i,j,k} \\
&+\left(\delta_{ij}(\cdot)+\delta_{jj}(\cdot)+\delta_{jk}(\cdot)\right)(\eta_z)_{i,j,k} \\
&+\left(\delta_{ik}(\cdot)+\delta_{jk}(\cdot)+\delta_{kk}(\cdot)\right)(\zeta_z)_{i,j,k} \\
&+\delta_i(\cdot)\left(\delta_i(\xi_z)(\xi_z)_{i,j,k}+\delta_j(\xi_z)(\eta_z)_{i,j,k}+\delta_k(\xi_z)(\zeta_z)_{i,j,k}\right) \\
&+\delta_j(\cdot)\left(\delta_i(\eta_z)(\xi_z)_{i,j,k}+\delta_j(\eta_z)(\eta_z)_{i,j,k}+\delta_k(\eta_z)(\zeta_z)_{i,j,k}\right) \\
&+\delta_k(\cdot)\left(\delta_i(\zeta_z)(\xi_z)_{i,j,k}+\delta_j(\zeta_z)(\eta_z)_{i,j,k}+\delta_k(\zeta_z)(\zeta_z)_{i,j,k}\right)
\end{aligned}
\tag{3.35}
$$

where

$$
\begin{aligned}
\delta_{ii}(\cdot) &= (\cdot)_{i+1,j,k}-2(\cdot)_{i,j,k}+(\cdot)_{i-1,j,k} \\
\delta_{ij}(\cdot) &= \left((\cdot)_{i+1,j+1,k}+(\cdot)_{i-1,j-1,k}-(\cdot)_{i+1,j-1,k}-(\cdot)_{i-1,j+1,k}\right)\Big/4 \\
\delta_{ik}(\cdot) &= \left((\cdot)_{i+1,j,k+1}+(\cdot)_{i-1,j,k-1}-(\cdot)_{i+1,j,k-1}-(\cdot)_{i-1,j,k+1}\right)\Big/4 \\
\delta_{jj}(\cdot) &= (\cdot)_{i,j+1,k}-2(\cdot)_{i,j,k}+(\cdot)_{i,j-1,k} \\
\delta_{jk}(\cdot) &= \left((\cdot)_{i,j+1,k+1}+(\cdot)_{i,j-1,k-1}-(\cdot)_{i,j+1,k-1}-(\cdot)_{i,j-1,k+1}\right)\Big/4 \\
\delta_{kk}(\cdot) &= (\cdot)_{i,j,k+1}-2(\cdot)_{i,j,k}+(\cdot)_{i,j,k-1}
\end{aligned}
\tag{3.36}
$$

The convection step can be written as

$$
\vec{Q}' = \vec{Q}-\Delta t\left(\left(\frac{\partial\vec{E}}{\partial x}\right)_c+\left(\frac{\partial\vec{F}}{\partial y}\right)_c+\left(\frac{\partial\vec{G}}{\partial z}\right)_c\right) \tag{3.37}
$$

Next the diffusion step

$$
\vec{Q}'' = \vec{Q}'+\Delta t\mu\left(\left(\frac{\partial^2\vec{Q}}{\partial x^2}\right)_c+\left(\frac{\partial^2\vec{Q}}{\partial y^2}\right)_c+\left(\frac{\partial^2\vec{Q}}{\partial z^2}\right)_c\right) \tag{3.38}
$$

Define the vorticity

$$
\vec{\omega} = \left(\omega_x,\omega_y,\omega_z\right) = \nabla\times\vec{Q} \tag{3.39}
$$

which can be calculated by

$$\omega_x = J\left(\left(\frac{\partial w}{\partial y}\right)_c - \left(\frac{\partial v}{\partial z}\right)_c\right)$$
$$\omega_y = J\left(\left(\frac{\partial u}{\partial z}\right)_c - \left(\frac{\partial w}{\partial x}\right)_c\right) \tag{3.40}$$
$$\omega_z = J\left(\left(\frac{\partial v}{\partial x}\right)_c - \left(\frac{\partial u}{\partial y}\right)_c\right)$$

For non-conservative vorticity confinement formulation, the $\hat{n}$ vector can be calculated by

$$\hat{n} = \left(n_x, n_y, n_z\right)^T = \left(\left(\frac{\partial|\vec{\omega}|}{\partial x}\right)_c, \left(\frac{\partial|\vec{\omega}|}{\partial y}\right)_c, \left(\frac{\partial|\vec{\omega}|}{\partial z}\right)_c\right)^T \tag{3.41}$$

The confinement term turns out to be

$$\left(\hat{n}\times\vec{\omega}\right)_c = \left(n_y w_z - n_z\omega_y, n_z w_x - n_x\omega_z, n_x w_y - n_y\omega_x\right)^T \tag{3.42}$$

adding which to the velocity field

$$\vec{Q}''' = \vec{Q}'' + \Delta t\varepsilon\left(\hat{n}\times\vec{\omega}\right)_c \tag{3.43}$$

For pressure correction, begin with the pressure equation

$$\frac{\partial\varphi}{\partial t} = c\left(\Delta t\left(\nabla^2\varphi\right)_c + \left(\nabla\cdot\vec{Q}'''\right)_c\right) \tag{3.44}$$

where c is a numerical coefficient. This step can be split into two steps

$$\left(\nabla\cdot\vec{Q}'''\right)_c = \left(\frac{\partial u}{\partial x}\right)_c + \left(\frac{\partial v}{\partial y}\right)_c + \left(\frac{\partial w}{\partial z}\right)_c \tag{3.45}$$

$$\varphi^{m+1} = \varphi^m + c\left(\Delta t\left(\frac{\partial^2\varphi}{\partial x^2}\right)_c + \Delta t\left(\frac{\partial^2\varphi}{\partial y^2}\right)_c + \Delta t\left(\frac{\partial^2\varphi}{\partial z^2}\right)_c + \left(\nabla\cdot\vec{Q}'''\right)_c\right) \tag{3.46}$$

Repeat the above iteration until the specified convergence condition satisfied. Finally the mass correction step

$$\left(\nabla\varphi\right)_c = \left(\left(\frac{\partial\varphi}{\partial x}\right)_c, \left(\frac{\partial\varphi}{\partial y}\right)_c, \left(\frac{\partial\varphi}{\partial z}\right)_c\right) \tag{3.47}$$

$$\vec{Q}^{n+1} = \vec{Q}''' + \Delta t\left(\nabla\varphi\right)_c \tag{3.48}$$

3.2.6 Boundary conditions: the coupling algorithm

The coupling algorithm between main grid and inner grid is discussed in this section. Here a 6:1 ellipsoid is used as an example.

The index of a grid point in main grid is denoted in uppercase (for example (*I ,J, K*)), while for inner grid it will be denoted in lowercase (for example (*i, j, k*))(See figure 3-12). Three regions are defined as region I, region II and region III (figure 3-11). Region I encloses all grid points inside the surface, and no computation should be involved here. Region II is the domain enclosed by the inner grid. Region III includes all the points that are not included in either region III or region II.

Mapping for boundaries of inner grid

First look at the boundaries of the inner grid. Three types of boundaries are defined for the inner grid: the surface boundary, the outer boundary and the inlet/outlet (figure 3-7 and 3-10).

a) Surface boundary

Both velocity and pressure boundary condition are required for the surface boundary due to the characteristics of the problem.

Non-slip velocity boundary condition is imposed on the surface boundary for viscous flow computation

$$\vec{q}_{b.c.} = 0 \tag{3.49}$$

where $\vec{q}_{b.c.}$ is the velocity vector on the boundary.

The pressure surface boundary condition is imposed as

$$\frac{\partial p}{\partial n} = 0 \tag{3.50}$$

where n is the normal direction of a given point on the surface.

b) The outer boundary

For the outer boundary, careful consideration is required for a well-behaved solution. For each inner grid point *(i , j, k)* on the outer boundary of the inner grid, the first step is to locate the grid points in the outer grid surrounding this inner point.

The algorithm for locating the enclosing outer grid points is simple in this case. A formula can be used to identify the outer surrounding point with the smallest index number

$$\begin{aligned} I &= \text{int}(x(i,j,k) + \Delta h \cdot (i\max + 1)/2) \\ J &= \text{int}(y(i,j,k) + \Delta h \cdot (j\max + 1)/2) \\ K &= \text{int}(z(i,j,k) + \Delta h \cdot (k\max + 1)/2) \end{aligned} \tag{3.51}$$

suppose the origin of the coordinate system (x,y,z) is located at the outer grid point ((*imax+1*)*/2*, (*jmax+1*)*/2*, (*kmax+1*)*/2*) and the cell size of the outer uniform Cartesian grid is Δh.

Only points in region III should be used to map the velocity boundary values for inner grid. A filter function is defined

$$f_{I,J,K} = \begin{cases} 1, & if \quad (I,J,K) \in III \\ 0, & otherwise \end{cases} \tag{3.52}$$

The final formula used to map the velocity values from the outer grid onto the outer boundary of the inner grid is

$$\begin{aligned} \vec{q}_{i,j,k} = \Big(& s_1 f_{I,J,K} \vec{Q}_{I,J,K} + s_2 f_{I+1,J,K} \vec{Q}_{I+1,J,K} + s_3 f_{I,J+1,K} \vec{Q}_{I,J+1,K} \\ & + s_4 f_{I+1,J+1,K} \vec{Q}_{I+1,J+1,K} + s_5 f_{I,J,K+1} \vec{Q}_{I,J,K+1} + s_6 f_{I+1,J,K+1} \vec{Q}_{I+1,J,K+1} \\ & + s_7 f_{I,J+1,K+1} \vec{Q}_{I,J+1,K+1} + s_8 f_{I+1,J+1,K+1} \vec{Q}_{I+1,J+1,K+1} \Big) \Big/ \\ & \Big(s_1 f_{I,J,K} + s_2 f_{I+1,J,K} + s_3 f_{I,J+1,K} + s_4 f_{I+1,J+1,K} + s_5 f_{I,J,K+1} \\ & + s_6 f_{I+1,J,K+1} + s_7 f_{I,J+1,K+1} + s_8 f_{I+1,J+1,K+1} \Big) \end{aligned} \tag{3.53}$$

where s_l, $l = 1,...,8$ are the weighting factors defined as

$$s_l = \left(\left(X_l - x_{i,j,k} \right)^2 + \left(Y_l - y_{i,j,k} \right)^2 + \left(Z_l - z_{i,j,k} \right)^2 \right)^{-1/2} \tag{3.54}$$

Similar mapping is performed for the pressure outer boundary, except that no filter function is needed since the outer pressure field resulted by the Poisson solver is smooth near the surface. The formula for mapping the pressure thus is simpler

$$\begin{aligned} p_{i,j,k} = & \left(s_1 P_{I,J,K} + s_2 P_{I+1,J,K} + s_3 P_{I,J+1,K} + s_4 P_{I+1,J+1,K} \right. \\ & \left. + s_5 P_{I,J,K+1} + s_6 P_{I+1,J,K+1} + s_7 P_{I,J+1,K+1} + s_8 P_{I+1,J+1,K+1} \right) \Big/ \\ & \left(s_1 + s_2 + s_3 + s_4 + s_5 + s_6 + s_7 + s_8 \right) \end{aligned} \tag{3.55}$$

where s_l are the same as those used in velocity boundary mapping.

c) Inlet/outlet

For the inlet of the inner grid (figure 3-7), the velocity and pressure are extrapolated from the outer grid using the same formulae as (3.53) and (3.55), respectively. For the outlet of the inner grid, the pressure is extrapolated from the outer grid using formula (3.55). The velocity of the outlet is extrapolated from the inside of the inner grid using a box scheme interpolation method [18][19].

$$\vec{q}_{i,j,k} = \frac{\sum_{l=1}^{8} a_l \vec{q}_l}{\sum_{l=1}^{8} a_l \vec{q}_l}$$

in which $\vec{q}_l$ (l = 1, ... , 8) are the velocities of the grid nodes of a grid cell, which contains the point (with coordinate (x_0, y_0, z_0)) where a flow particle currently at the grid node (*i, j, k*) was located at one time step earlier, and

$$a_l = \left| \left(x_0 - x_l \right) \left(y_0 - y_l \right) \left(z_0 - z_l \right) \right|^{-1}$$

Mapping for outer grid boundary

The far field boundary conditions are the same as those described in chapter 2. Only the surface conditions are different.

First a "boundary node" of a three-dimensional outer grid is defined as:

1) It must be outside the body,

2) At least one of its 26 surrounding nodes is inside the surface.

For a "boundary node" identified by this definition, its velocity is extrapolated from the inner grid.

One must locate the grid cells of the inner grid that encloses the point (*I , J, K*). First the distance *d* from a "boundary node" to the surface is calculated, the *i* index of the surrounding surface node point with the smallest indices can be identified as

$$i = int\ (\ d / d\xi\ ) + 1$$

where $d\xi$ is the grid increment in ξ direction. Similar to what is used in the inviscid model, the projection of a boundary point on the surface can be used to locate the other two indices. Next a similar weighting function is calculated by

$$S_l = \left(\left(x_l - X_{I,J,K} \right)^2 + \left(y_l - Y_{I,J,K} \right)^2 + \left(z_l - Z_{I,J,K} \right)^2 \right)^{-1/2} \tag{3.56}$$

and the velocity can be calculated by

$$\begin{aligned} \vec{Q}_{i,j,k} = & \left(S_1 \vec{q}_{i,j,k} + S_2 \vec{q}_{i+1,j,k} + S_3 \vec{q}_{i,j+1,k} + S_4 \vec{q}_{i+1,j+1,k} \right. \\ & \left. + S_5 \vec{q}_{i,j,k+1} + S_6 \vec{q}_{i+1,j,k+1} + S_7 \vec{q}_{i,j+1,k+1} + S_8 \vec{q}_{i+1,j+1,k+1} \right) \Big/ \\ & \left(S_1 + S_2 + S_3 + S_4 + S_5 + S_6 + S_7 + S_8 \right) \end{aligned} \tag{3.57}$$

There is no pressure information is extrapolated from the inner grid to the outer grid. The pressure for a "boundary node" is obtained from the outer Poisson solver.

4. Numerical Simulations of Flow over 6:1 Ellipsoid at Incidence

4.1 Flow over 6:1 Ellipsoid at Incidence

High Reynolds number flow over a 6:1 ellipsoid at incidence is selected to test the previously described models. Flow over a 6:1 ellipsoid at incidence is a well-defined, relatively simple 3-D flow which exhibits all the fundamental separation phenomena of 3-D flow, such as the complicated cross plane separation [4][6][7][10]. Most importantly, there are well-documented and very consistent experimental data available from different sources [6][7][8][9][10][11]. Numerical results obtained using various advanced numerical methods are also available for comparison [4][5][19][27]. All of these make the flow over 6:1 ellipsoid an excellent test case for the new computational models described in the previous chapters.

4.1.1 The cross flow separation

The separations that typically form on bodies at angles of attack are called cross flow separation [4][7] due to the dominance of the circumferential pressure gradient in the separation process. These separations typically develop from the rear of the body at very low angle of attack and move forward as the angle of attack increases.

Figure 4-1 (a) contains a sketch of the cross plane separation behavior of the flow. The primary separation happens at point P on the lee-side of the ellipsoid, rolling up into

a strong vortex on both sides of the body. Secondary vortices are generated at the same time, which separate from the surface at the points T1 and T2. The flow reattaches at point R1 and R2. From figure 4-1 (b), one can see the primary separation line as well as the secondary vortex located underneath the primary vortex. The existence of the secondary separation depends on flow conditions. The cross plane separation variations along the length of the body, together with complex interactions between the various types of vortex structures, result in a highly complicated three-dimensional separated flow.

4.1.2 Experimental results, description of the devices

The experimental results used for comparison include those of Ahn and Simpson [6][8][9]. The experiments were conducted at the Virginia Polytechnic Institute and State University 6'x6' Stability Wind Tunnel. The test model was a 6:1 ellipsoid, which had a 54-inch long major axis. The surface of the testing model was made of fiberglass reinforced plastic. The Reynolds number for the tests was 4.2×10^6. The pressure data were measured by pressure transducers mounted through pinhole cover adaptor bonded to the inside surface of the fiberglass skin of the model. Experimental data from Mier and Kreplin [11] on a 2.4 meter long 6:1 ellipsoid are also used for some of the comparisons.

4.1.3 Numerical results for comparisons

Most recent CFD simulations of the flow over a 6:1 ellipsoid include those of Tsai *et al* [4], Constantinecu *et al*l [27], Kim *et al* [5], and Carsten Braun [19]. Their results are used later for comparison purpose.

Tsai *et al* [4] used a three-dimensional incompressible finite volume RANS solver for the computation, and applied a standard k-ε model, using a multi-block structured body fitted grid (figure 4-14). They performed the computations for incidence angles

from 10° to 30°, which are the most extensive numerical results available. However, the results of the pressure coefficient included in their paper [4] are limited to only the cross plane X/L=0.77.

Constantinecu *et al*l [27] performed their simulations using both the Detached Eddy Simulation (DES) method and RANS method with Spalart-Allmaras (SA) one-equation turbulence model. DES is a hybrid approach which attempts to capitalize on the often adequate performance of RANS models in predicting boundary layer growth and separation, and to use LES away from solid surfaces to model the typically geometry-dependent and unsteady scales of motion in separated regions [45]. The DES formulation they used was based on a modification to the SA RANS model such that the model reduced to its RANS formulation near solid surfaces and to a subgrid Smagorinsky model away from the wall. They also performed a computation using a method named Monotone Integrated Large Eddy Simulation (MILES), which simply speaking is LES without an explicit turbulence model [46]. The results for pressure coefficient shown in their paper [27] are limited to 20° and at only the cross plane X/L= 0.77.

Kim and Rhee [5] also used a finite volume RANS solver, but applied several different turbulence models for there computations, including a one-equation SA model, and three two-equation k-ω models, denoted as KO-1, KO-2 and SST. KO-1 and KO-2 refer to the revised Wilcox' models without and with the low Reynolds number modification, respectively [47]. SST refers to Shear Stress Transport k-ω model [48]. They performed the computation for 20° incidence angle and showed the pressure coefficient plots for cross planes X/L=0.60 and 0.77.

In his master thesis, Carsten Braun [19] computed the same flow using the non-conservative vorticity confinement on uniform Cartesian grid with and without refined surface conditions. The computation without refined surface condition uses simple non-slip boundary condition near the surface (equation (2.107)). The refined surface condition refers to a so-called "reflection" condition, which applies a linear type extrapolation to

obtain a velocity for the point just inside the body (details can be found in [19]). The computations covered the incidence angles from 10 to 30°. He also made comparisons with experimental data and solution from Tsai *et al* [4].

4.2 Numerical Simulations Using the Inviscid Surface Model

Inviscid flow over a 6:1 ellipsoid is first studied before advancing to the computation of viscous three-dimensional separated flows.

Fortunately, flow over an ellipsoid is the one of the rare fully three-dimensional flows whose exact inviscid solution is derivable. The numerical solution thus can be verified by comparing it to the analytical solution.

4.2.1 Pressure coefficient on the surface: exact inviscid solution

For an ellipsoid with semi-axes along the *x, y, z* coordinate axes. If free stream velocity is parallel to y plane, and the free velocity components are (U0, 0, W0), the solution of the surface pressure (Ahn [8]) on the surface takes the simple form of

$$C_p = 1 - \left[\left(A \cos\alpha \cos\beta - B \sin\alpha \sin\beta \right)^2 + \left(B \sin\alpha \sin\theta \right)^2 \right] \tag{4.1}$$

where α is the incidence angle, β is the angle between the tangent plane of a point on the ellipsoid surface and the x axis, which is positive for $\frac{x}{l}$ less than 0.5 and negative otherwise

$$\cos\beta = \sqrt{\frac{1 - \left(\frac{2x}{l} - 1 \right)^2}{\left(\lambda^2 + 1 \right) \left(\frac{2x}{l} - 1 \right)^2 - 1}} \tag{4.2}$$

where λ is the thickness ratio. For 6:1 ellipsoid

$$\lambda = \frac{1}{6} \tag{4.3}$$

and θ is the rotation angle within a cross plane. A and B are parameters calculated by the following formulae

$$A = \frac{(1-\lambda^2)^{3/2}}{(1-\lambda^2)^{1/2} - \frac{1}{2}\lambda^2 \log\left(\frac{1+\sqrt{1-\lambda^2}}{1-\sqrt{1-\lambda^2}}\right)} \tag{4.4}$$

$$B = \frac{2A}{2A-1}$$

4.2.2 Numerical simulation and the results

First, inviscid flows over a 6:1 ellipsoid at various incidence angles were computed using the inviscid model previously described. A uniform Cartesian grid with dimension 180 x 70 x 100 was used for all the computation. The free stream speed was set to be 1, with a time step 0.4. The CFL number was expected to be close to 0.8 based on the maximum velocity which typically located somewhere on the surface. The long major axis of the ellipsoid is 120 grid cells. The confinement parameters used were

$$\mu = 0.25$$
$$\varepsilon = 0.375$$

The solution converged typically after 100 time steps. 200 time steps were performed for each computation. The computations were done for incidence angle 0°, 5°, 15°, 30°, 45°, 60°, 75° and 90°. Plots made include vector plots from the output velocity field and pressure coefficient at various cross plane calculated from the output pressure field.

The pressure coefficient was calculated by two ways: the first one uses the Bernoulli relation

$$C_p = 1 - \frac{|\vec{q}|^2}{|\vec{q}_\infty|^2} \tag{4.5}$$

and the other one uses the pressure field output from the "FISHPACK" solver

$$C_{p,fishpack} = -\frac{2(\varphi - \varphi_\infty)}{\Delta t \left|\vec{q}_\infty\right|^2} \tag{4.6}$$

Equation (4.5) can be considered as the exact formula for inviscid flow. The reason to look at the results derived by "FISHPACK" is to check the accuracy of the "FISHPACK" solver on resolving the pressure field, which is very important because for viscous computations discussed later, there is no explicit way to calculate the pressure and one must rely on the "FISHPACK" solver to provide output for the pressure information, and for the input pressure boundary condition of the viscous surface model. Since no explicit boundary condition is specified on the surface in this case, and the grid is not aligned with the surface, the "FISHPACK" may introduce errors near the surface. The pressure coefficient calculated using the "FISHPACK" output thus might not represent the correct pressure coefficient near the surface.

The planes on which the data were extracted are shown in figure 4-2. The pressure coefficient distributions at the symmetry plane (theta = 0) is shown in figure 4-3. From this figures, one can see that the results computed by the inviscid model match very well with the analytical solution, in the whole range of the incidence angles from 0° to 90°.

From the vector plots (figure 4-4 to 4-9) at the symmetry plane for various incidence angles, one can see how the stagnation point shifts from X/L = 0 (0° incidence) to X/L = 0.5 (90° incidence). The velocity of the cross plane X/L = 0.5 for 90° incidence is plotted in figure 4-10.

The pressure coefficients of various cross planes for 90° incidence are plotted in figure 4-11. However, it is observed that the "FISHPACK" solver has difficulty in computing the lower pressure, especially near the low-pressure peaks. The influence of this property will be discussed later after the solutions for the viscous cases are presented.

Figure 4-12 shows the vector plots on various cross planes for incidence angle 30°. These plots are made to show the shift of the maximum cross plane velocity along the body. At X/L = 0.11, the maximum velocity is located approximately at 75°, and gradually shifts to 105° at the end of the ellipsoid near position X/L = 0.9.

The study of the inviscid flow over the 6:1 ellipsoid reveals very import information about the basic flow structure. Although the real viscous flow is very different from the inviscid case, the similarity between them is important, especially for regions of attached flow, which are present even at large angle of attack. For regions where the flow is separated from the surface, the inviscid study can serve as the starting point for understanding the formation of the separation. It reveals some basic information, such as the flow structure before the onset of separation, and provides better capability for understanding the separation process. Another fact that is very important is that from inviscid flow, one can calculate the pressure coefficient using the exact formula and thus can test the accuracy of the Poisson solver, which is used for all the computations on uniform Cartesian grid of the present study.

4.3 Numerical Simulations Using the Surface Boundary Layer Model

4.3.1 Problem setup

The outer uniform Cartesian grid is shown in figure 4-13, whose dimensions are 244 x 46 x 130, with unit cell size. Because of the symmetry of the flow set up, the computation was performed only on half of the space, as shown in figure 4-13. The long major axis of the ellipsoid is 156 grid cells. The velocity magnitude of the free stream was set to 1, with a time step 0.2 and a corresponding CFL number 0.4 (based on the maximum velocity). The conservative vorticity confinement was used for outer grid. The stability condition

$$\frac{|\vec{q}|^2 \Delta t}{2} \le \mu \le \frac{1}{2\Delta t N}$$

requires $0.4 \le \mu \le 0.83$. The numerical coefficients for the outer computation were selected as

$$\mu = 0.75$$
$$\varepsilon = 1.3\mu = 0.975$$

Computations are performed both with and without the surface boundary layer model. For the computations without the surface boundary layer model, all the calculations were performed on the outer uniform Cartesian grid. For computations with the surface model, separate computations were performed on the inner grid shown in figure 3-6. The inner grid was generated using the method described in 3.2.2. The dimension of the inner grid was 270 in the axial direction, 78 in the circumferential direction and 5 in the direction normal to the surface. To avoid making the grid cell overly dense at both ends of the ellipsoid, the grid was clipped at 4 cells from the ends of the ellipsoid. Since the flow near the two ends has limited effect on the separation process, the computational resources saved by making this compromise can be expected to outweigh the minimal loss of the accuracy.

The computations for inner grid were performed on half of the ellipsoid and the corresponding computational space. The thickness of the inner grid in the direction normal to the ellipsoid surface was about 2 outer grid cells. The time step for the inner grid was 0.2. One time step on the outer grid was followed by two time steps on the subgrid, since the time step for the outer grid is two times of that for the inner grid. Non-conservative confinement was used on the inner grid, for the reason that was discussed in 3.2.5. The numerical coefficients used on subgrid were

$$\mu = 0.06$$
$$\varepsilon = 1.6\mu = 0.096$$

The diffusion coefficient is smaller compared to that of the outer computation, because the minimum grid space is only 0.1. The stability condition (equation (2.117)) requires $0.04 \le \mu \le 0.083$. For each computation, the results were output after 400 time steps. To

ensure that the flow was fully converged, a computation of 1500 time steps was performed for 30° incidence angle, from which the flow change from 400 to 1500 time step was verified to be negligible.

The pressure coefficient was calculated using the pressure field φ from the "FISHPACK" Poisson solver

$$C_p = -\frac{2(\varphi - \varphi_\infty)}{\Delta t \left|\vec{q}_\infty\right|^2} \tag{4.7}$$

Computations were done for incidence angles from 10° to 30°, with 5° intervals. The main output from the computation were the velocity field, the vorticity field and the pressure coefficient.

For computation without the surface model, the total running time for 400 time steps was about 1 hour. For computation with the surface model, total running time for 400 time steps was two and a half hours. All the computations were done on a PC with 1.7 GHZ AMD Atholon XP processor and 512 MB system memory.

4.3.2 Discussions of the results

Computations with uniform Cartesian grid without the boundary layer model

a) Pressure distribution

1) Pressure distribution in the cross plane at X/L=0.77 at various incidence angles

Figure 4-15 shows the surface pressure distribution on the cross plane located at x/L=0.77 for various incidence angle from 10° to 30°. CFD result retained by Tsai *et al* [4] and the experimental result by Simpson *et al* [6][10] are also plotted together for comparison.

2) Comparison with solution using non-conservative vorticity confinement

Figure 4-15 shows the comparison between the non-conservative vorticity confinement and conservative confinement, at cross plane x/L=0.77 and 30° incidence angle. The results of non-conservative confinement are those of Braun [19], in which separate computations were done using a simple non-slip surface boundary condition as well as a refined surface boundary condition. The comparison shows the dramatic enhancement made by changing the non-conservative confinement to the conservative formulation. For both of the solutions of the non-conservative confinement, the low-pressure peak induced by the streamwise vortex is indiscernible, while in the result using the conservative confinement, it is well defined and has good agreement with the experimental data. The primary and secondary separation line can be clearly seen from the curves of the conservative confinement, which is not the case for either of the results from the non-conservative confinement.

3) Comparison with MILES solution

Figure 4-17 incorporates the many results from various CFD methods for incidence angle 20° and at the cross plane X/L=0.77, including that from Constantinecu *et al* [27] using MILES method for comparison, which is very interesting since MILES is similar to the confinement method, in a manner that both apply no explicit turbulence model on the surface. The solutions from the vorticity confinement are better than those of MILES in this comparison. From the results of MILES, one cannot tell any distinct characteristics of the flow separation. By comparison, the results obtained by using vorticity confinement are well behaved, with clearly defined separation feature and comparing well with the experiment.

Using the new confinement without an explicitly defined surface gives good results near the middle. However, the resolutions deteriorate towards the front and rear end of the body. Figure 4-39 shows the jagged definition of the surface at cross plane x/L=0.2. Poor resolution at the cross plane near the two end is expected since there are

only very few grid points to define the surface.

b) Vorticity iso-surface

Iso-surface for computation without the surface model are plotted in figure 4-40 to 4-44. The incidence angles range from 10° to 90°. The vorticity magnitude of the displayed iso-surfaces is one third of the maximum vorticity magnitude.

Computations with the boundary layer model

a) Pressure distribution

1) Comparison with CFD data, solutions without the surface model and experimental data

The pressure coefficient at cross plane X/L=0.77 for incidence angles 10°, 15°, 20°, 25°, and 30° are plotted in 4-20 to 4-24. Incorporated in the same plots are the CFD data from Whitney *et al* [4], data from the computation without the surface model, and experimental data from Simpson *et al* [6][10]. One can see enhancement on the resolution by applying the surface model over that of the computation without the model. The results are qualitatively correct, and reasonably close to the experimental data.

In section 4.2.2, the difficulty for the "FISHPACK" Poisson solver to derive the lower pressure peaks has been discussed. Similar behavior can be observed from the results from the computations with or without the surface model. Because the "FISHPACK" Poisson solver used in the computation does not allow explicit pressure boundary condition on the surface, the pressure field must be smoothly extended into the surface. The solution near the surface thus is "smeared", which causes the difficulty in getting the lower pressure peaks.

What is interesting is that the results from the k-ε method, in the contrary to those from the confinement method, tend to exhibit lower low-pressure peaks than the experiment data.

2) Comparison with various results from different methods

Figure 4-17 shows the results from different CFD methods. The plots is for the pressure coefficient at the incidence angle of 20° in the cross plane at X/L = 0.77. The methods used for these computations are those discussed in 4.1.3. The first thing to notice is these results are very different quantitatively. Compare to the experimental data, all the CFD results are qualitatively good except for that of MILES [27]. Other than the difficulty on getting the lower pressure peak, the result from the surface boundary layer is very close to the results obtained by the DES [27] and the SA [5] methods. The results from the three k-ω models (KO1, KO2 and SST) [5] yield better results especially for the pressure drop induced by the streamwise vortex. Considering its simplicity and high efficiency, and no efforts have been engaged in refining the pressure solver, this comparison shows the great potential of the new method.

3) Detailed comparison for 10° and 30° incidence angles

In figure 4-23 to 4-38, the results for cross planes covering the whole range of the body are plotted. Comparisons are limited to only 10° and 30° incidence angles, due to the availability of the experimental data. The experimental data used are from Meier *et al* [11]. Unfortunately, none of the numerical results in the literature covered more than one (typically X/L=0.77) or at most two cross planes.

One can see from these figures that the results agree reasonably well with the experiment for the computation with the surface model. The result from the computation without the surface model however is not acceptable for small incidence angle, and for all incidence angles near the front end and the rear end of the ellipsoid.

Accurate simulation along the whole ellipsoid body is very important for accurately simulating the separation lines and stream-wise vortex, which proposes a real challenge for CFD methods. However, most of the simulations found in the literature seem to focus on the X/L=0.77 cross plane only. Though the result could be very good for one cross plane, it could be totally wrong for other cross planes. Conservative

confinement coupled with the simple boundary model seems to be able to globally achieve reasonably accurate results.

b) Flow pattern

1) The overlapping velocity field

Figure 4-57 to 4-62 show the cross plane velocity of the overlapped grids near the surface for different incidence angles. In all these charts, the velocity matches very well between the outer grid and the inner grid inside the whole domain of the inner grid. This means the coupling algorithm is successful for the computation.

2) Compare to the experiment data

In figure 4-65, the streamlines obtained by using the surface model are compared to the experiment data from Simpson *et al* [9]. One can see that the separation point and the streamline patterns are similar between the computation results and the experimental data. The computed boundary layer is thicker than the experimental result, which can be expected due to the coarse grid used. It is very difficult for the plotting software to deal with the velocity vectors forming the secondary vortex since there are only several grid nodes involved. The plotted streamlines just point inwards and it should not have much meaning about those inward-pointing streamlines.

3) Compare to CFD results of Whitney and Tsai [4]

In figure 4-49 to 4-51, the flow patterns by using the surface model and those by Tsai *et al* are compared. The similarities between these two different simulations are visible. Since the simulation using the surface boundary model uses much coarser grid near the surface, much higher efficiency is expected.

4) Vorticity contour on cross planes

For the vorticity contour plots, the contour levels are from the maximum to one third of the maximum vorticity magnitude. Figure 4-46 shows the vorticity contour at cross plane 0.6 and 0.77 for an incidence angle of 20°, which are similar to the

experiment result from Wetzel *et al* [10](figure 4-45). Figure 4-47 shows the vorticity contours of several cross planes for 30° incidence angle.

c) Vorticity iso-surface

Iso-surfaces of vorticity magnitude for computation with model are plotted in figure 4-53 to 4-56. The vorticity magnitude of the displayed iso-surfaces is one third of the maximum vorticity magnitude. At 10°, vortex shedding is minimal, and the streamwise vortex is very close to the surface. As the incidence angle increases, the amount of shedding increases, also the separation stretches forward and the shedding vortex goes further away from the surface.

4.4 Discussion of the Surface Models

Qualitatively reasonable results are obtained for flow over a 6:1 ellipsoid at various incidence angles, from viscous computations with or without the surface model. The computational models used are simple and efficient.

However, the vorticity confinement methods are not complete and future enhancement is needed but should be well worth the endeavor. Currently, one of the main concerns on applying it to incompressible flow problems would be find a better way to solve the lower pressure peaks near the body. Further application of the method to compressible flows still needs to be explored.

The inviscid surface model, which is based on a solid mathematical model, worked well considering its minimal requirement of additional complexity, though its usage still needs to be explored.

The incorporation of the surface boundary model is successful, though the use of two sets of grid systems increases the complexity of the confinement method. The

enhancement gained after applying the model is appreciable and is indispensable for some flow problems. The surface model studied in this section is one of the simplest models that can be used with vorticity confinement. One can certainly devise other more sophisticated surface models and incorporate them into the vorticity confinement method. The most important thing is not the form of the model, but the essence of the vorticity confinement concepts.

5. Conclusion

New developments in vorticity confinement methods are covered in the present study. The newly developed conservative confinement method is studied and tested. A new surface boundary layer model, which intends to incorporate the explicitly defined surface boundary condition and resolve a thin artificial boundary layer near the surface, is devised and demonstrated by applying it to flow over a 6:1 ellipsoid. Results show that the conservative confinement give better result than the non-conservative scheme, from simple flows such as a convecting vortex to a complicated three-dimensional separated flow. The addition of the surface model further enhances the accuracy of the existing method.

To demonstrate the capability of the methods, comparisons have been made with experimental data or the exact solutions, and data obtained with conventional CFD methods. The computational results from the new models show good comparison with either experimental data or exact solutions (for inviscid computation). The new methods use simpler grid than conventional methods and are considerably more efficient, while the solutions are reasonably accurate compared to other conventional CFD methods. Although the details within very small features cannot be solved due to the limitation of the grid resolution, the dominant properties of the flow can be predicted reliably. The main characteristics of the flow problems can be resolved economically and efficiently by using these new methods.

The addition of surface boundary layer model adds the capability of applying accurate surface boundary conditions for the confinement method. Enhancement is observed from the solutions by applying this surface model to full three-dimensional

separated flows.

The methods may be applied to flows with complicated body configurations, because of the easy grid setup, simple numerical model and standard central difference discretization scheme.

For future work, further refinement of the surface model is recommended, especially the development of a better method that enables explicit surface pressure conditions. The confinement method has already been successfully applied in solving compressible flows [20][57][58], although they are not covered in this context. However, the surface model still needs to be extended to solve full compressible flows. A thorough study of the conservative confinement on curvilinear grids is also encouraged for the future studies.

LIST OF REFERENCES

LIST OF REFERENCES

1) " Application of Vorticity Confinement to the Prediction of Flow over Complex Bodies", AIAA Journal, Vol. 41, NO. 5, May 003. Y. Wenren, M. Fan, L. Wang, M. Xiao, J. Steinhoff.
2) "Convection of Concentrated Vortices and Passive Scalars as Solitary Waves", Journal of Scientific Computing, to be published in December 2003. J. Steinhoff, M. Fan and L. Wang.
3) "Development of Simple Boundary Layer Model Including Separation Using Surface Coordinates", proposal for ARO contract DAAG55-98-1-0316, John Steinhoff.
4) "Numerical Study of Three-dimensional Flow Separation for a 6:1 Ellipsoid", AIAA-99-0172, C. Y. Tsai and A.K. Whitney.
5) "Application of Modern Turbulence Models to Vortical Flow around a 6:1 Prolate Spheroid at Incidence", AIAA 2003-429, S.E. Kim and S.H. Rhee.
6) "Full Three Dimensional Measurement of the Cross-flow Separation Region of a 6:1 Prolate Spheroid", Experiments in Fluids 17(1994) 68-74, C.J. Chesnakas, R.L. Simpson.
7) "The flow structure in the lee of an inclined 6:1 prolate spheroid", Journal of Fluid Mechanics, 1994, vol. 269, pp. 79-106, T.C. Fu, A. Shekarriz, J. Katz and T.T. Huang.
8) "An Experimental Study of Flow Over a 6 to 1 Prolate Spheroid at Incidence", doctoral dissertation, Virginia Polytechnic Institute and State University, 1992, Seungki Ahn
9) "Mean Velocity and Pressure and Velocity Spectral Measurement within a Separated Flow around a Prolate Spheroid at Incidence", AIAA-98-0630, M. Goody, R.L. Simpson, M. Engel.
10) "Measurement of Three Dimensional Crossflow Separation", AIAA Journal, vol. 36, No. 4. April 1998, G. Wetzel, R. L. Simpson, C.J. Chesnakas.

11) Data Report DFVLR 1B 222-84/A10, Fottingen, 1984, H. Meire, H. Kreplin, A. Landauber.
12) "A New Eulerian Method for the Computation of Propagating Short Acoustic and Electromagnetic Pulses", Journal of Computational Physics, vol. 157, 2000. J. Steinhoff, M. Fan and L. Wang.
13) "The Computation of Flow over Helicopter Rotors and Complex Bodies Using Vorticity Confinement", Computational Fluid Dynamics Journal, vol. 9, No. 1, 2000. J. Steinhoff, Y. Wenren, L. Wang, M. Fan and C. Braun.
14) "Application of Vorticity Confinement to the prediction of the Flow over Complex Bodies", Frontiers of Computational Fluid Dynamics-2002 (D. Caughey and M. Hafez, eds). J. Steinhoff, Y. Wenren, C. Braun, L. Wang and M. Fan.
15) "A New Eulerian Computational Method for Propagation and Scattering of Short Acoustic and Electromagnetic Pulses", Advances in Fluid Mechanics 2000, May 2000, Montreal, Canada. J. Steinhoff, M. Fan and L. Wang.
16) "Numerical Simulation of Vortical Flows Using Vorticity Confinement Coupled with Unstructured Grid", AIAA-2001-0606, Mitsuhiro Murayama, Kazuhiro Nakahashi, Shigeru Obayashi.
17) "Efficient Computation of Separating High Reynolds Number Incompressible Flows Using Vorticity Confinement", AIAA-99-3316, 1999, Norfolk, VA. J. Steinhoff, W. Yonghu and L. Wang.
18) "A New Numerical Method for Computing Flow over Complex Aerodynamic Configurations and Its Application to Rotor/Body Computation Using Cartesian Grids", Yonghu Wenren, Doctoral Dissertation, May 1997, University of Tennessee, Knoxville.
19) Master thesis, Carsten Braun, Rheinsch - Westf" Alische Technische Hochschule, Aachen, April 2000.
20) "The computation of Massively Separated Flows Using Compressible Vorticity Confinement Methods", AIAA-2002-0136, G. Hu and B. Grossman.
21) "Numerical Computation of Internal and External Flows", ISBN 0-471-92385-0, 1990, Charles Hirsch.

22) "Computational Fluid Dynamics, An Introduction for Engineers", ISBN 0-582-01365-8, 1989, M. B. Abbott, D. R. Basco.

23) "Surface Boundary Conditions for the Numerical Solution of the Euler Equations", AIAA Journal, vol. 32, No. 2, February 1994, A. Dadone, B. Grossman.

24) "An Accurate Cartesian Grid Method for Viscous Incompressible Flow with Complex Immersed Boundaries", Journal of Computational Physics 156, 209-240, 1999, T. Ye, R. Mittal, H.S. Udaykumar, W. Shyy.

25) "The Spontaneous Generation of the Singularity in a Separating Laminar Boundary Layer", Journal or Computational Physics 38, 125-140, 1980, L.L. van Dommelen and S.F. Shen.

26) "Detached Eddy Simulation of Massively Separated Flows", AIAA-2001-0879, M. Strelets.

27) "Numerical Investigation of Flow Past a Prolate Spheroid", AIAA-2002-0588, G. Constantinescu, H. Pasinato, Y. Wang, K. Squires.

28) "Large-eddy Simulation: A critical review of the technique", Q. J. R. Meteorol. soc. 1994,120,pp1-26, P.J. Mason.

29) "50 Years of Turbulence Research in China", Annu. Rev. Fluid Mech. 1995, 27: 1-15, Pei-Yuan Chou, Ru-Ling Chou.

30) "Direct Numerical Simulation: A Tool in Turbulence Research", Annu. Rev. Fluid Mech. 1998. 30:539-578, P. Moin and K. Mahesh.

31) "Numerical Solution of Flow Problems Using Body-fitted Coordinate Systems", Joe F. Thompson.

32) "Application of a Fractional-step Method to Incompressible Navier-Stokes Equations", Journal of Computational Physics, Vol. 59, 1985, J. Kim, and P. Moin.

33) "The artificial Compression Method for Computation of Shocks and Contact Discontinuities", Mathematics of Computation, Vol. 32, No. 142, April 1978, A. Harten.

34) "Composite Overlapping Meshes for the Solution of Partial Differential

Equation", Journal of Computational Physics, vol. 90, pp 1-64, 1990, G. Chesshire and W.D. Henshaw.

35) "Reynolds-Averaged Navier-Stokes Calculations of Unsteady Turbulent Flow", AIAA 2000-0143, H. L. Zhang, C. R. Bachman and H. F. Fasel.

36) "Prediction of Turbulent Flow over a Sphere", G.S. Constantinescu, M.C. Chapelet, and K.D. Squires, unpublished

37) "Computational Fluid Dynamics of Inviscid and High Reynolds Number Flows", 1998, Charles L. Merkle, Sheng-Tao Yu.

38) "Investigation of the Vorticity Confinement Method for Flows with Separation", doctoral dissertation, University of Tennessee, Knoxville, 1997, David B. Underhill.

39) "A First Course in Turbulence", ISBN 0-262-20019-8, 1997, H. Tennekes and J.L. Lumley.

40) "Mathematical Methods for Physicists", fourth edition, ISBN 0-12-059815-9, 1995, George B. Arfken and Hans J. Weber.

41) "Incompressible Flow", second edition, ISBN 0-471-59358-3, 1996, Ronald L. Panton.

42) "Partial Differential Equations of Mathematical Physics and Integral Equations", ISBN 0-486-68889-5, 1988, Ronald B. Guenther and John W. Lee.

43) "Boundary-Layer Theory", seventh edition, ISBN 0-07-055334-3, 1987, Hermann Schlichting.

44) "Viscous Fluid Flow", second edition, ISBN 0-07-069712-4, 1991, Frank M. White.

45) "Comments on the Feasibility of LES for Wings, and on a Hybrid RANS/LES Approach", First AFOSR International Conference on DNS/LES, Ruston, Louisana, USA, 1997, P. R. Spalart, W. H. Jou, M. Strelets and S.R. Allmaras.

46) "Monotonically Integrated Large Eddy Simulation of Free Shear Flows", AIAA Journal, Vol. 37, pp. 544-556, 1999, C. Fureby and F. F. Grinstein.

47) "Turbulence Modeling for CFD", second edition, July 1998, D. C. Wilcox.

48) "Two-equation Eddy-viscocity Turbulence Models for Engineering Applications",

AIAA Journal, Vol. 32, No. 8, pp 1598-1605, 1994, F. R. Menter.

49) “Computing Complex Flows on Coarse Grids Using Vorticity Confinement”, AIAA-2002-0135, M. Fan, W. Dietz , Y. Wenren, and J. Steinhoff.

50) “Computational Vorticity Confinement: Two Dimensional Incompressible Flow”, Proceedings of the Sixteenth Southeastern Conference on Theoretical and Applied Mechanics, 1992, J. Steinhoff, T. Mersch, and Y. Wenren.

51) “Vorticity Confinement: A New Technique for Computing Vortex Dominated Flows,” In D.A. Caughey and M.M. Hafez, editors, *Frontiers of Computational Fluid Dynamics*. John Wiley & Sons, 1994, J. Steinhoff.

52) “Computation of Thin Features Over Long Distances Using Solitary Waves,” AIAA Proceedings, 13th Computational Fluid Dynamics Conference, July 1997, J. Steinhoff, E. Puskas, S. Babu, Y. Wenren, and D. Underhill.

53) “Modification of the Euler Equations for Vorticity Confinement Application to the Computation of Interacting Vortex Rings,” *Physics of Fluids*, 6, 1994, J. Steinhoff, and D. Underhill.

54) “Computing Blunt Body Flows On Coarse Grids Using Vorticity Confinement”, *Journal of Fluids Engineering*, December, 2002, M. Fan, Y. Wenren, W. Dietz, M. Xiao, J. Steinhoff.

55) "Application of Vorticity Confinement to the Prediction of the Wake of Helicopter Rotors ans Complex Bodies", AIAA-99-3200, June 1999, Y. Wenren, J. Steinhoff.

56) "An Automatic Anti-diffusion Method for Vortical Flows Based on Vorticity Confinement", Aerospace Science and Technology 7, Germany, June 2003, M. Costes, G. Kowani.

57) "Analysis of Vorticity Confinement for Compressible Flow", America Helicopter Society 59th Annual Forum, Phoenix, AZ, 2003, M. Costes, G. Kowani.

58) "Capture of Contact Discontinuities and Shock Waves Using a Discontinuity Confinement Procedure", AIAA 97-0874, Reno, NV, 1997, S. Pevchin, J. Steinhoff, B. Grossman.

59) "FISHPACK: Efficient FORTRAN Subprograms for the Solution of Elliptic

Partial Differential Equations", UCAR Publication, July 1999, P. Swarztraouber, R. Sweet and J. Adams.

APPENDIX

Appendix I: Figures

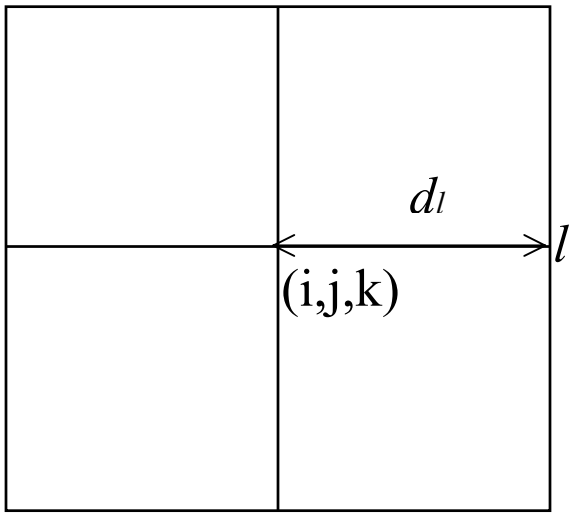

Figure 2-1. Harmonic mean on discrete lattice.

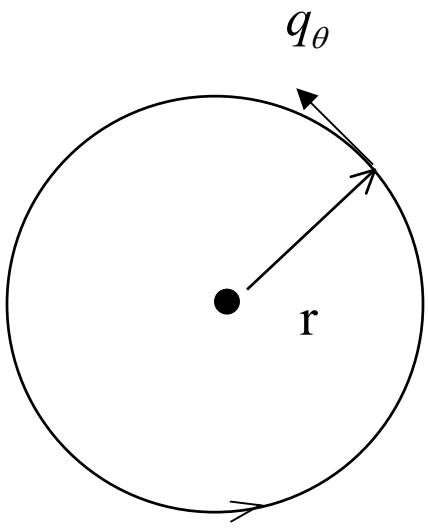

Figure 2-2. Analytical solution for an axisymmetric vortex.

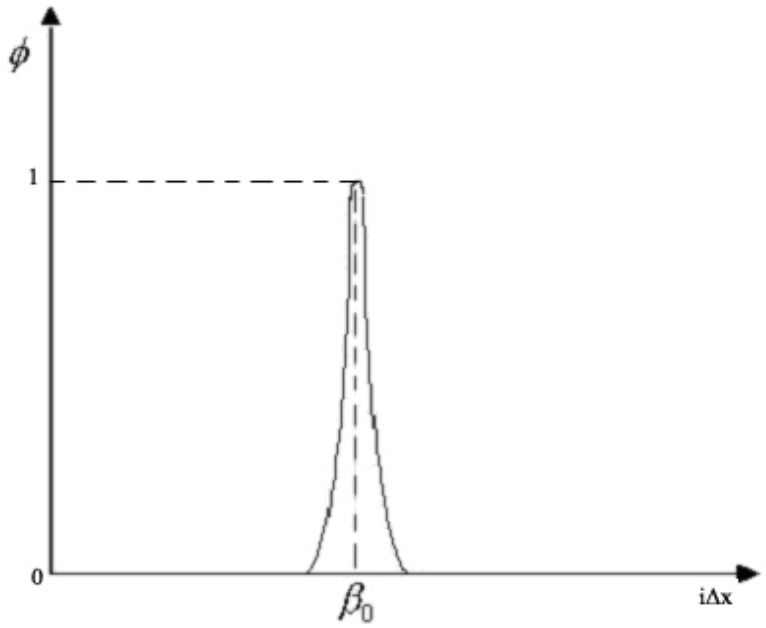

Figure 2-3. The analytical solution of a one-dimensional pulse.

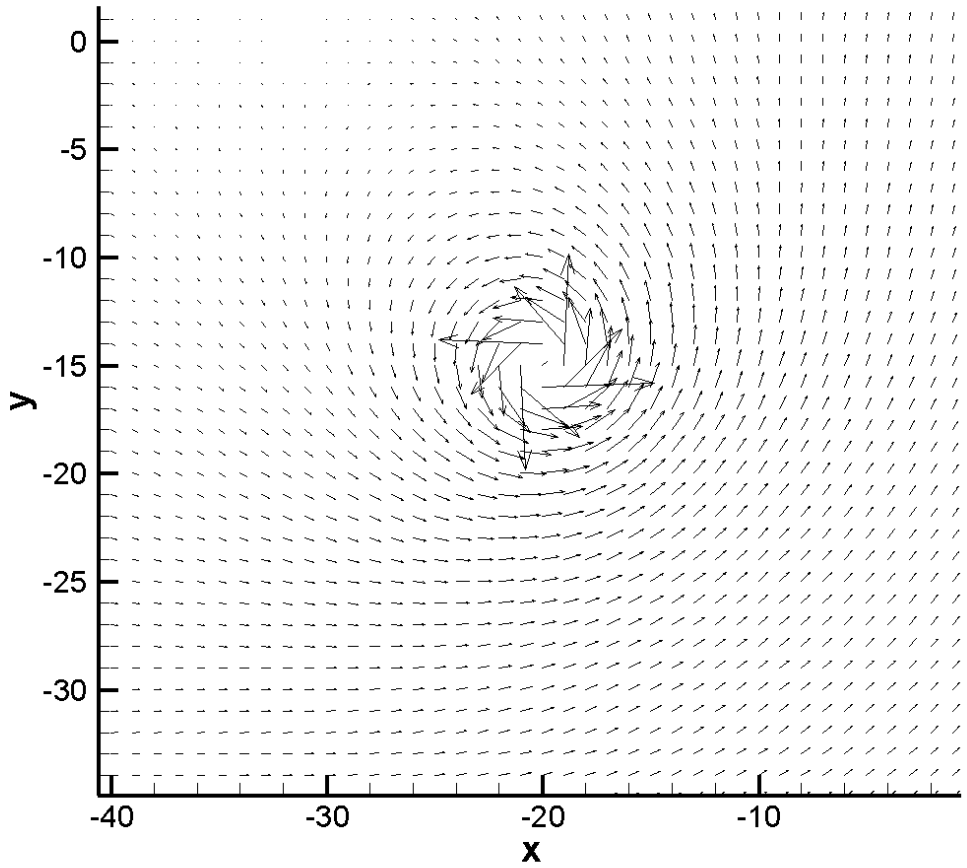

Figure 2-4. Initial velocity field of a single convecting vortex.

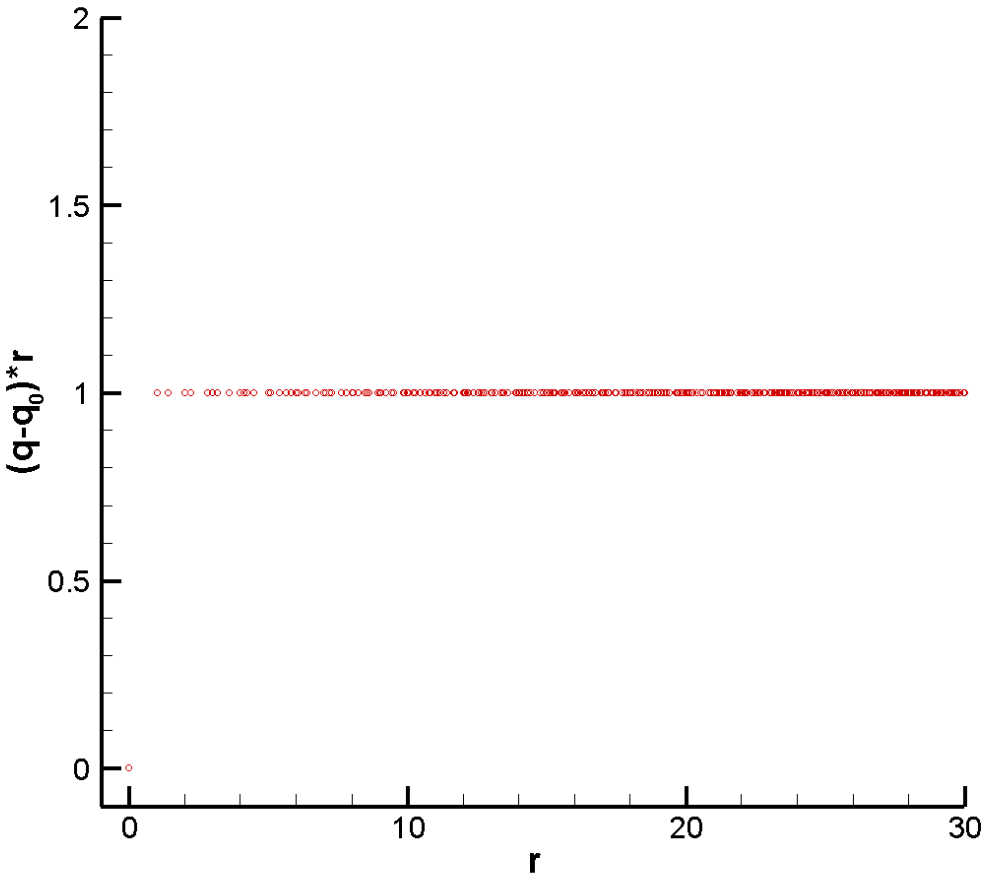

Figure 2-5. Initial velocity distribution of a single convecting vortex.
($(q-q_0)*r$ denotes the normalized velocity defined by equation (2.121).)

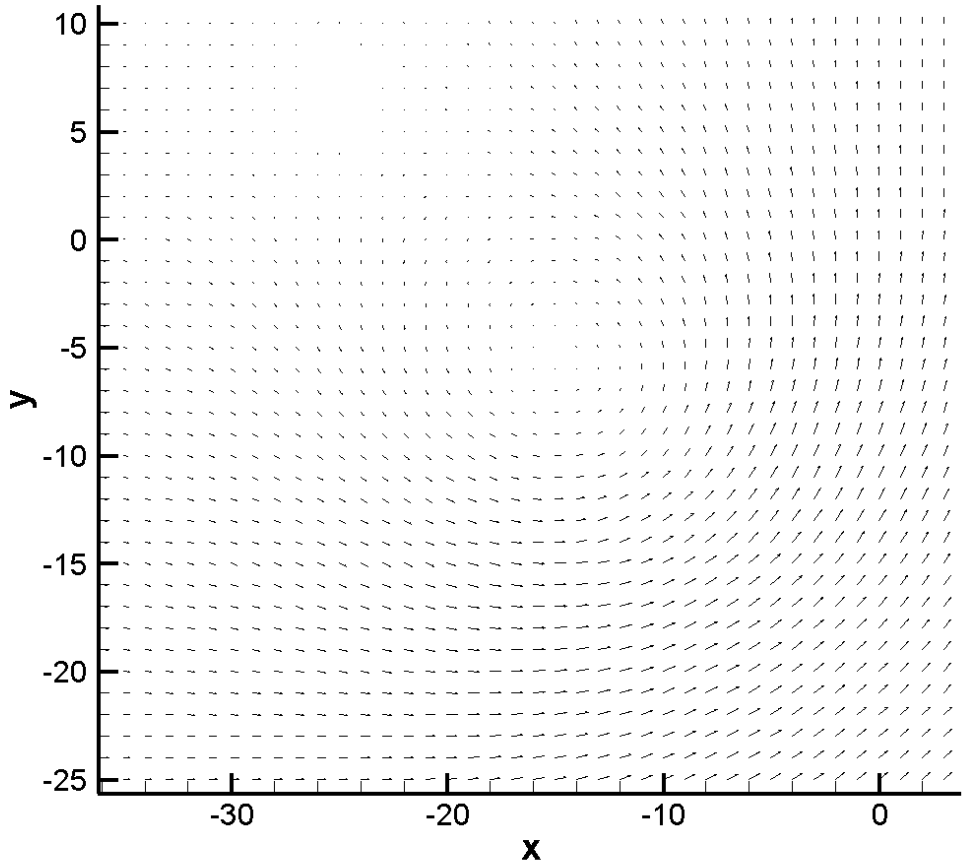

Figure 2-6. Velocity field of a single convecting vortex after 1000 time steps, without vorticity confinement.

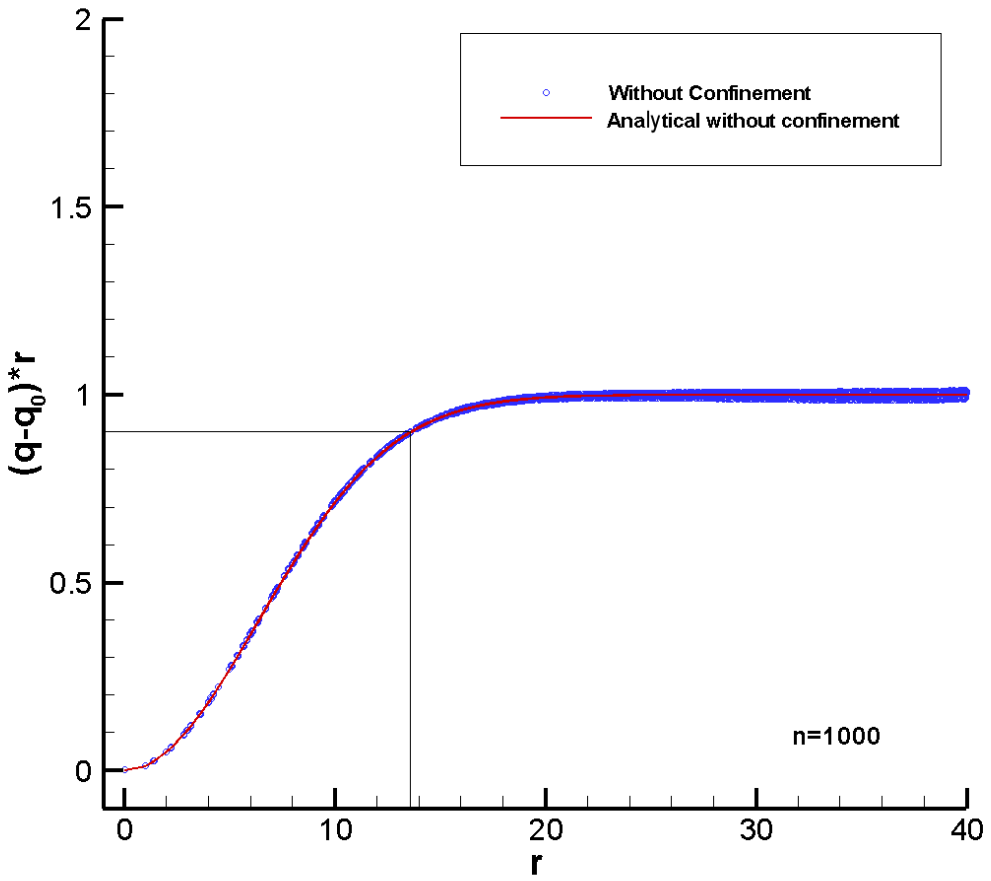

Figure 2-7. Velocity distribution of a single convecting vortex after 1000 time steps, without vorticity confinement.

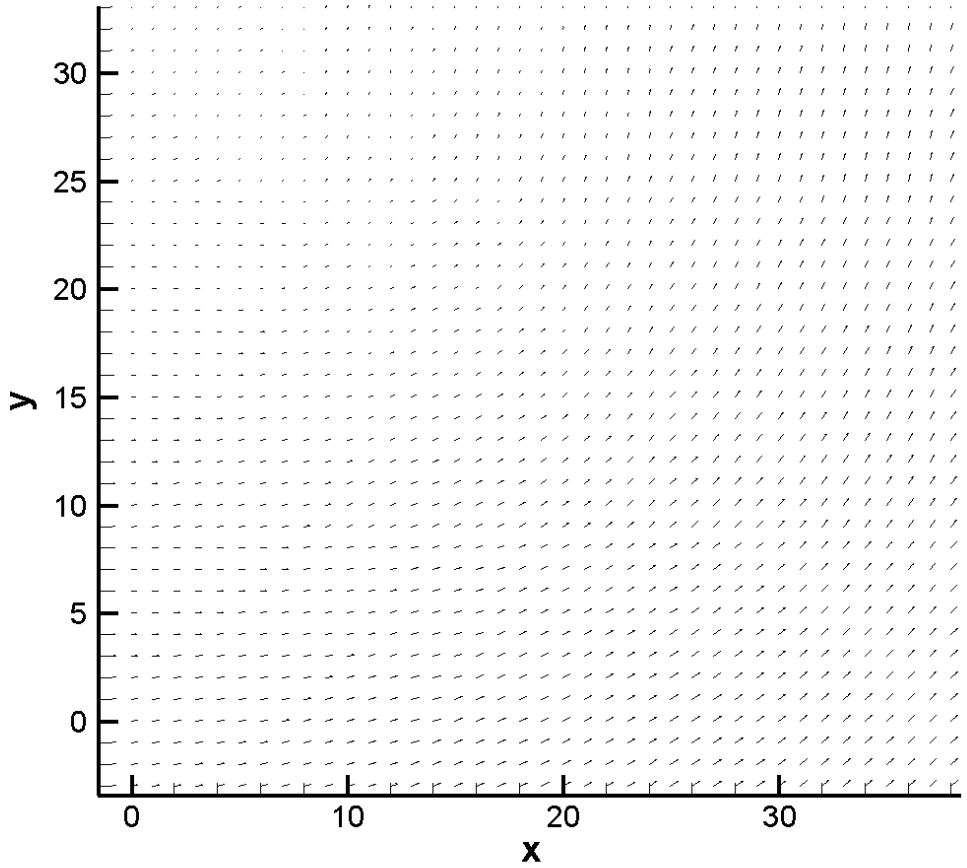

Figure 2-8. Velocity field of a single convecting vortex after 5000 time steps, without vorticity confinement

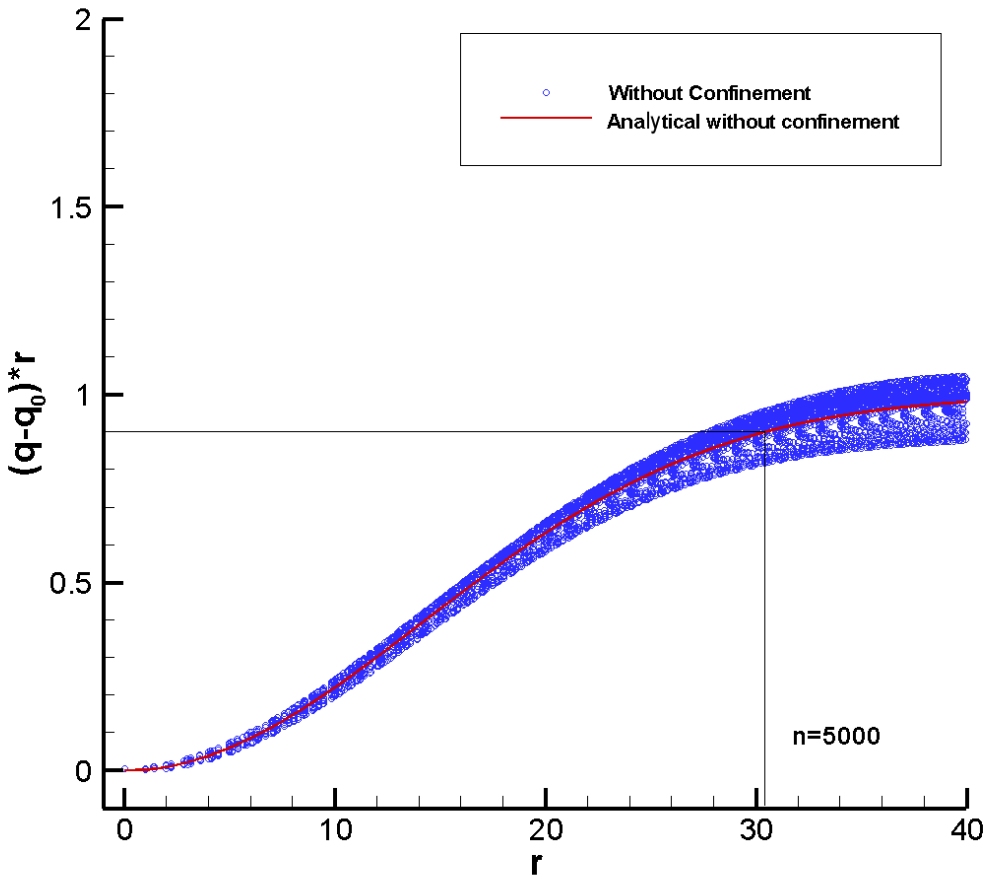

Figure 2-9. Velocity distribution of a single convecting vortex after 5000 time steps, without vorticity confinement.

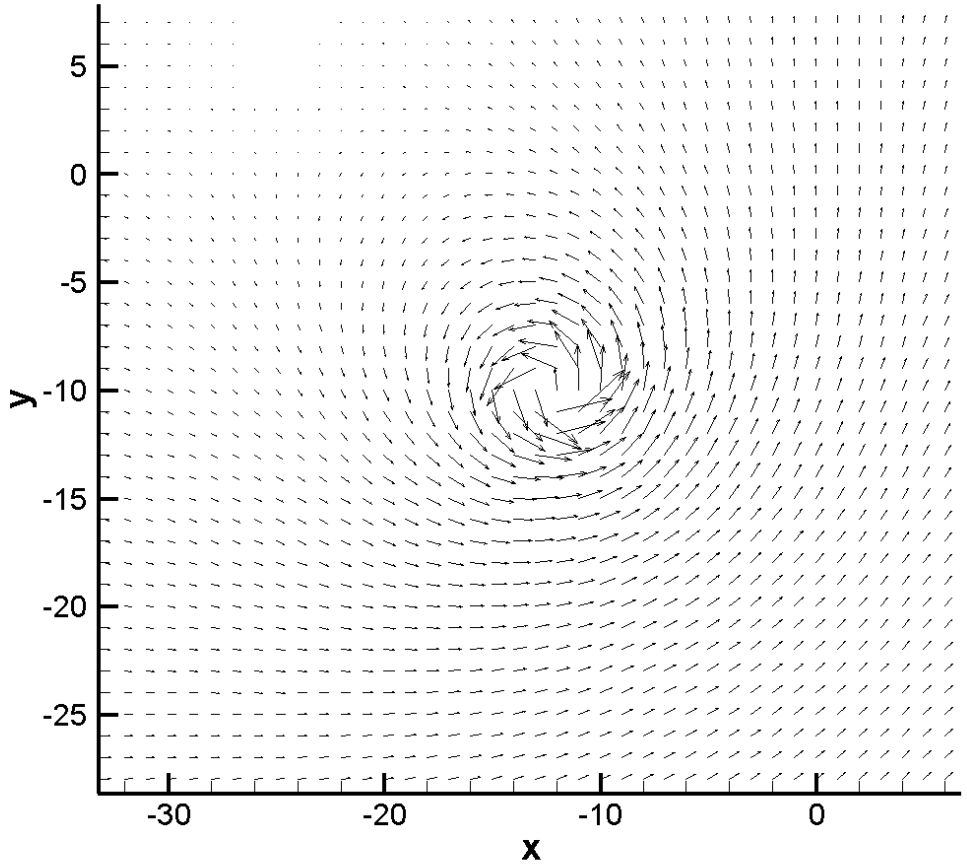

Figure 2-10. Velocity field of a single convecting vortex after 1000 time steps, with non-conservative vorticity confinement.

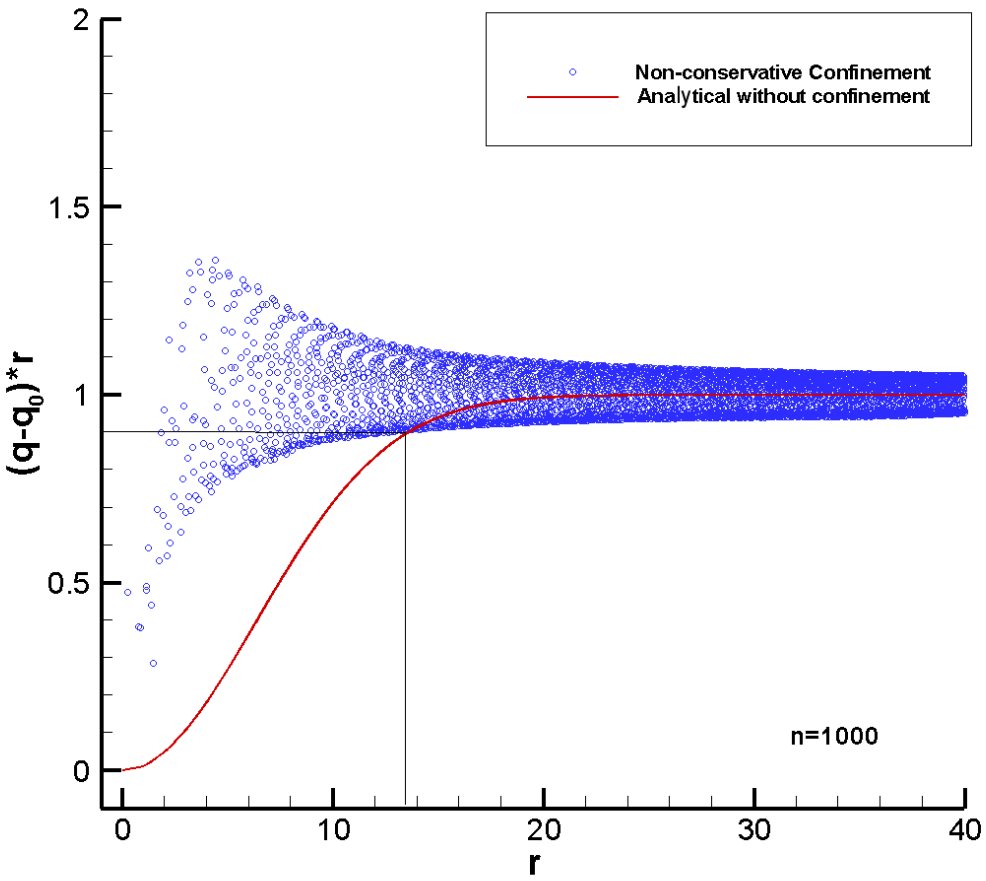

Figure 2-11. Velocity distribution of a single convecting vortex after 1000 time steps, with non-conservative vorticity confinement.

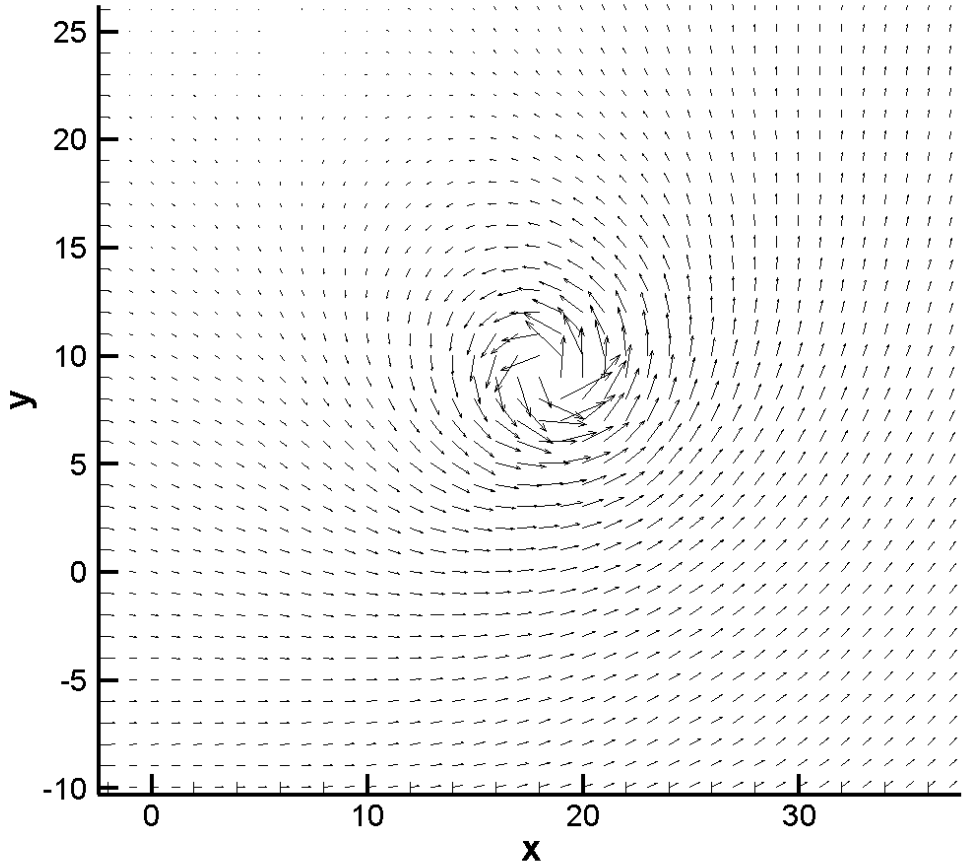

Figure 2-12. Velocity field of a single convecting vortex after 5000 time steps, with non-conservative vorticity confinement.

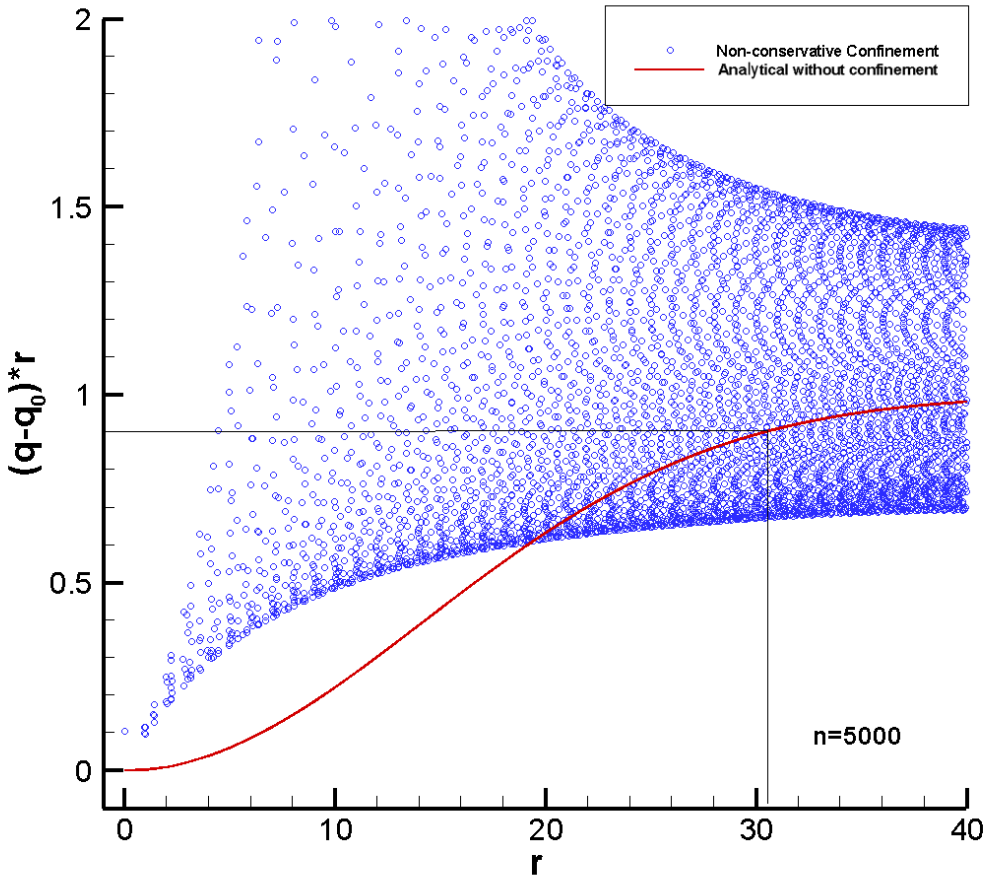

Figure 2-13. Velocity distribution of a single convecting vortex after 5000 time steps, with non-conservative vorticity confinement.

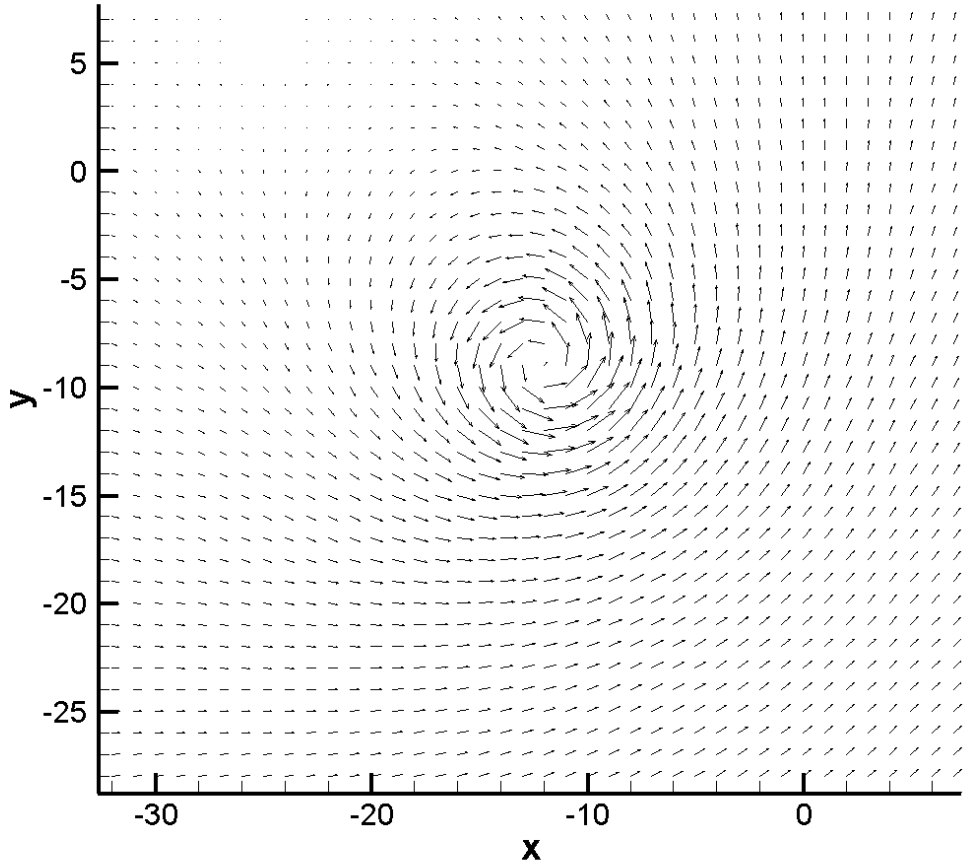

Figure 2-14. Velocity field of a single convecting vortex after 1000 time steps, with conservative vorticity confinement.

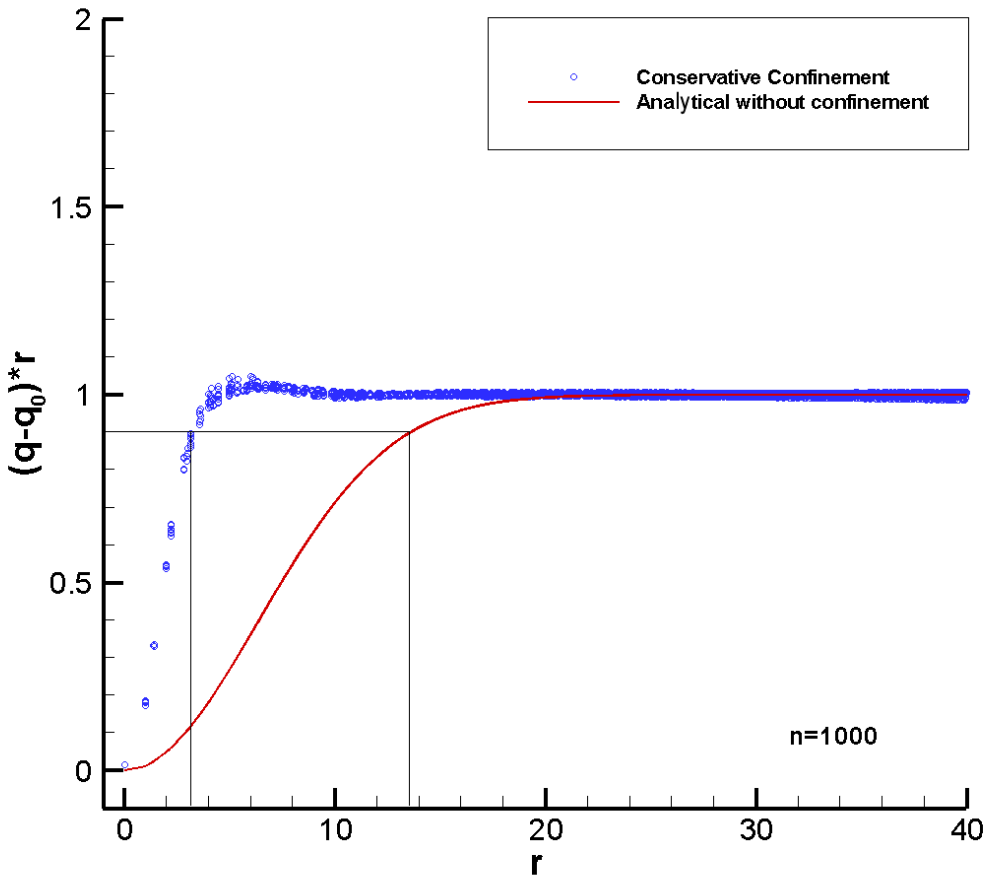

Figure 2-15. Velocity distribution of a single convecting vortex after 1000 time steps, with conservative vorticity confinement.

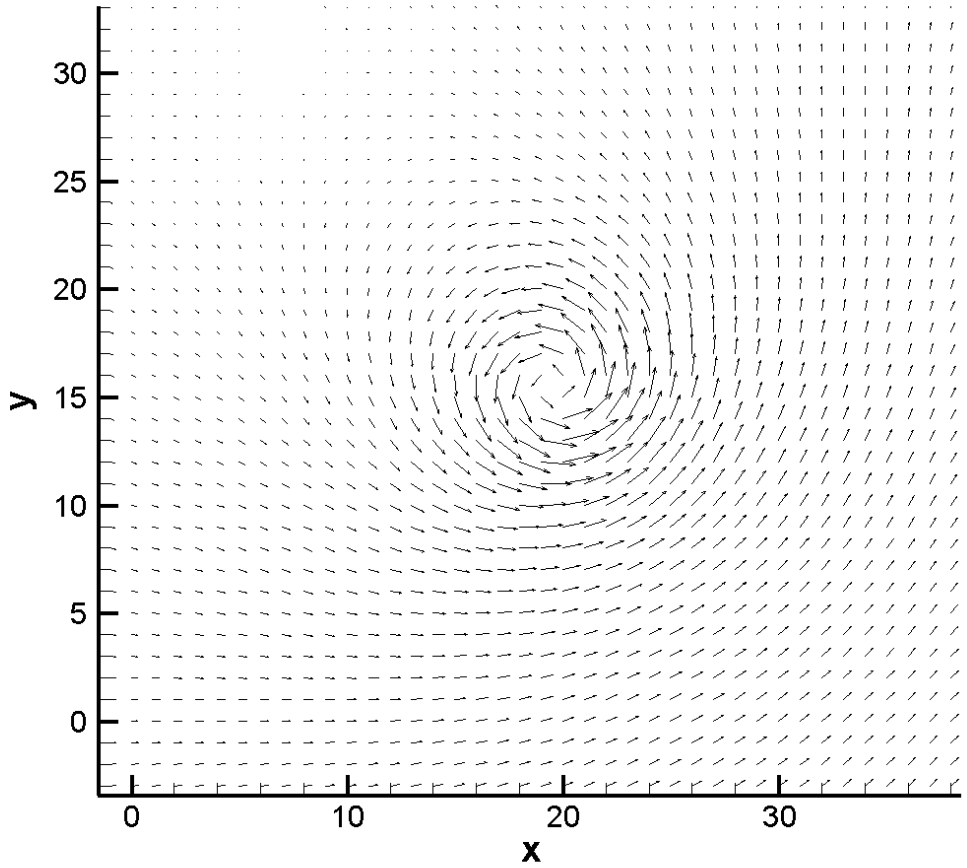

Figure 2-16. Velocity field of a single convecting vortex after 5000 time steps, with conservative vorticity confinement.

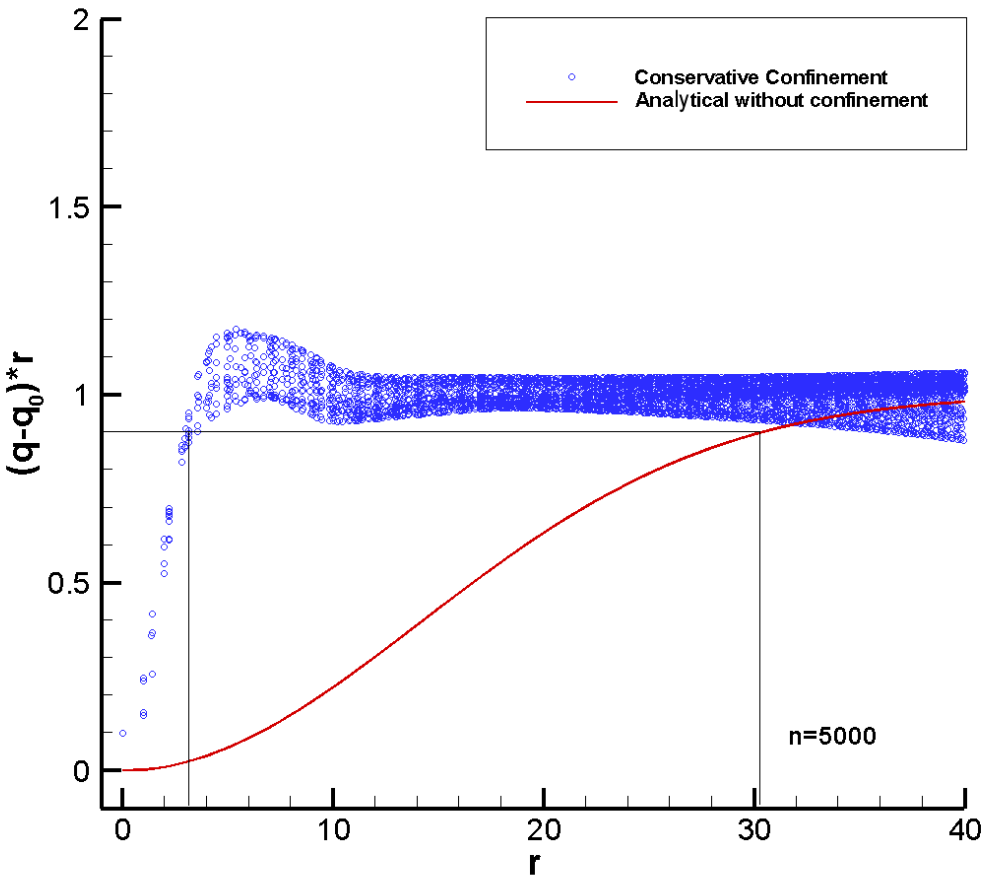

Figure 2-17. Velocity distribution of a single convecting vortex after 5000 time steps, with conservative vorticity confinement.

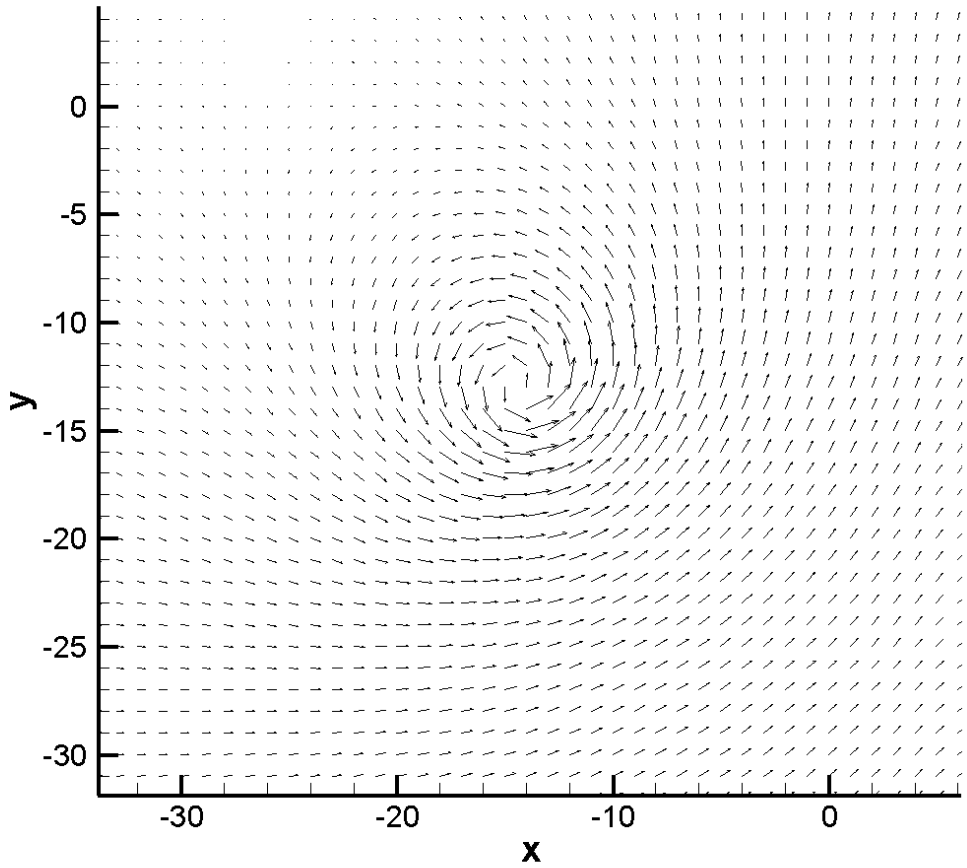

Figure 2-18. Velocity field of a single convecting vortex after 1000 time steps, with old confinement scheme.

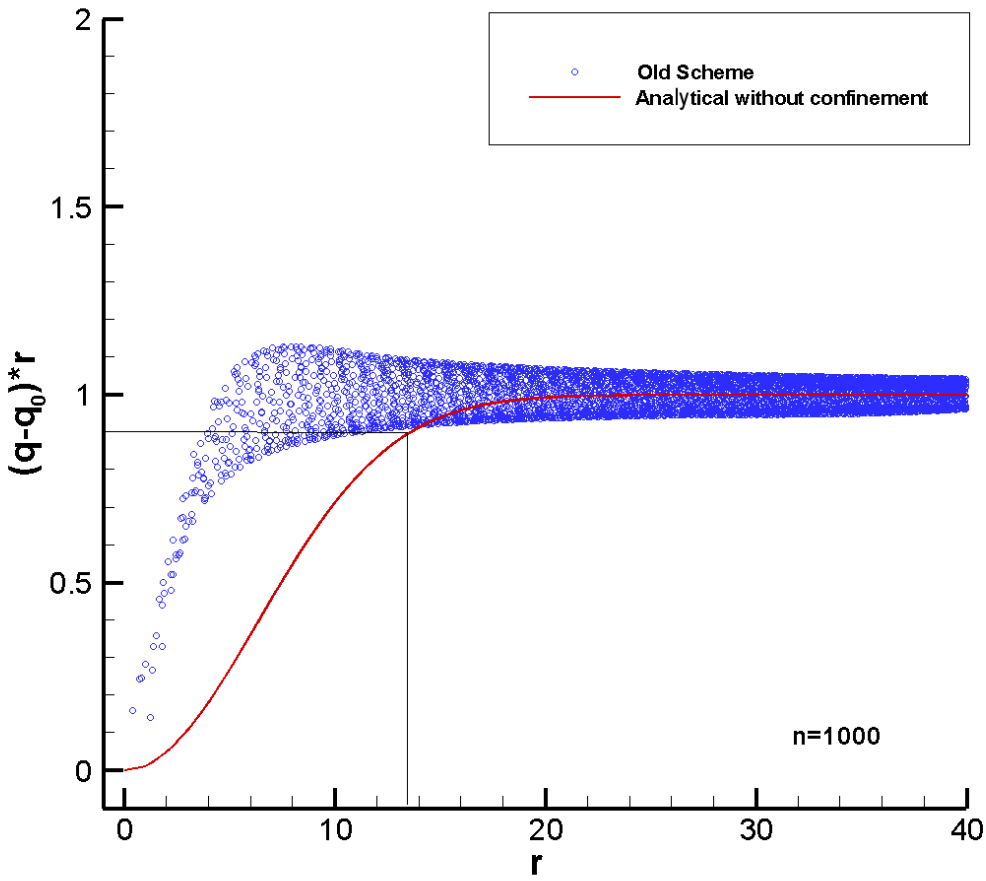

Figure 2-19. Velocity distribution of a single convecting vortex after 1000 time steps, with old confinement scheme.

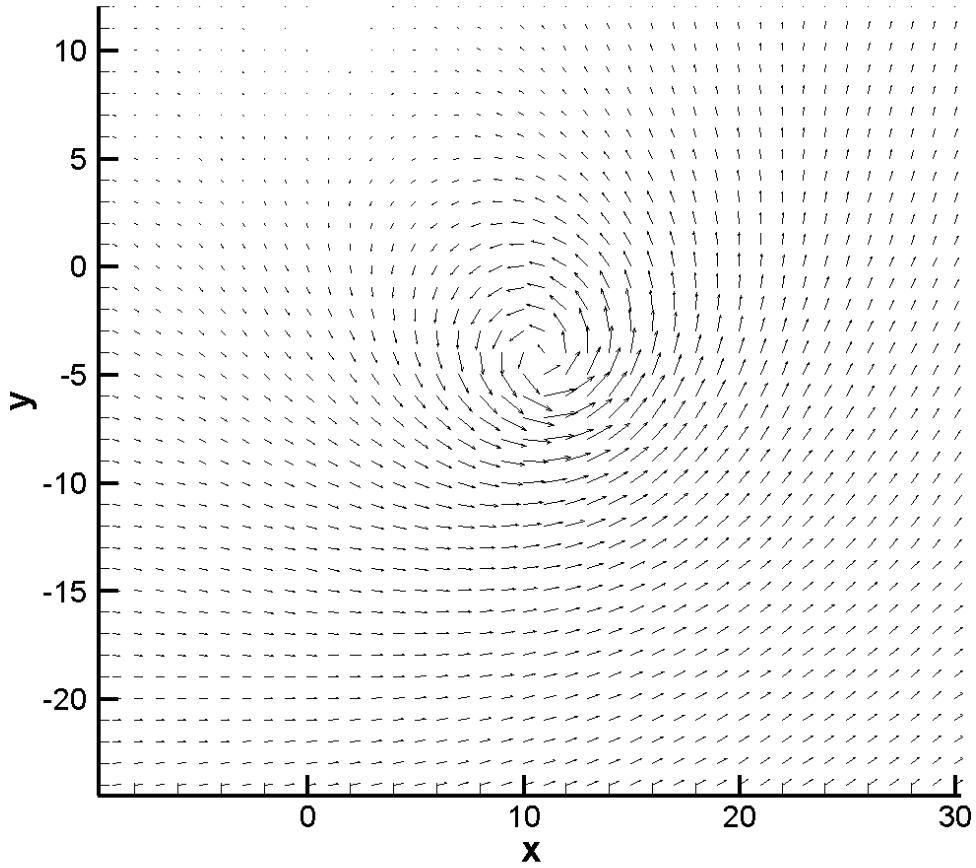

Figure 2-20. Velocity field of a single convecting vortex after 5000 time steps, with old confinement scheme.

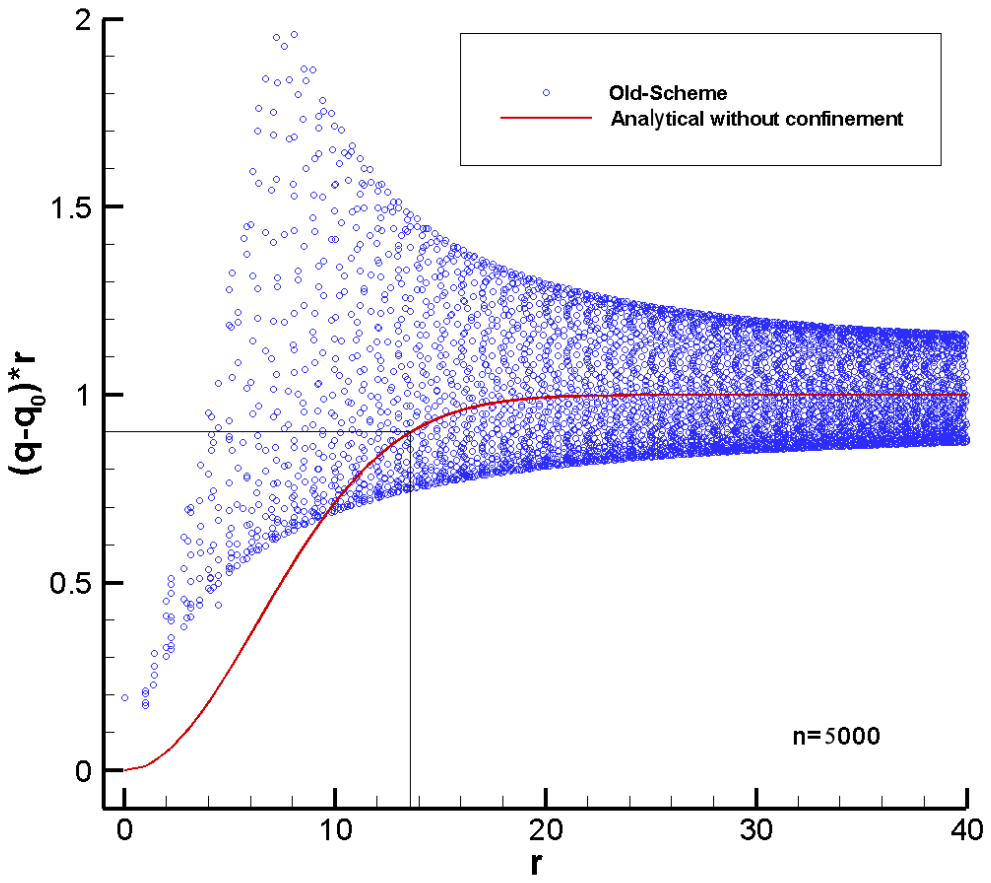

Figure 2-21. Velocity distribution of a single convecting vortex after 5000 time steps, with old confinement scheme.

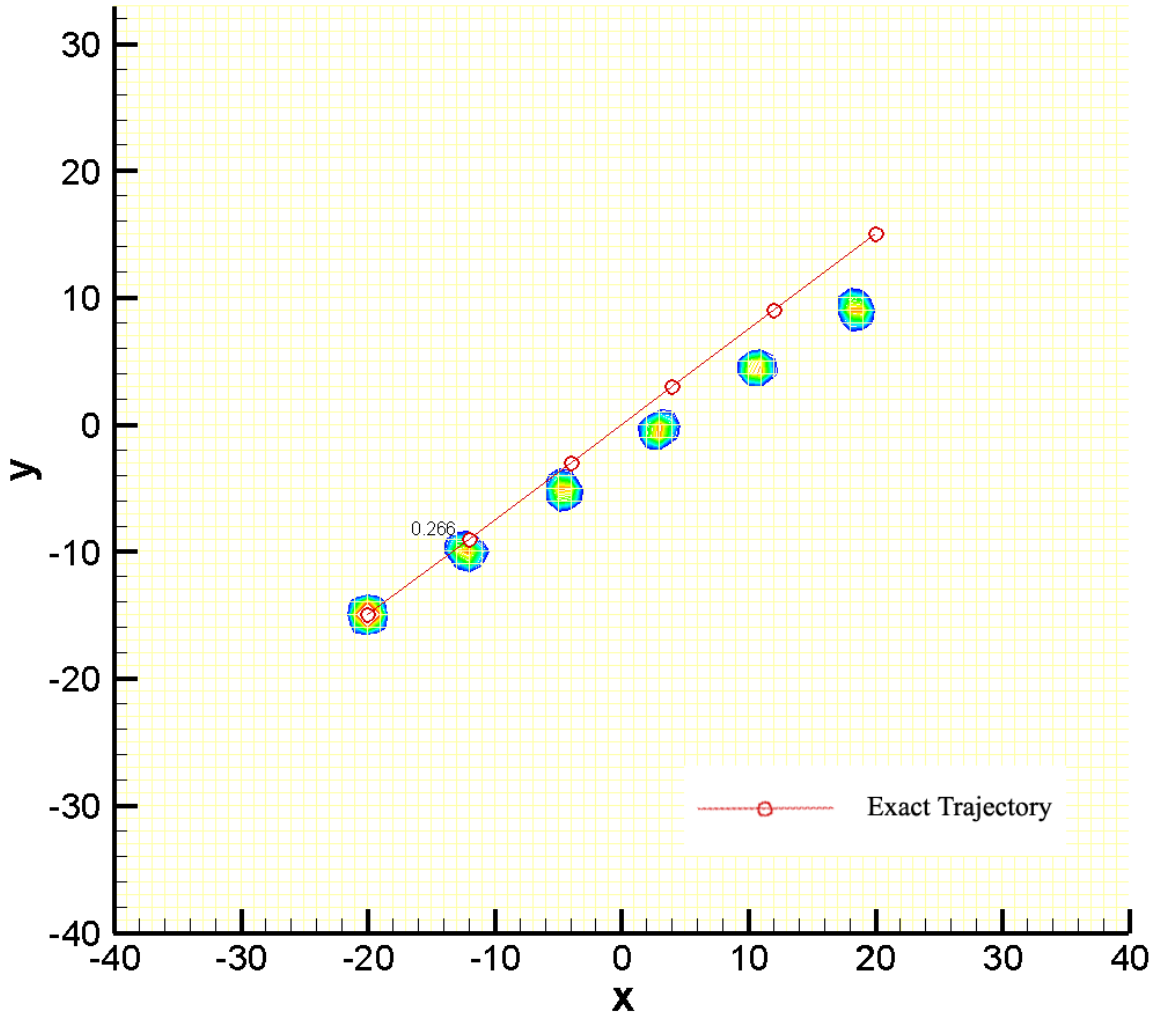

Figure 2-22. Contour plots for a single convecting vortex, with non-conservative vorticity confinement.

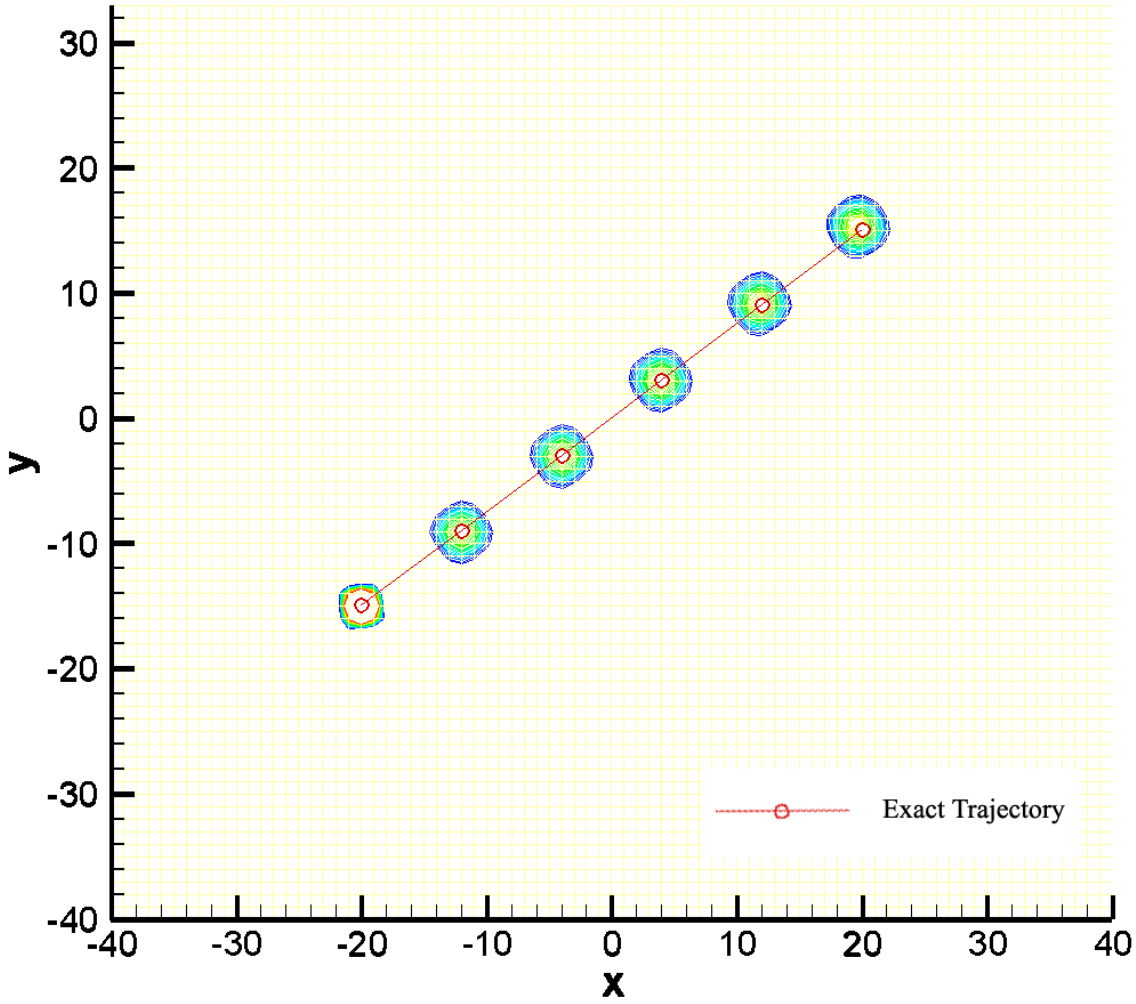

Figure 2-23. Contour plots for a single convecting vortex, with conservative vorticity confinement.

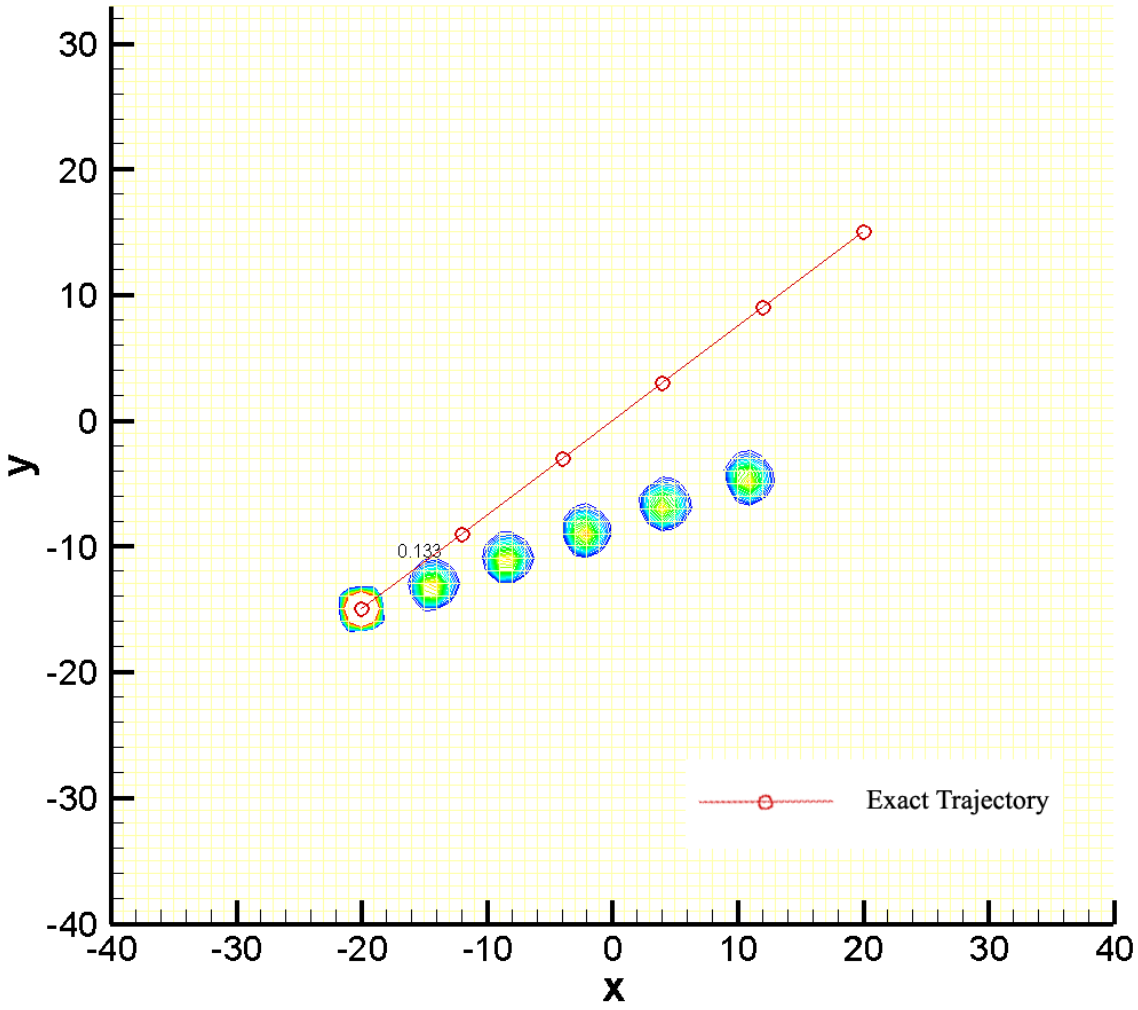

Figure 2-24. Contour plots for a single convecting vortex, with old vorticity confinement scheme.

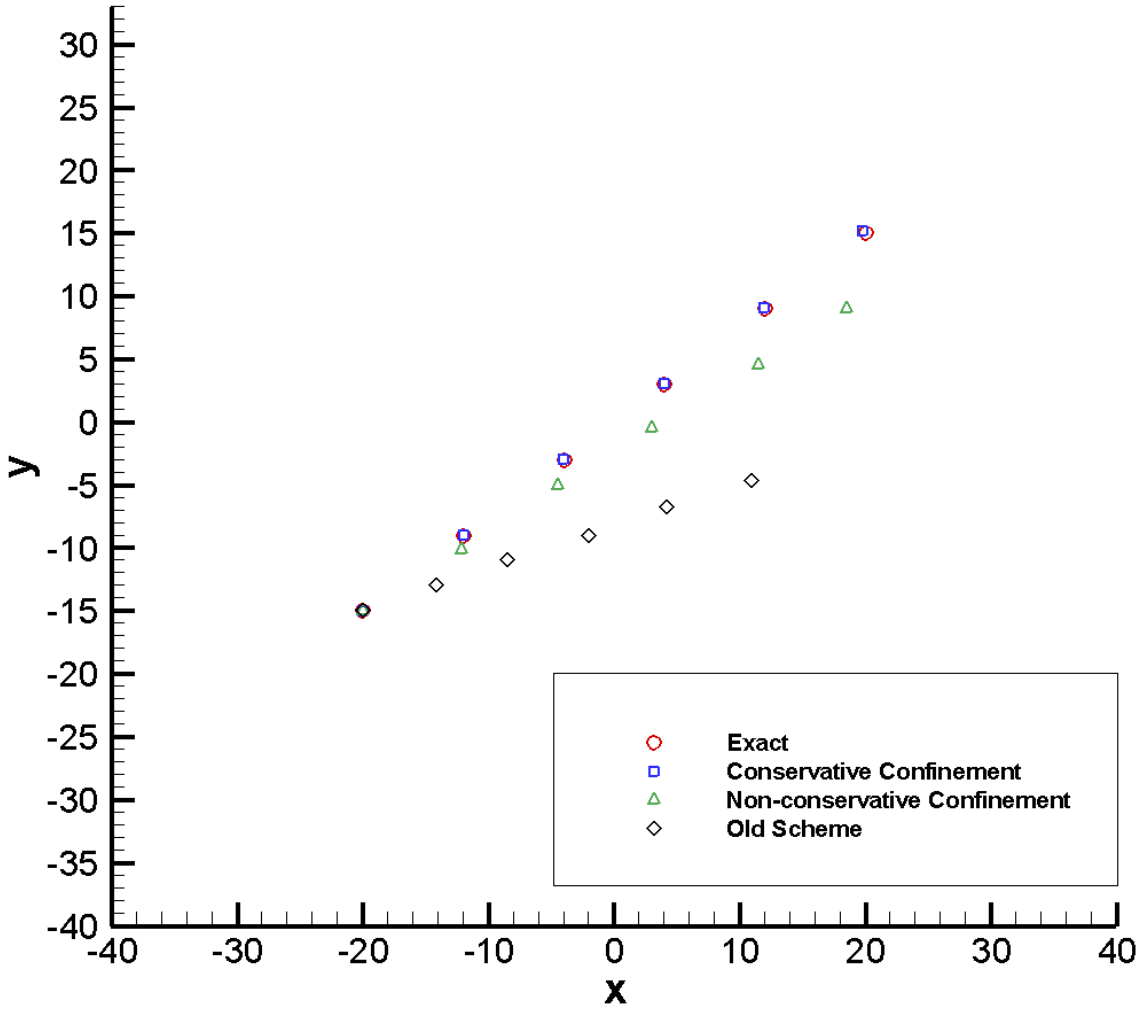

Figure 2-25. The trajectories of a single convecting vortex computed by various methods.

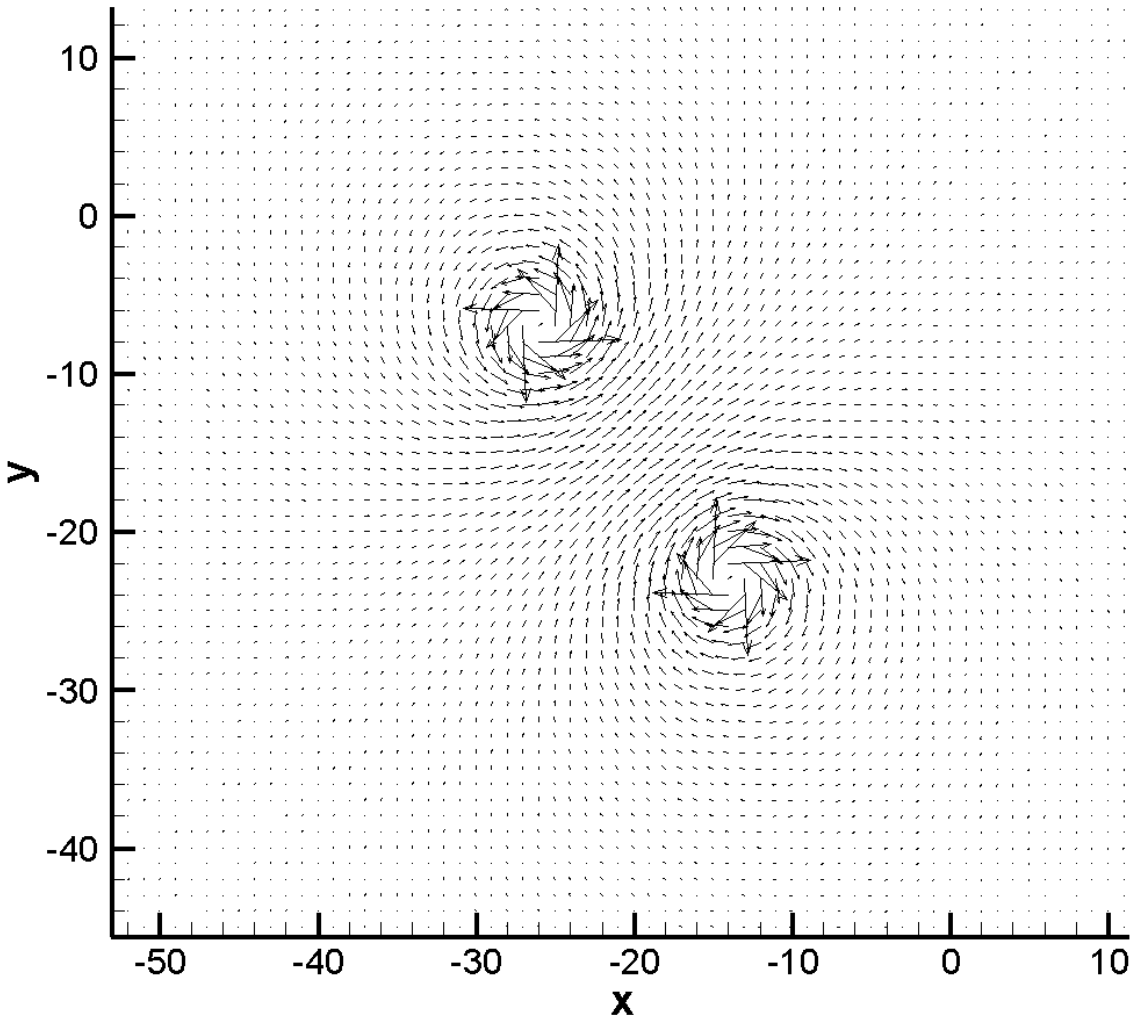

Figure 2-26. Initial velocity field induced by a vortex pair with opposite rotation.

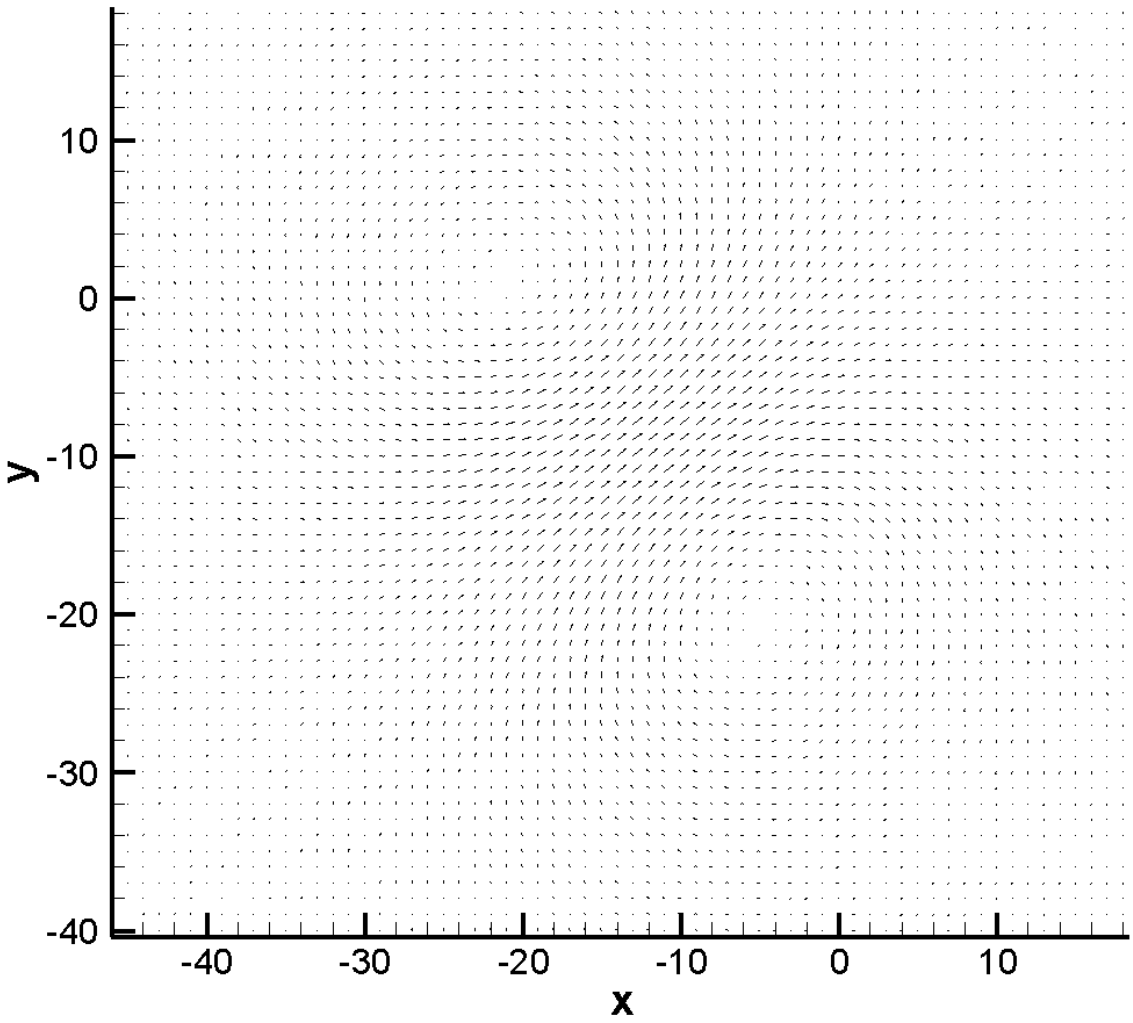

Figure 2-27. Velocity field of a vortex pair after 1000 time steps, without vorticity confinement.

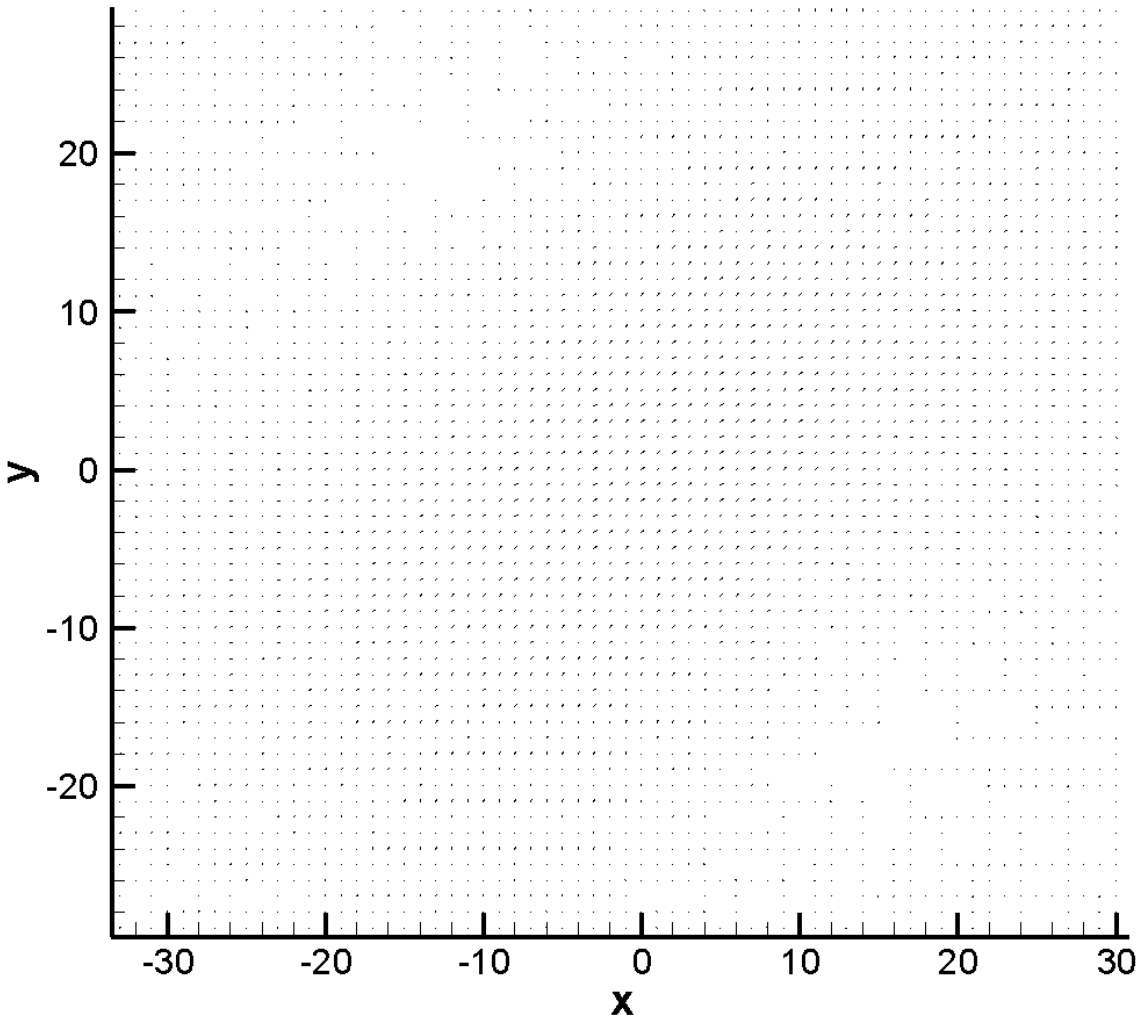

Figure 2-28. Velocity field of a vortex pair after 5000 time steps, without vorticity confinement.

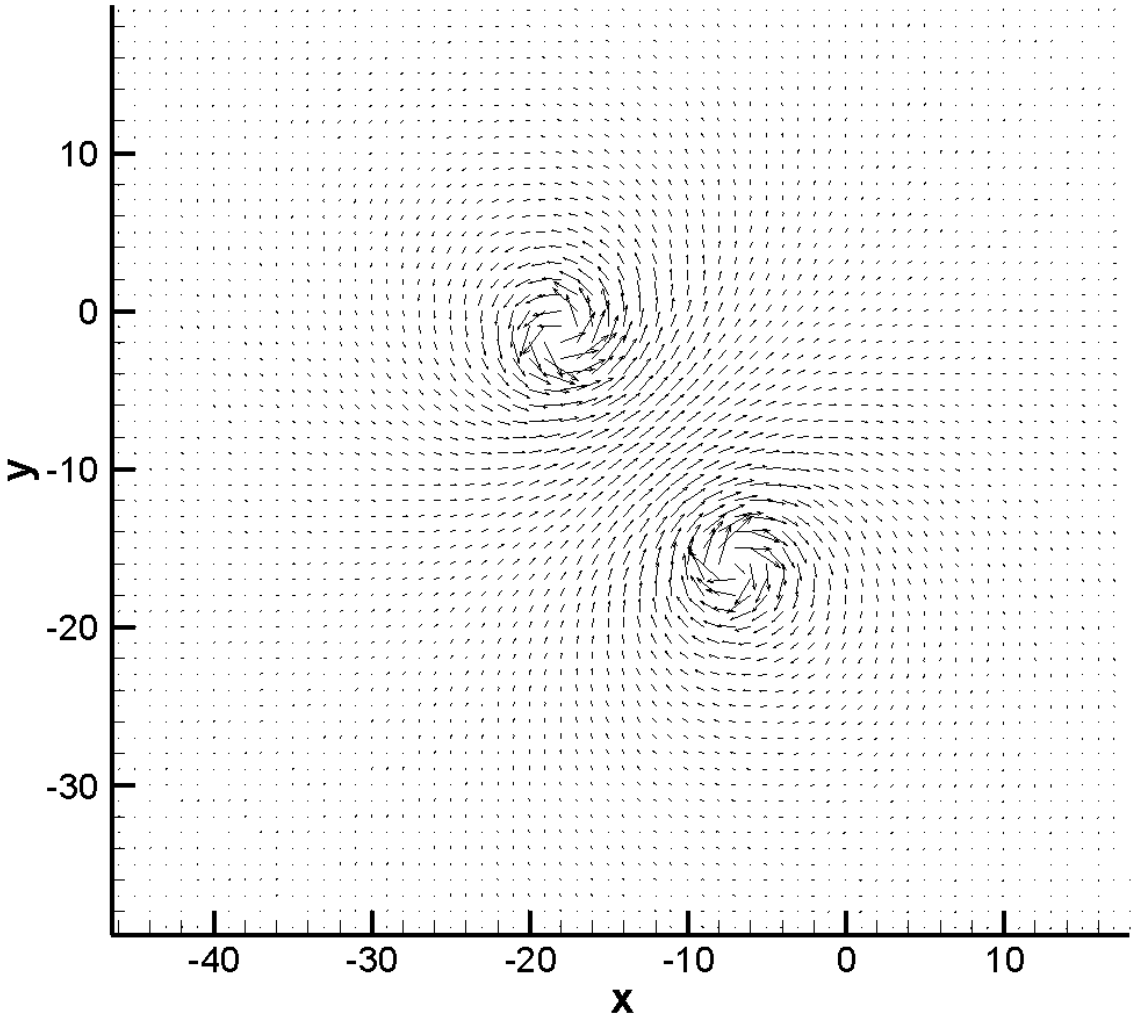

Figure 2-29. Velocity field of a vortex pair after 1000 time steps, with non-conservative vorticity confinement.

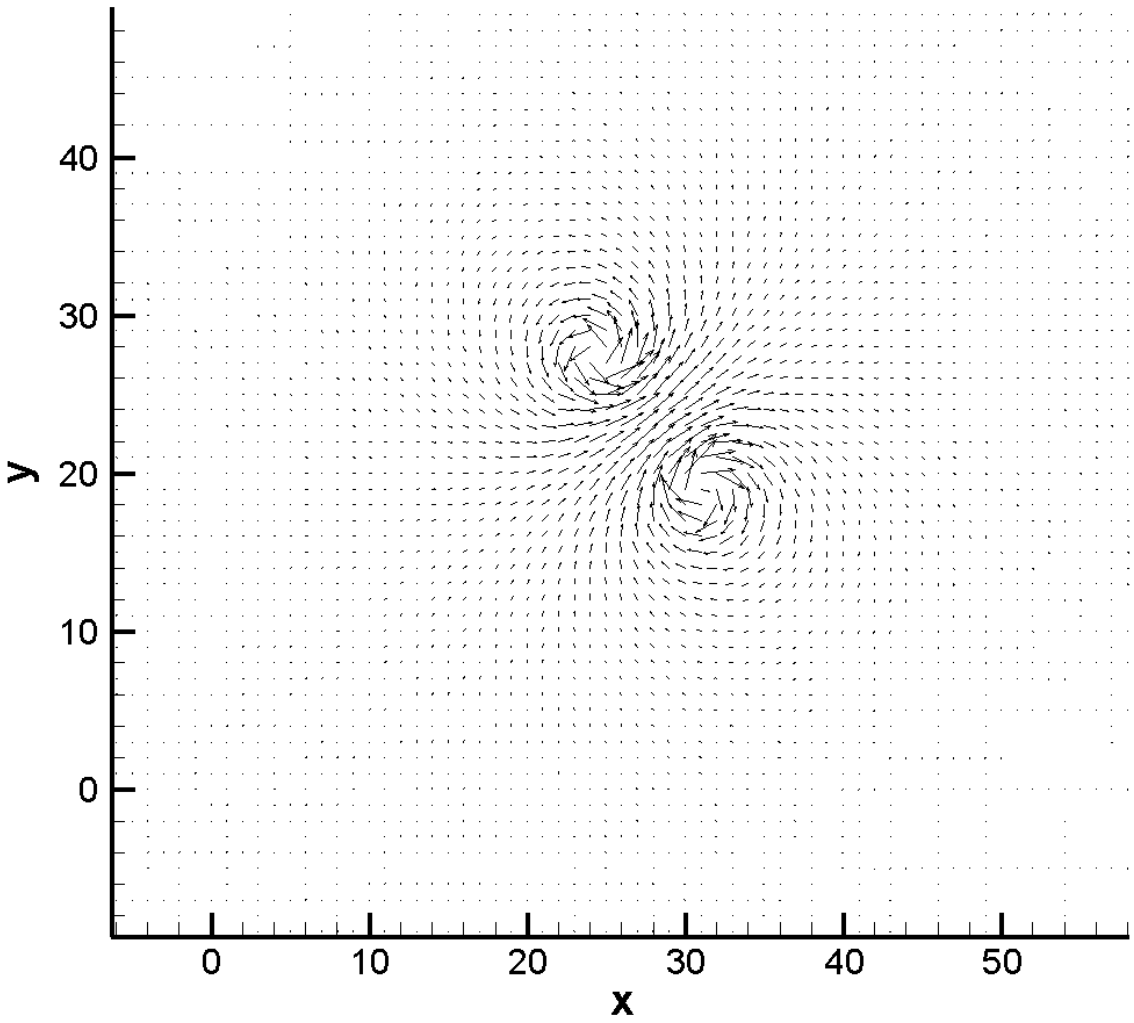

Figure 2-30. Velocity field of a vortex pair after 5000 time steps, with non-conservative vorticity confinement.

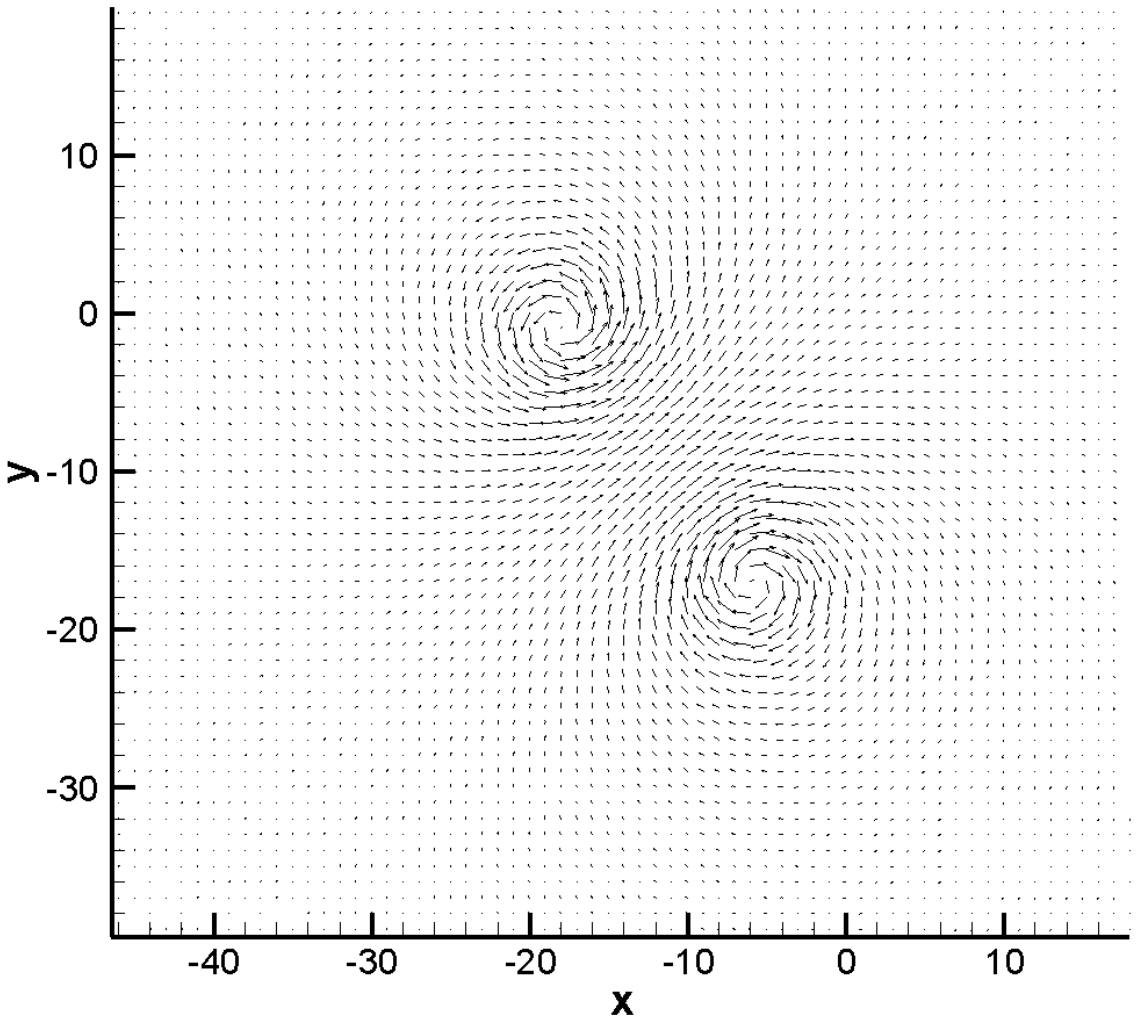

Figure 2-31. Velocity field of a vortex pair after 1000 time steps, with conservative vorticity confinement.

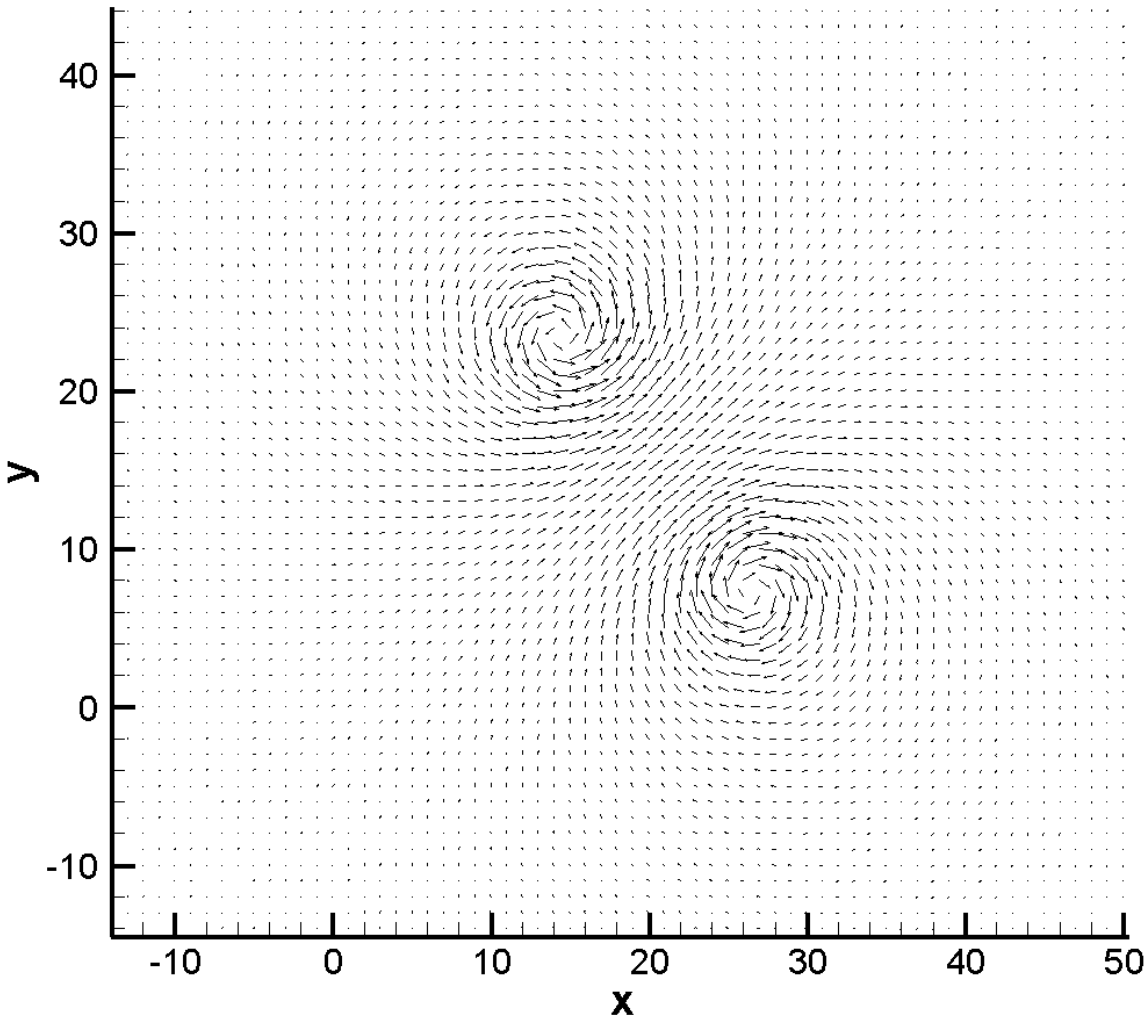

Figure 2-32. Velocity field of a vortex pair after 5000 time steps, with conservative vorticity confinement.

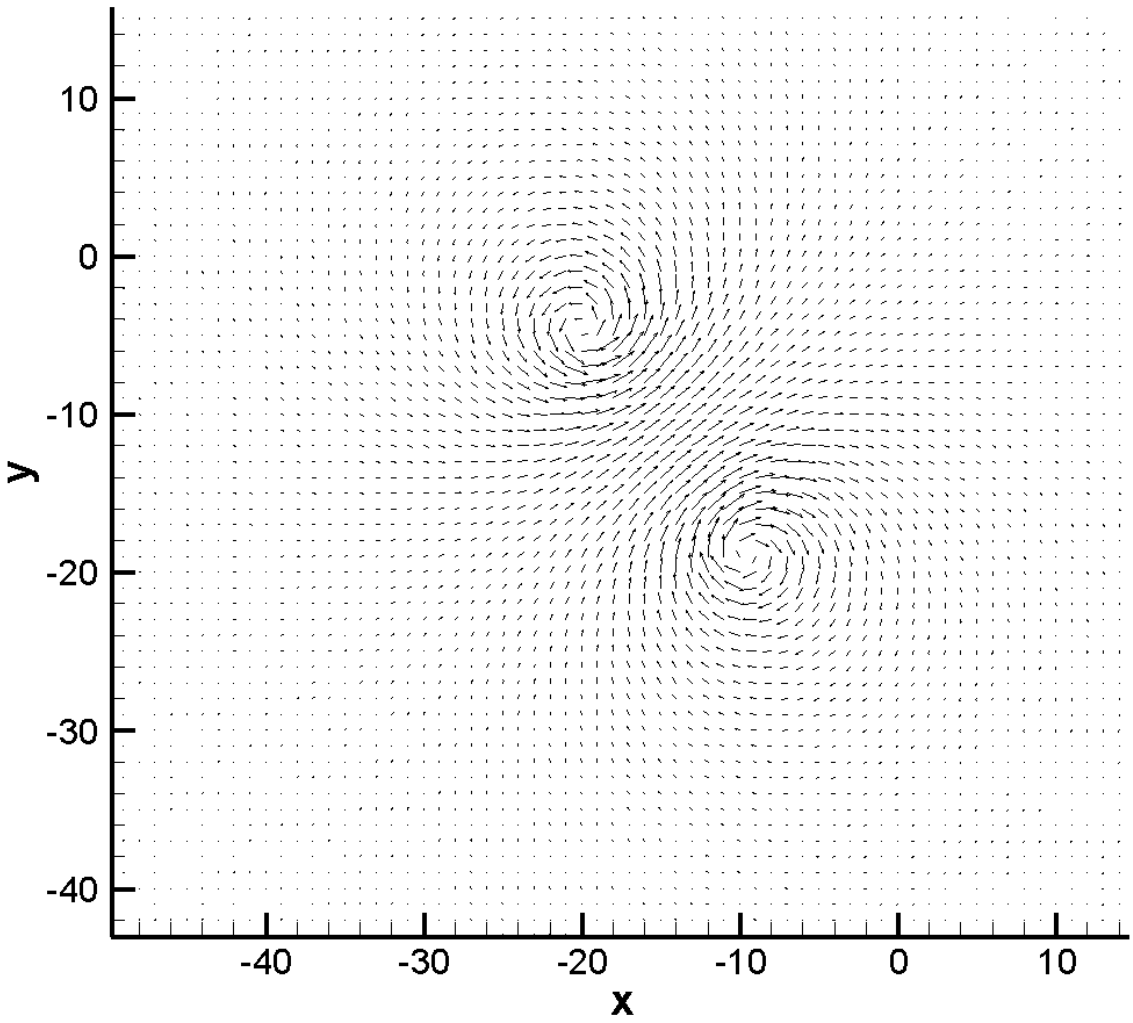

Figure 2-33. Velocity field of a vortex pair after 1000 time steps, with old confinement scheme.

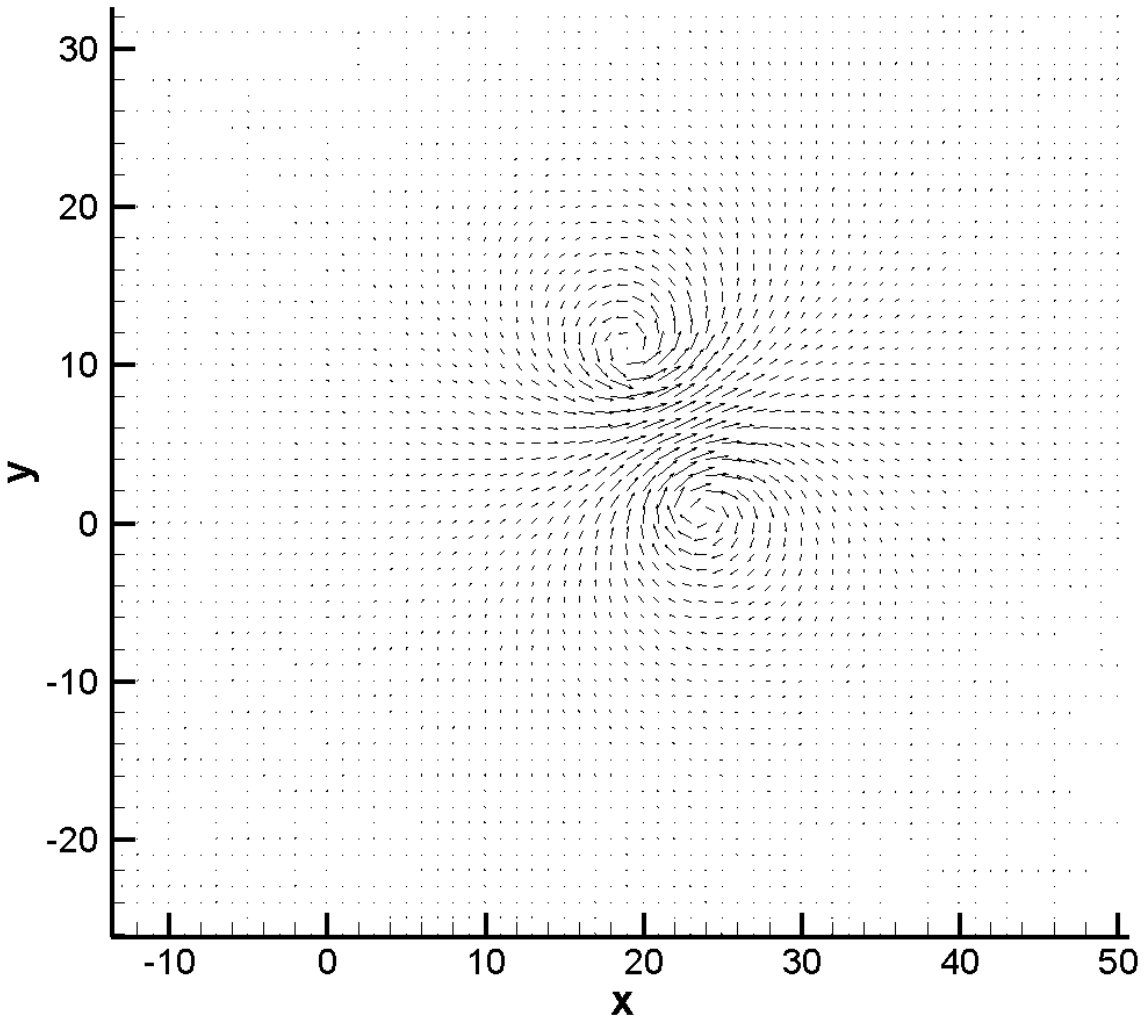

Figure 2-34. Velocity field of a vortex pair after 5000 time steps, with old confinement scheme.

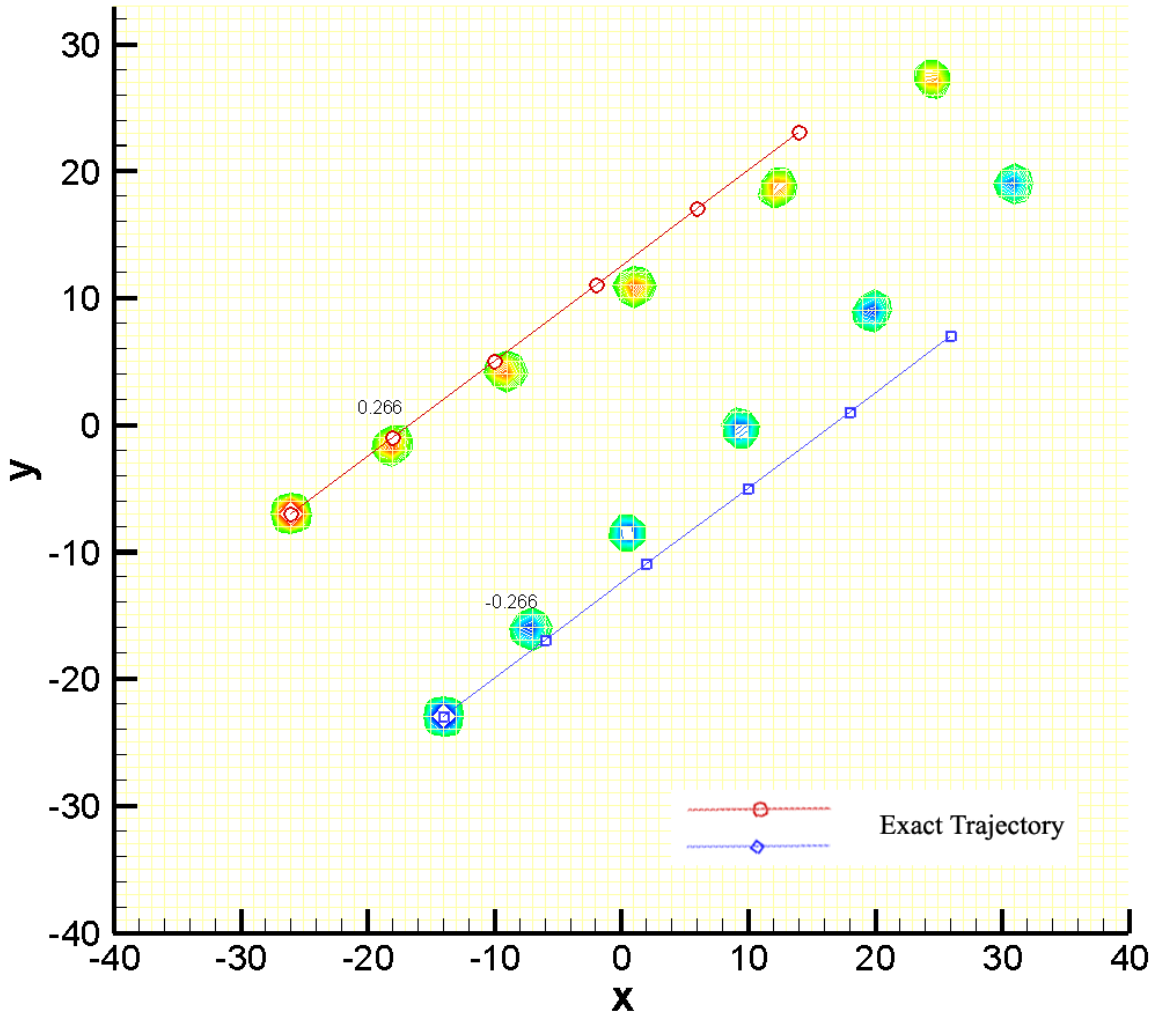

Figure 2-35. Contour plots for a vortex pair, with non-conservative vorticity confinement.

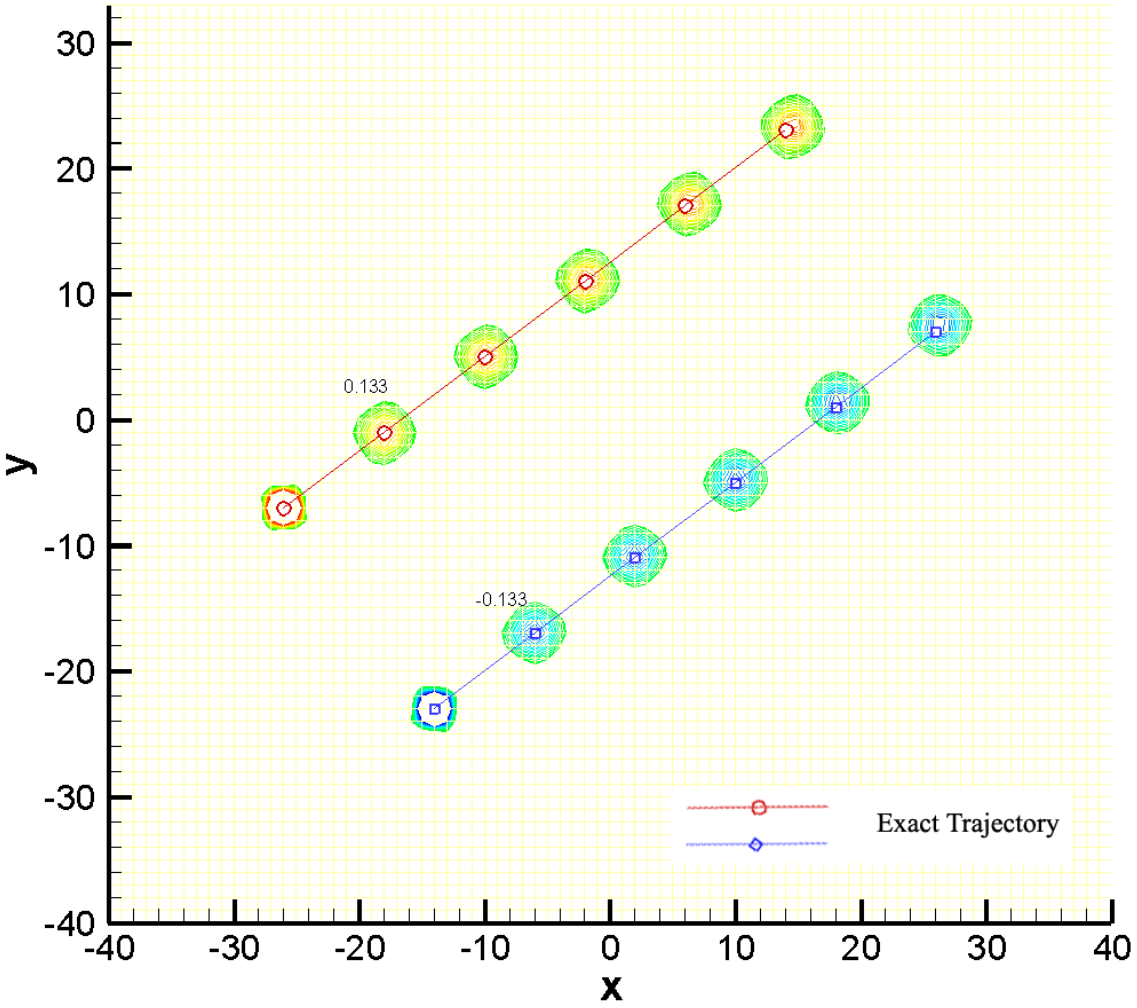

Figure 2-36. Contour plots for a vortex pair, with conservative vorticity confinement.

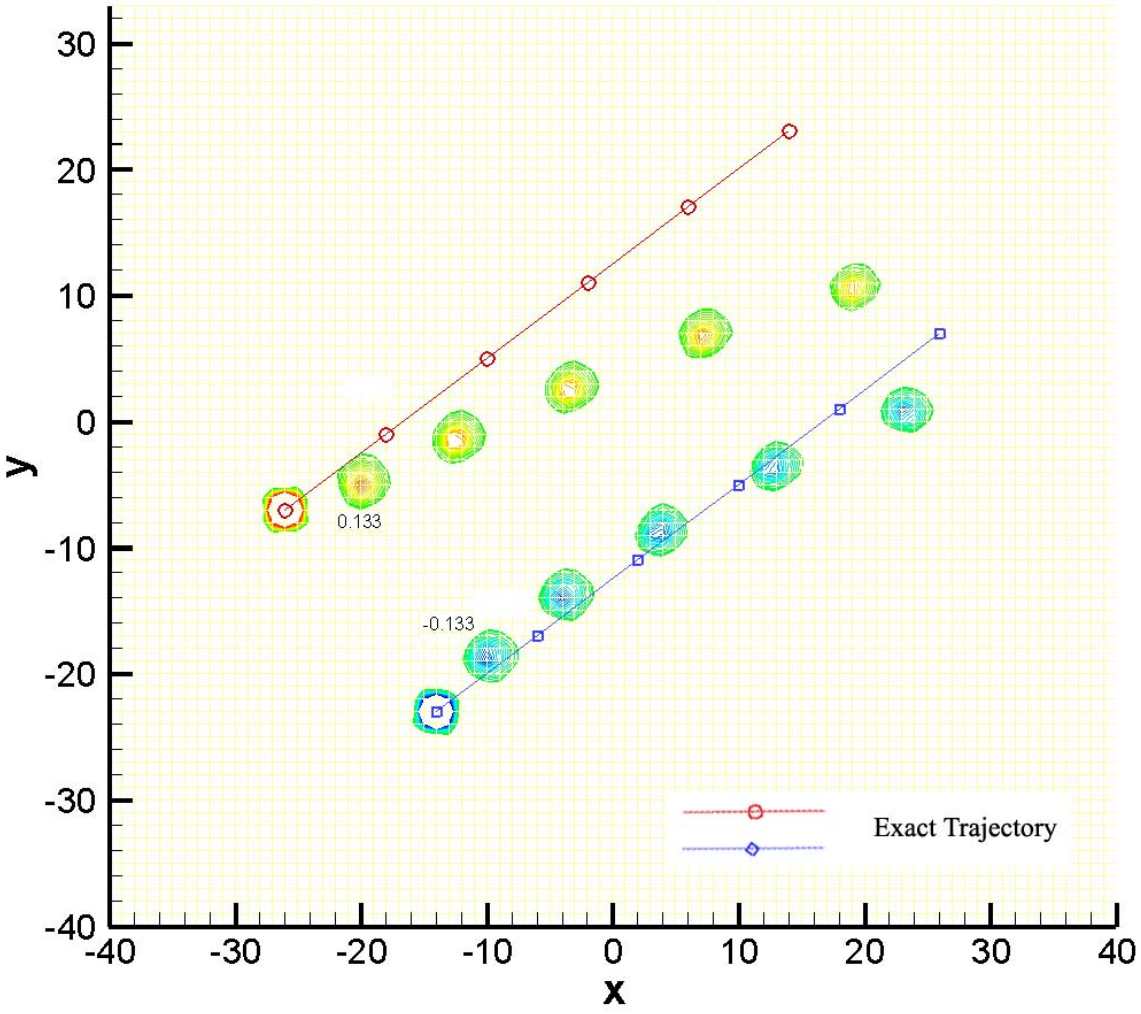

Figure 2-37. Contour plots for a vortex pair, with old vorticity confinement scheme.

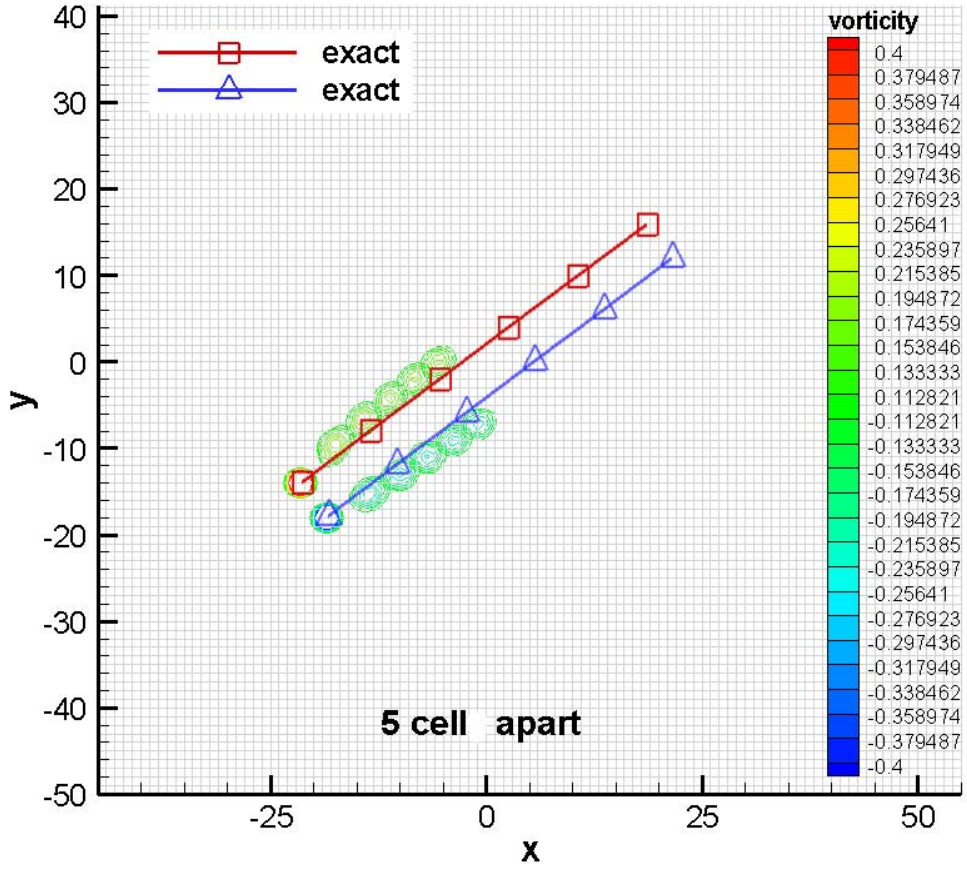

Figure 2-38. Contour plots for a vortex pair, 5 cell apart.

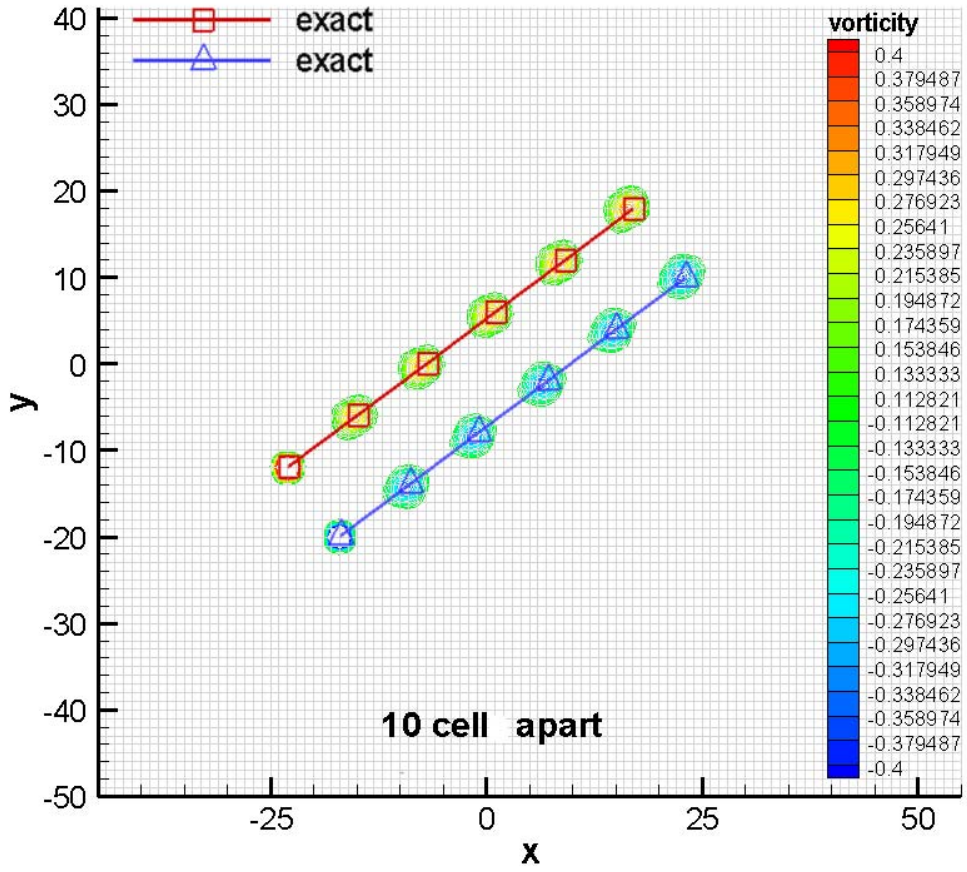

Figure 2-39. Contour plots for a vortex pair, 10 cell apart.

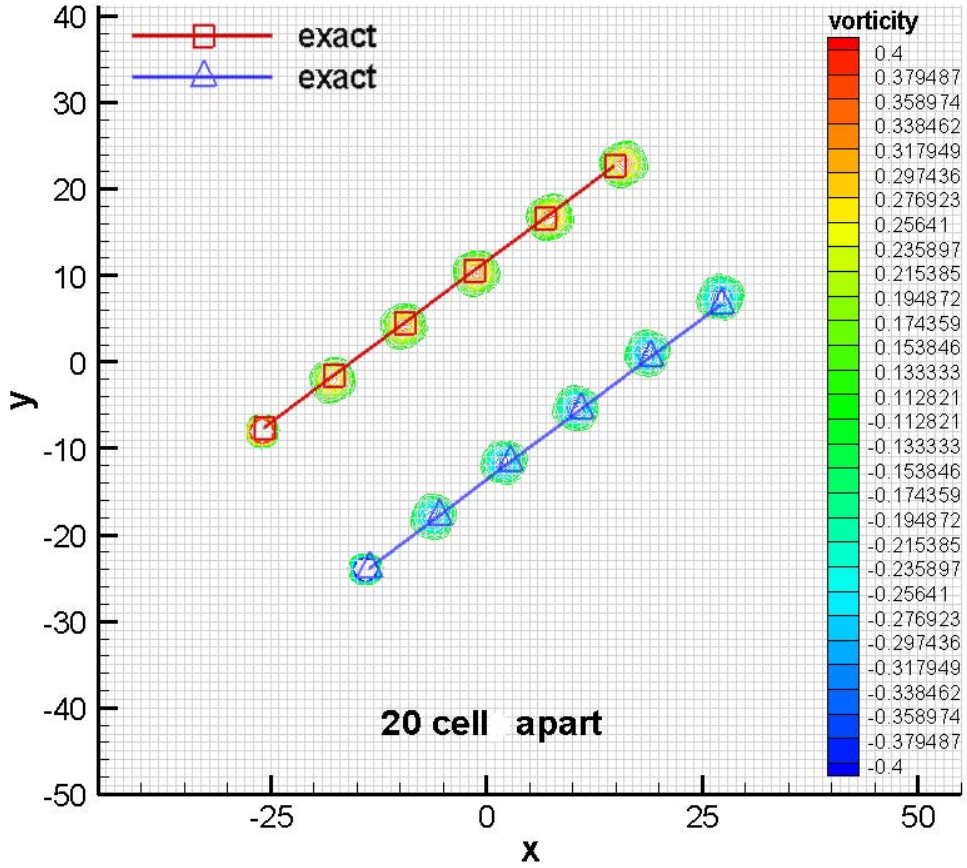

Figure 2-40. Contour plots for a vortex pair, 20 cell apart.

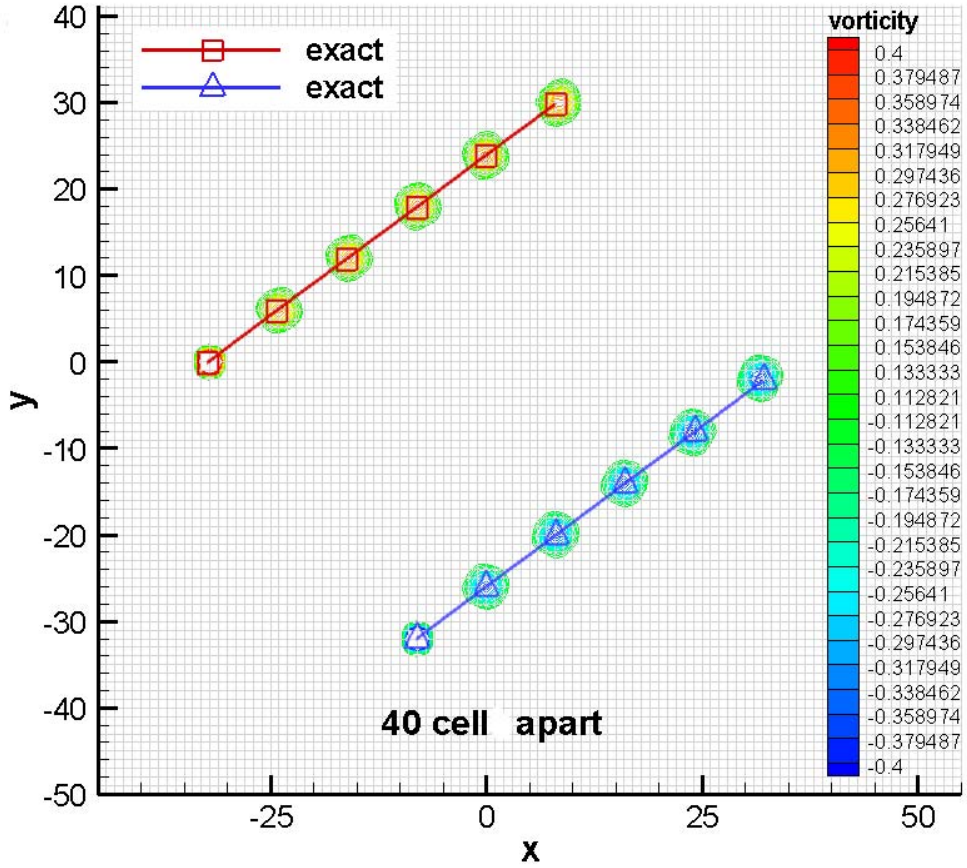

Figure 2-41. Contour plots for a vortex pair, 40 cell apart.

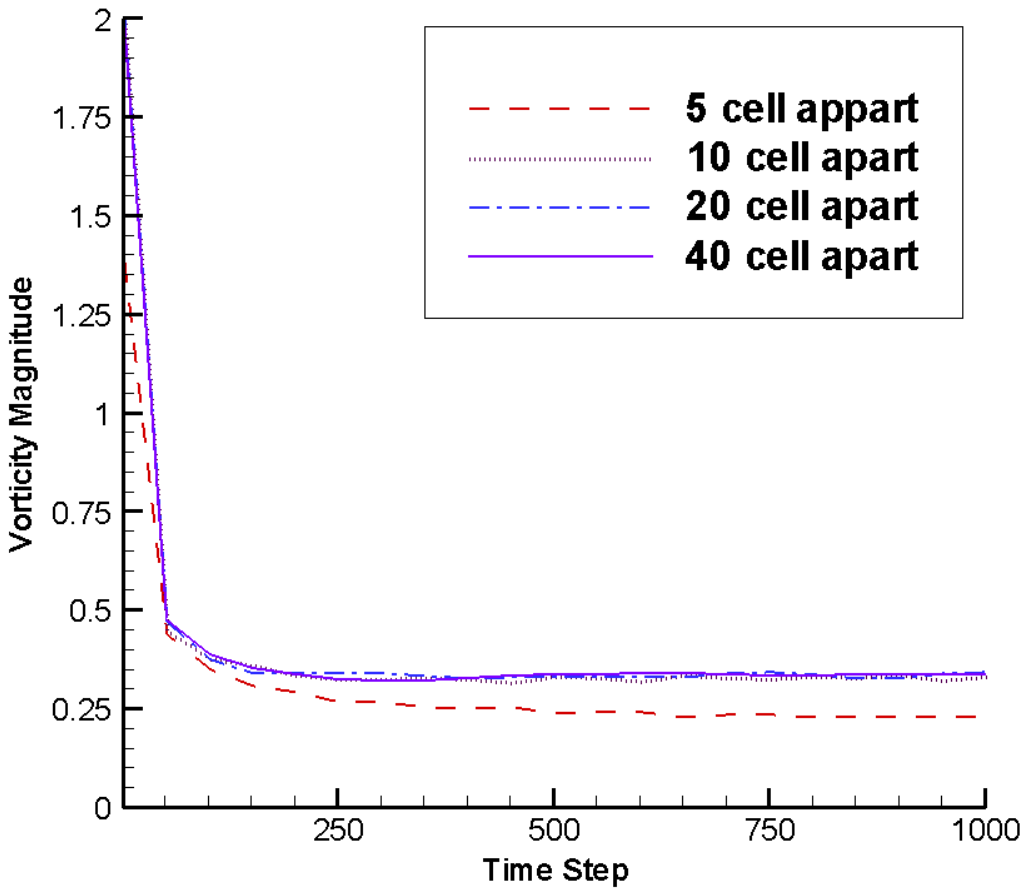

Figure 2-42. Convergence history of a vortex pair.

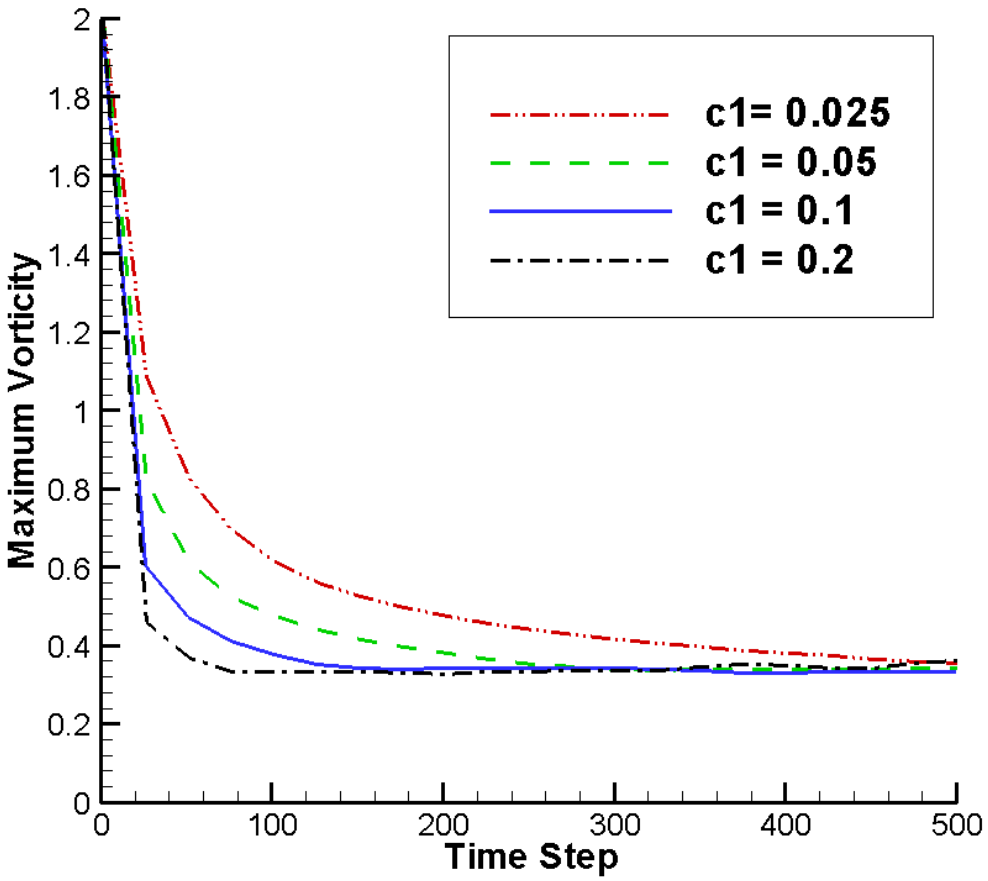

Figure 2-43. Evolution of the maximum velocity and vorticity, different c1.

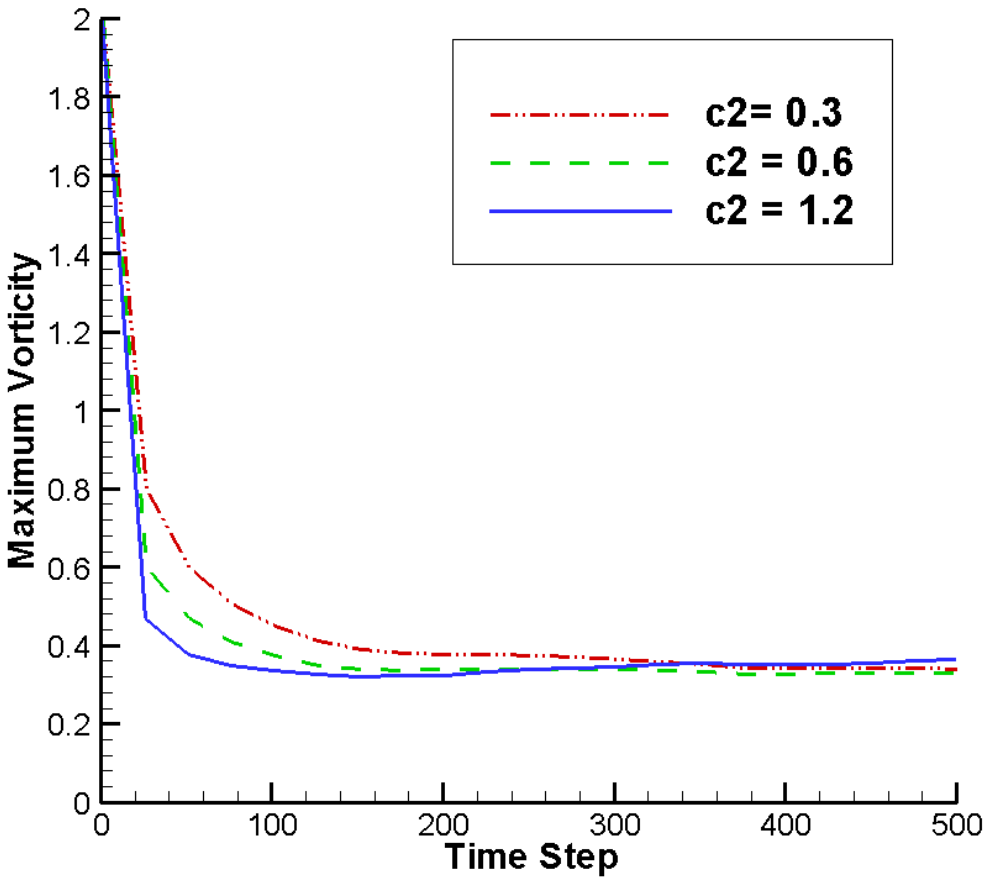

Figure 2-44. Evolution of the maximum velocity and vorticity, different c2.

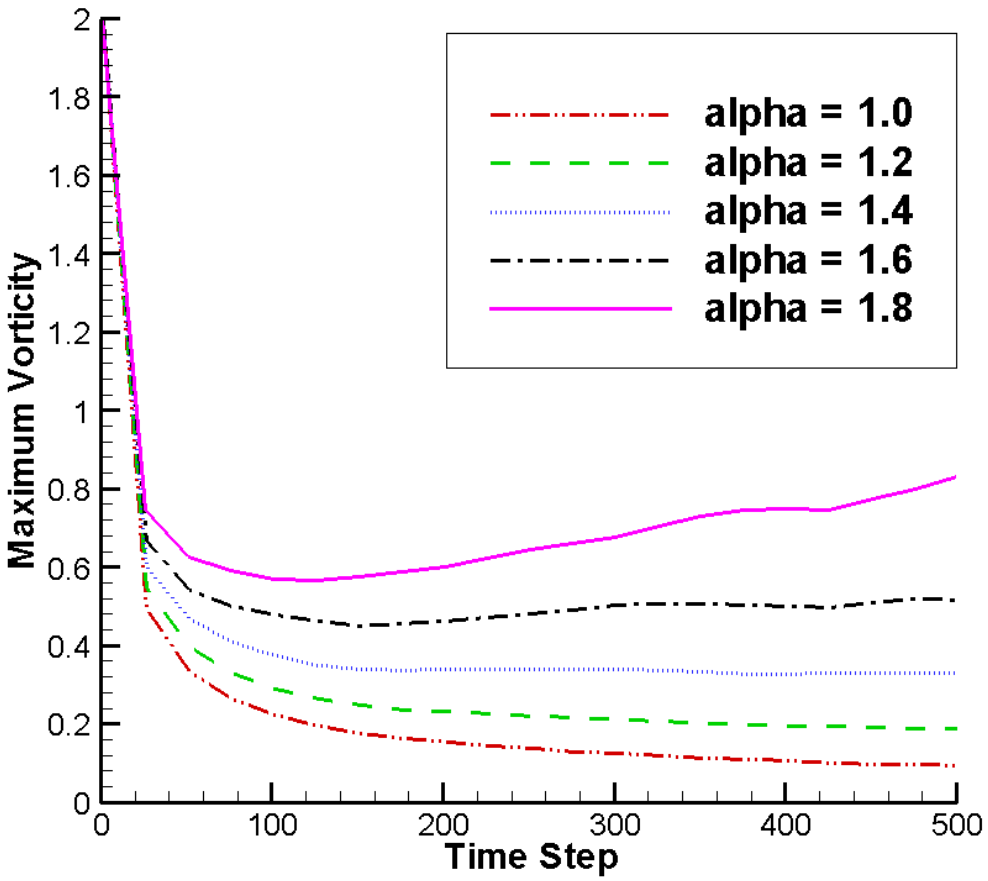

Figure 2-45. Evolution of the maximum velocity and vorticity, different α.

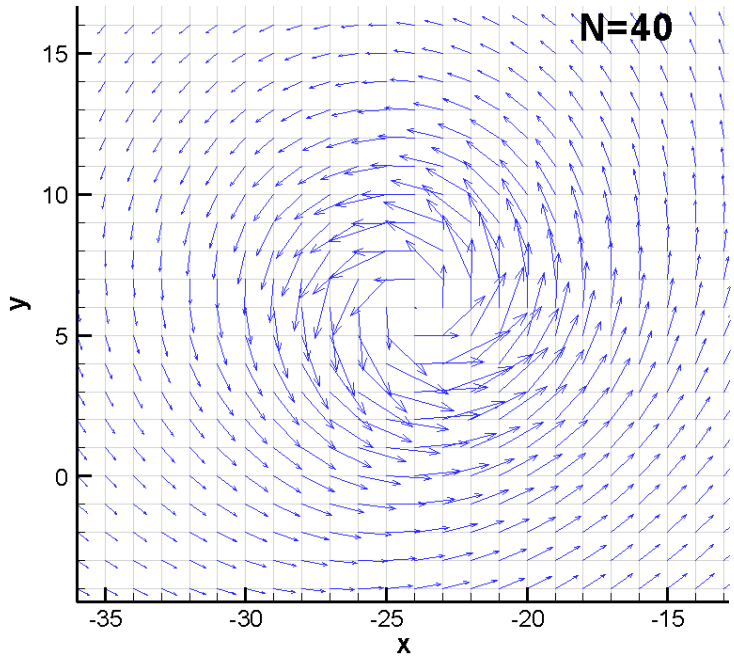

(a) n = 40

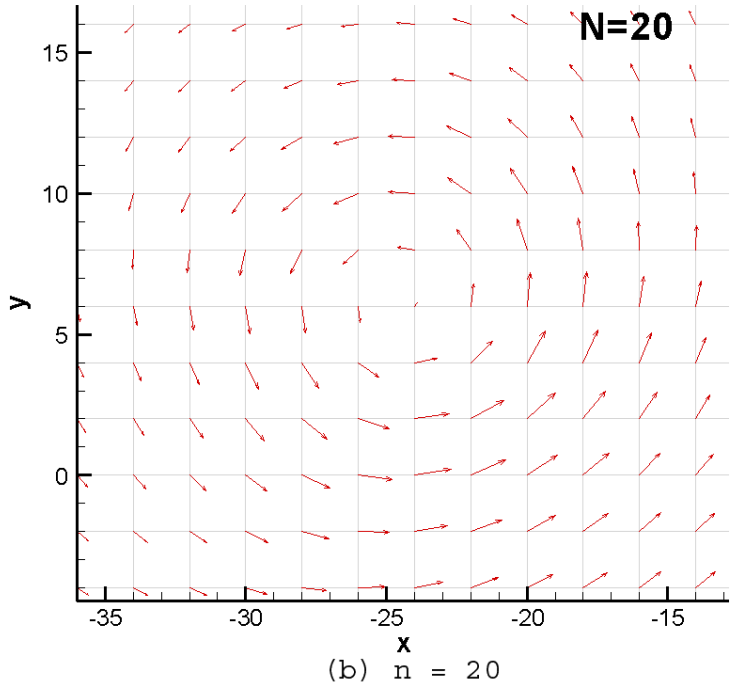

(b) n = 20

Figure 2-46. Equivalent physical vector field, comparison between N = 20 and N = 40.

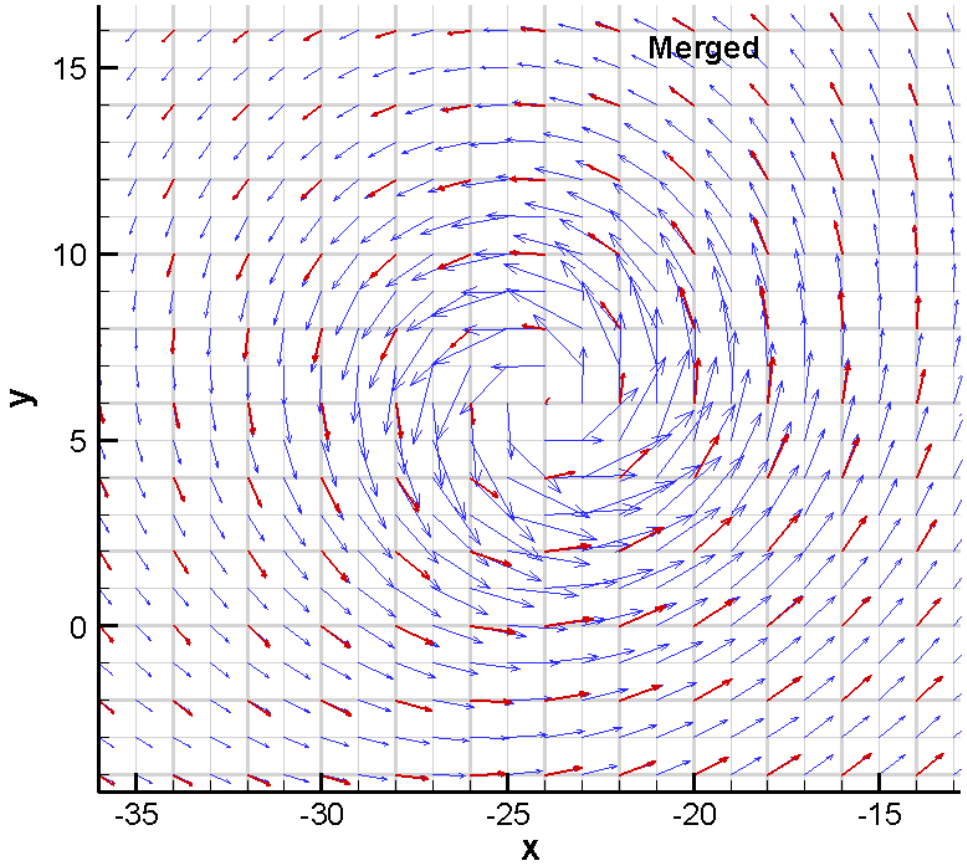

Figure 2-47. Scaled vector field merged, comparison between N = 20 and N = 40.

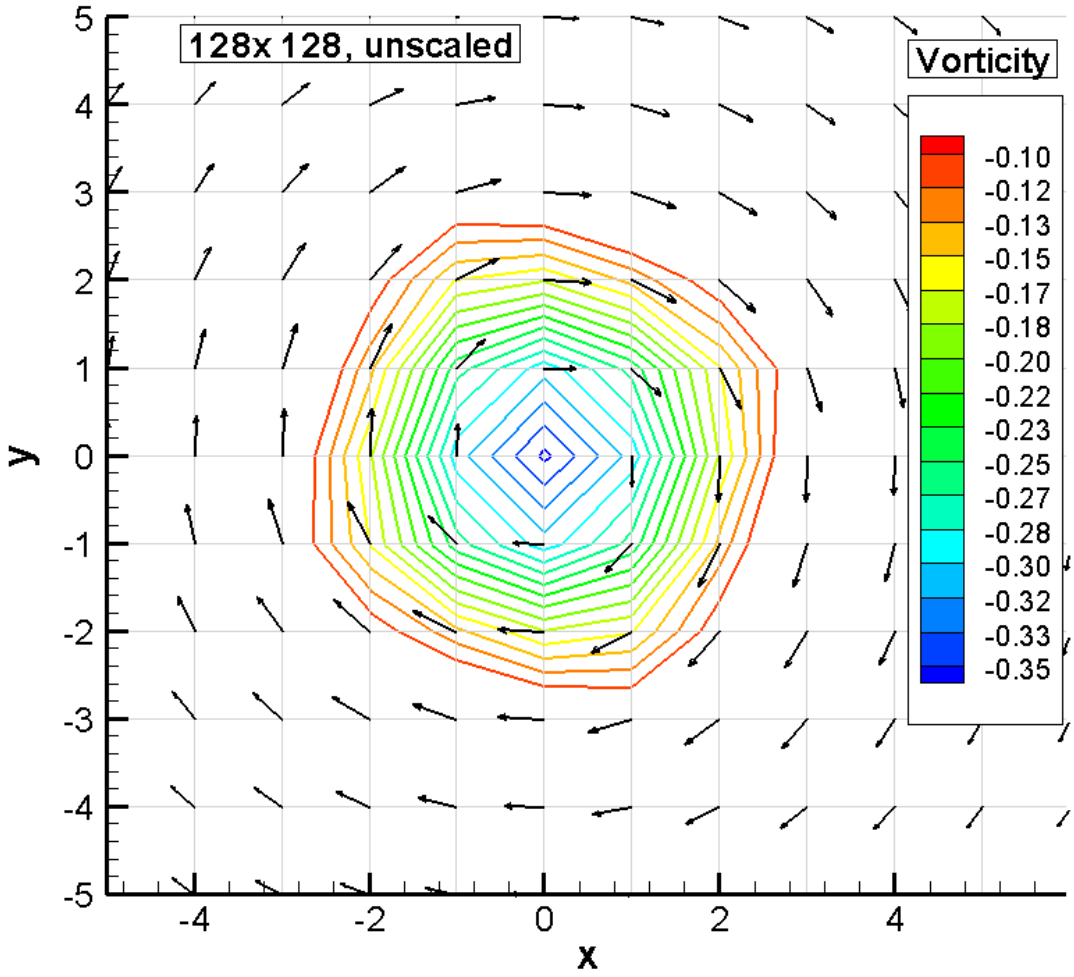

Figure 2-48. Flow field of a stationary single vortex, with grid dimension 128 x 128.

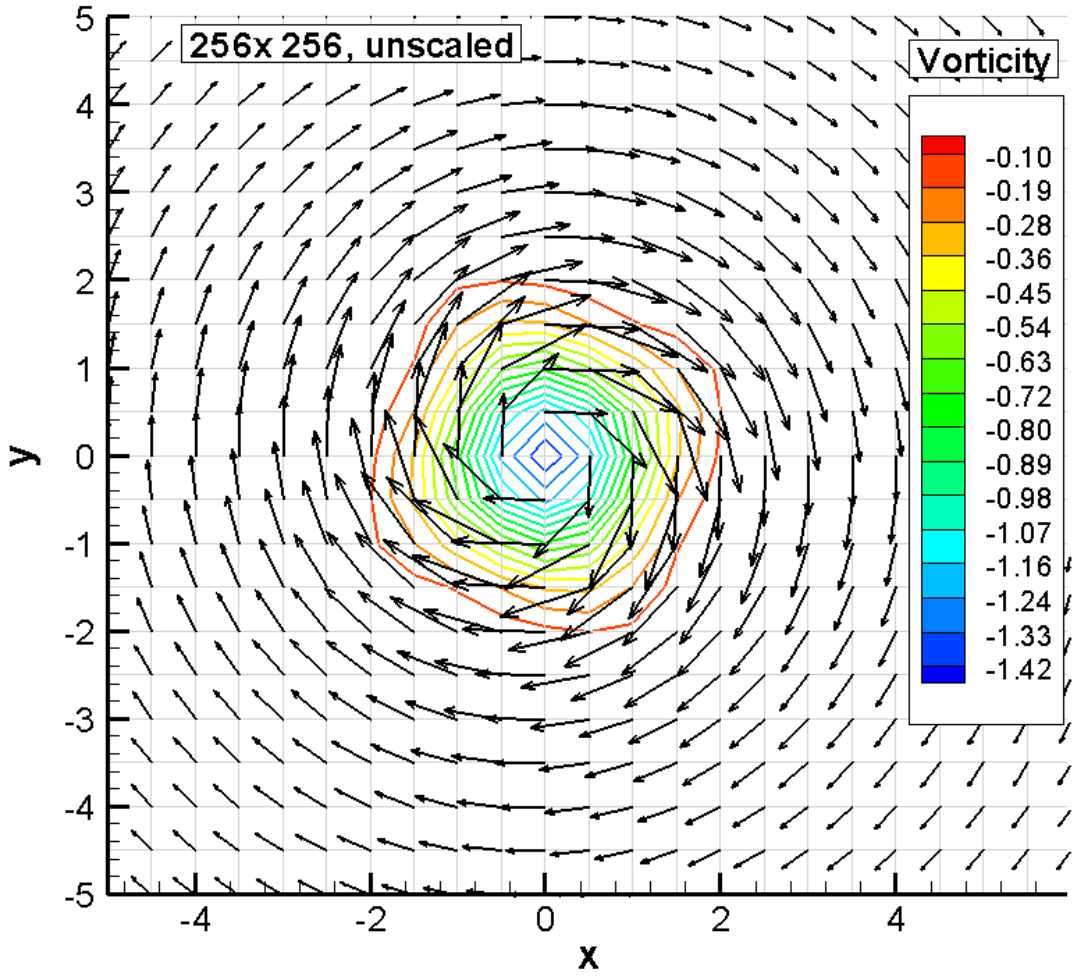

Figure 2-49. Flow field of a stationary single vortex, with grid dimension 256 x 256.

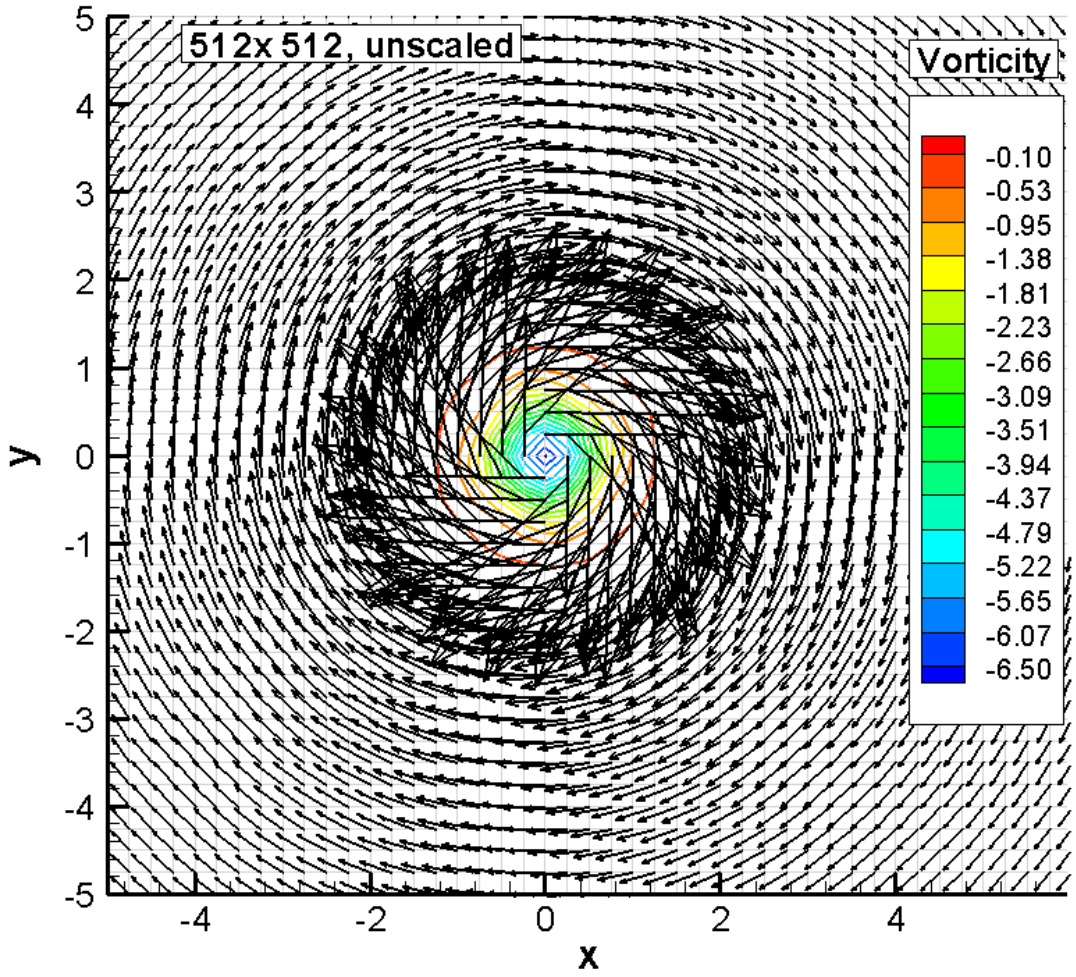

Figure 2-50. Flow field of a stationary single vortex, with grid dimension 512 x 512.

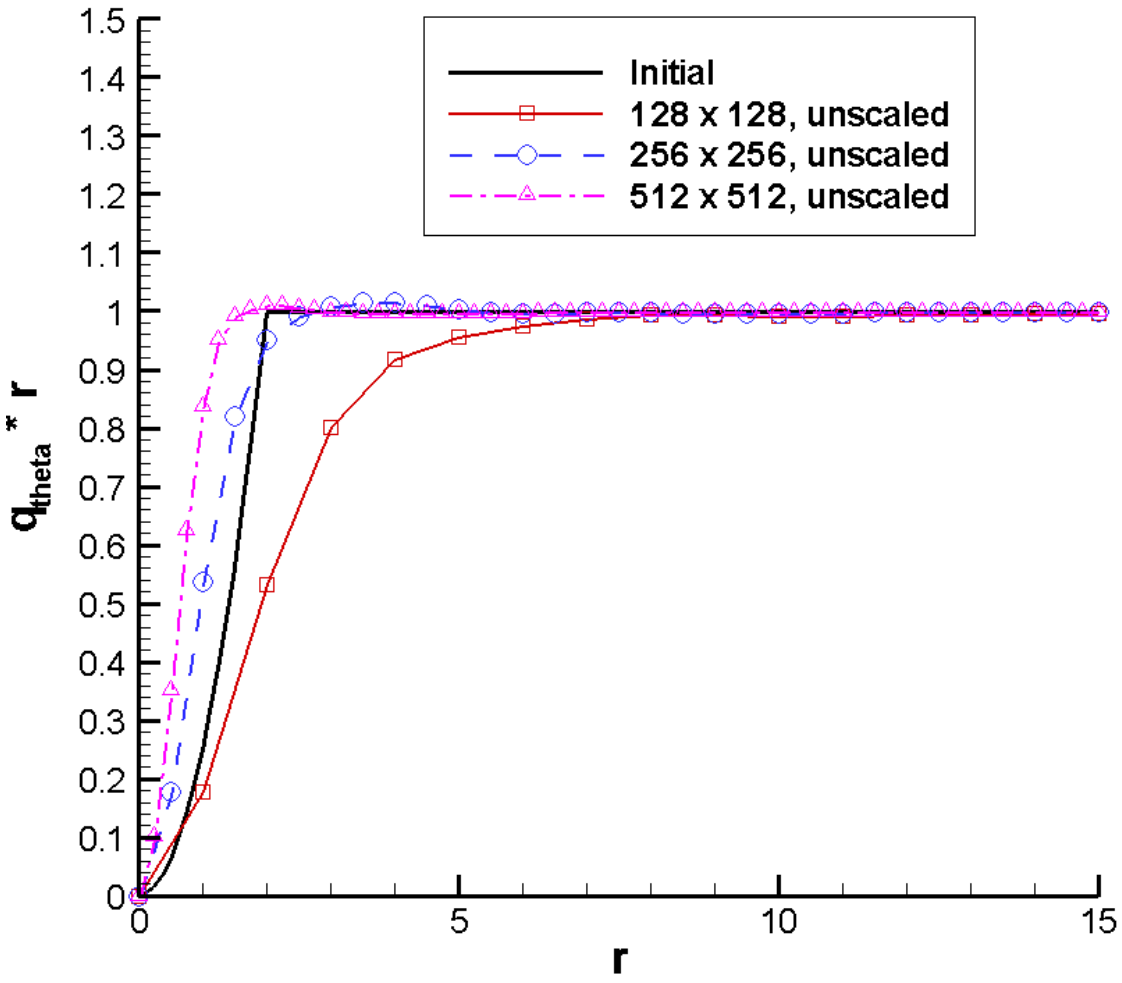

Figure 2-51. Velocity distribution of a stationary single vortex.

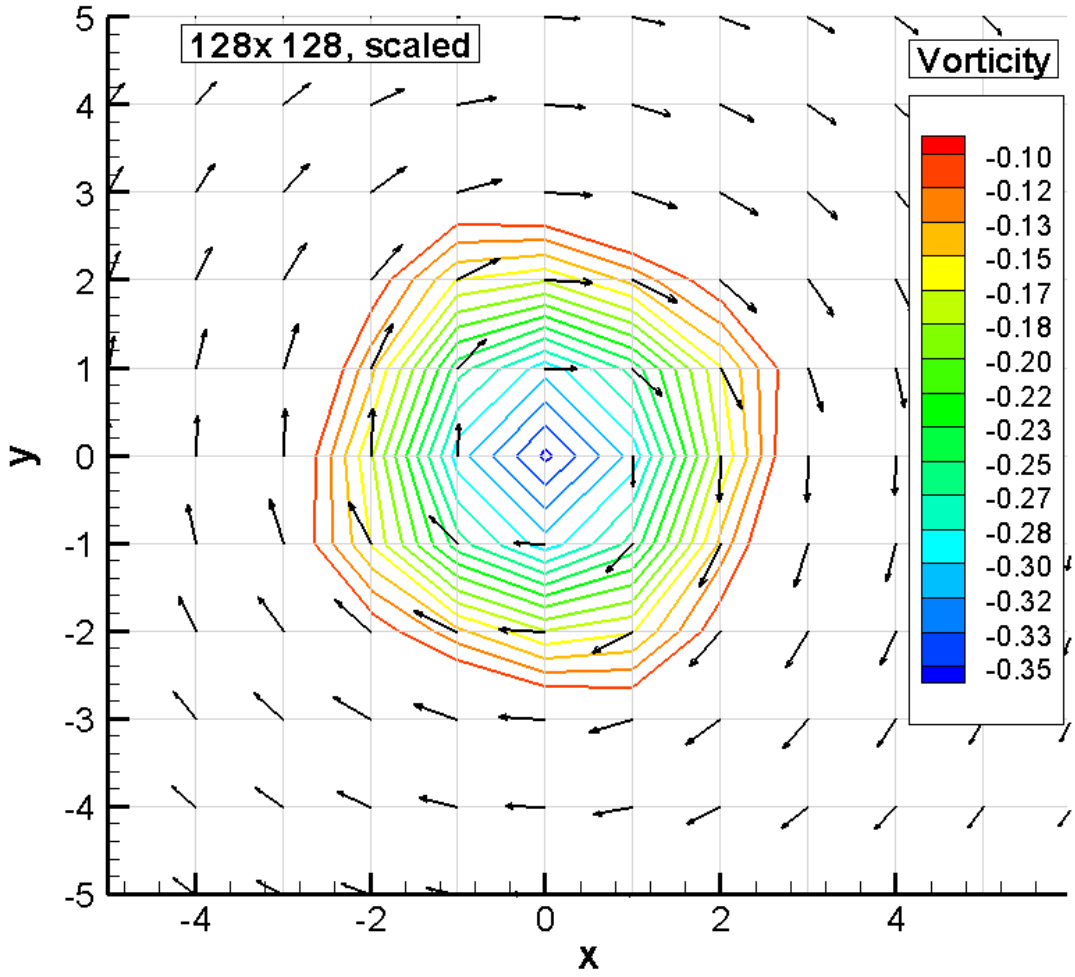

Figure 2-52. Flow field of a single vortex after scaling, with grid dimension 128 x 128.

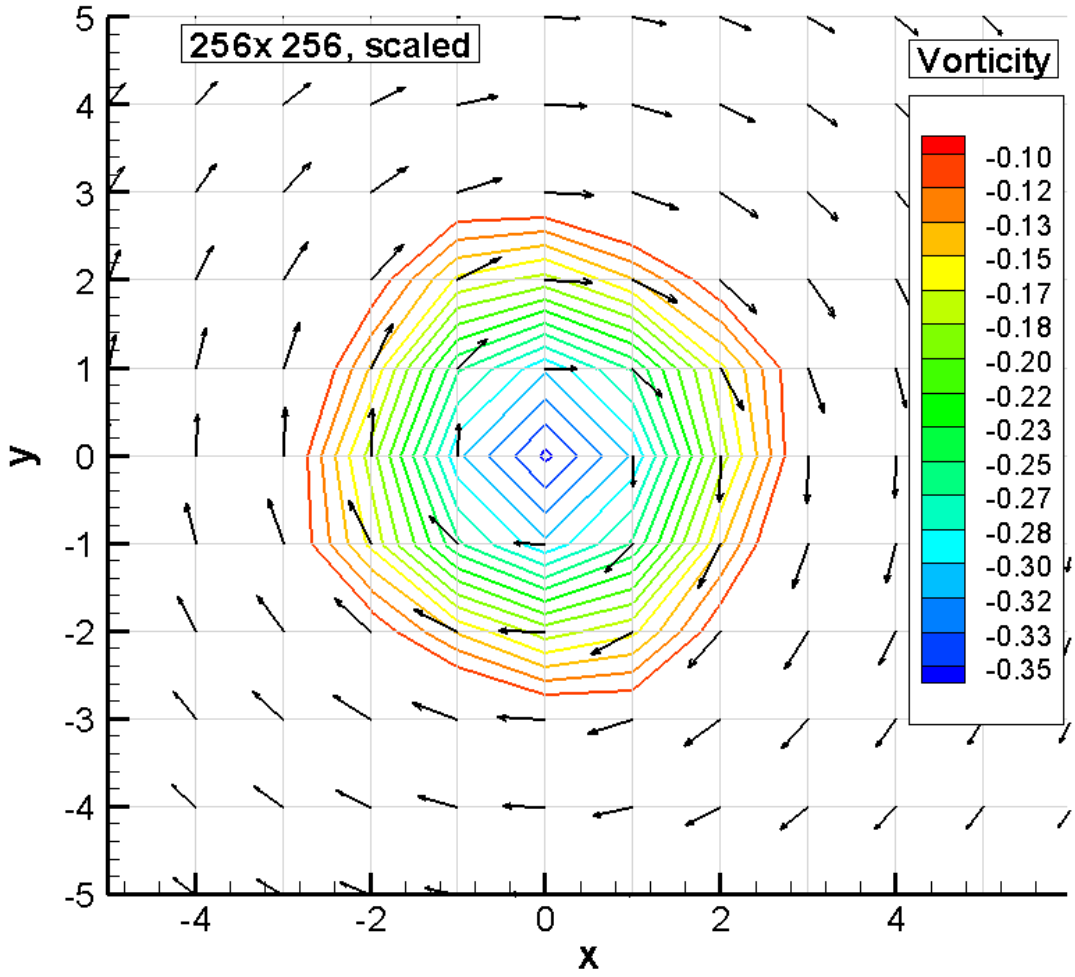

Figure 2-53. Flow field of a single vortex after scaling, with grid dimension 256 x 256.

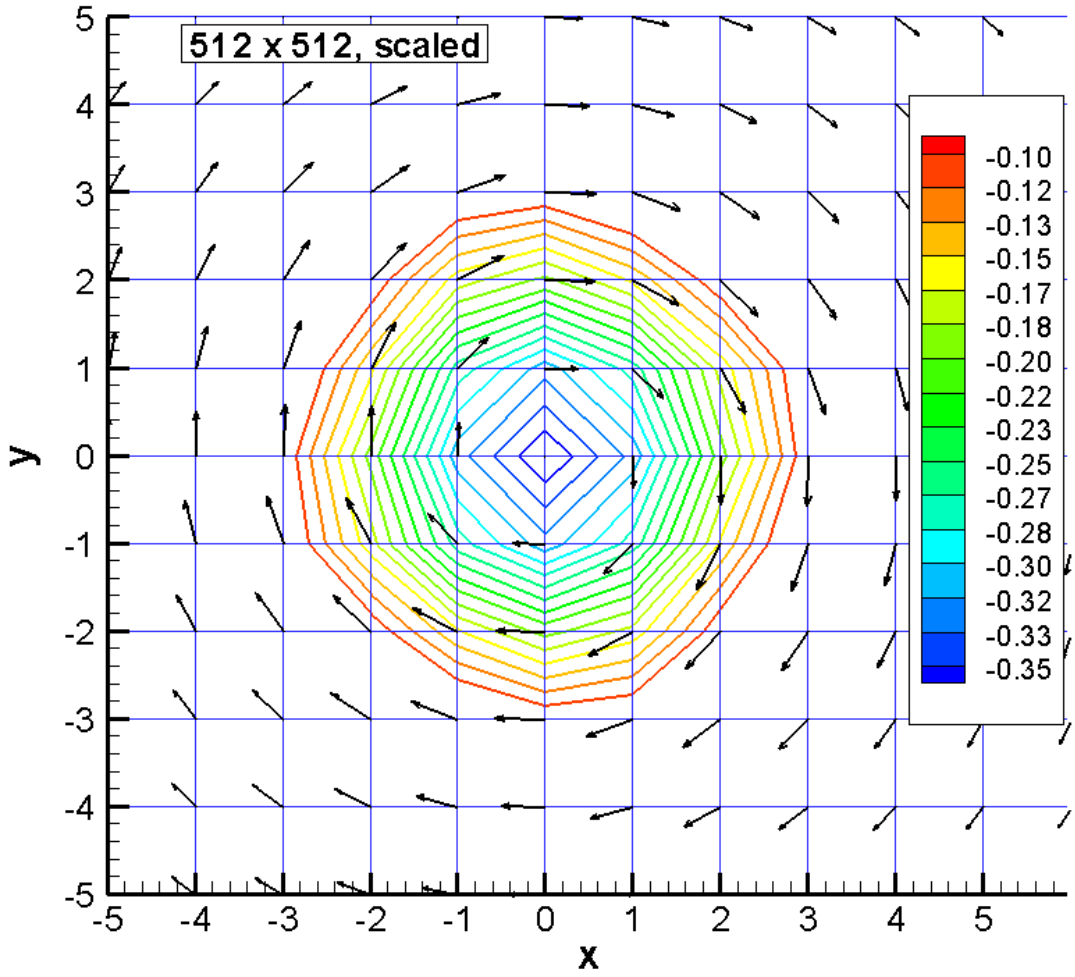

Figure 2-54. Flow field of a single vortex after scaling, with grid dimension 512 x 512.

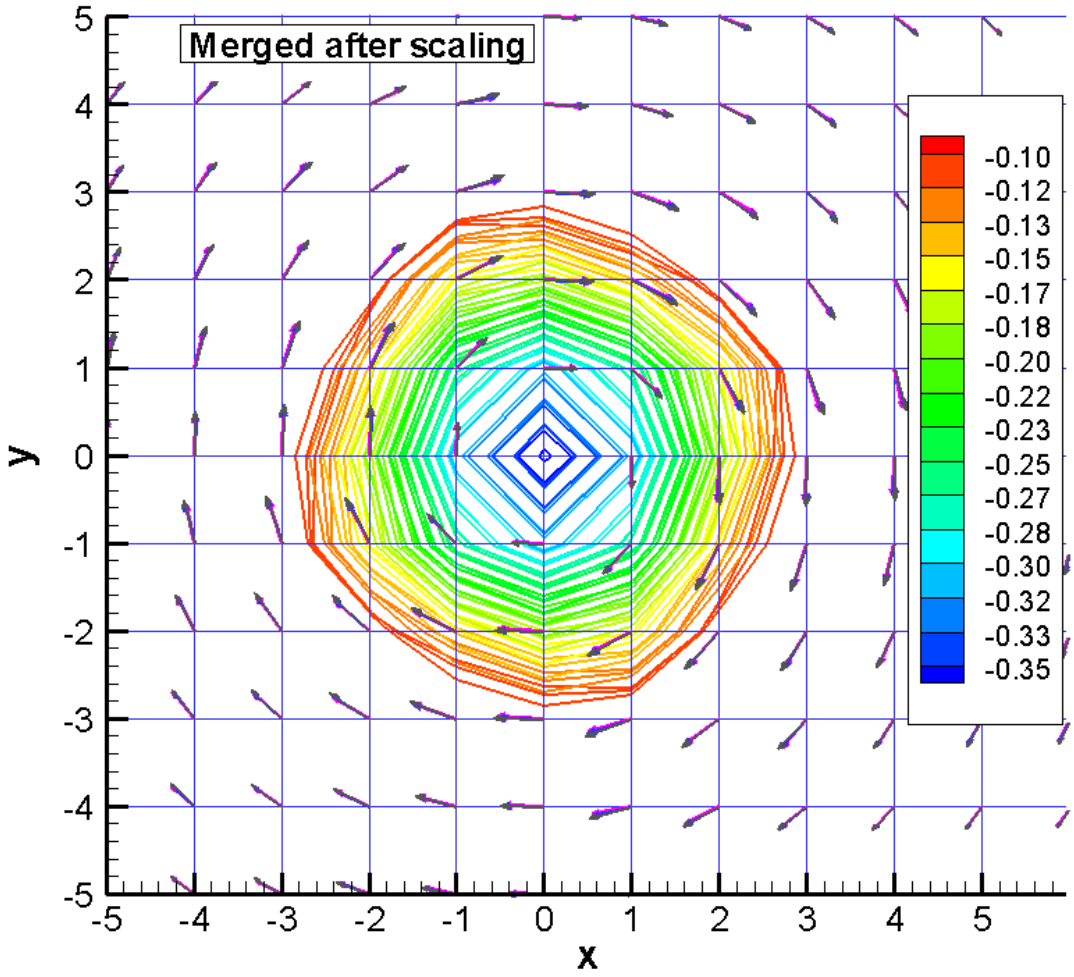

Figure 2-55. Merged Flow field of a stationary single vortex after scaling.

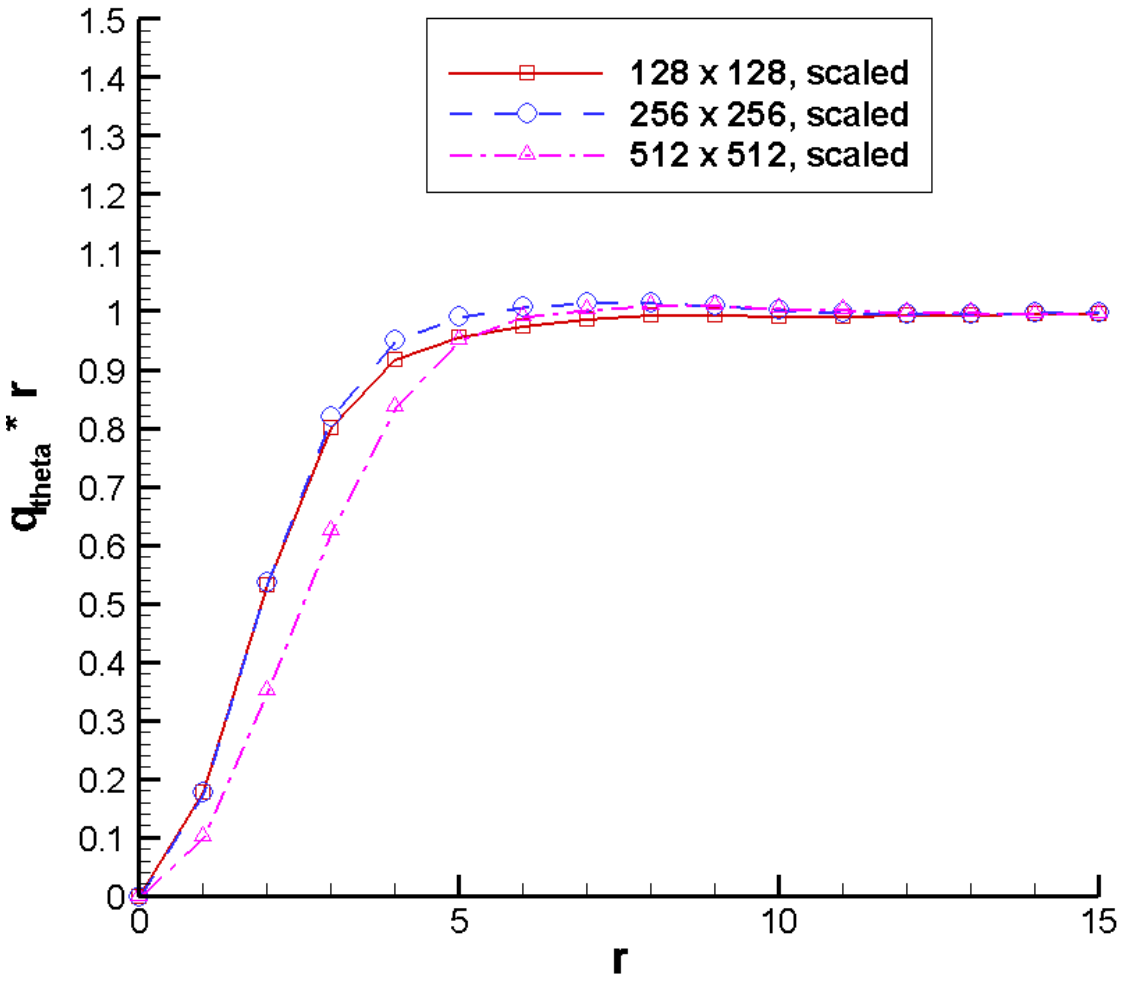

Figure 2-56. Velocity distribution of a stationary single vortex after scaling.

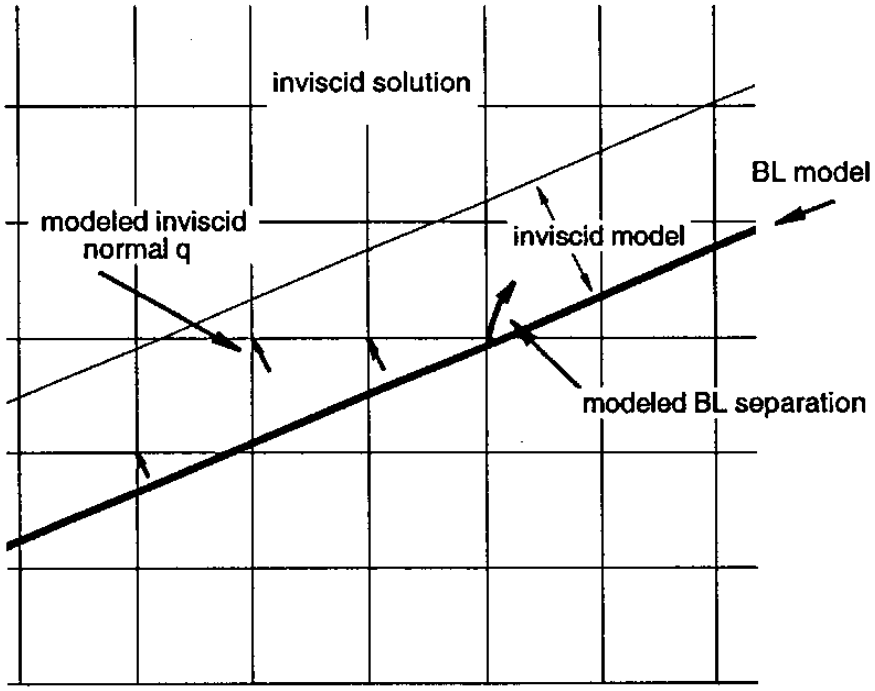

Figure 3-1. The initial surface boundary layer model [3].

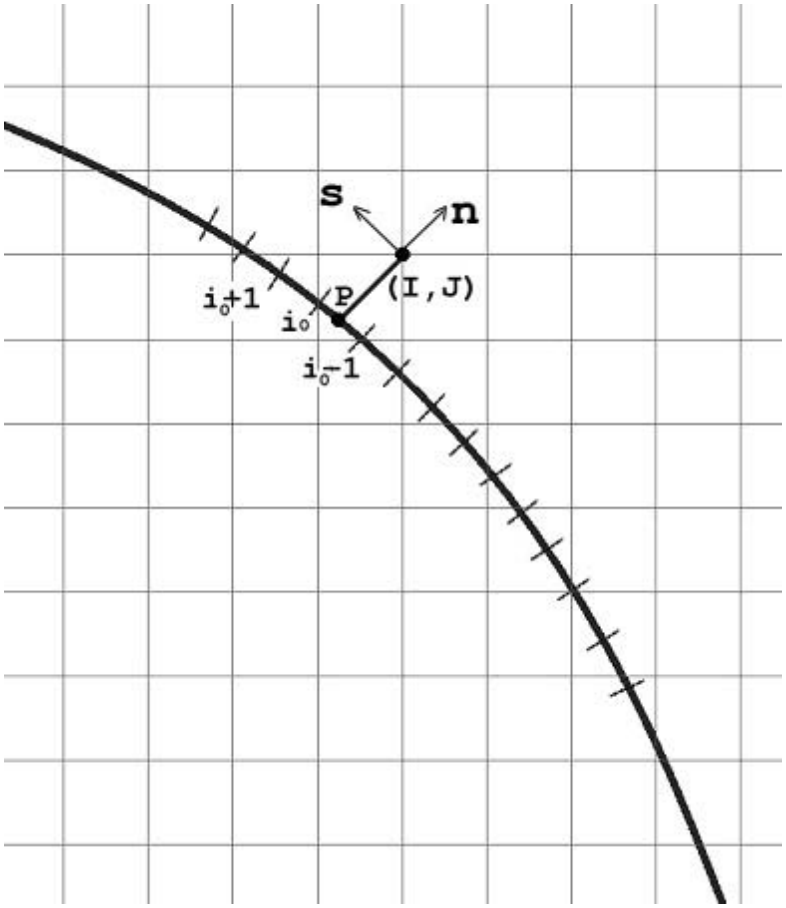

Figure 3-2. The projection from outer grid onto the surface.

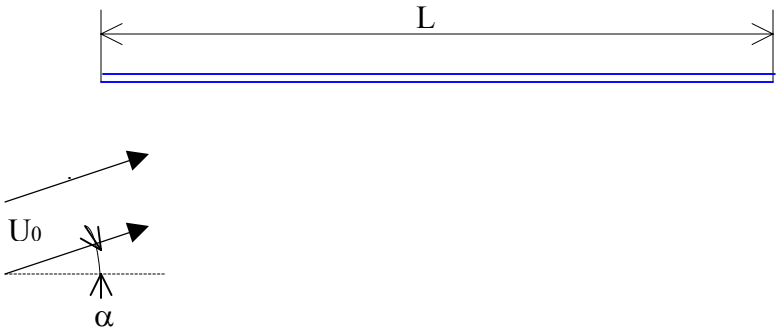

Figure 3-3. Flow over a flat plate

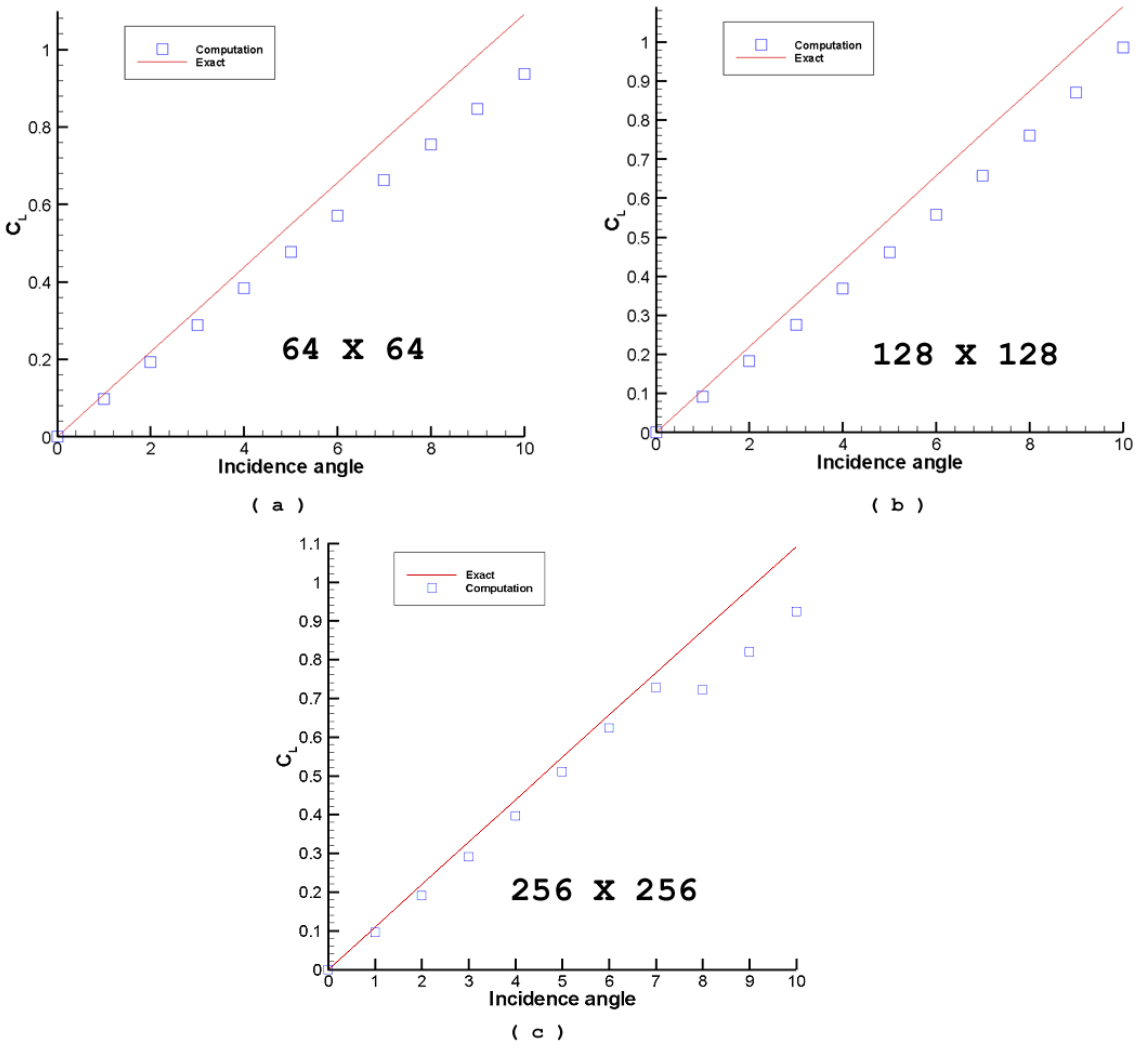

Figure 3-4. Lift coefficient for flow over flat plat, inviscid surface model.
(Grid dimension: (a) 64 x 64, (b) 128 x 128, (c) 256 x 256.)

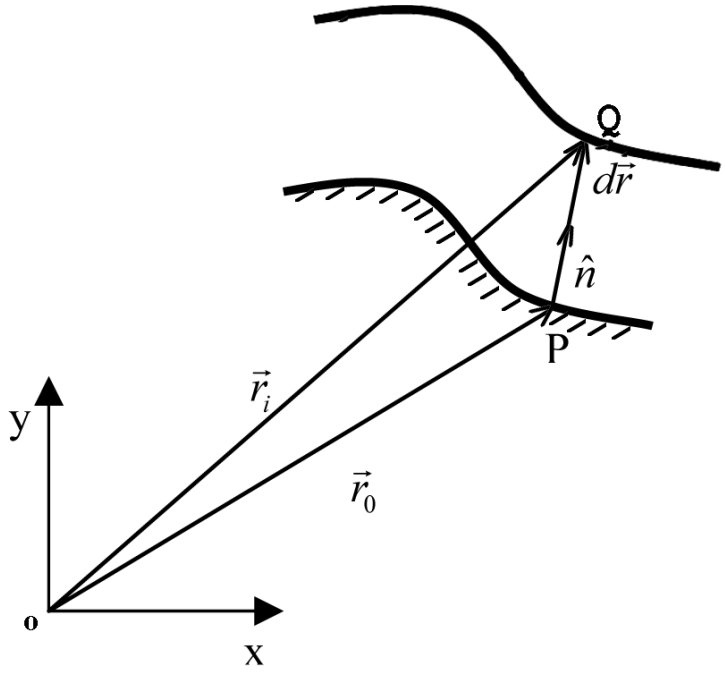

Figure 3-5. Body-conforming grid generation.

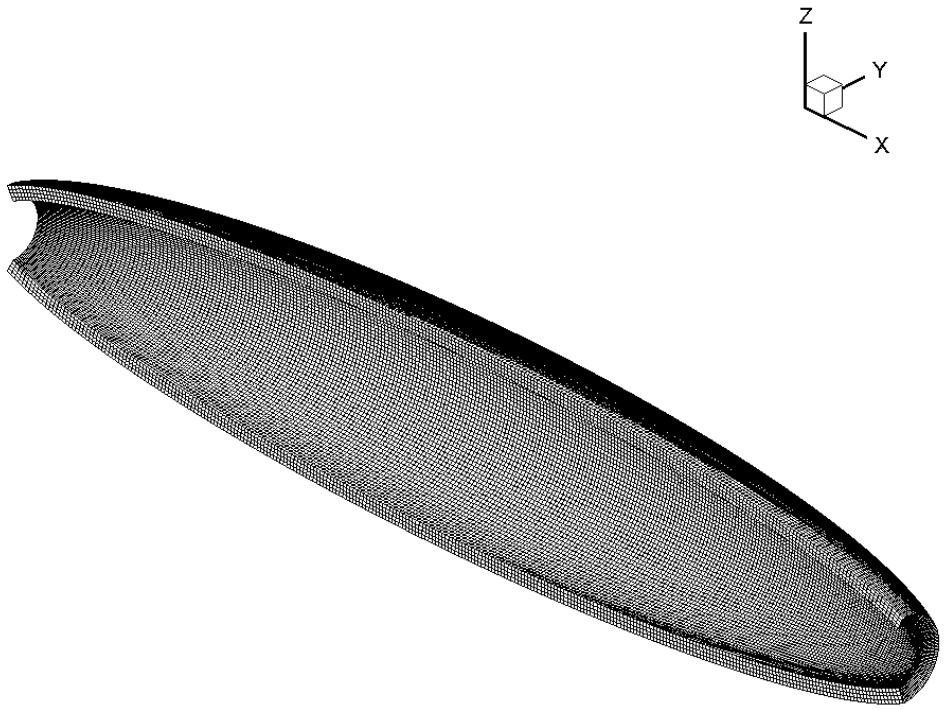

Figure 3-6. Inner grid around a 6:1 ellipsoid.

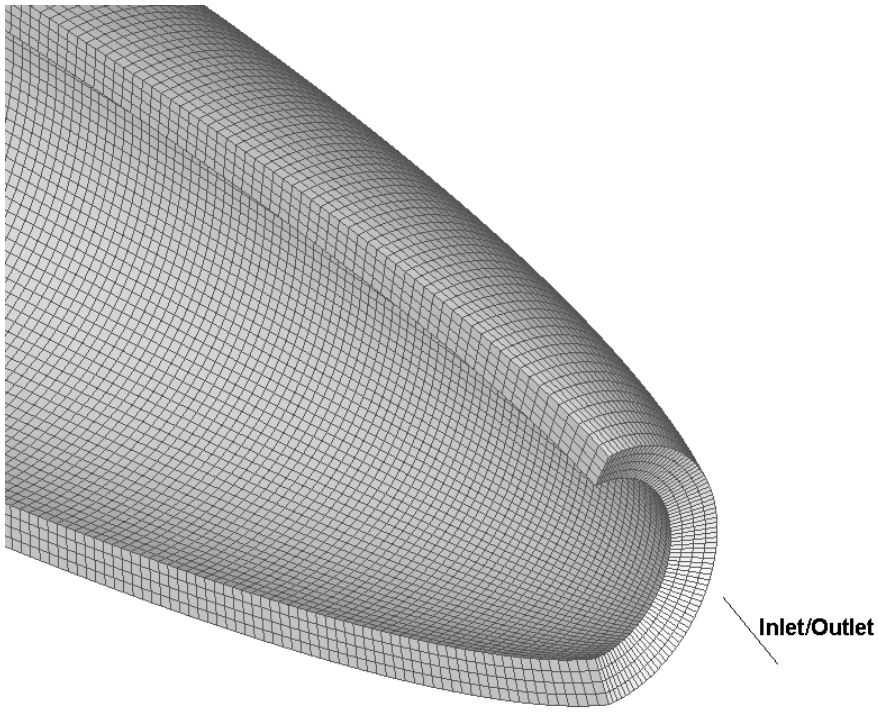

Figure 3-7. Detailed view of the inlet/outlet of the inner grid.

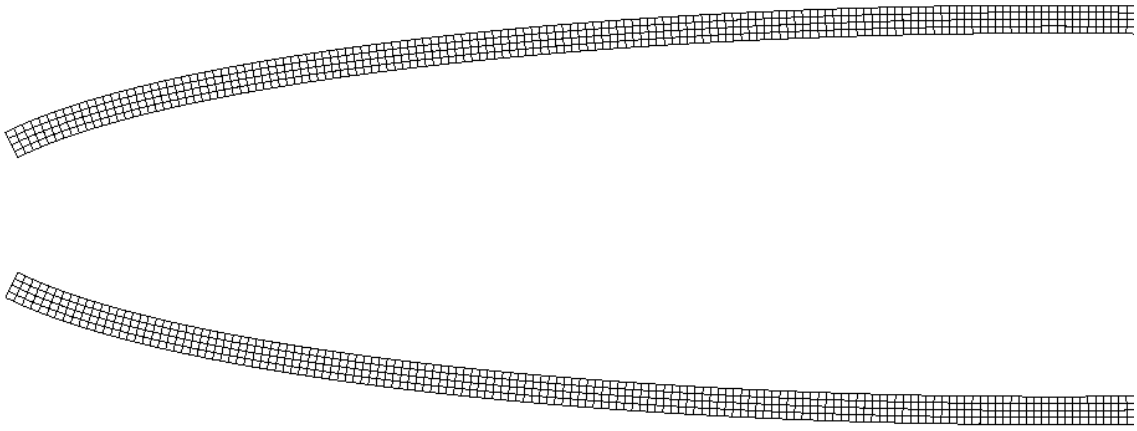

Figure 3-8. Inner grid around a 6:1 ellipsoid, crop of y=0 symmetry plane.

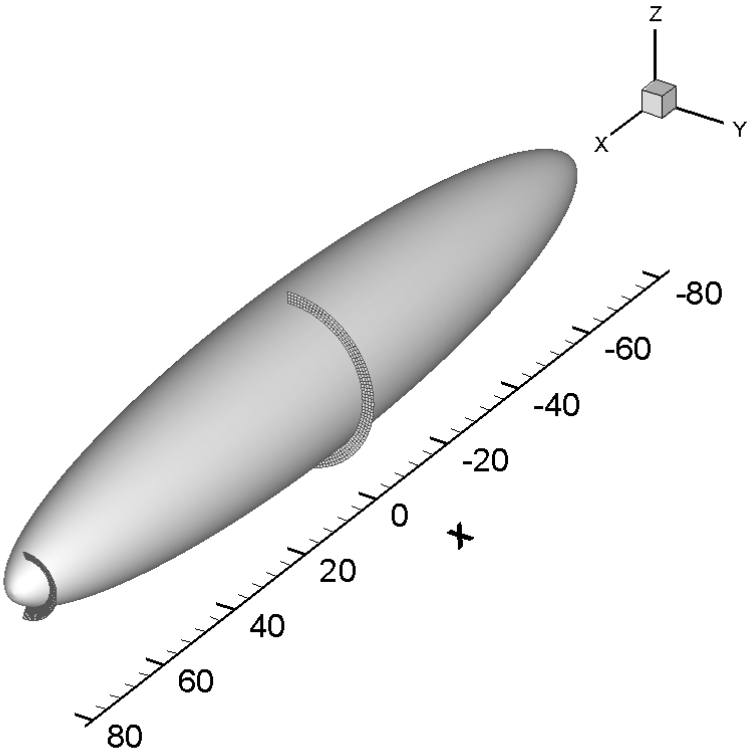

Figure 3-9. Inner grid around a 6:1 ellipsoid, cuts at the middle and the inlet/outlet.

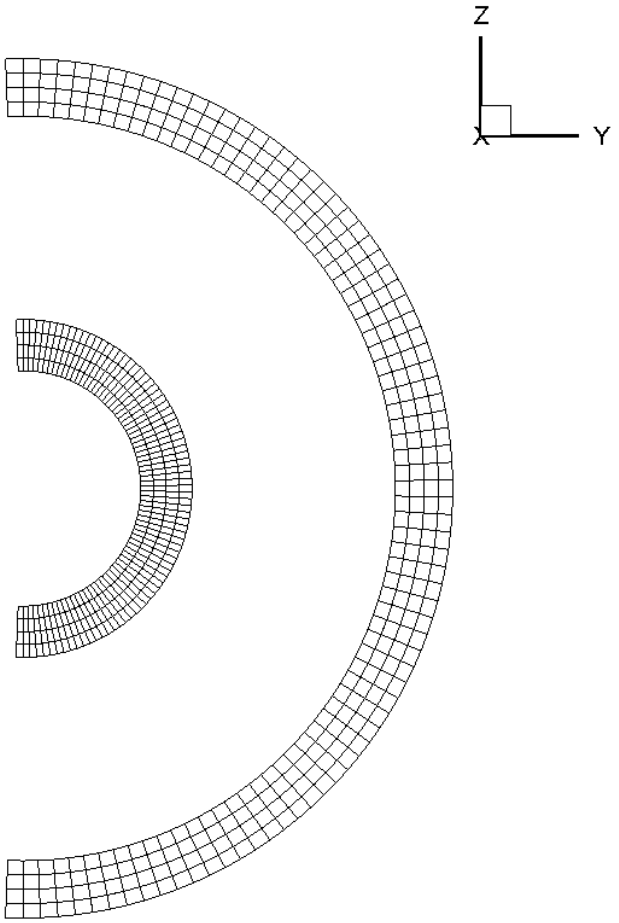

Figure 3-10. Inner grid around a 6:1 ellipsoid, details of the two planes in figure 3-9.

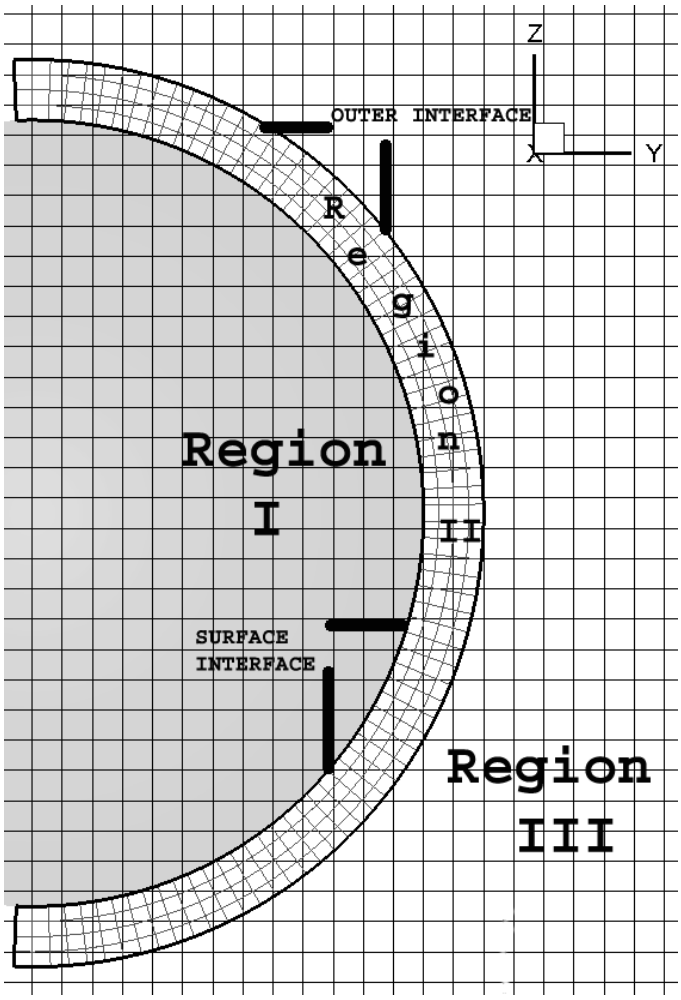

Figure 3-11. Overlapped grid systems, view of a cross plane.

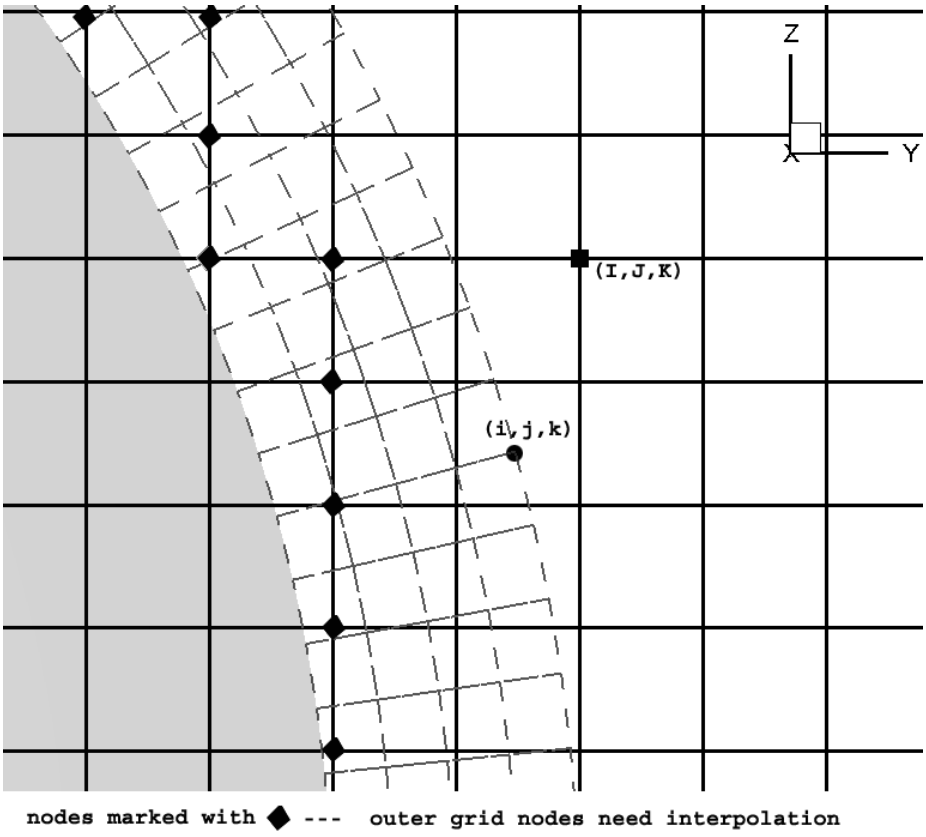

Figure 3-12. Enlarged view of the overlapped grid systems, view of a cross plane.

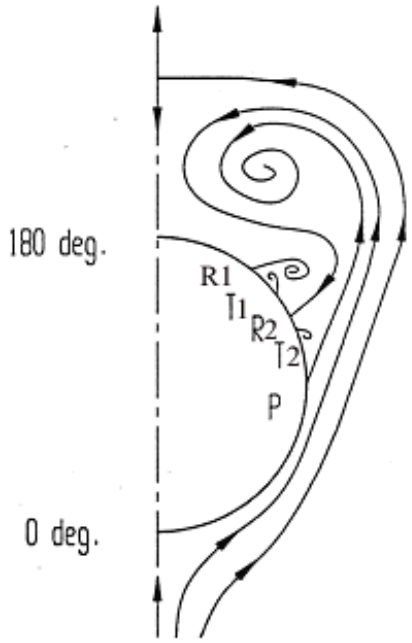

(a)

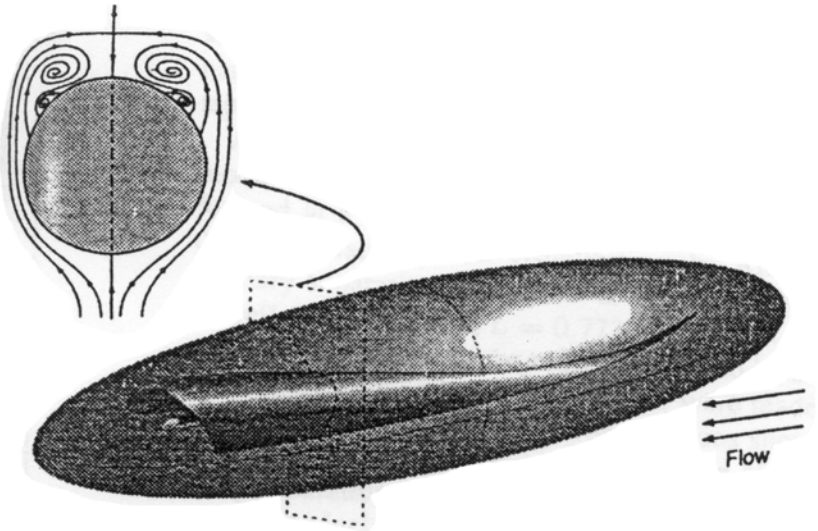

(b)

Figure 4-1. Cross plane separation.
(Figures from Simpson *et al* [6].)

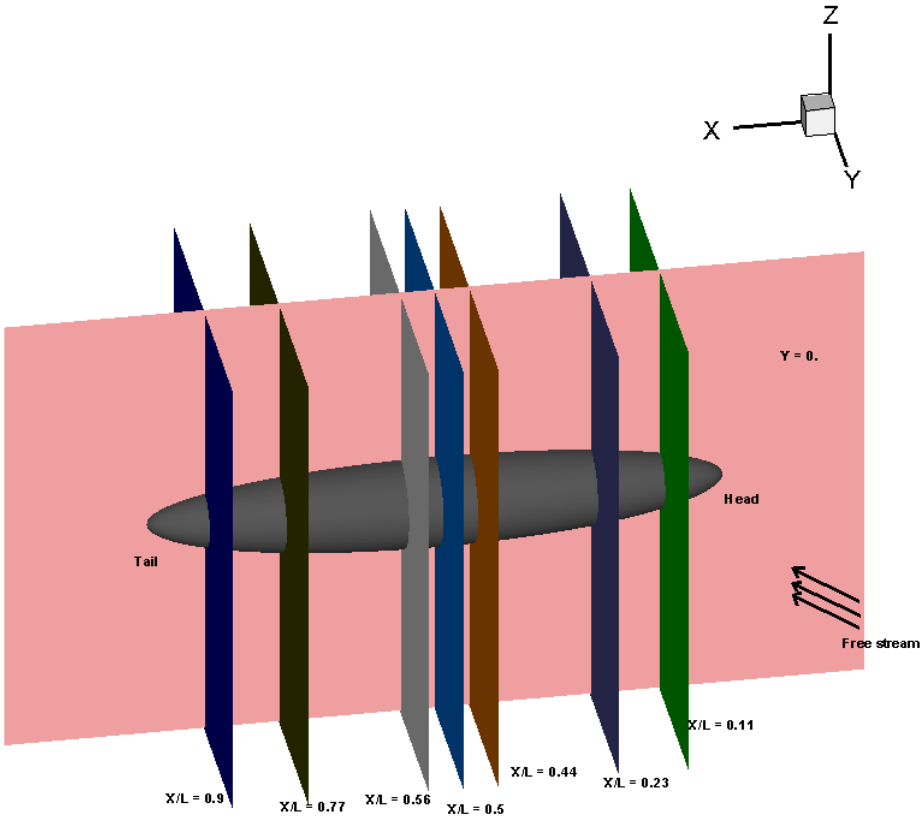

Figure 4-2. The 6:1 ellipsoid configuration, data planes.

.

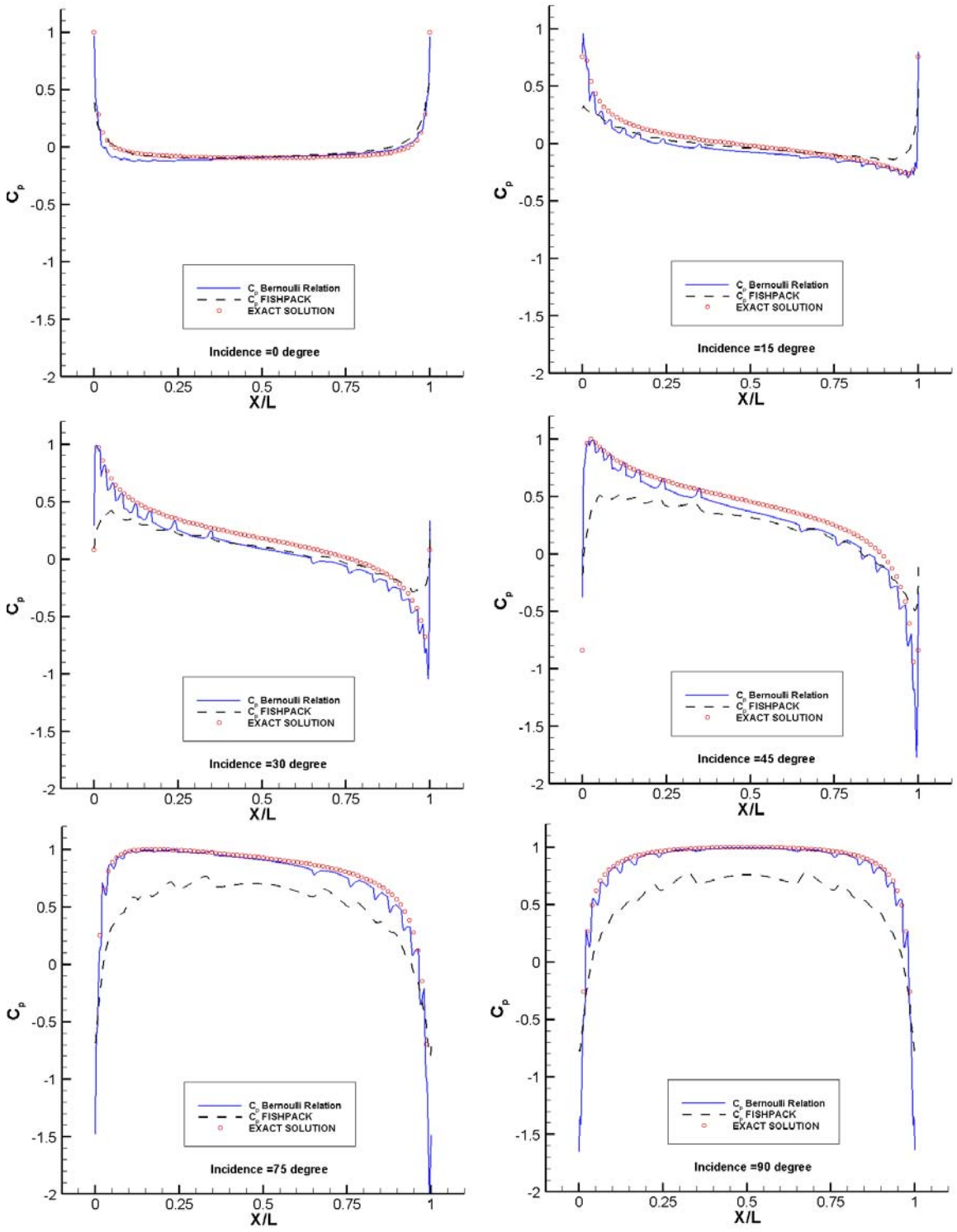

Figure 4-3. Pressure Coefficient, symmetry plane (theta = 0), inviscid surface model.

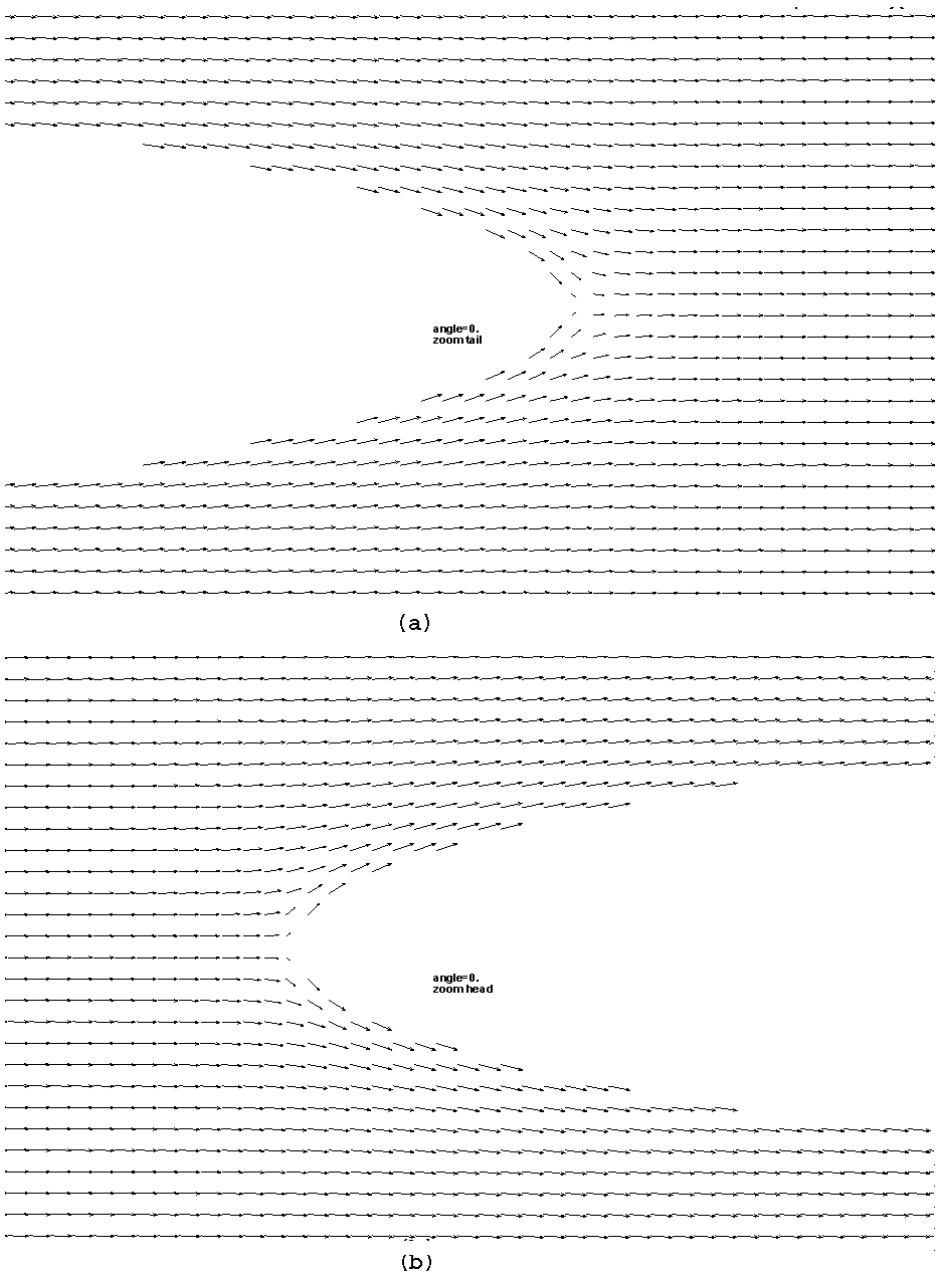

Figure 4-4. Velocity of the symmetry plane, 0° incidence, inviscid surface model.

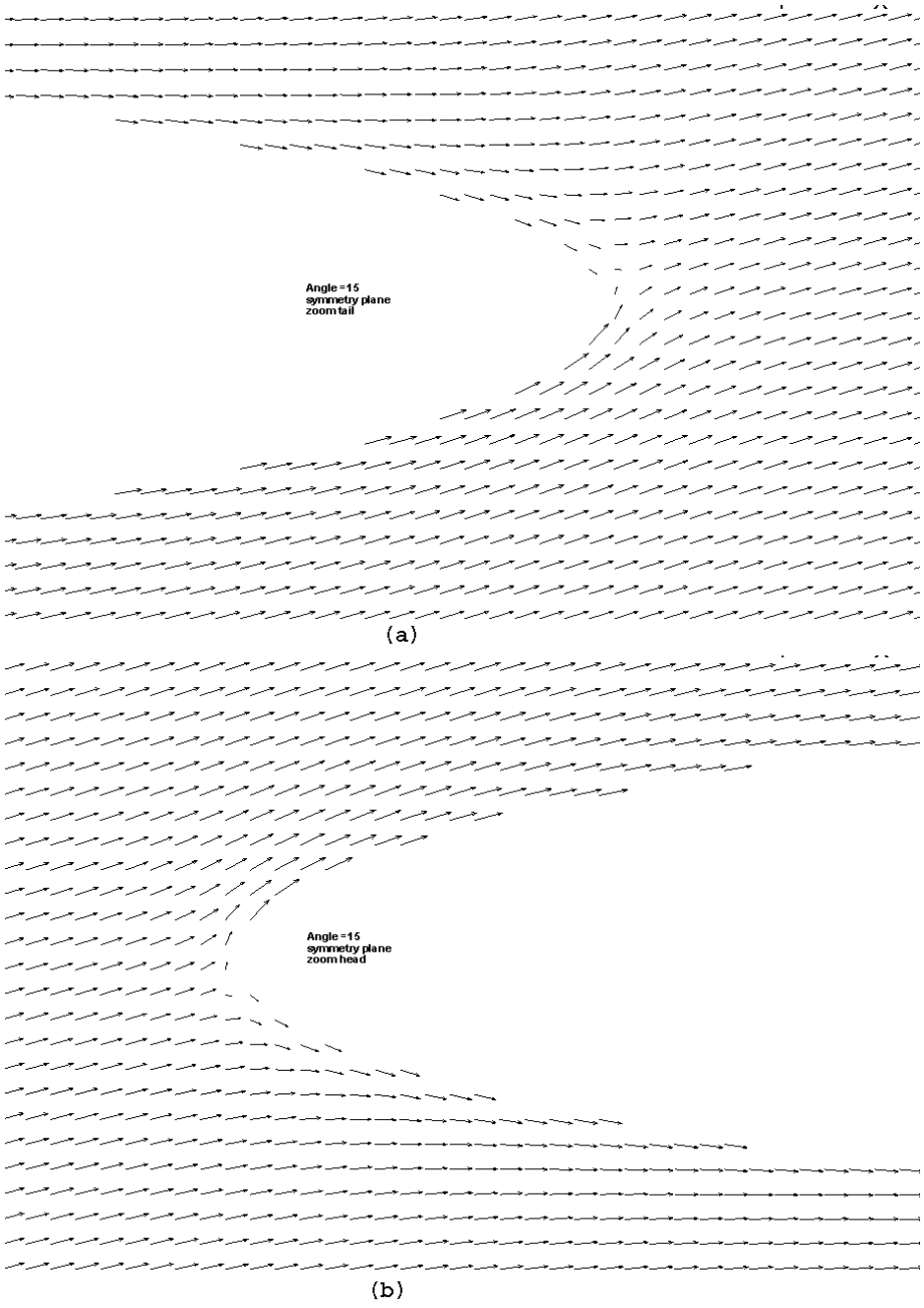

Figure 4-5. Velocity of the symmetry plane, 15° incidence, inviscid surface model.

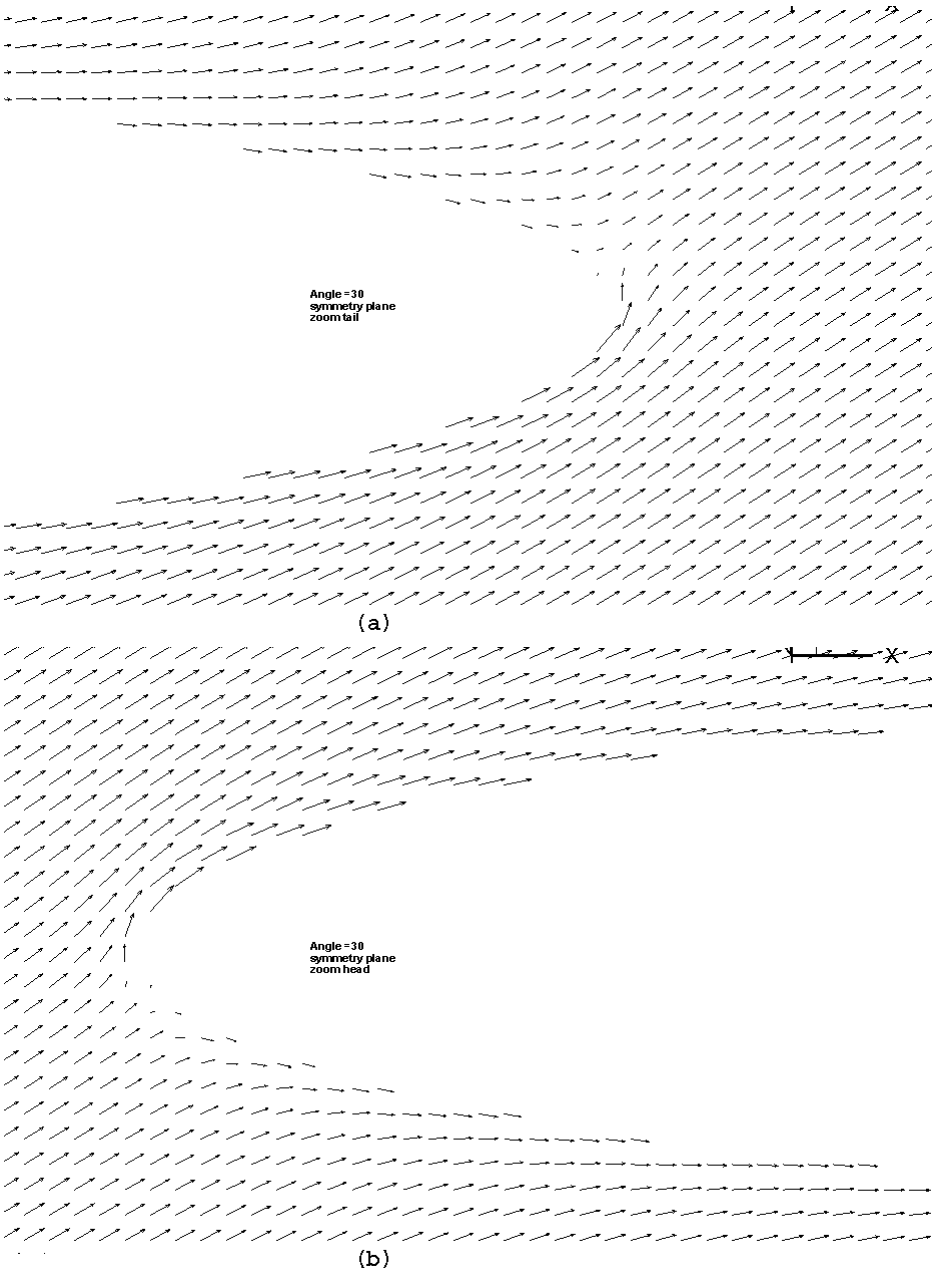

Figure 4-6. Velocity of the symmetry plane, 30° incidence, inviscid surface model.

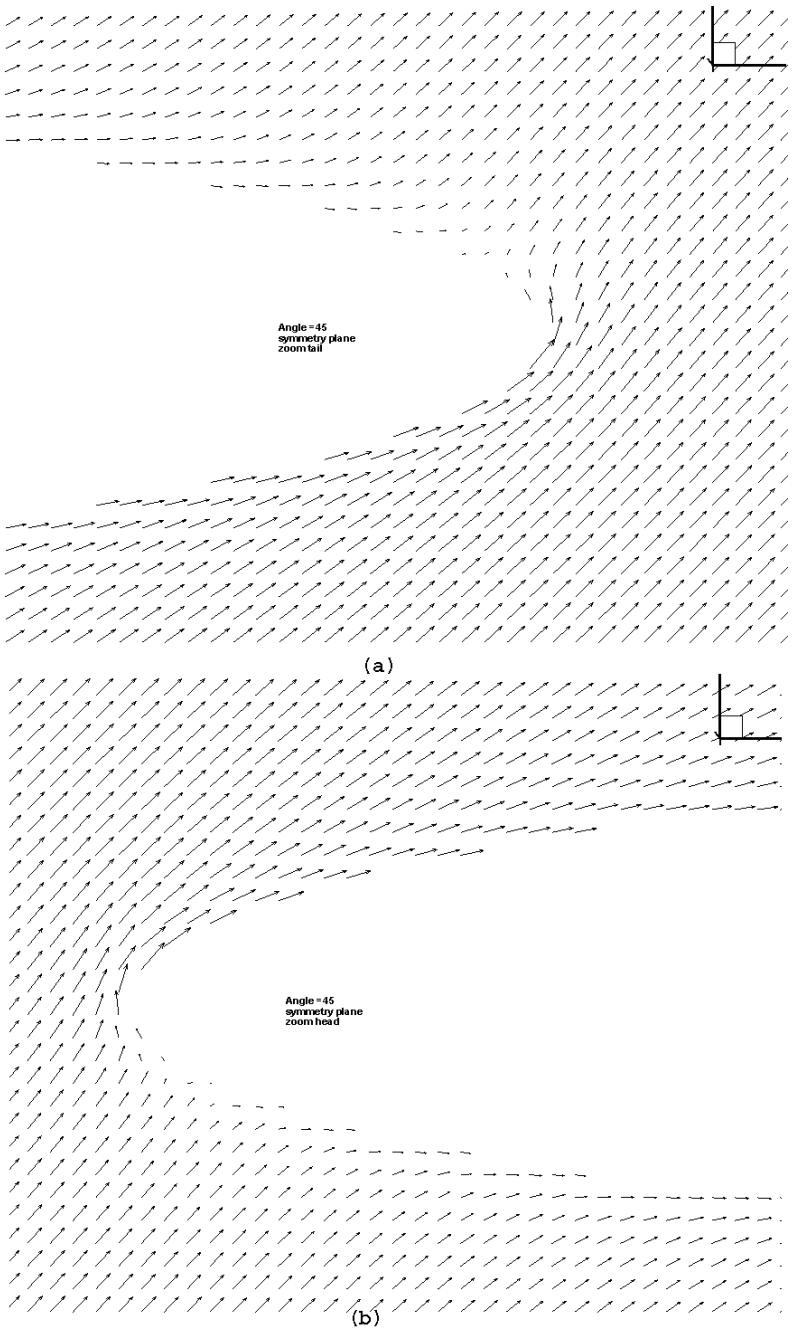

Figure 4-7. Velocity of the symmetry plane, 45° incidence, inviscid surface model.

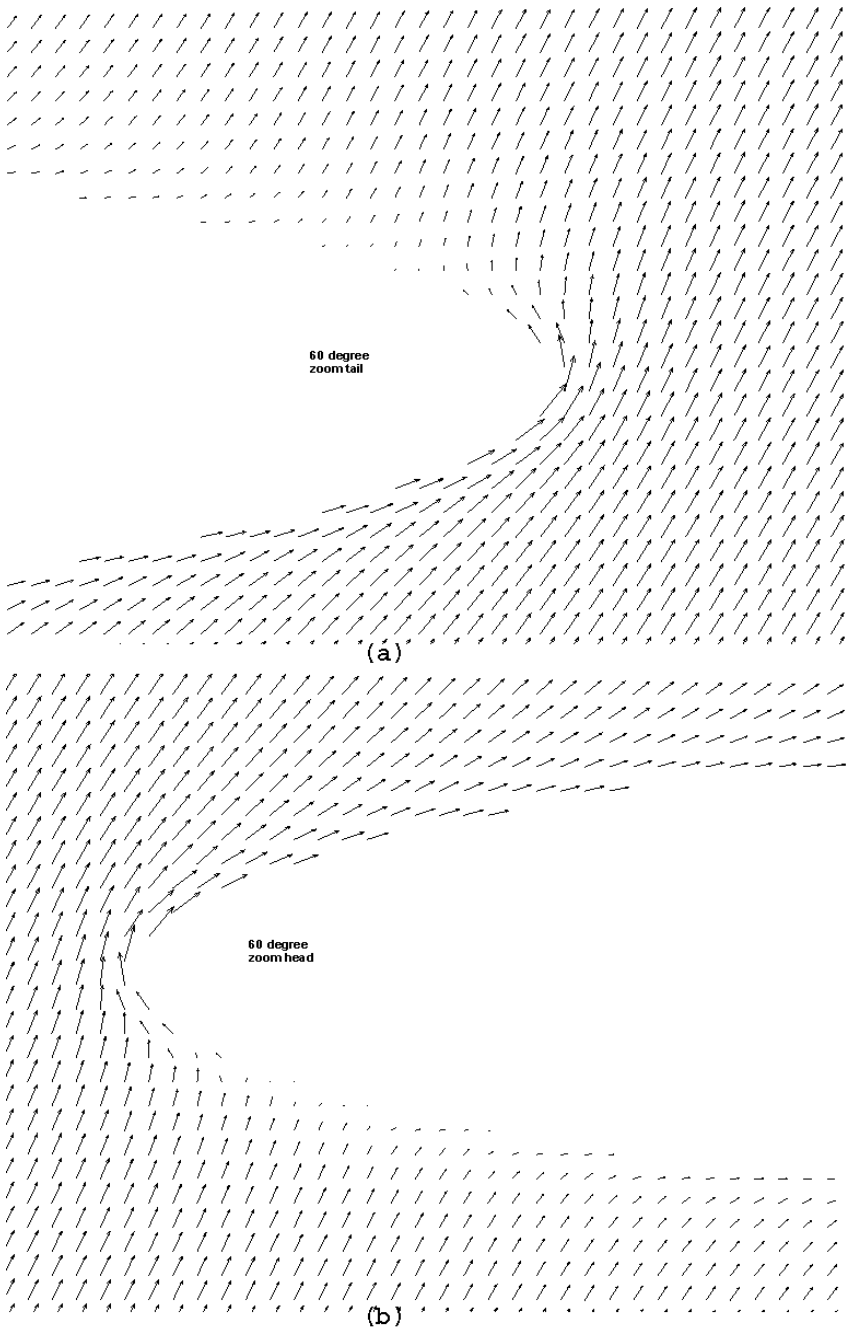

Figure 4-8. Velocity of the symmetry plane, 60° incidence, inviscid surface model.

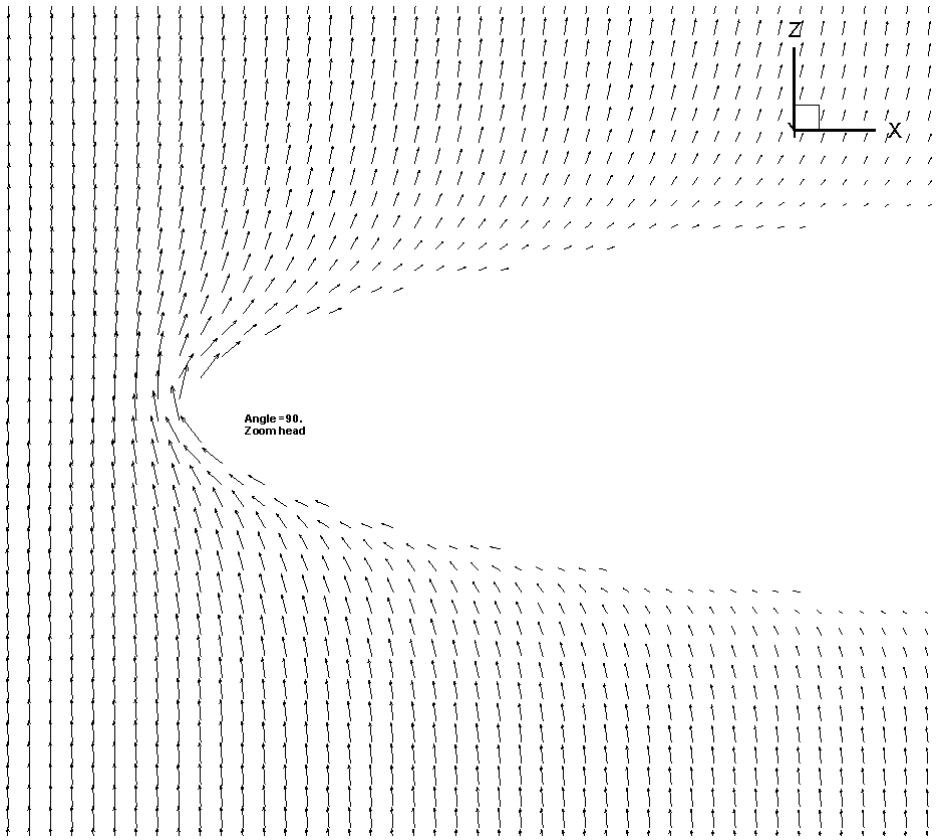

Figure 4-9. Velocity of the symmetry plane, 90° incidence, inviscid surface model.

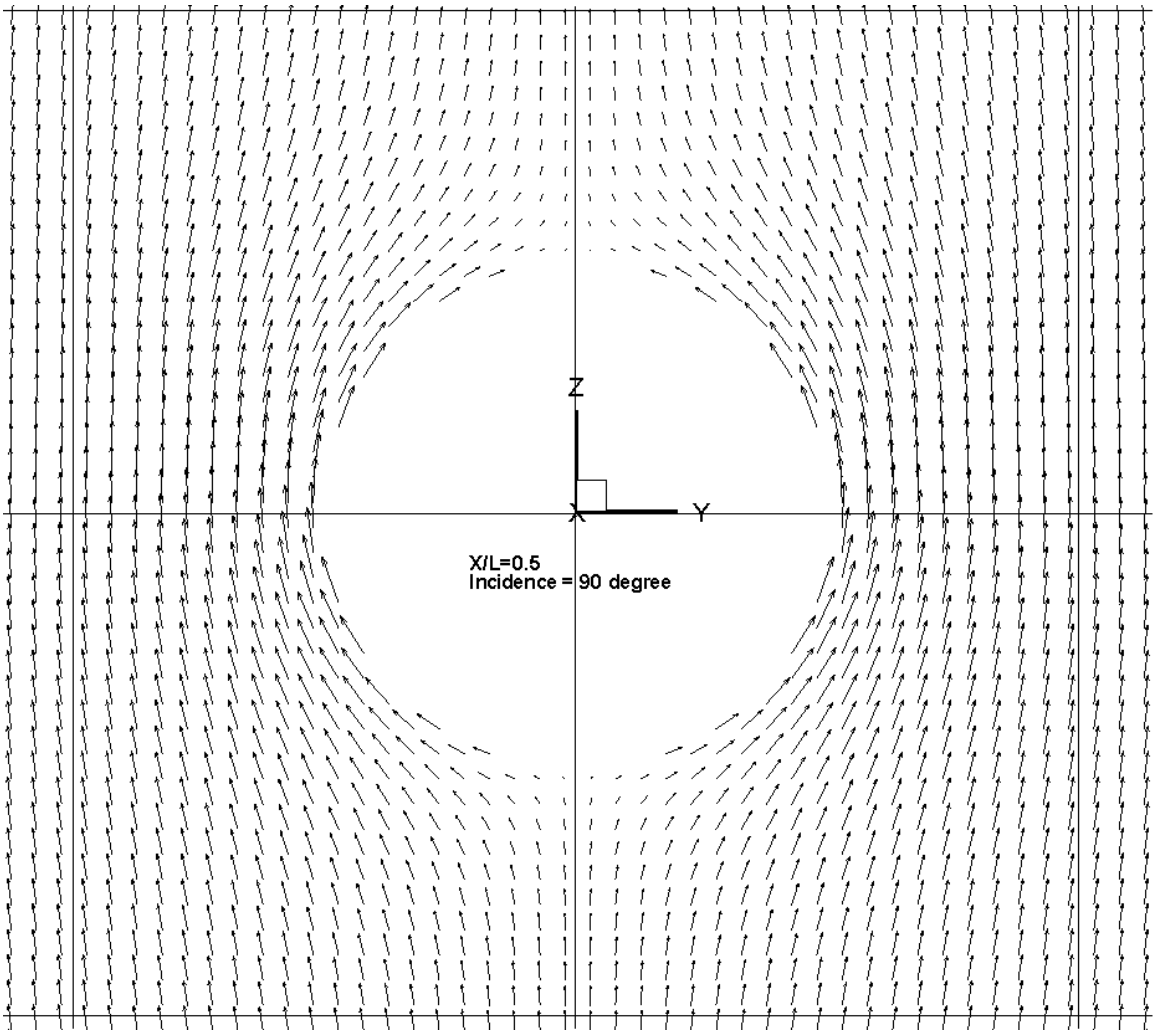

Figure 4-10. Cross plane velocity, X/L = 0.5, 90° incidence, inviscid surface model.

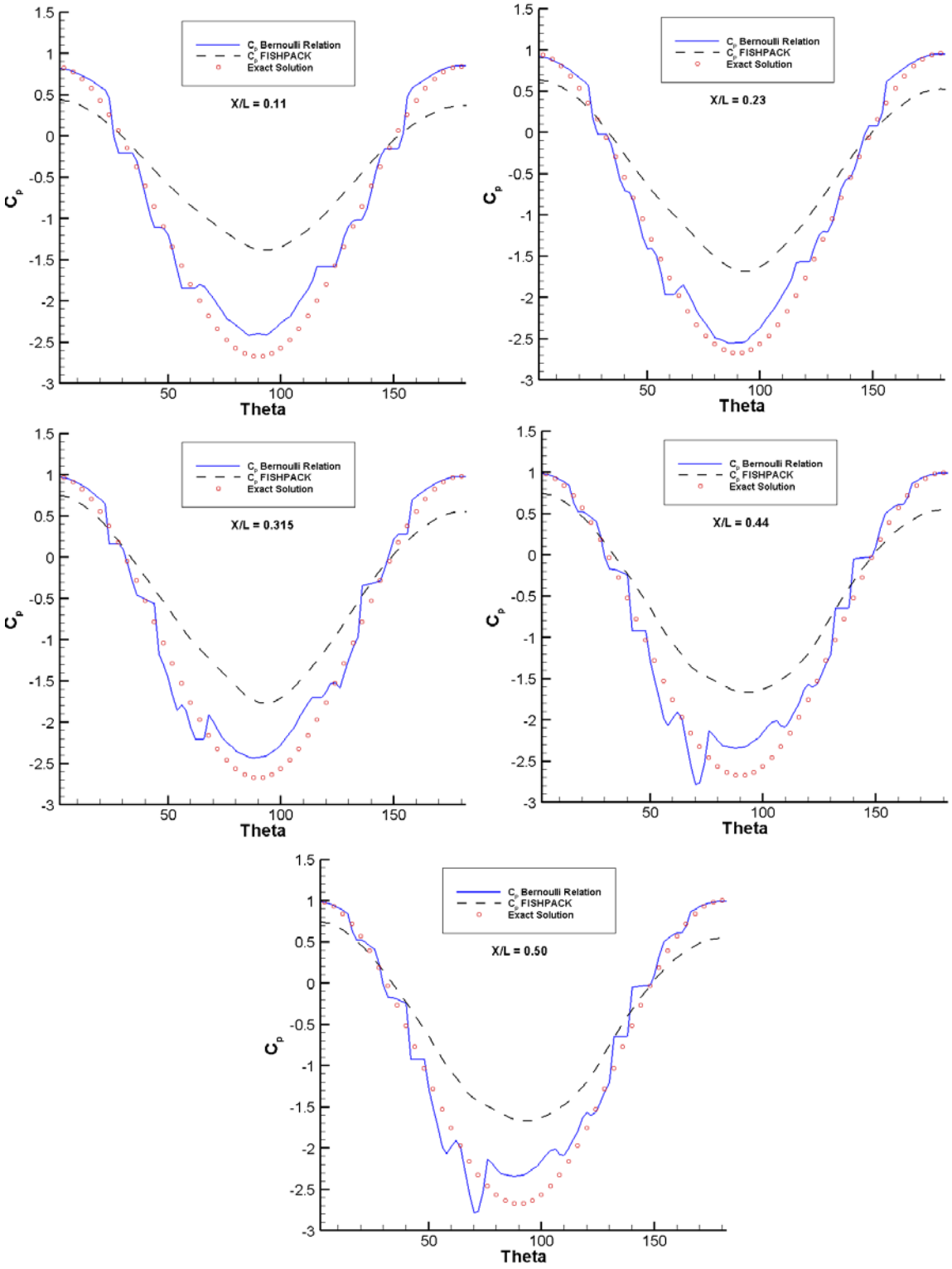

Figure 4-11. Pressure Coefficient, cross planes, 90° incidence, inviscid surface model.

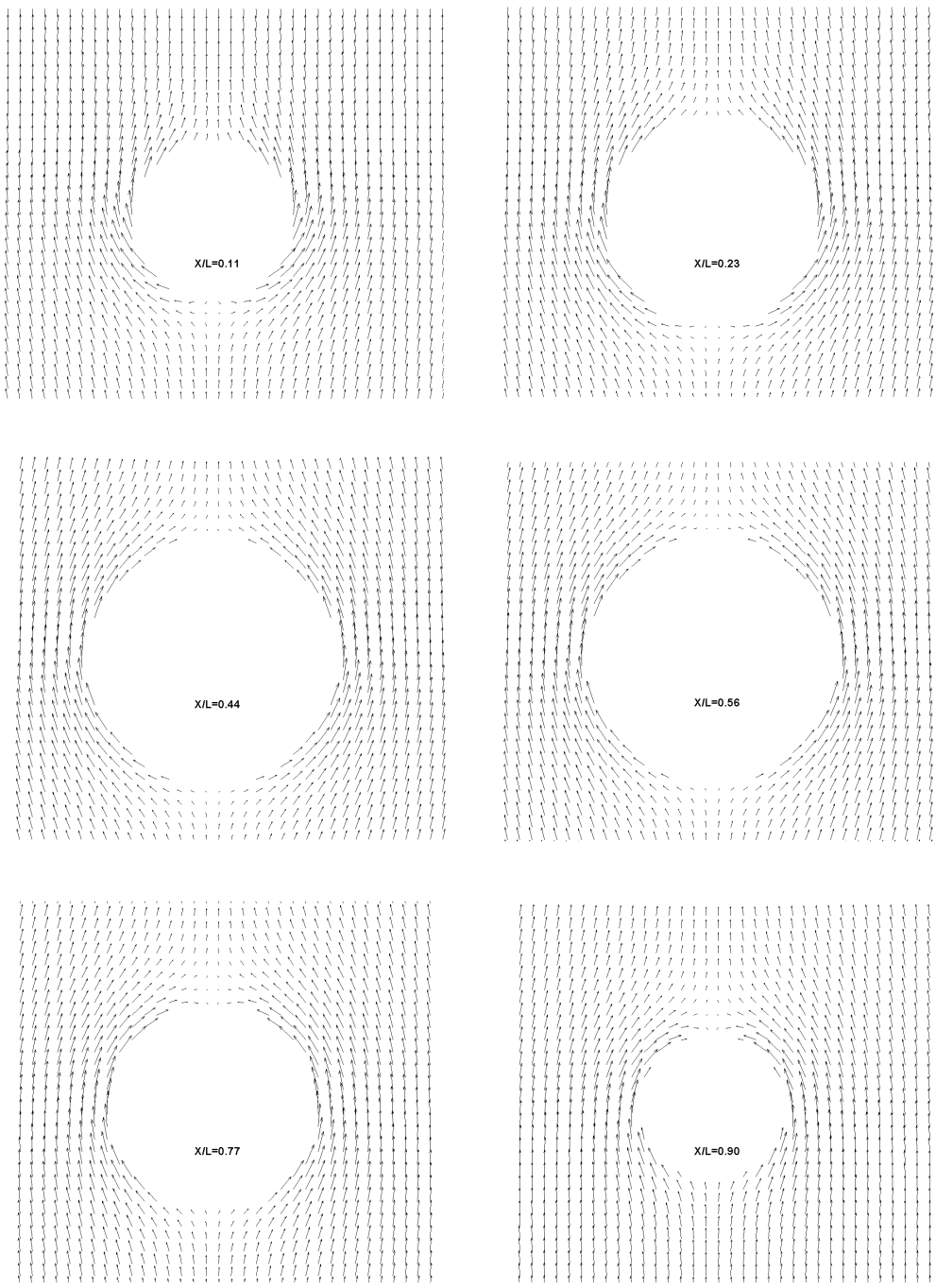

Figure 4-12. Cross plane velocity, 30° incidence, inviscid surface model.

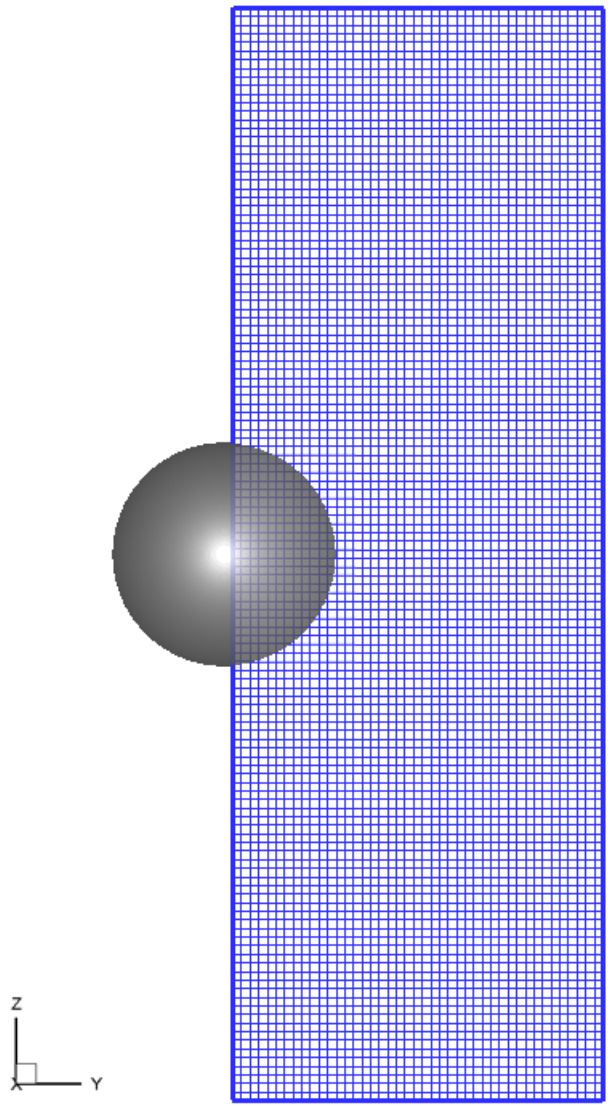

Figure 4-13. The uniform Cartesian grid

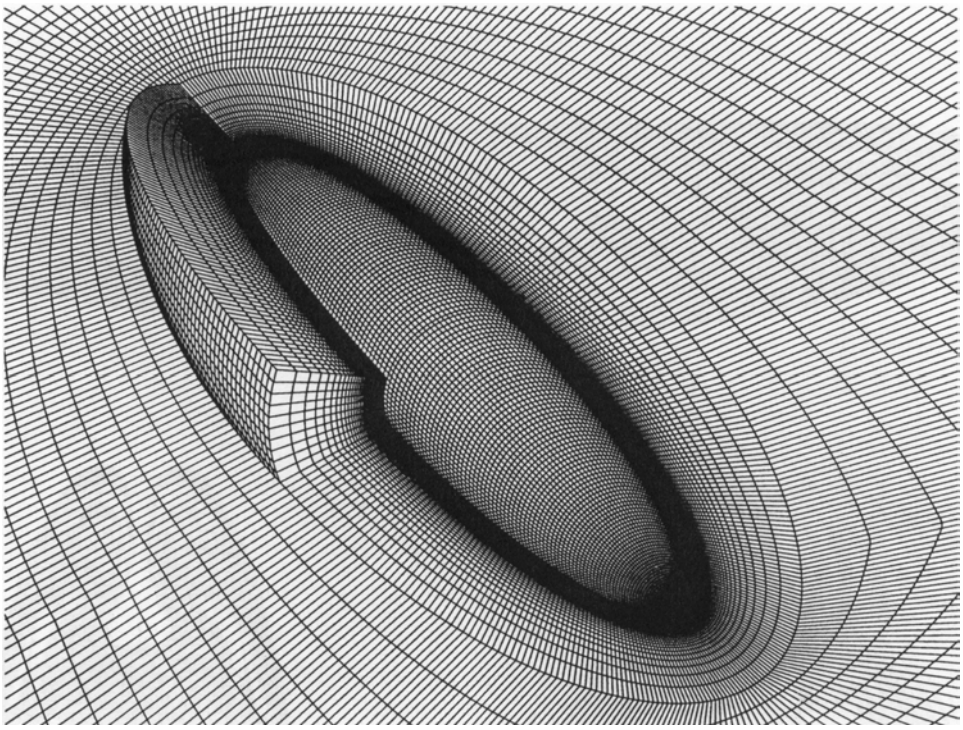

Figure 4-14. The structured grid used by Tsai *et al* [4].

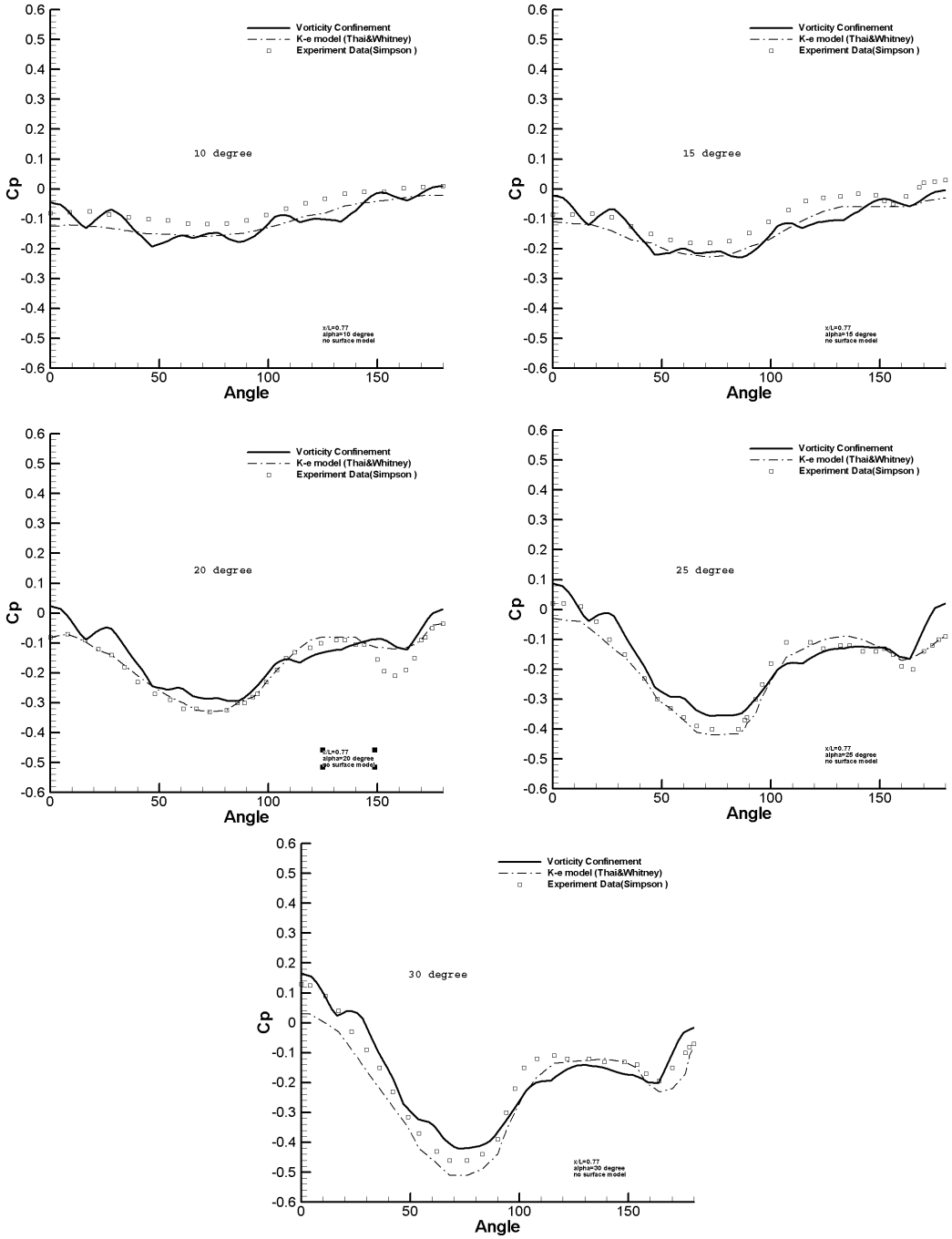

Figure 4-15. Pressure coefficient, X/L = 0.77, 10° to 30° incidence, without surface model.

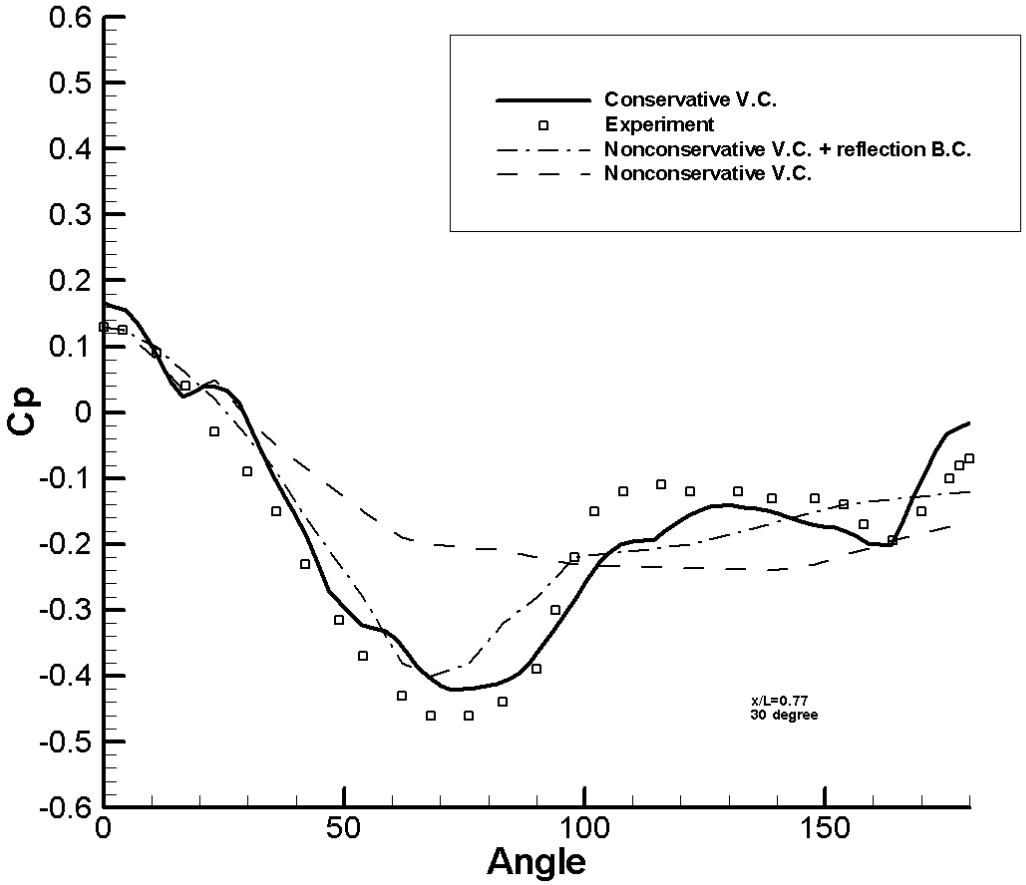

Figure 4-16. Pressure coefficient, X/L = 0.77, 30° incidence, without surface model. (Compared to non-conservative vorticity confinement solution (Carsten Braun [19]).)

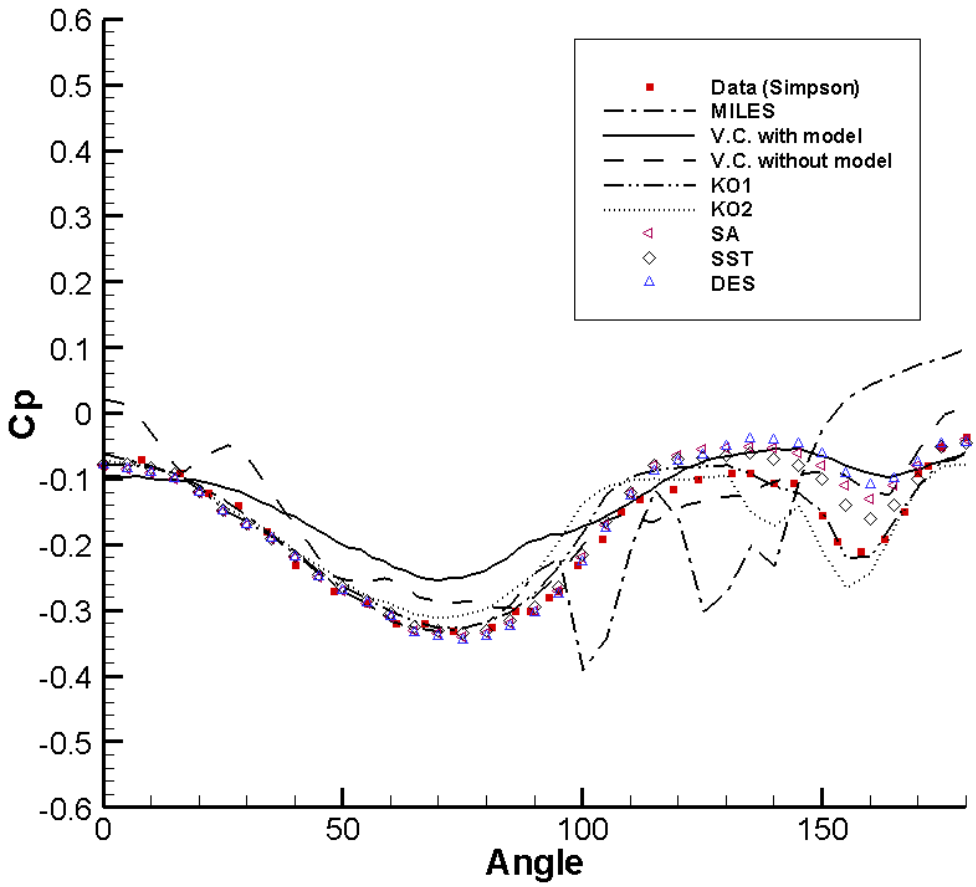

Figure 4-17. Variation of the solutions, X/L = 0.77, 20° incidence.

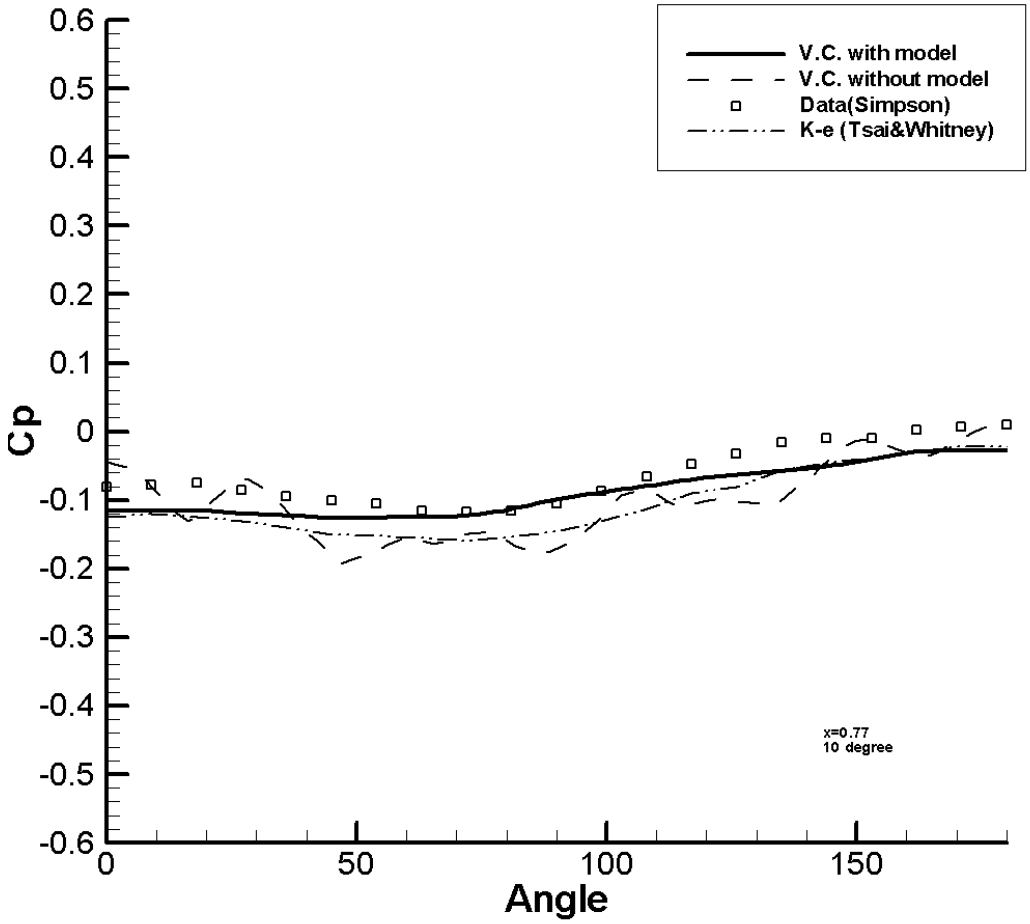

Figure 4-18. Pressure coefficient, X/L = 0.77, 10° incidence, with surface model.

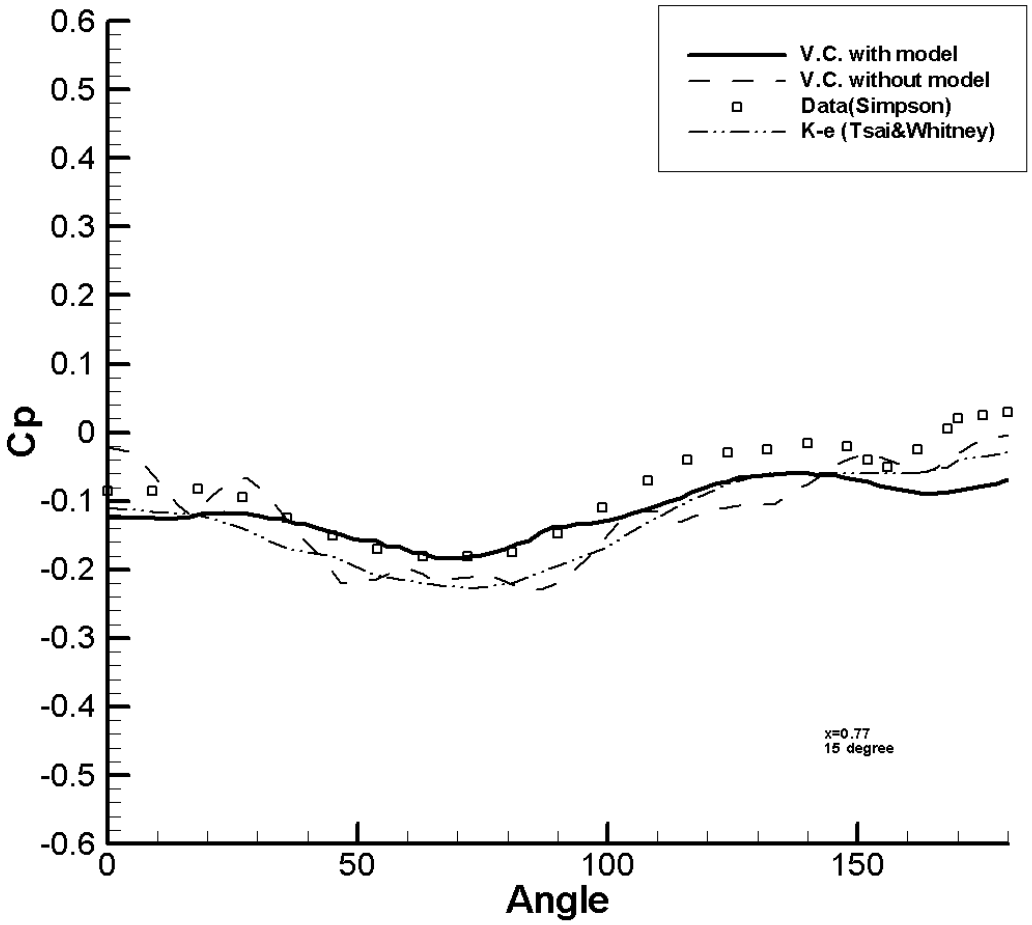

Figure 4-19. Pressure coefficient, X/L = 0.77, 15° incidence, with surface model.

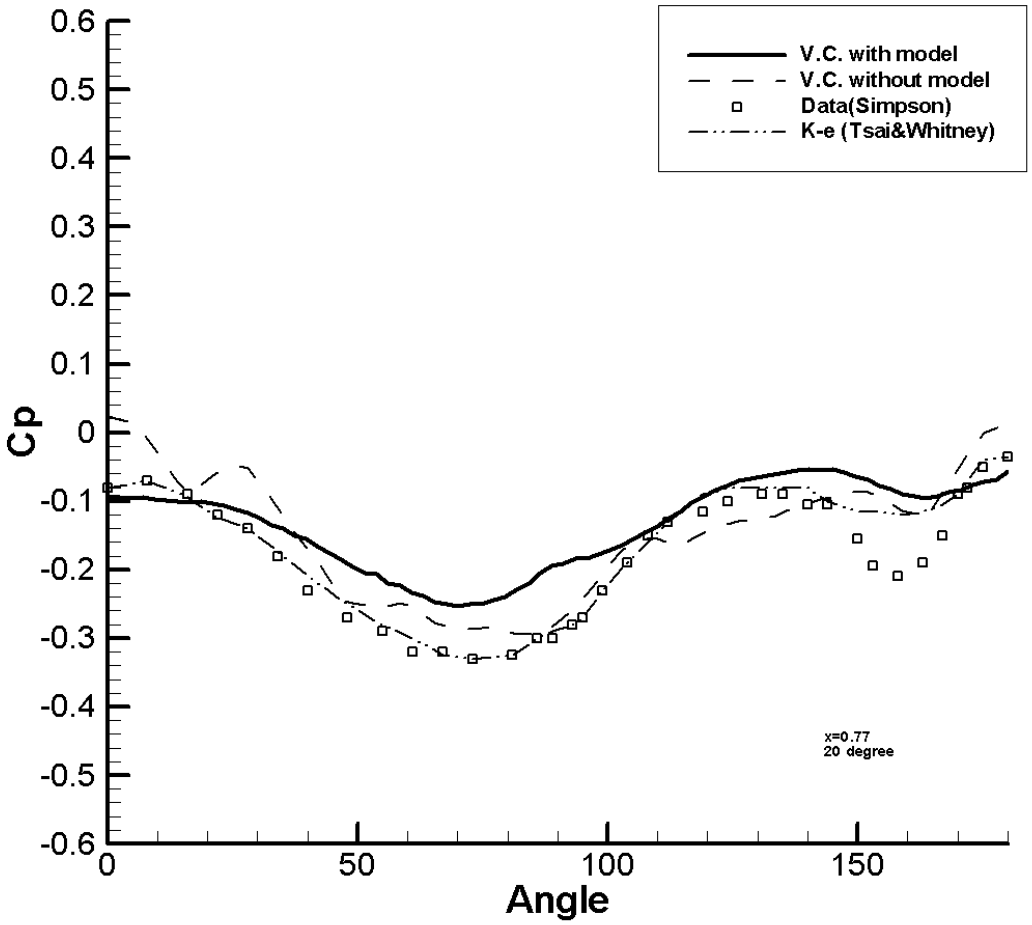

Figure 4-20. Pressure coefficient, X/L = 0.77, 20° incidence, with surface model.

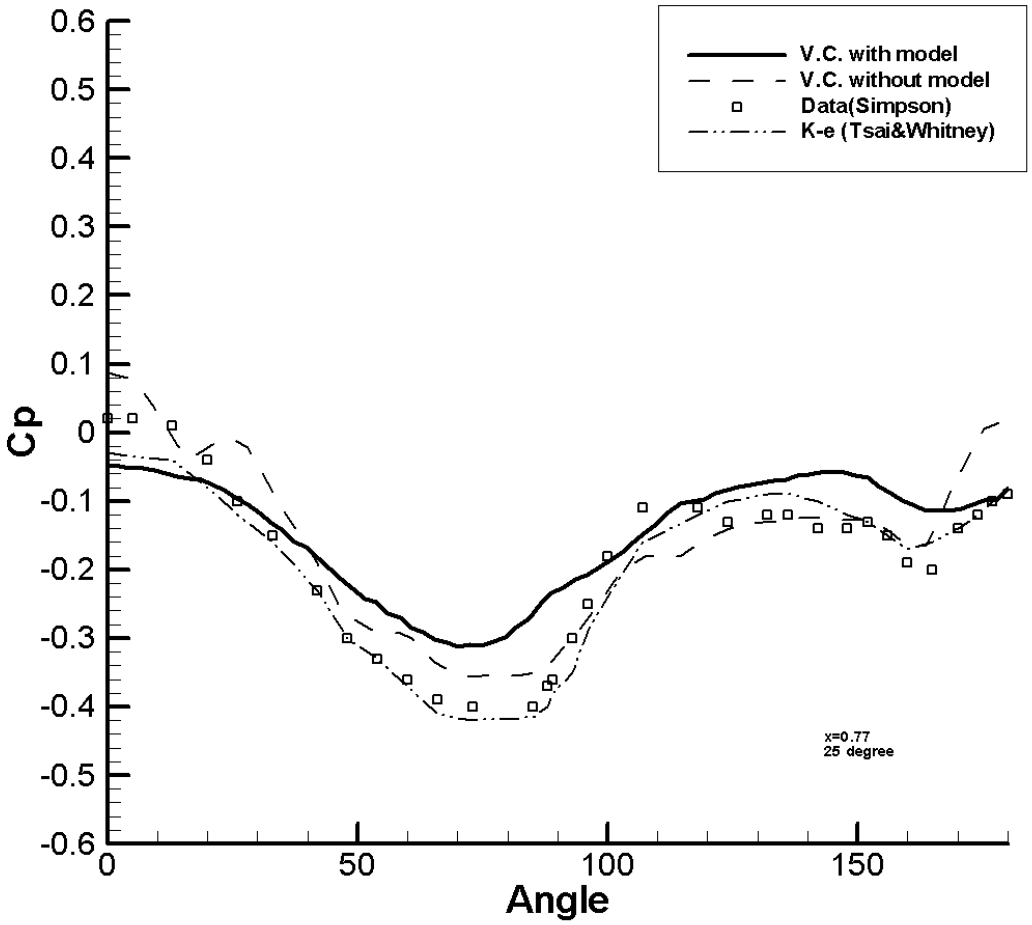

Figure 4-21. Pressure coefficient, X/L = 0.77, 25° incidence, with surface model.

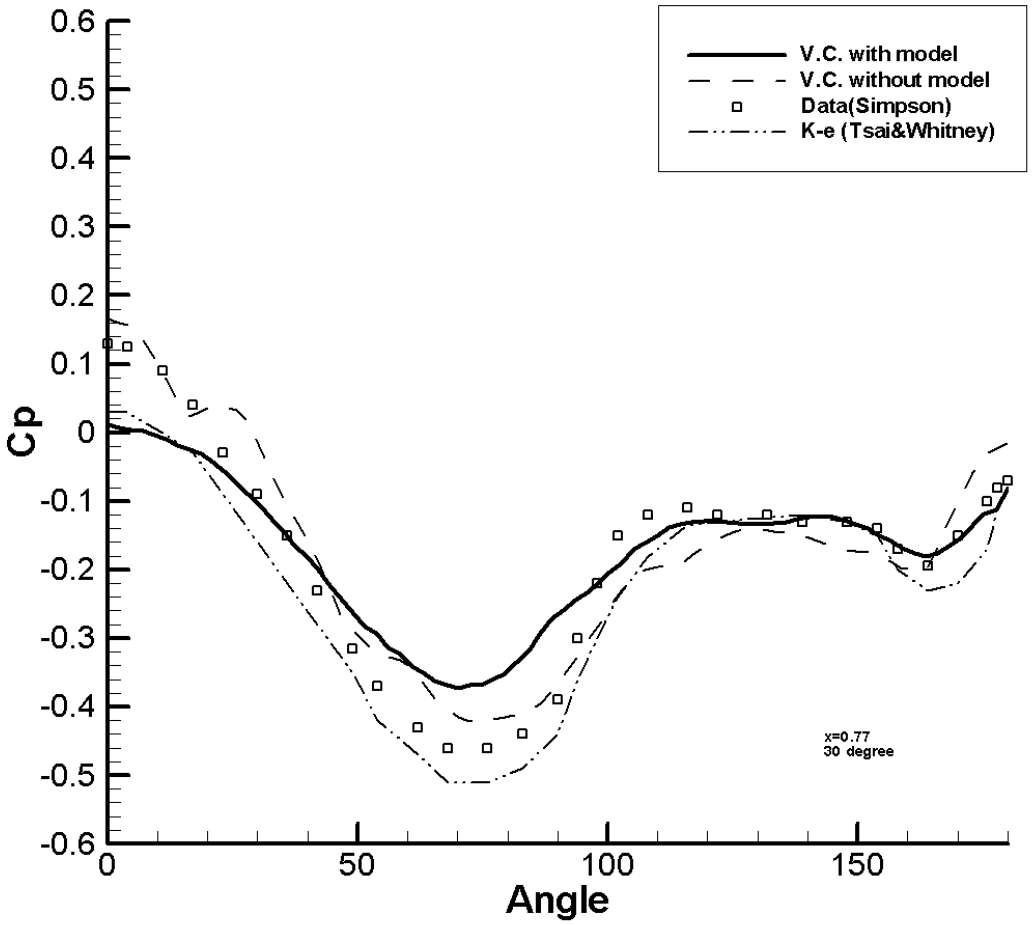

Figure 4-22. Pressure coefficient, X/L = 0.77, 30° incidence, with surface model.

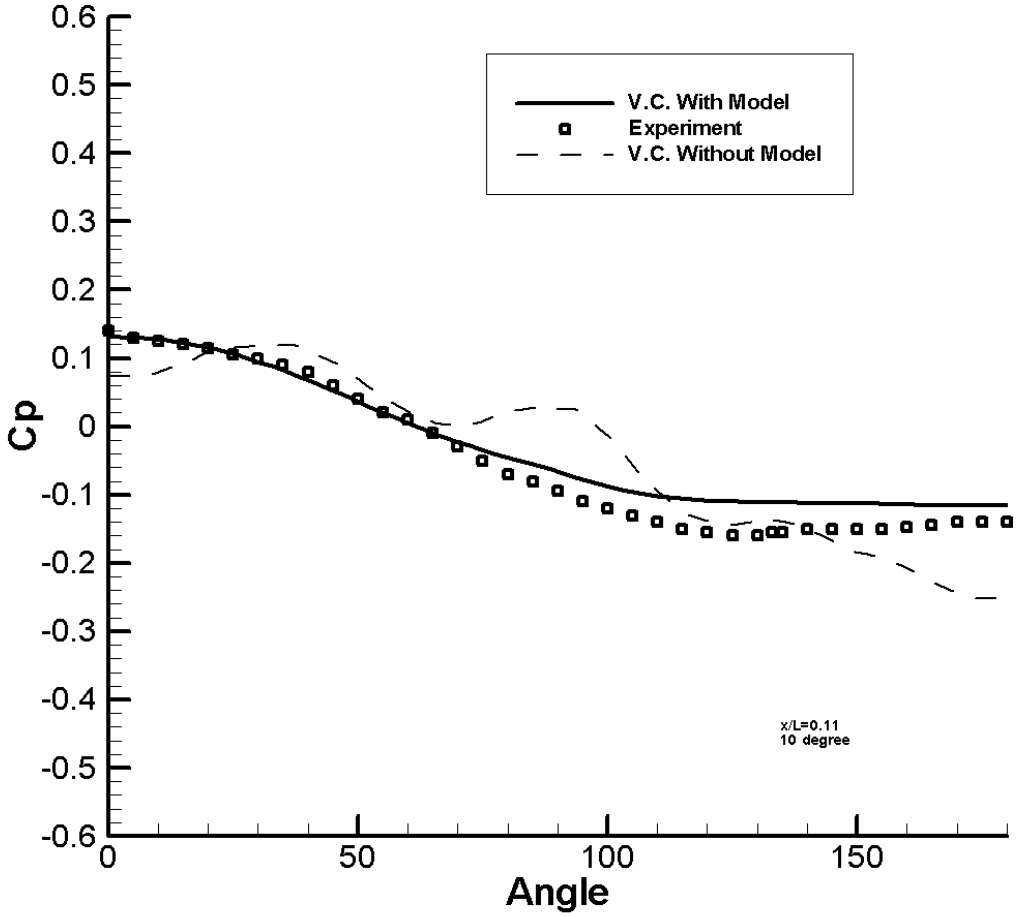

Figure 4-23. Pressure coefficient, X/L = 0.11, 10° incidence, with surface model.

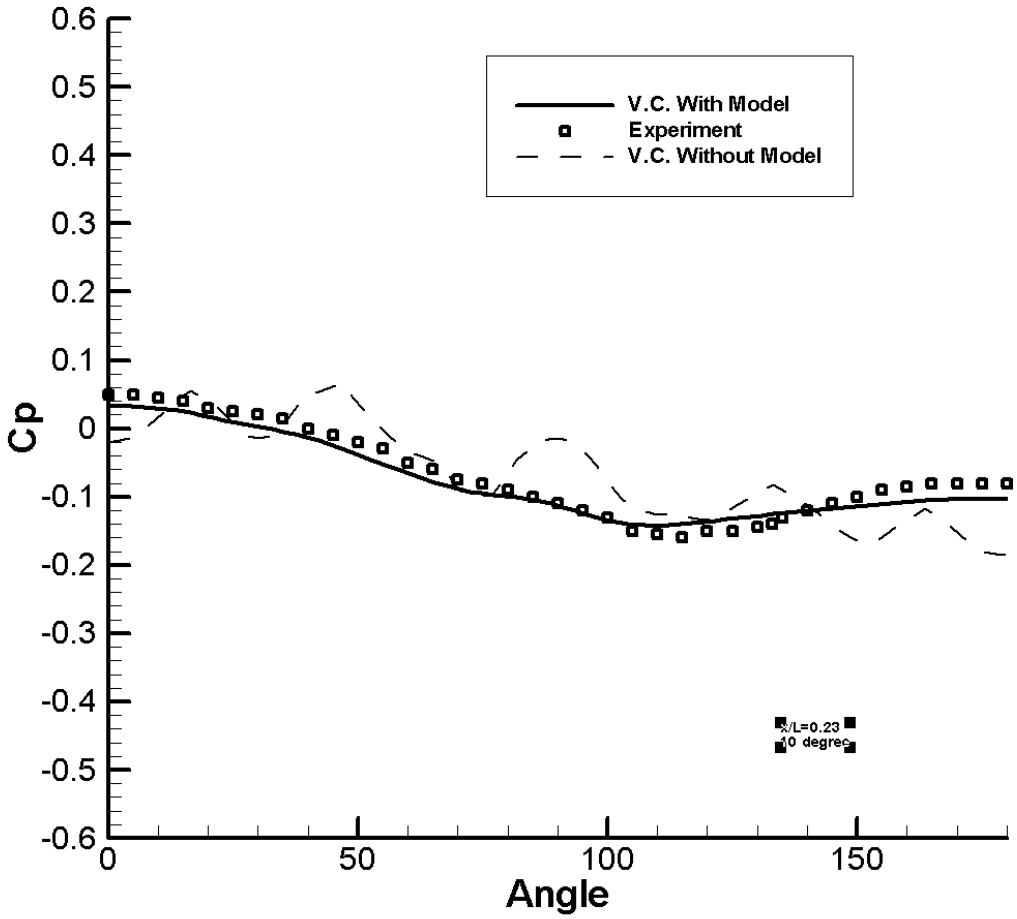

Figure 4-24. Pressure coefficient, X/L = 0.23, 10° incidence, with surface model.

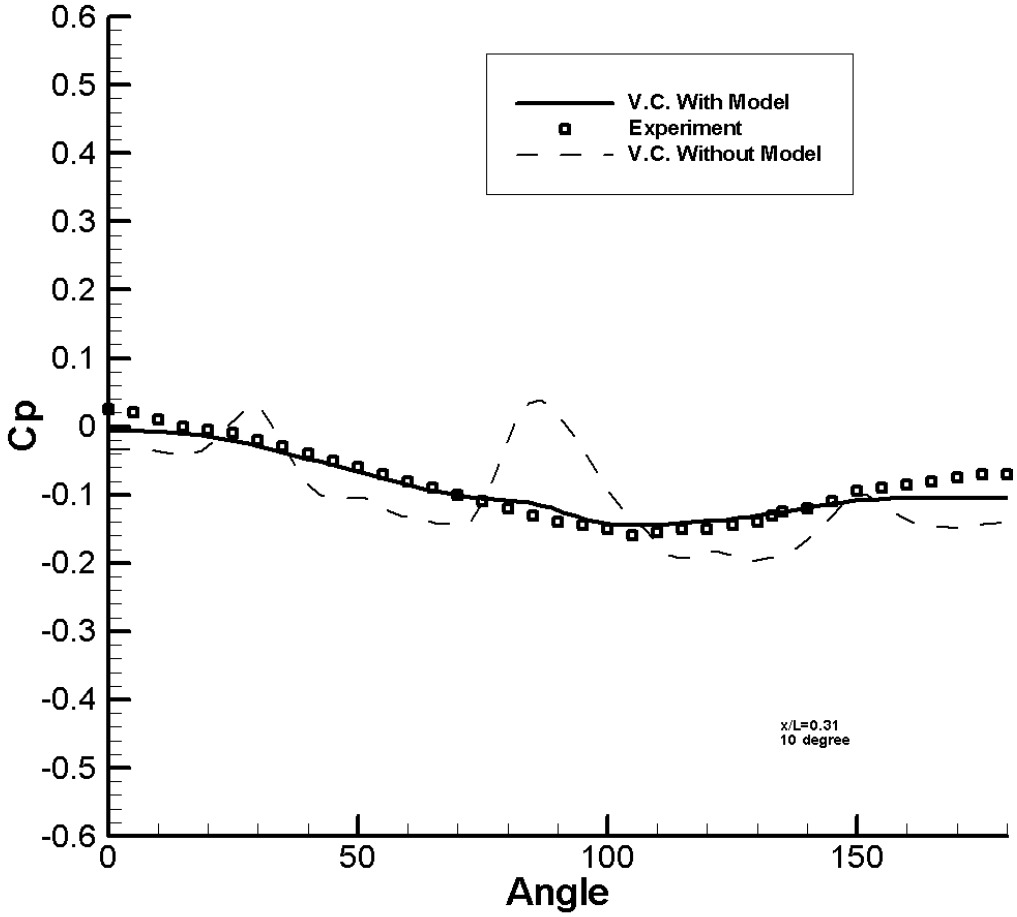

Figure 4-25. Pressure coefficient, X/L = 0.31, 10° incidence, with surface model.

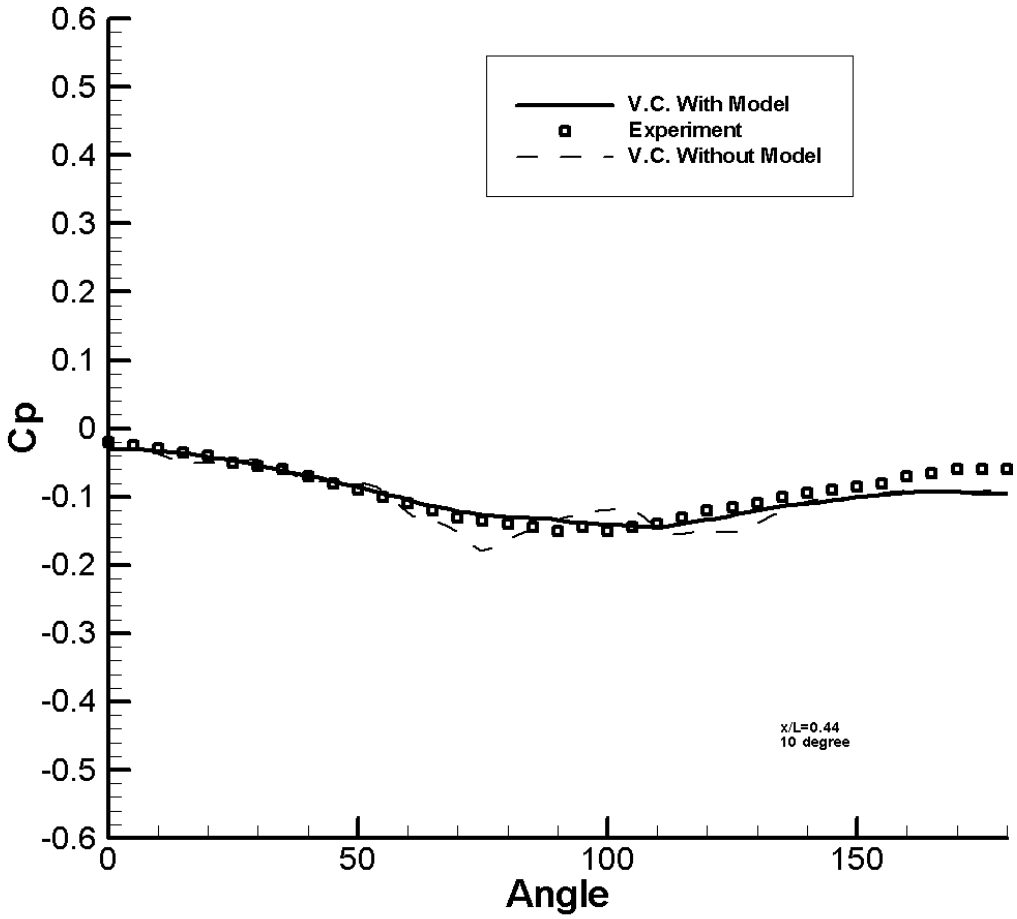

Figure 4-26. Pressure coefficient, X/L = 0.44, 10° incidence, with surface model.

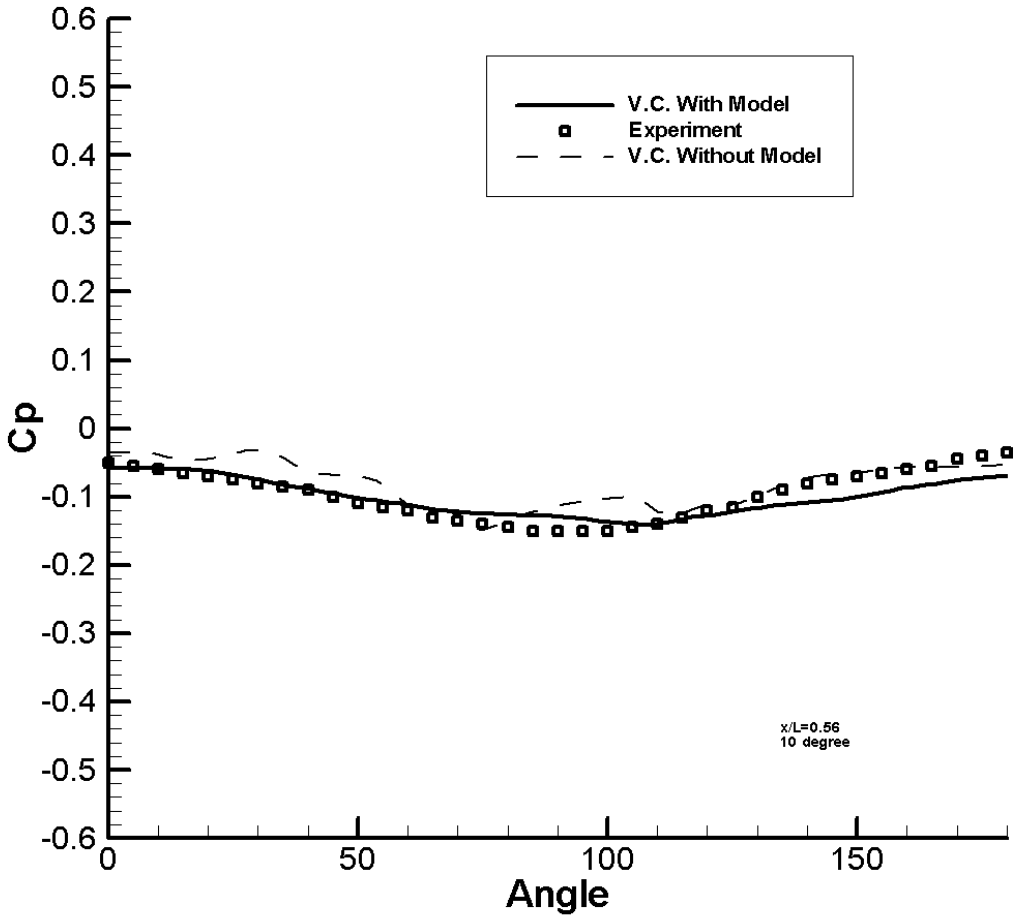

Figure 4-27. Pressure coefficient, X/L = 0.56, 10° incidence, with surface model.

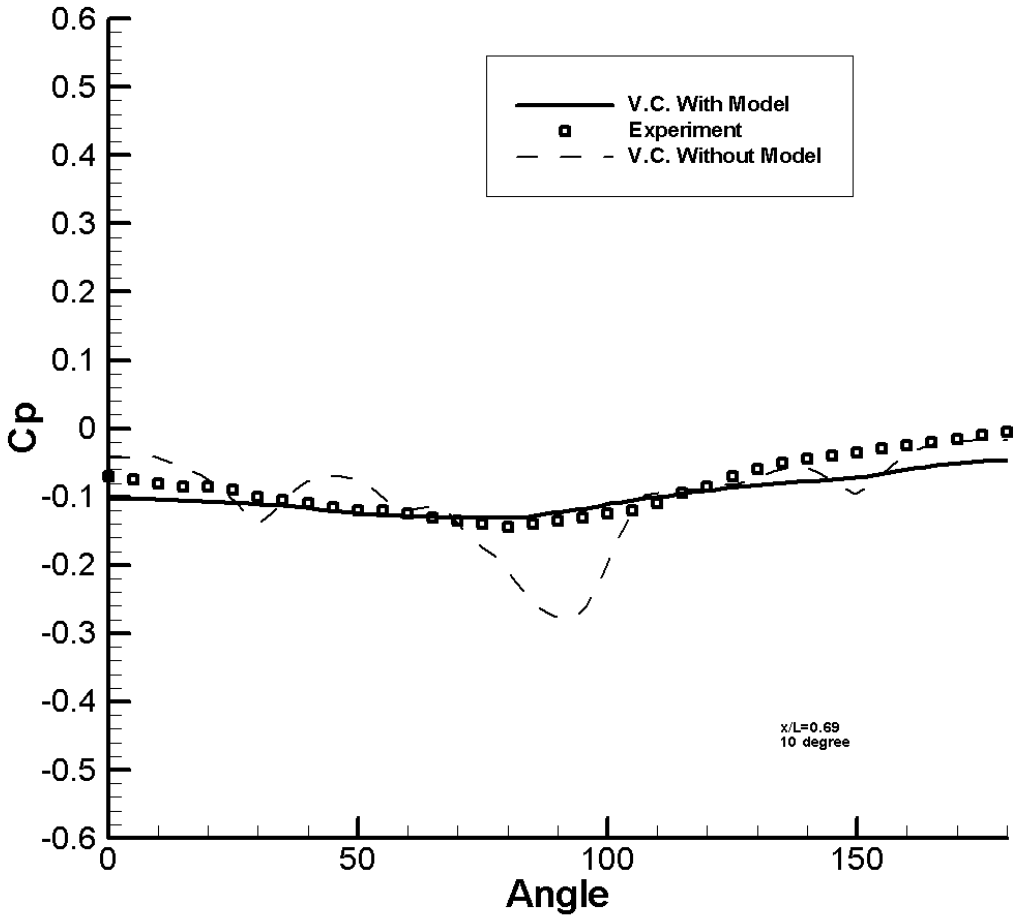

Figure 4-28. Pressure coefficient, X/L = 0.69, 10° incidence, with surface model.

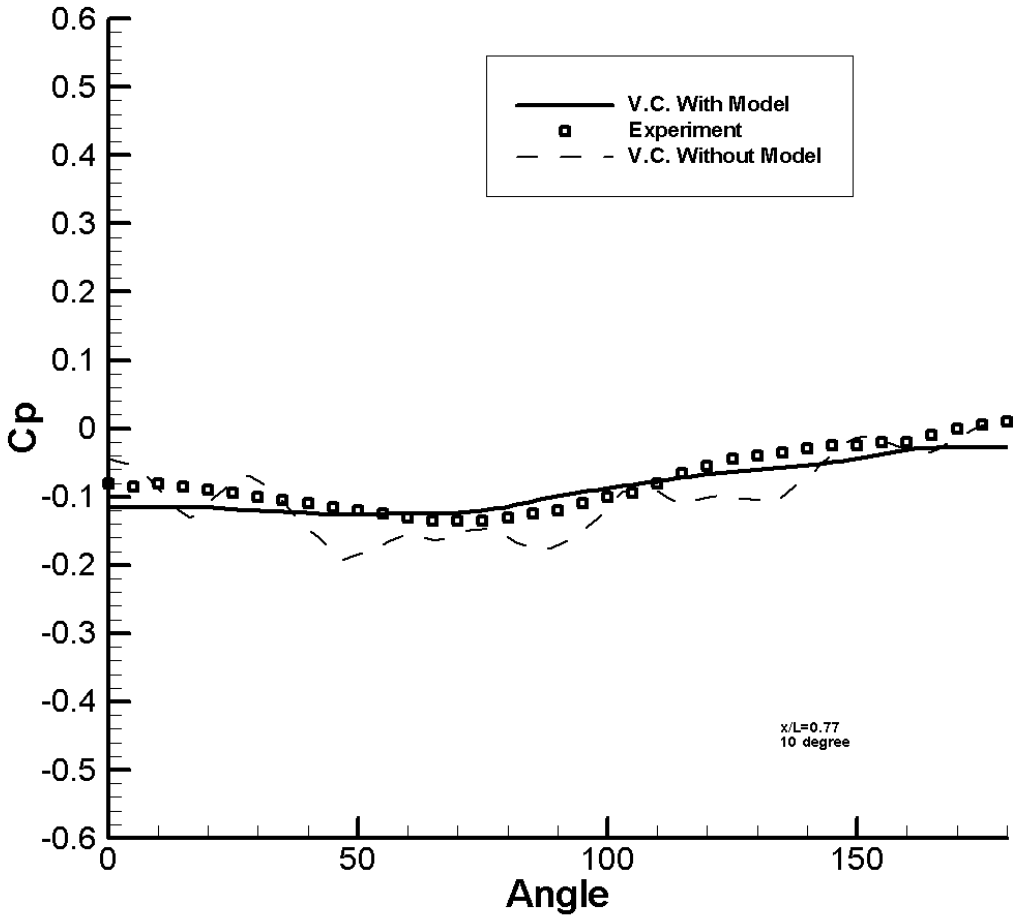

Figure 4-29. Pressure coefficient, X/L = 0.7725, 10° incidence, with surface model.

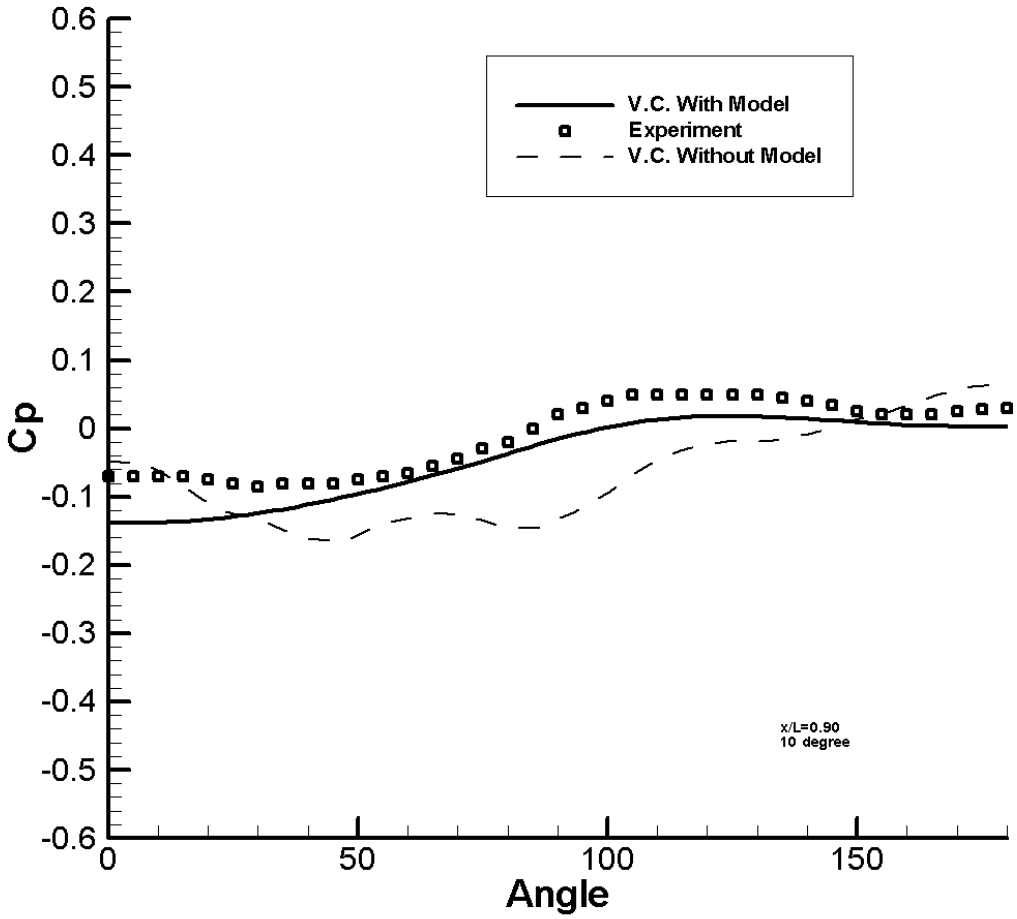

Figure 4-30. Pressure coefficient, X/L = 0.90, 10° incidence, with surface model.

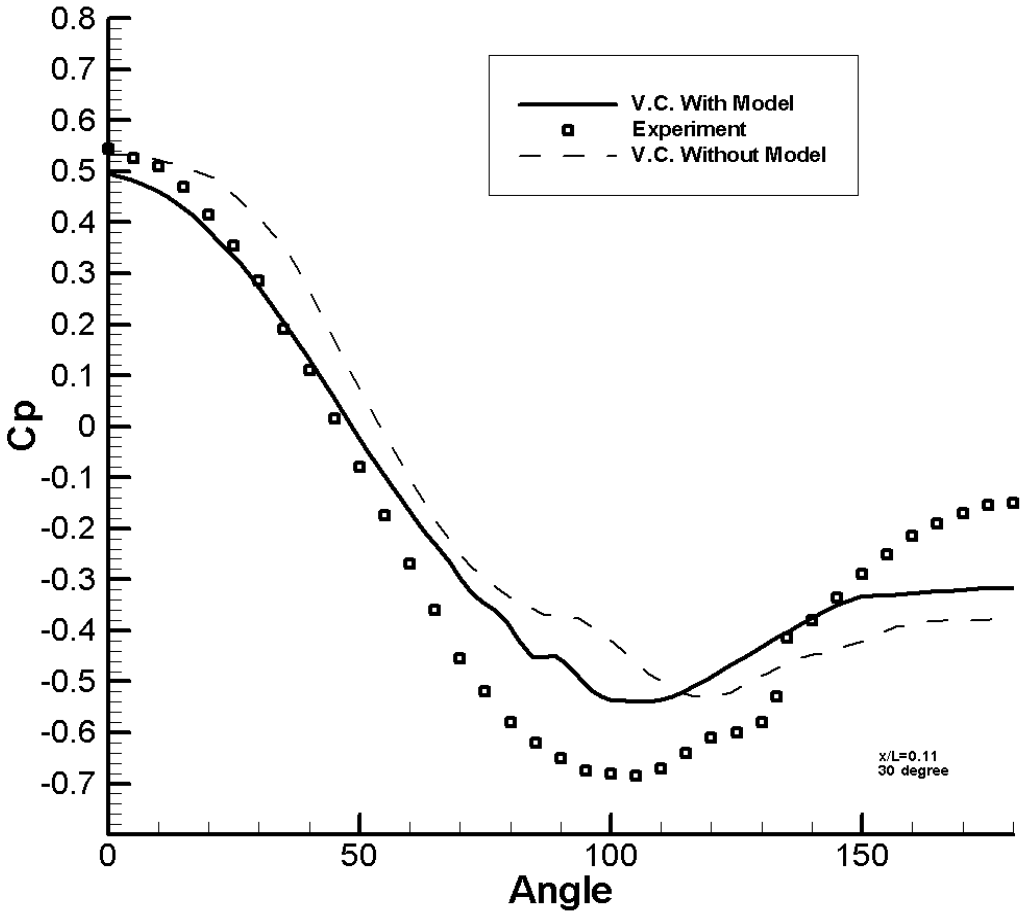

Figure 4-31. Pressure coefficient, X/L = 0.11, 30° incidence, with surface model.

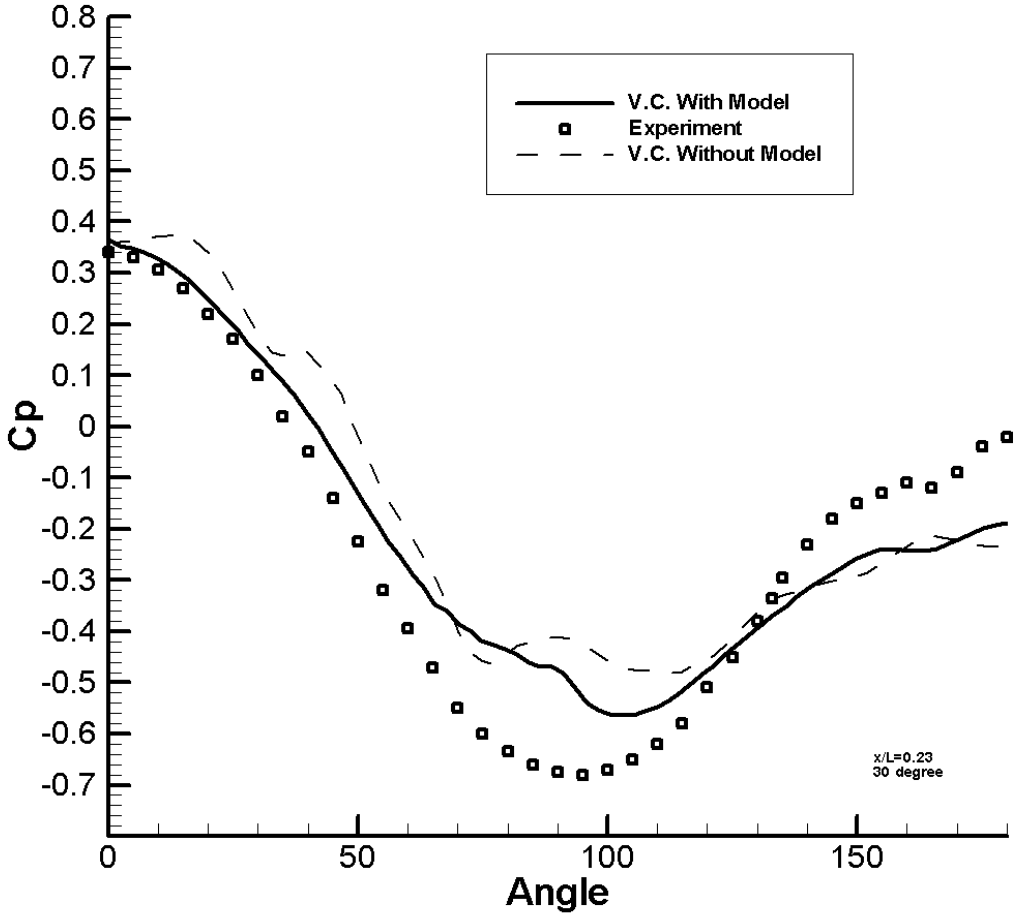

Figure 4-32. Pressure coefficient, X/L = 0.23, 30° incidence, with surface model.

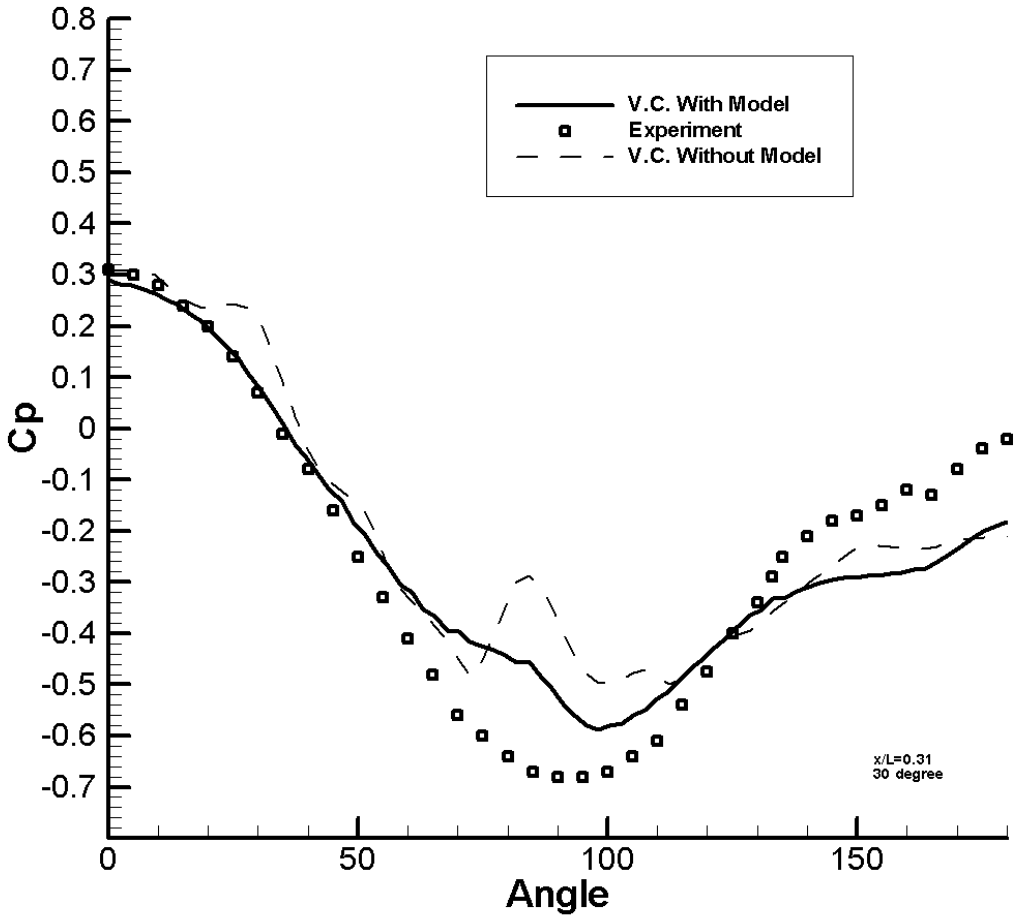

Figure 4-33. Pressure coefficient, X/L = 0.31, 30° incidence, with surface model.

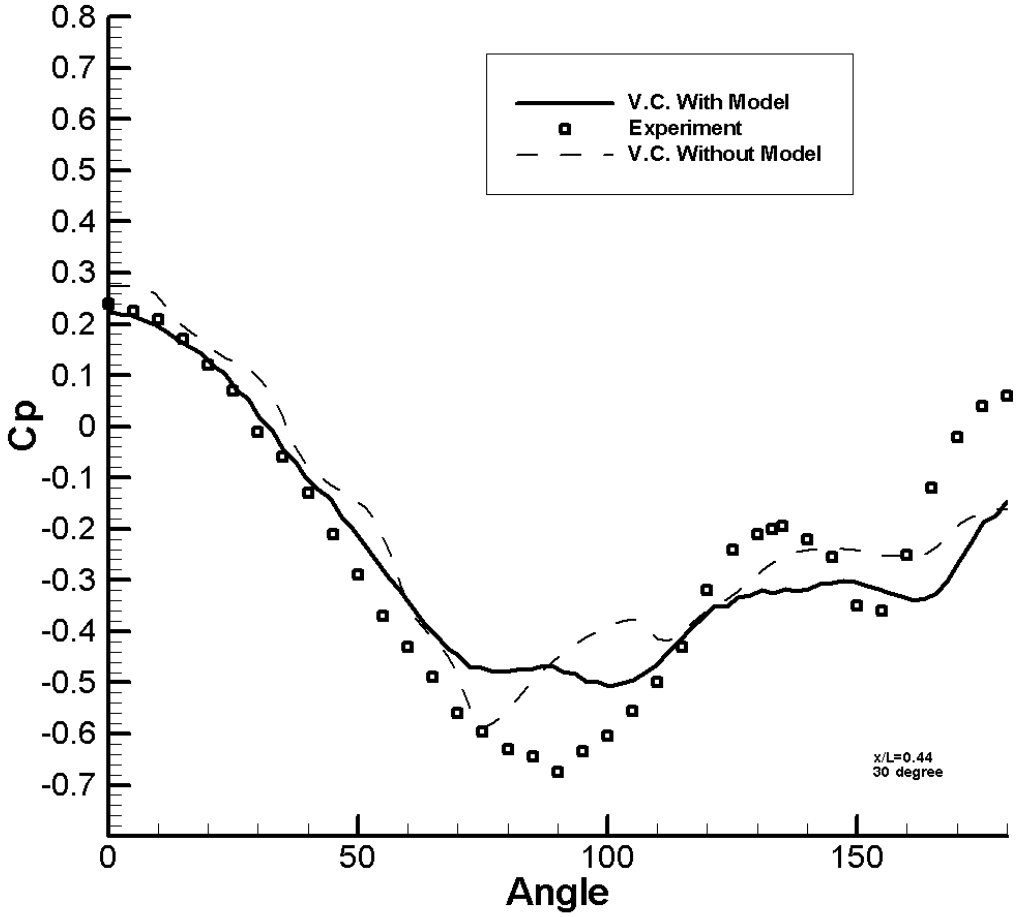

Figure 4-34. Pressure coefficient, X/L = 0.44, 30° incidence, with surface model.

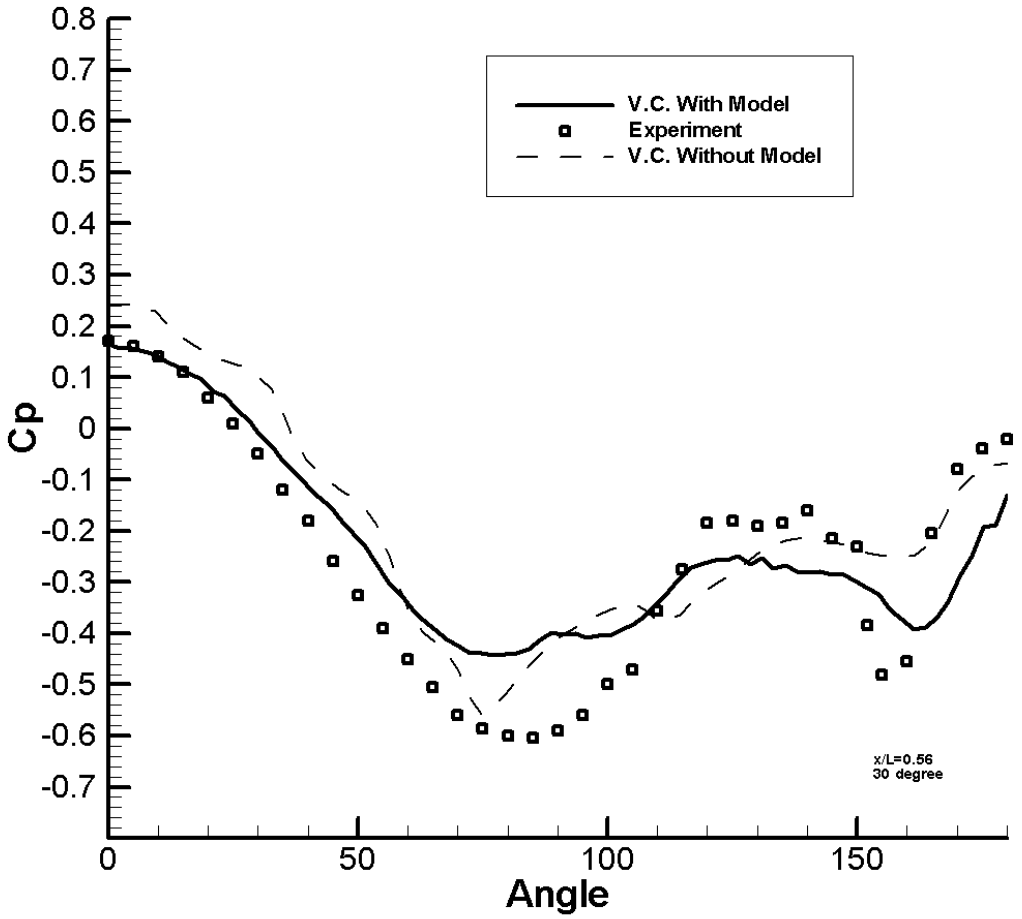

Figure 4-35. Pressure coefficient, X/L = 0.56, 30° incidence, with surface model.

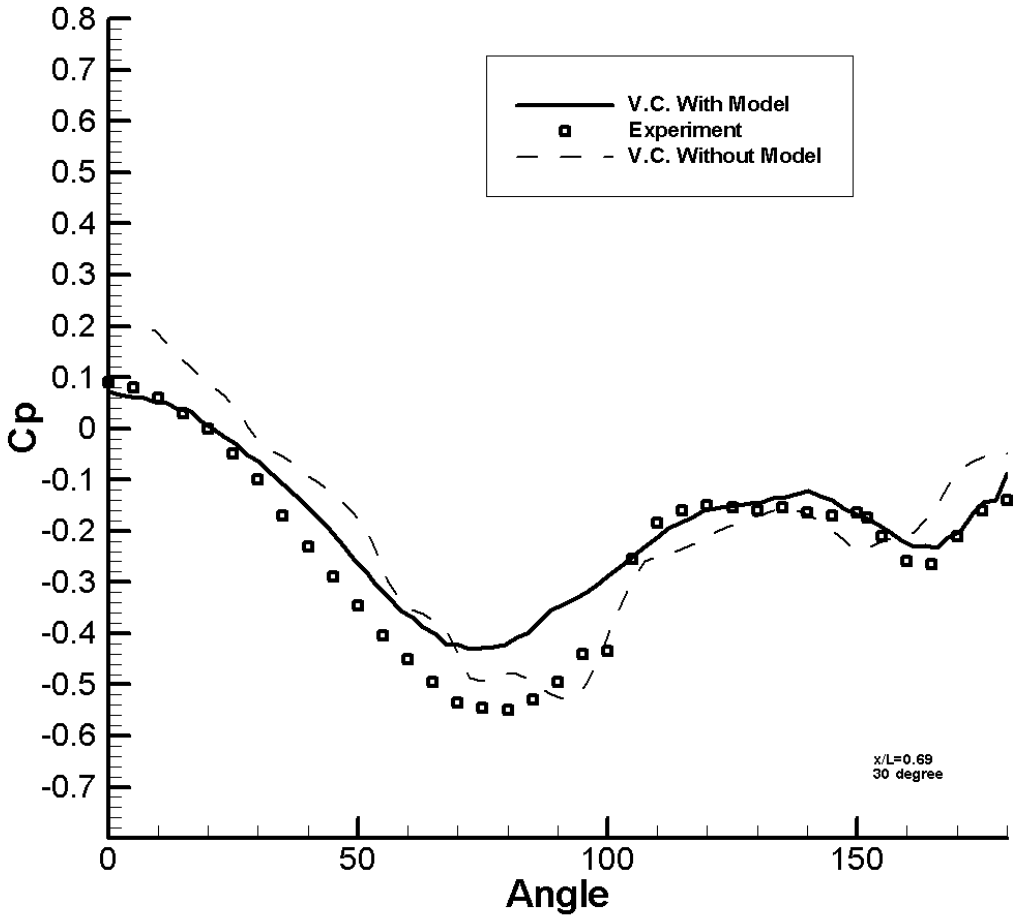

Figure 4-36. Pressure coefficient, X/L = 0.69, 30° incidence, with surface model.

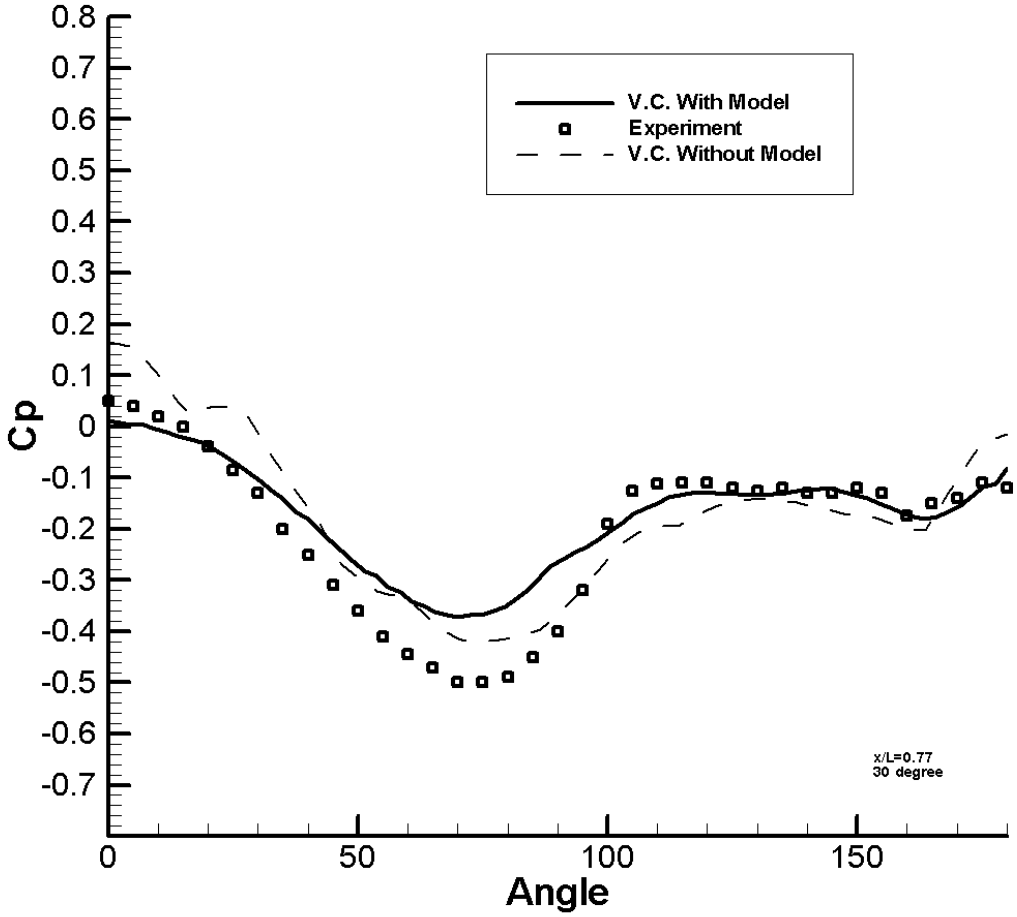

Figure 4-37. Pressure coefficient, X/L = 0.7725, 30° incidence, with surface model.

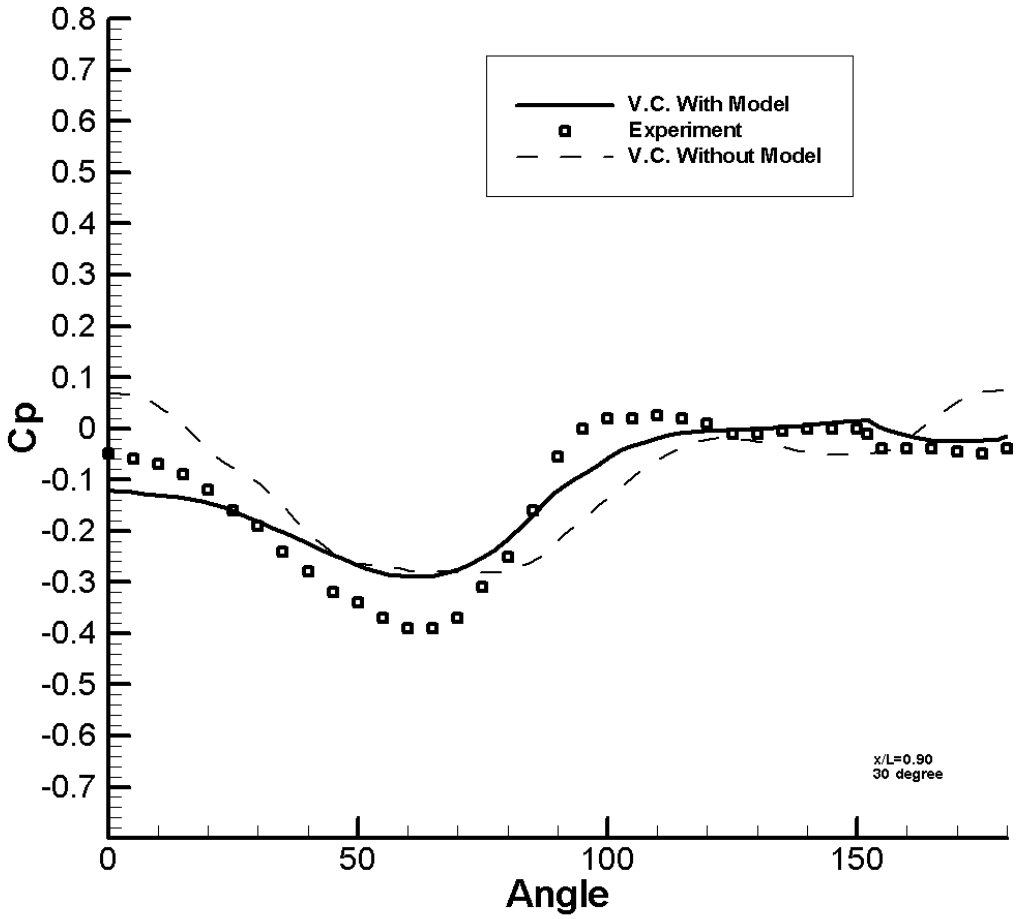

Figure 4-38. Pressure coefficient, X/L = 0.90, 30° incidence, with surface model.

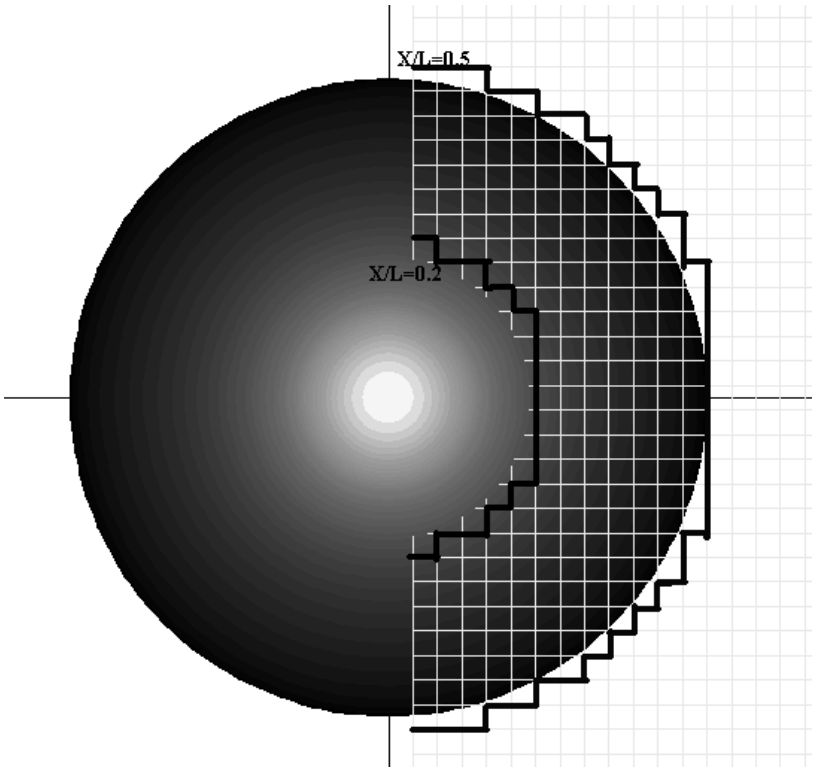

Figure 4-39. Jagged definition of the ellipsoid surface for uniform Cartesian grid

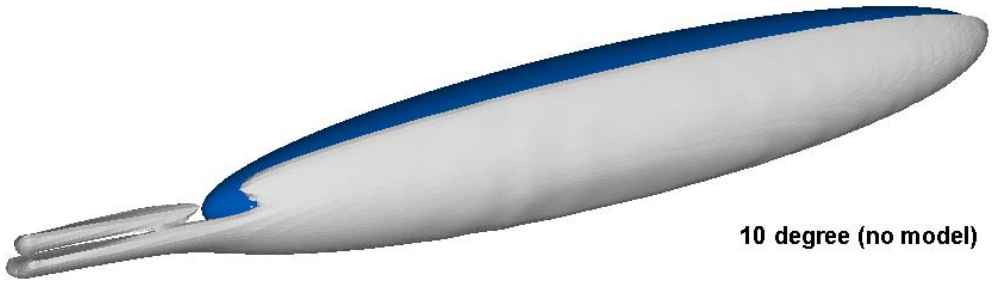

Figure 4-40. Vorticity iso-surface, 10° incidence, without surface model.

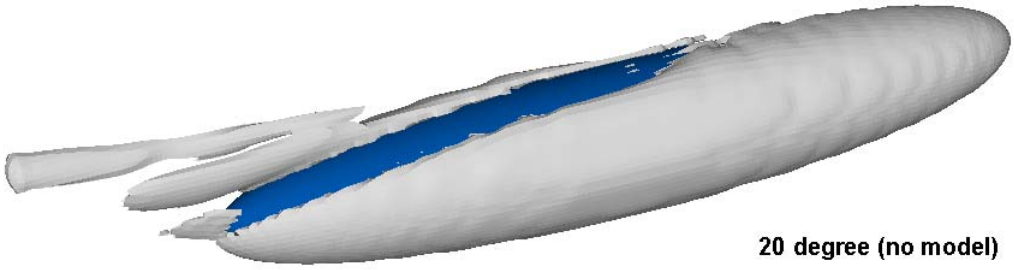

Figure 4-41. Vorticity iso-surface, 20° incidence, without surface model.

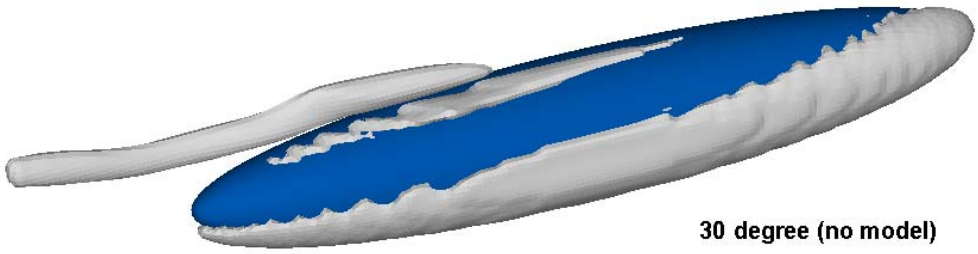

Figure 4-42. Vorticity iso-surface, 30° incidence, without surface model.

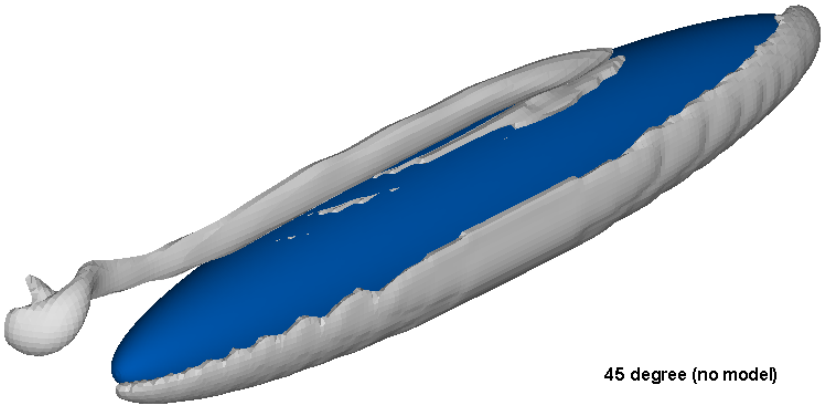

Figure 4-43. Vorticity iso-surface, 45° incidence, without surface model.

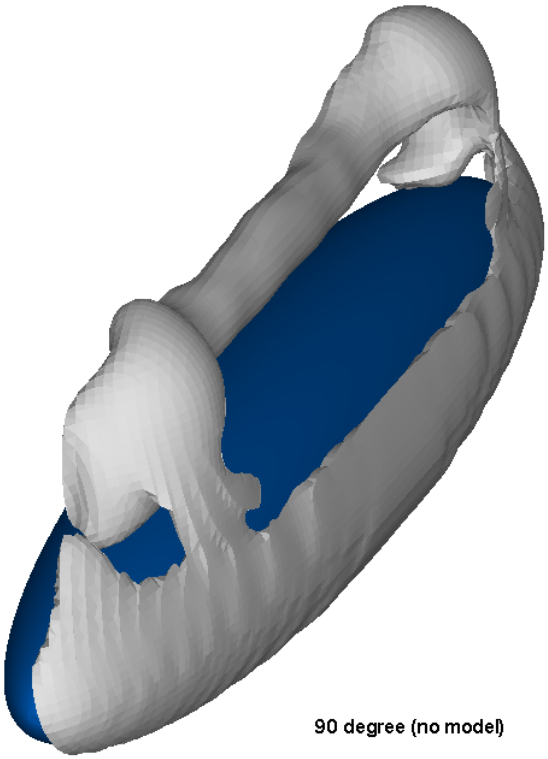

Figure 4-44. Vorticity iso-surface, 90° incidence, without surface model.

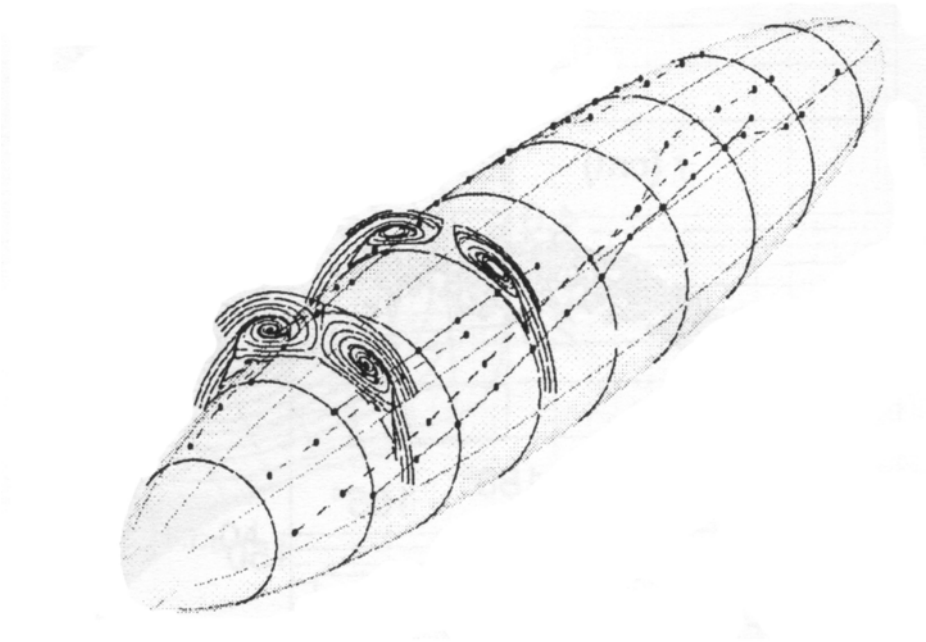

Figure 4-45. Cross flow separation on a 6:1 ellipsoid, X/L = 0.6 and 0.77, 20° incidence. (From Wetzel *et al* [10].)

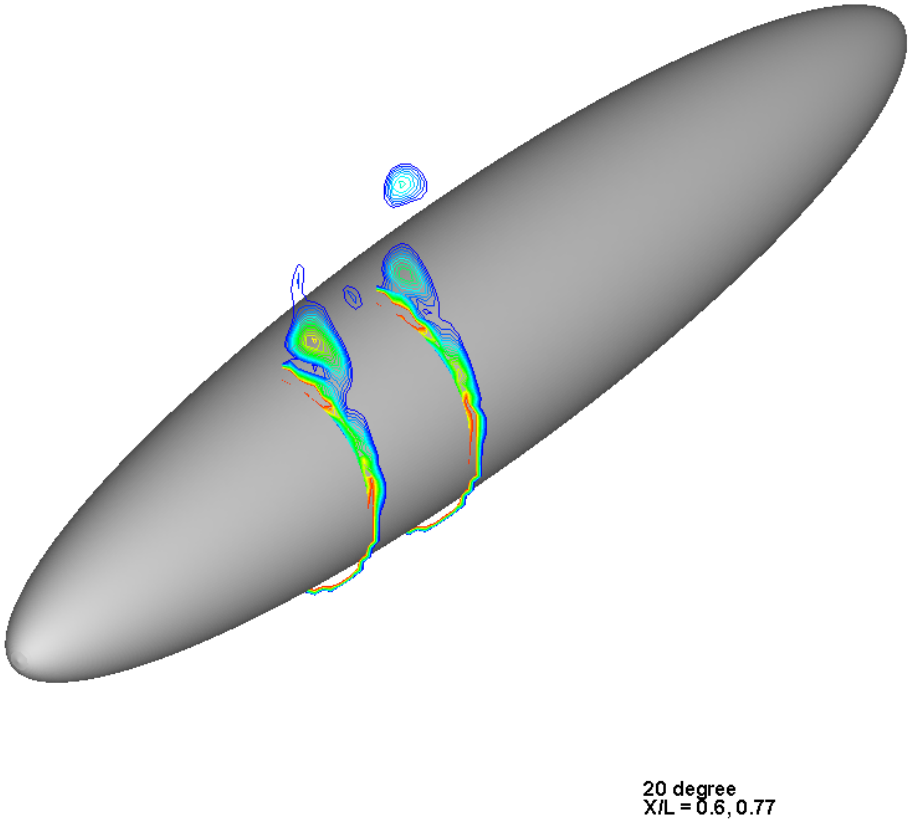

Figure 4-46. Vorticity contours, X/L = 0.6 and 0.77, 20° incidence, with surface model.

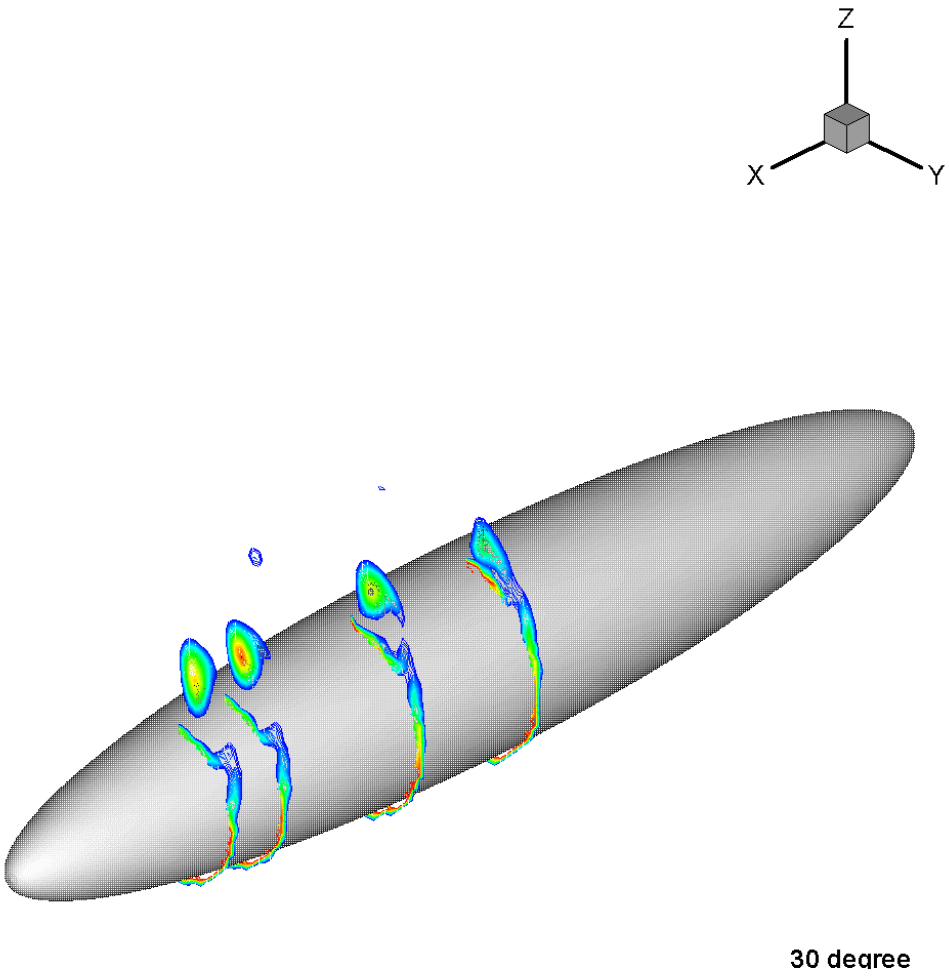

Figure 4-47. Cross plane vorticity contours, 30° incidence, with surface model.

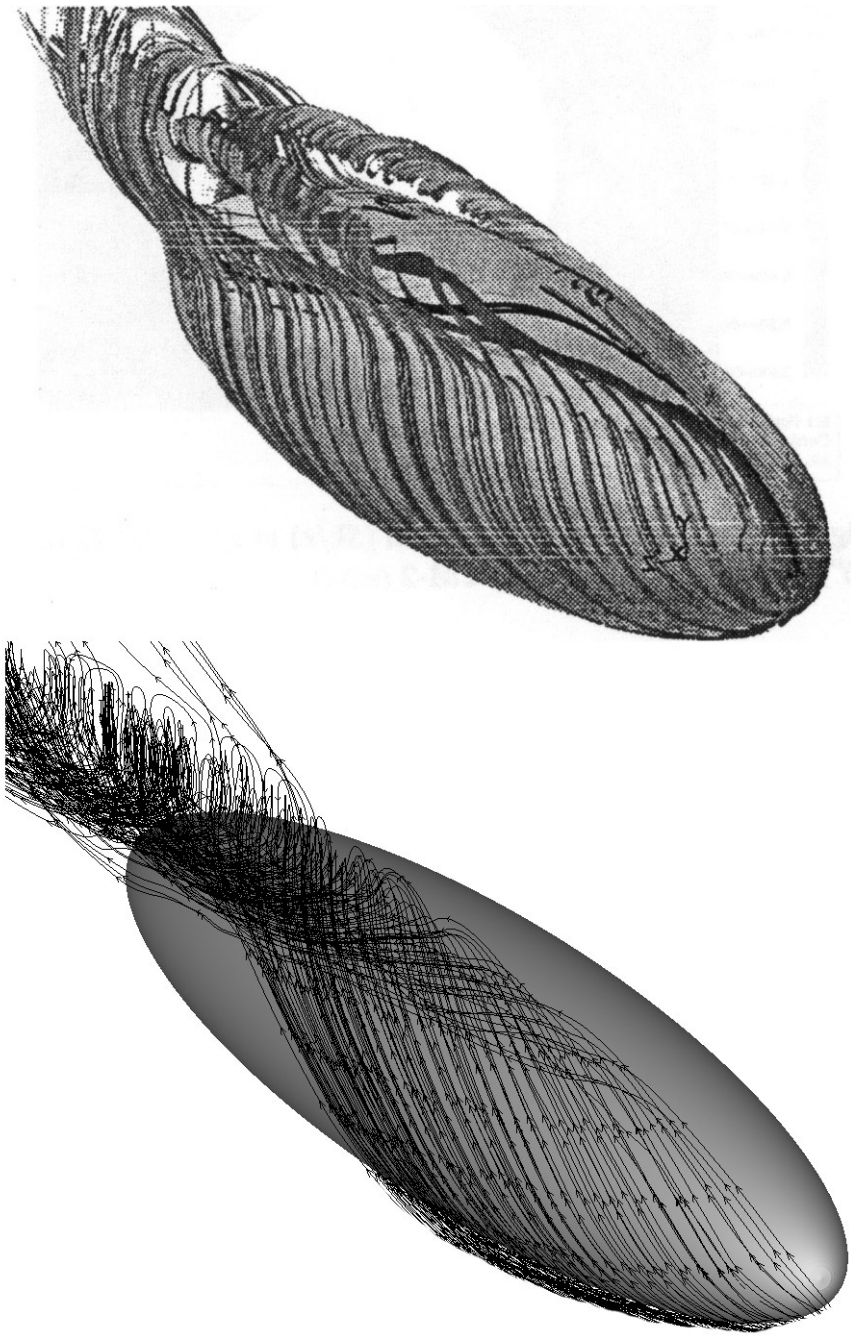

Figure 4-48. Cross-flow separation, 30° incidence, with surface model.
(Compared to plots (top) from S. Kim&S. Rhee [5].)

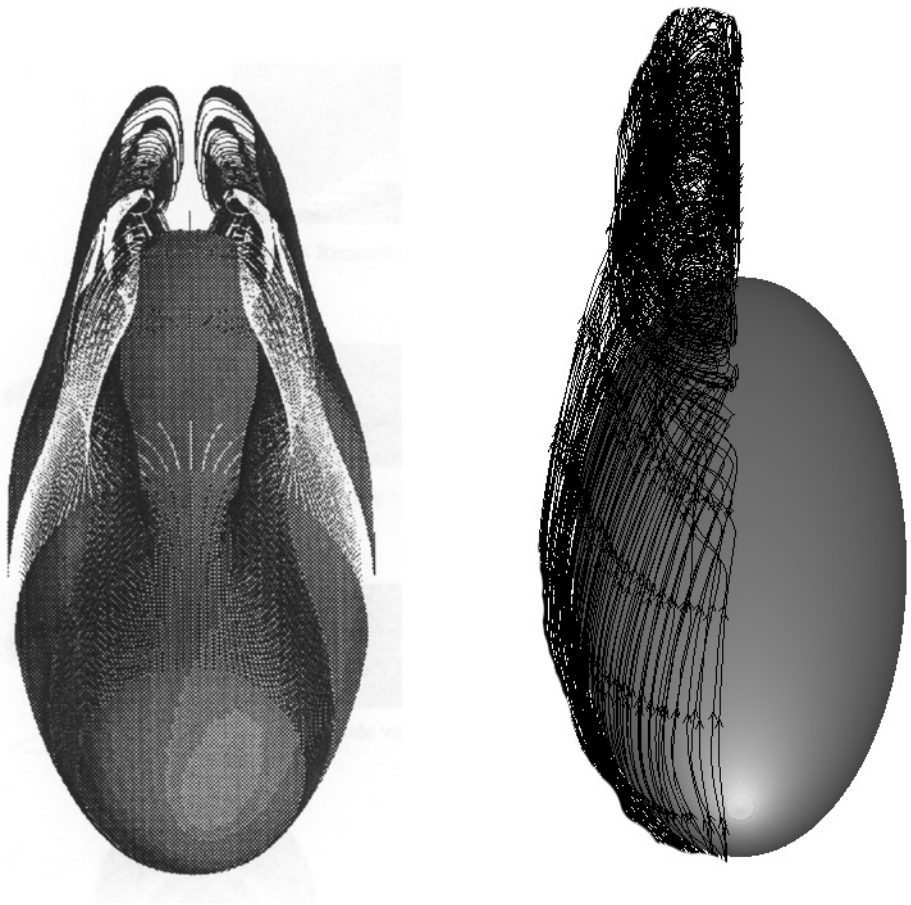

Figure 4-49. Front view of cross-flow separation, 30° incidence, with surface model. (Compared to plots (left) from Tsai & Whitney [4].)

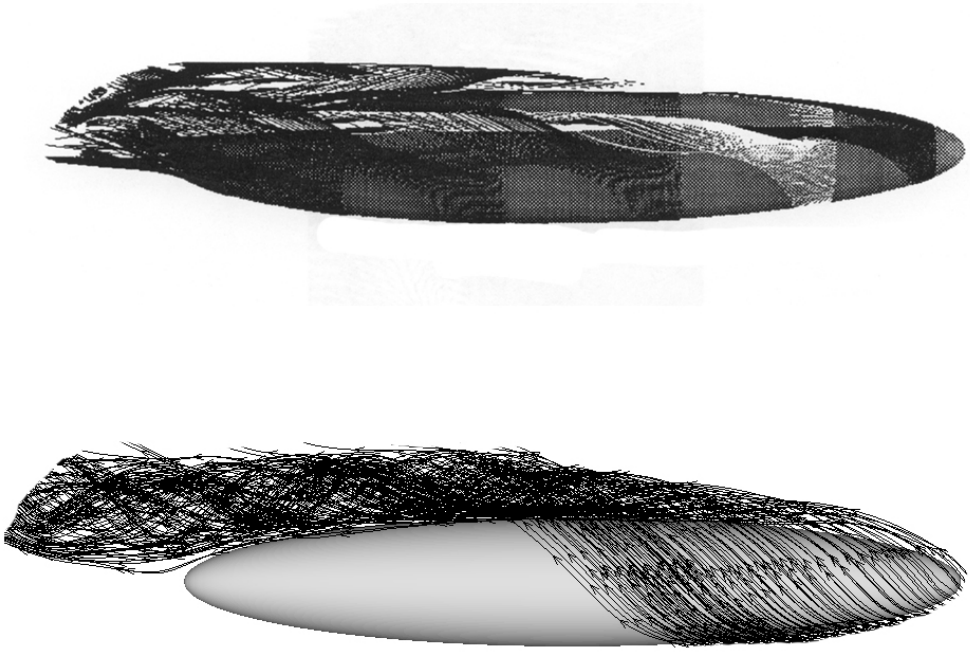

Figure 4-50. Side view of cross-flow separation, 30° incidence, with surface model. (Compared to plots (top) from Tsai & Whitney [4].)

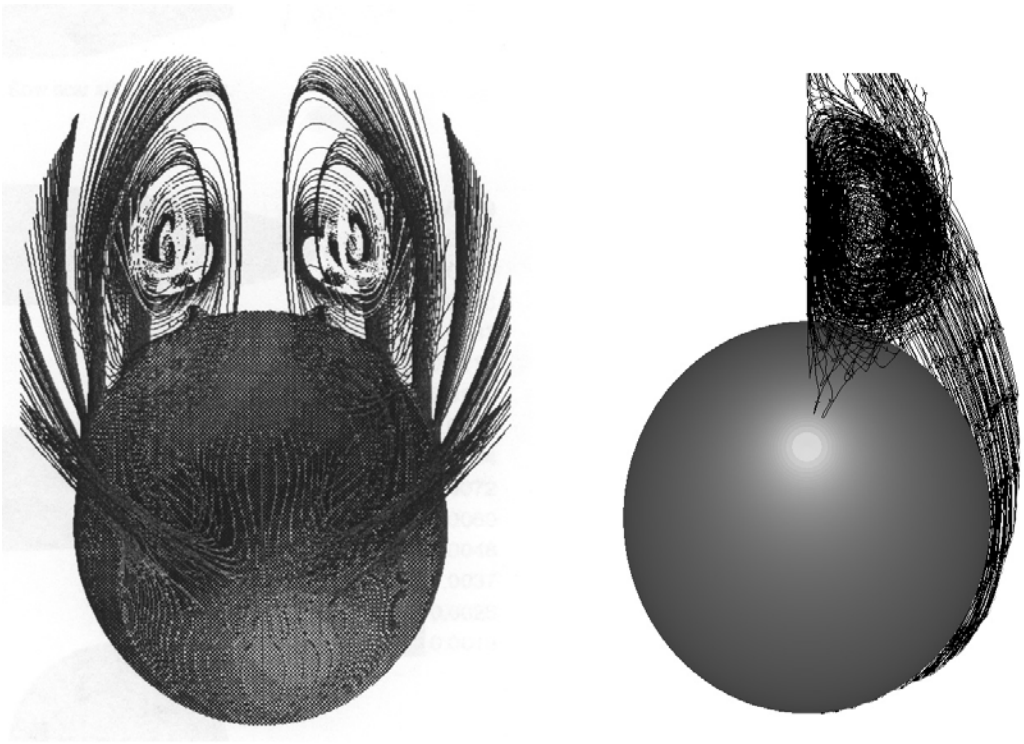

Figure 4-51. Rear view of cross-flow separation, 30° incidence, with surface model. (Compared to plots (left) from Tsai & Whitney [4].)

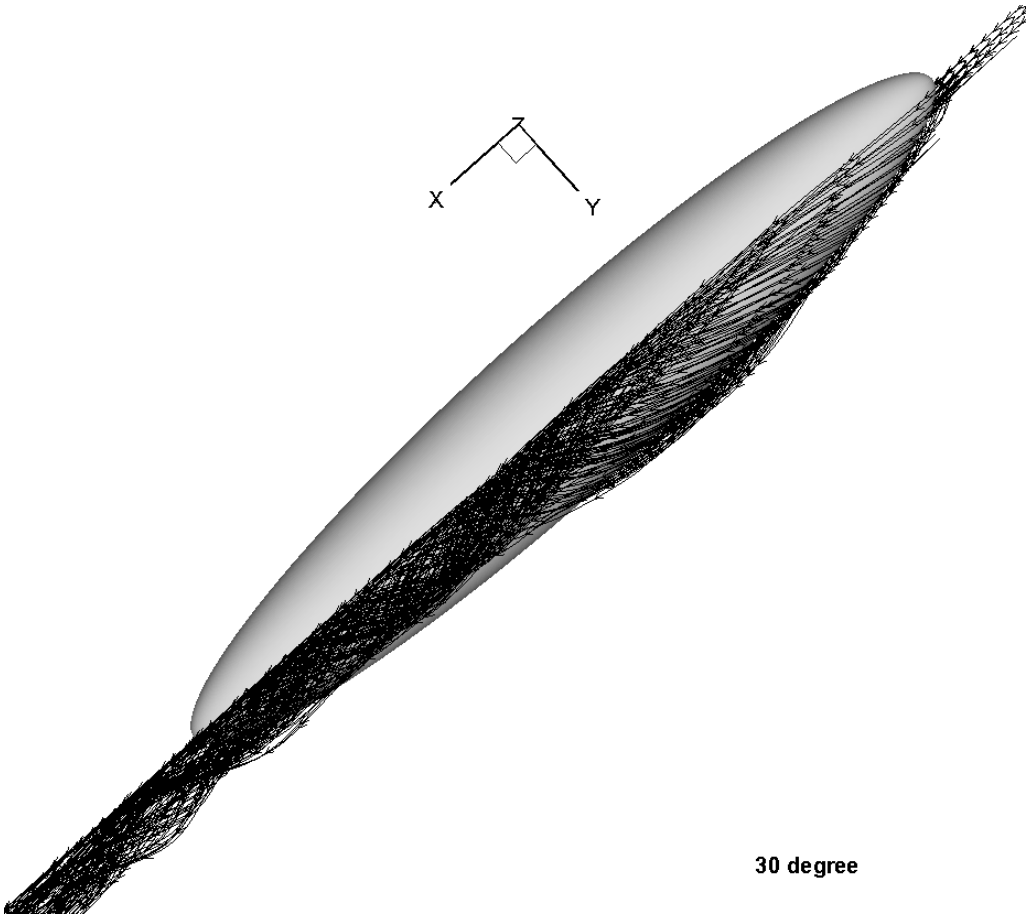

Figure 4-52. Overhead view of cross-flow separation, 30° incidence, with surface model.

Figure 4-53. Vorticity iso-surface, 10° incidence, with surface model.

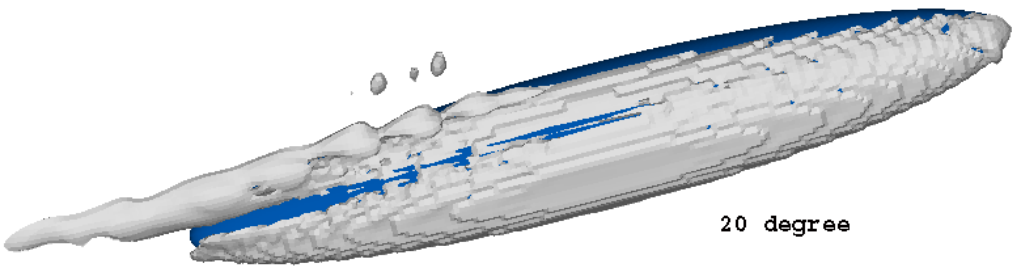

Figure 4-54. Vorticity iso-surface, 20° incidence, with surface model.

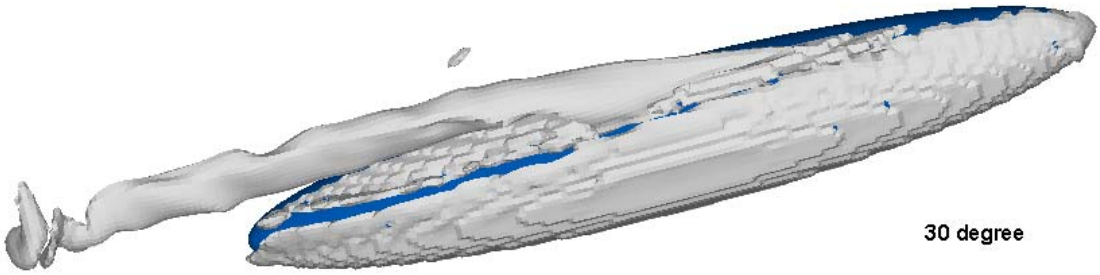

Figure 4-55. Vorticity iso-surface, 30° incidence, with surface model.

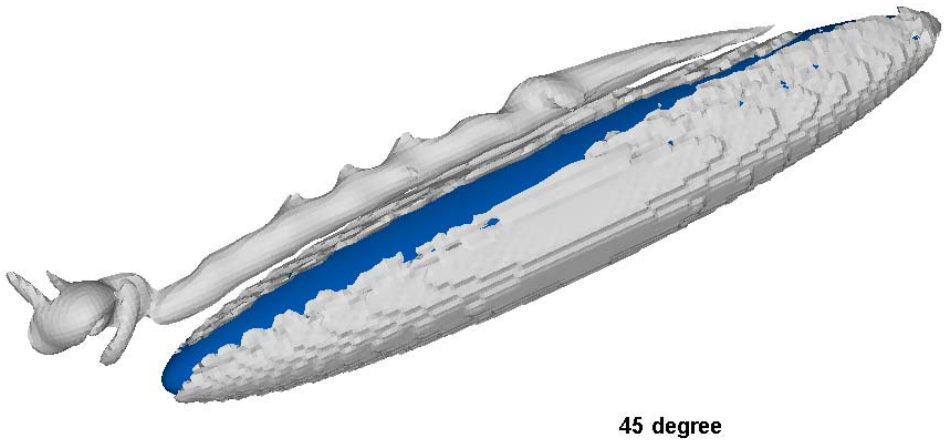

Figure 4-56. Vorticity iso-surface, 45° incidence, with surface model.

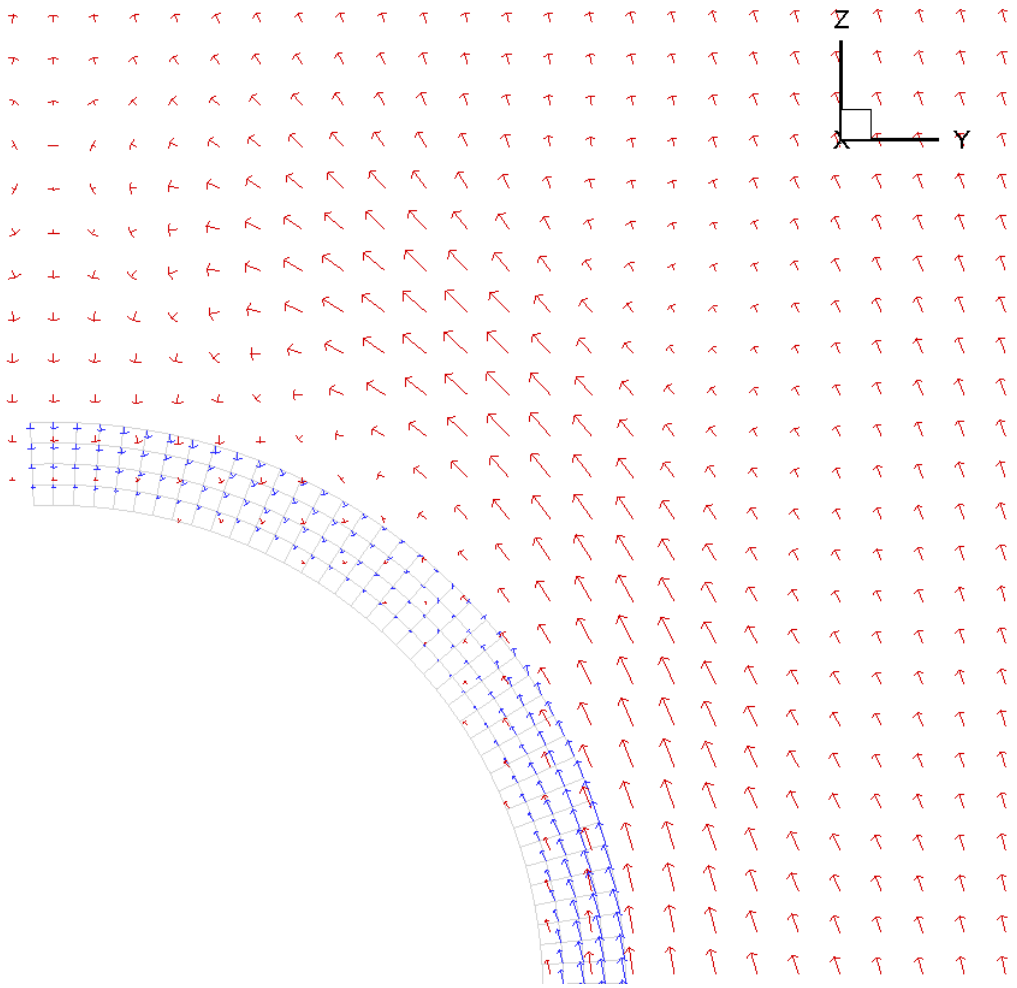

Figure 4-57. Overlapping vector field, X/L = 0.77, 10° incidence, with surface model.

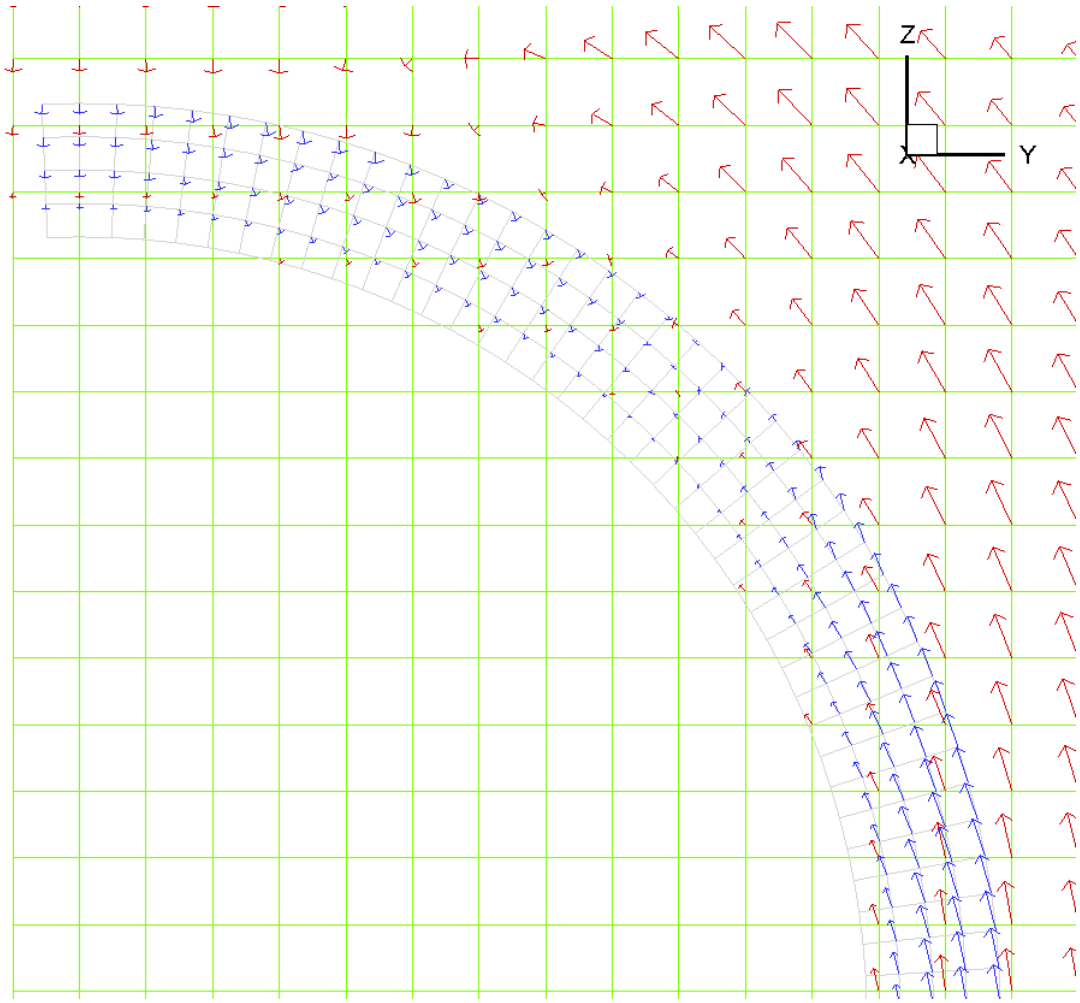

Figure 4-58. Details of overlapping vector field, X/L = 0.77, 10° incidence.

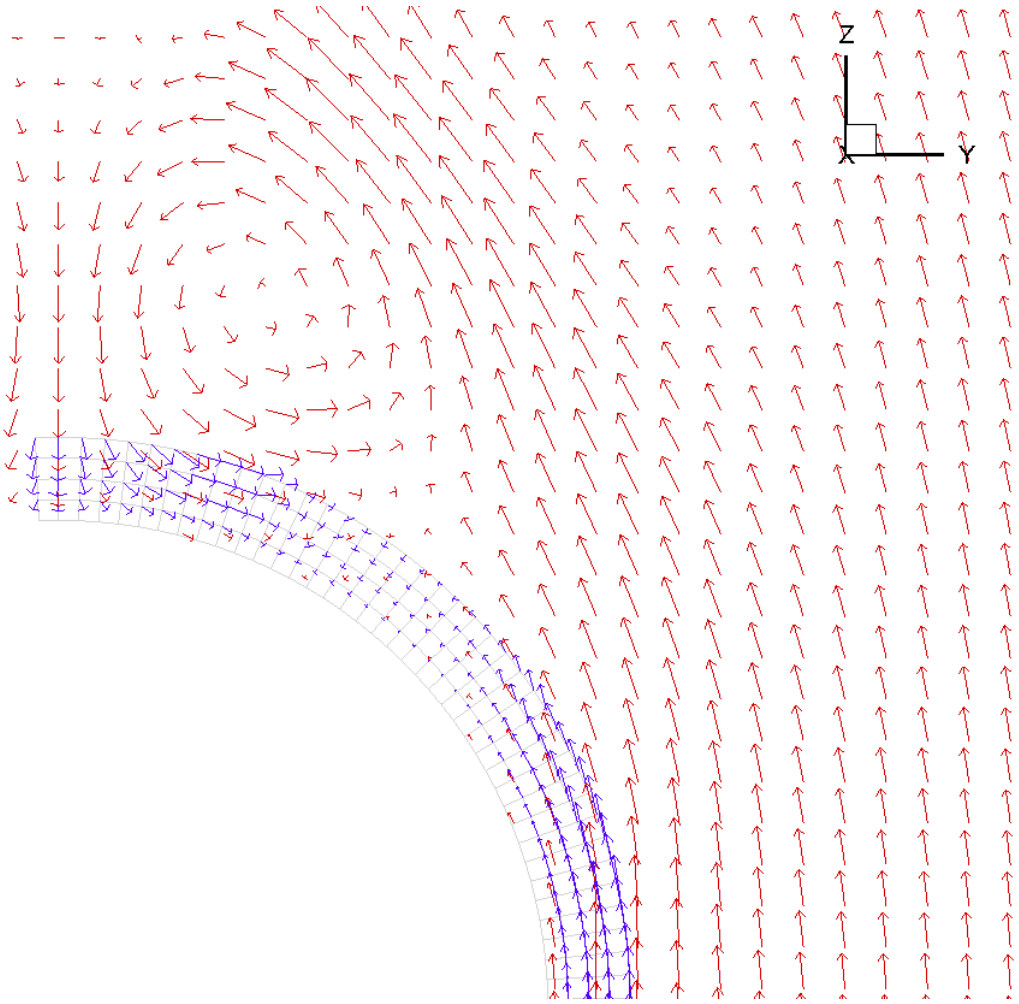

Figure 4-59. Overlapping vector field, X/L = 0.77, 20° incidence, with surface model.

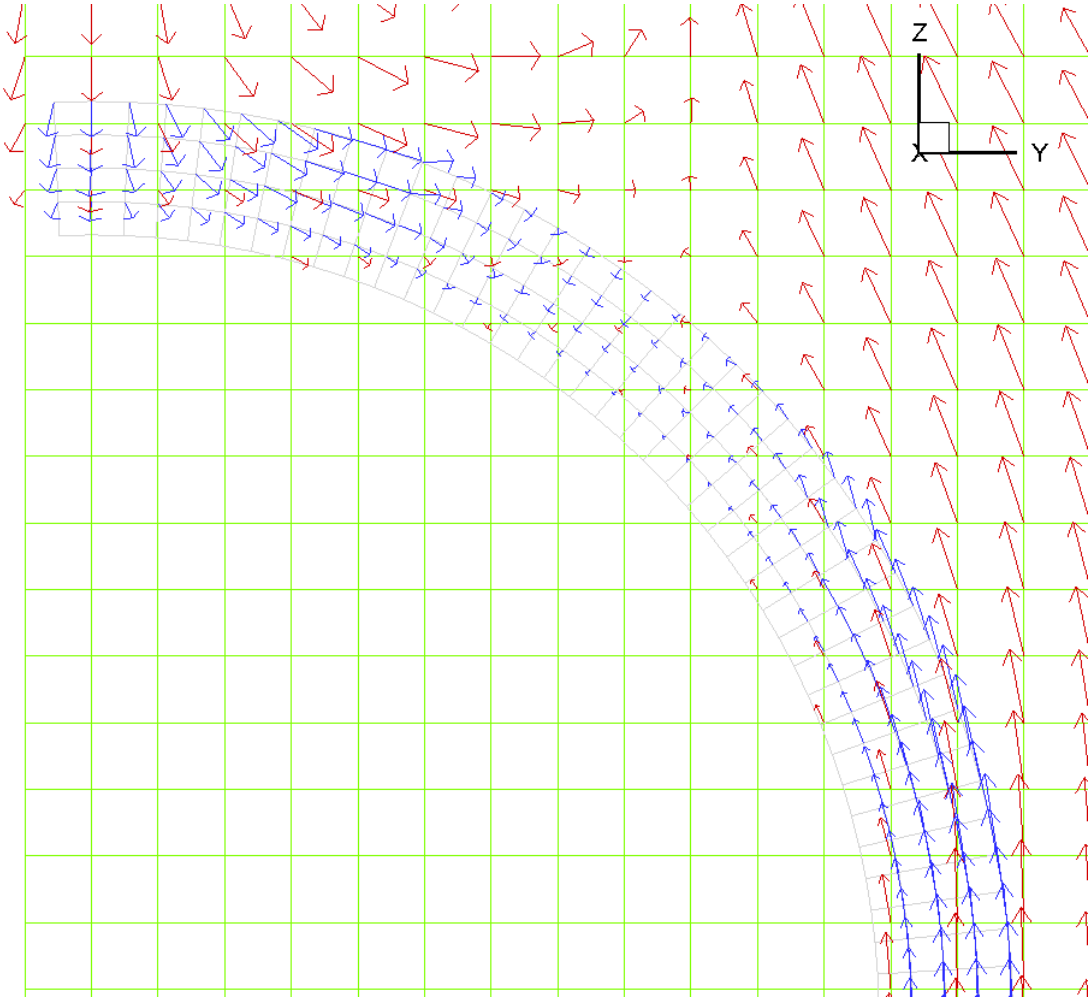

Figure 4-60. Details of overlapping vector field, X/L = 0.77, 20° incidence.

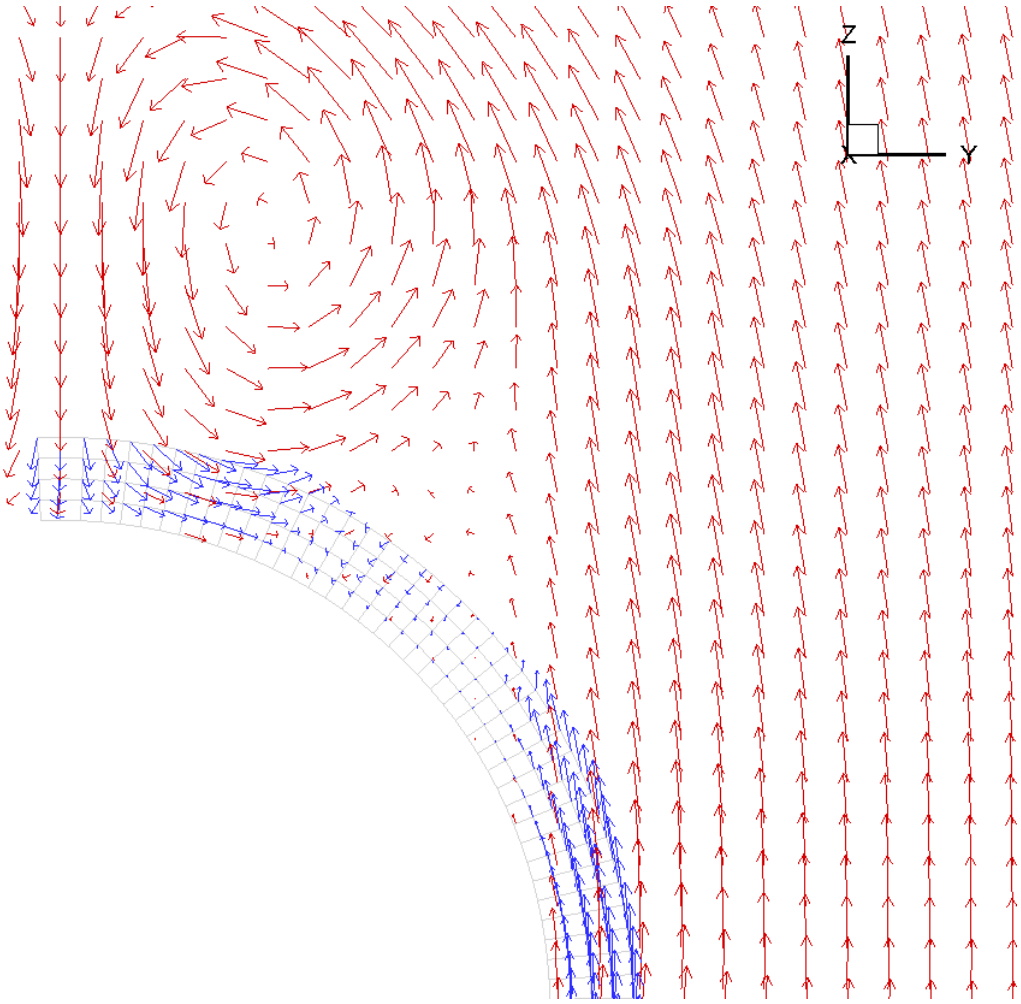

Figure 4-61. Overlapping vector field, X/L = 0.77, 30° incidence, with surface model.

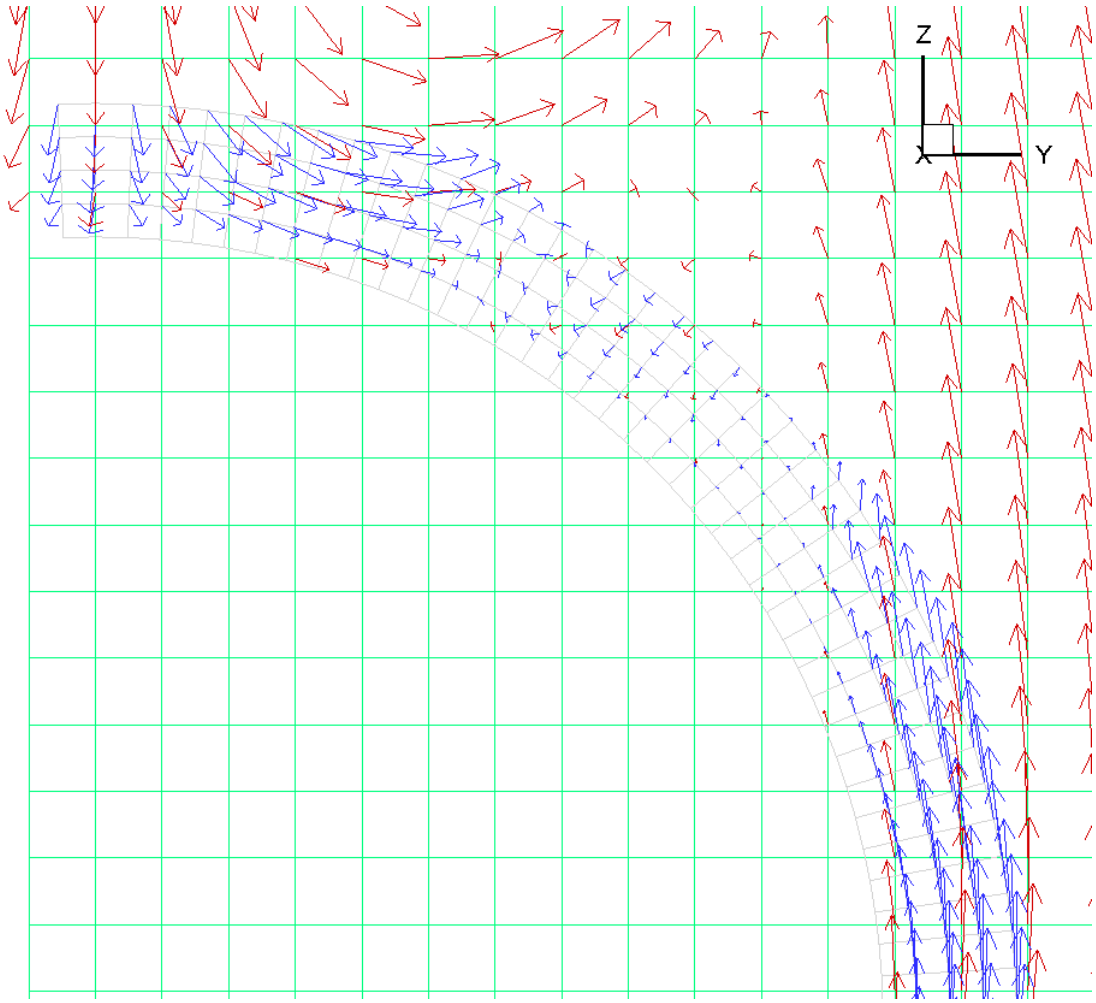

Figure 4-62. Details of overlapping vector field, X/L = 0.77, 30° incidence.

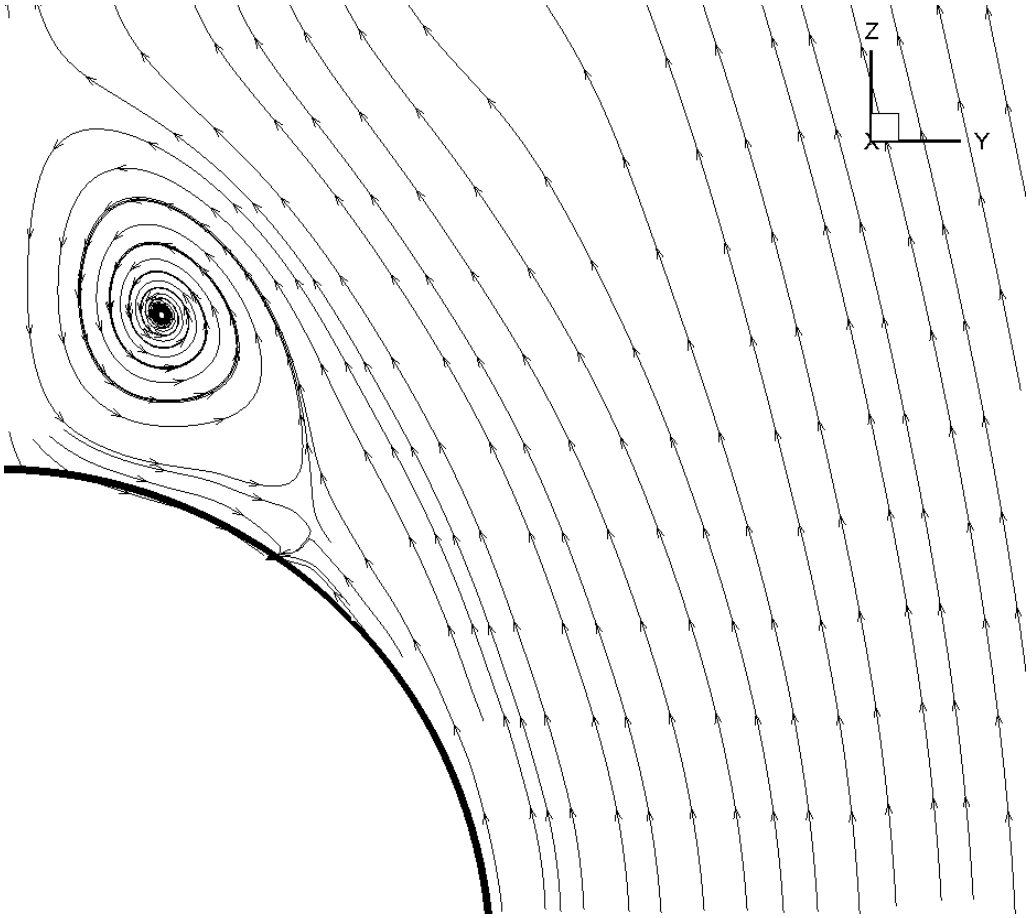

Figure 4-63. Cross Plane streamlines, X/L = 0.60, 20° incidence, with surface model.

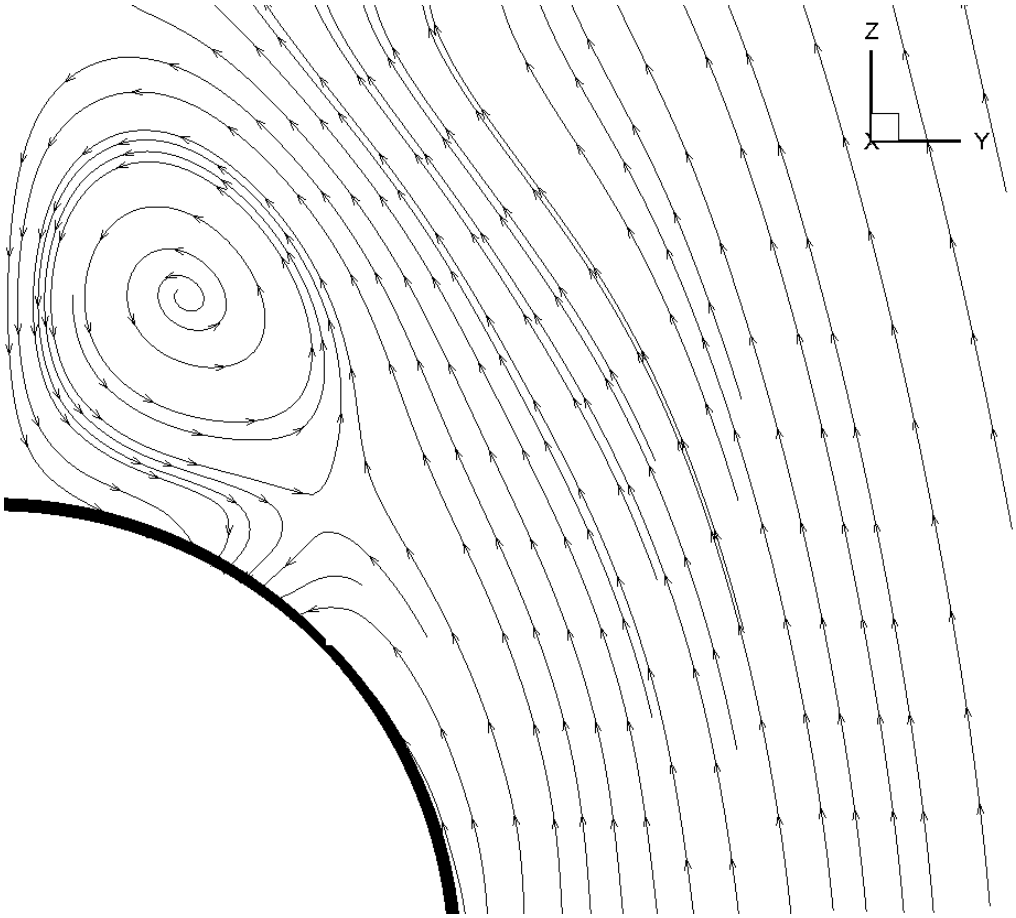

Figure 4-64. Details of cross Plane streamlines, X/L = 0.60, 20° incidence.

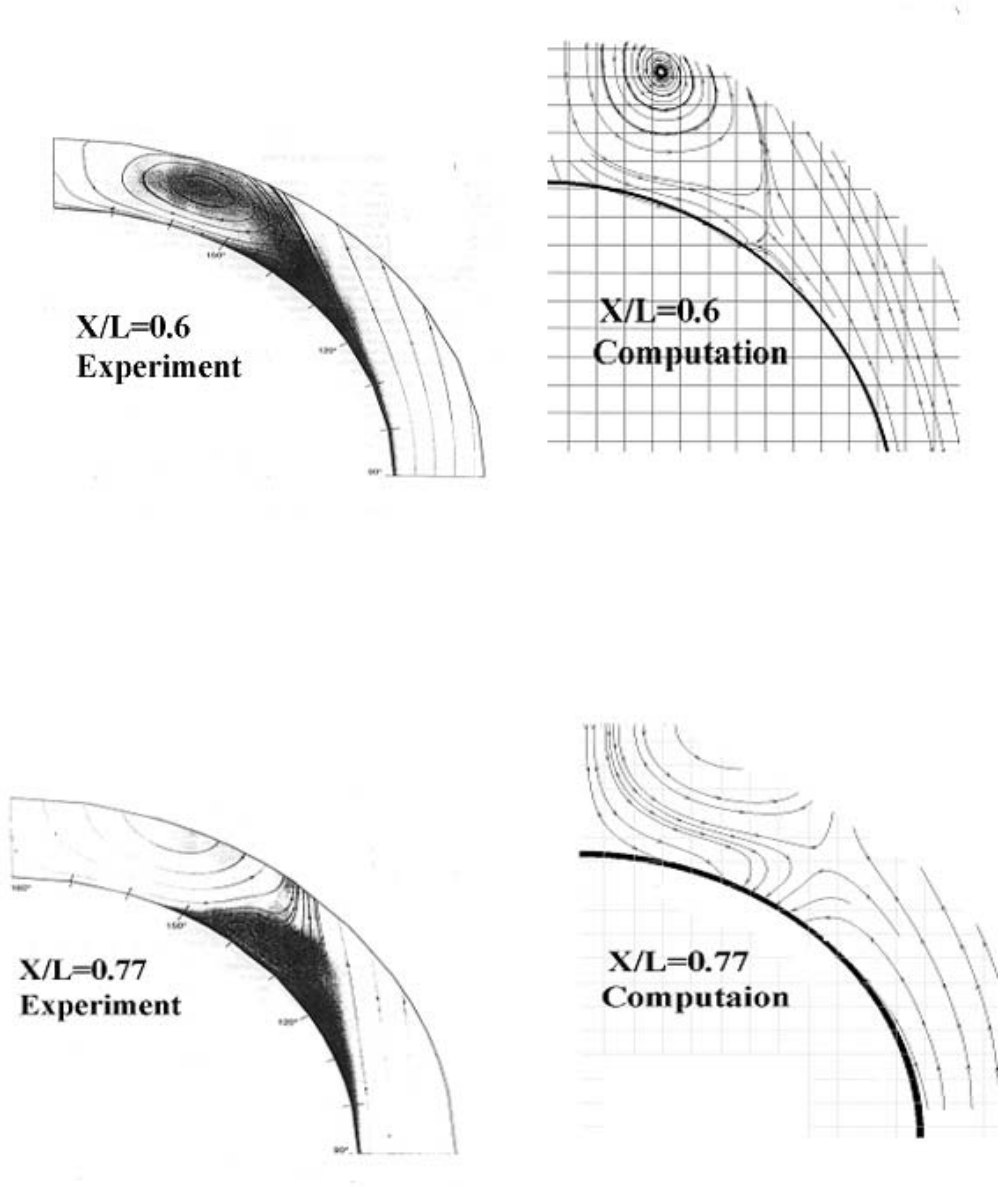

Figure 4-65. Cross plane streamlines, 20° incidence, compared to data (Simpson [6]).

Appendix II: The Centroid Motion of a Convecting Scalar Field

It was proved in 2.1.5 that the confinement term does not alter the centroid motion of a convecting scalar field. The evolution of the centroid of a convecting scalar field is derived next. The discussion in this context is limited to uniform Cartesian grid only, although similar results can be extended to general curvilinear grid.

For a scalar field ϕ, the following property can be proved if the contribution from the boundary values can be neglected

$$\sum_{\Omega} \hat{x} \nabla_c^{\,2} \phi = 0 \tag{6.1}$$

where $\sum_{\Omega}$ represents the sum over all the grid nodes of a computational grid, and $\hat{x}$ is the physical coordinate of a given node. $\nabla_c^{\,2}$ represent the central difference formula for the Laplace operator.

For a three dimensional uniform Cartesian grid with grid spacing Δh, the left hand side of equation (6.1) can be written as

$$\begin{aligned} \sum_{\Omega} \hat{x} \nabla_c^{\,2} \phi = \sum_{i=2}^{i\max-1} \sum_{j=2}^{j\max-1} \sum_{k=2}^{k\max-1} \Big(& \hat{x}_{i,j,k} \phi_{i+1,j,k} + \phi_{i-1,j,k} + \phi_{i,j+1,k} \\ & + \phi_{i,j-1,k} + \phi_{i,j,k+1} + \phi_{i,j,k-1} - 6\phi_{i,j,k} \Big) \Big/ \Delta h^2 \end{aligned} \tag{6.2}$$

which can be split into three terms by the following way

$$\begin{aligned} \sum_{\Omega} \hat{x} \nabla_c^{\,2} \phi = \frac{1}{\Delta h^2} \Bigg(& \sum_{j=2}^{j\max-1} \sum_{k=2}^{k\max-1} \sum_{i=2}^{i\max-1} \hat{x}_{i,j,k} \left(\phi_{i+1,j,k} + \phi_{i-1,j,k} - 2\phi_{i,j,k} \right) \\ & + \sum_{k=2}^{k\max-1} \sum_{i=2}^{i\max-1} \sum_{j=2}^{j\max-1} \hat{x}_{i,j,k} \left(\phi_{i,j+1,k} + \phi_{i,j-1,k} - 2\phi_{i,j,k} \right) \\ & + \sum_{i=2}^{i\max-1} \sum_{j=2}^{j\max-1} \sum_{k=2}^{k\max-1} \hat{x}_{i,j,k} \left(\phi_{i,j,k+1} + \phi_{i,j,k-1} - 2\phi_{i,j,k} \right) \Bigg) \end{aligned} \tag{6.3}$$

The first term in the outer bracket can be transformed to

$$
\begin{aligned}
&\sum_{j=2}^{j\max-1}\sum_{k=2}^{k\max-1}\sum_{i=2}^{i\max-1}\hat{x}_{i,j,k}\left(\phi_{i+1,j,k}+\phi_{i-1,j,k}-2\phi_{i,j,k}\right)\\
&=\sum_{j=2}^{j\max-1}\sum_{k=2}^{k\max-1}\left(\sum_{i=3}^{i\max}\hat{x}_{i-1,j,k}\phi_{i,j,k}+\sum_{i=1}^{i\max-2}\hat{x}_{i+1,j,k}\phi_{i,j,k}-2\sum_{i=2}^{i\max-1}\hat{x}_{i,j,k}\phi_{i,j,k}\right)\\
&=\sum_{j=2}^{j\max-1}\sum_{k=2}^{k\max-1}\sum_{i=2}^{i\max-1}\left(\hat{x}_{i-1,j,k}+\hat{x}_{i+1,j,k}-2\hat{x}_{i,j,k}\right)\phi_{i,j,k}\\
&+\sum_{j=2}^{j\max-1}\sum_{k=2}^{k\max-1}\left(x_{i\max-1,j,k}\phi_{i\max,j,k}-x_{i\max,j,k}\phi_{i\max-1,j,k}+x_{2,j,k}\phi_{1,j,k}-x_{1,j,k}\phi_{2,j,k}\right)
\end{aligned}
\tag{6.4}
$$

Since

$$
\begin{aligned}
&\hat{x}_{i-1,j,k}+\hat{x}_{i+1,j,k}-2\hat{x}_{i,j,k}\\
&=\hat{x}_{i+1,j,k}-\hat{x}_{i,j,k}-\left(\hat{x}_{i,j,k}-\hat{x}_{i-1,j,k}\right)\\
&=\Delta h-\Delta h\\
&=0
\end{aligned}
\tag{6.5}
$$

and at the same time if the boundary contribution is neglected, i.e.

$$
\sum_{j=2}^{j\max-1}\sum_{k=2}^{k\max-1}\left(x_{i\max-1,j,k}\phi_{i\max,j,k}-x_{i\max,j,k}\phi_{i\max-1,j,k}+x_{2,j,k}\phi_{1,j,k}-x_{1,j,k}\phi_{2,j,k}\right)=0 \tag{6.6}
$$

substituting (6.5) and (6.6) into (6.4) yields

$$
\sum_{j=2}^{j\max-1}\sum_{k=2}^{k\max-1}\sum_{i=2}^{i\max-1}\hat{x}_{i,j,k}\left(\phi_{i+1,j,k}+\phi_{i-1,j,k}-2\phi_{i,j,k}\right)=0 \tag{6.7}
$$

Similarly, we have

$$
\begin{aligned}
&\sum_{k=2}^{k\max-1}\sum_{i=2}^{i\max-1}\sum_{j=2}^{j\max-1}\hat{x}_{i,j,k}\left(\phi_{i,j+1,k}+\phi_{i,j-1,k}-2\phi_{i,j,k}\right)=0\\
&\sum_{i=2}^{i\max-1}\sum_{j=2}^{j\max-1}\sum_{k=2}^{k\max-1}\hat{x}_{i,j,k}\left(\phi_{i,j,k+1}+\phi_{i,j,k-1}-2\phi_{i,j,k}\right)=0
\end{aligned}
\tag{6.8}
$$

Substituting (6.7) and (6.8) into (6.3) yields

$$
\sum_{\Omega}\hat{x}\nabla_c{}^2\phi=0 \tag{6.9}
$$

For a vector field $\vec{A}=\left(a,b,c\right)^T$, if neglecting the boundary effect, the following properties can be derived

$$\sum_{\Omega} \hat{x} \nabla_c \cdot \vec{A} = -\sum_{\Omega} \vec{A} \cdot \vec{I} \tag{6.10}$$

where $\nabla_c \cdot$ represents the central difference formula for the divergence operator, and is $\vec{I}$ the identity vector

$$\vec{I} = (1,1,1)^T \tag{6.11}$$

For a three dimensional uniform Cartesian grid, the left hand side of (6.10) can be written as

$$\begin{aligned} \sum_{\Omega} \hat{x} \nabla_c \cdot \vec{A} = \frac{1}{2\Delta h} \Bigg(& \sum_{j=2}^{j\max-1} \sum_{k=2}^{k\max-1} \sum_{i=2}^{i\max-1} \hat{x}_{i,j,k} \left(a_{i+1,j,k} - a_{i-1,j,k} \right) \\ & + \sum_{k=2}^{k\max-1} \sum_{i=2}^{i\max-1} \sum_{j=2}^{j\max-1} \hat{x}_{i,j,k} \left(b_{i,j+1,k} - b_{i,j+1,k} \right) \\ & + \sum_{i=2}^{i\max-1} \sum_{j=2}^{j\max-1} \sum_{k=2}^{k\max-1} \hat{x}_{i,j,k} \left(c_{i,j+1,k} - c_{i,j+1,k} \right) \Bigg) \end{aligned} \tag{6.12}$$

The first term in the outer bracket can be transformed as

$$\begin{aligned} \sum_{j=2}^{j\max-1} \sum_{k=2}^{k\max-1} \sum_{i=2}^{i\max-1} \hat{x}_{i,j,k} \left(a_{i+1,j,k} - a_{i-1,j,k} \right) = & \sum_{j=2}^{j\max-1} \sum_{k=2}^{k\max-1} \sum_{i=2}^{i\max-1} \left(\hat{x}_{i-1,j,k} - \hat{x}_{i+1,j,k} \right) a_{i,j,k} \\ + \sum_{j=2}^{j\max-1} \sum_{k=2}^{k\max-1} & \left(\hat{x}_{i\max-1,j,k} a_{i\max,j,k} - \hat{x}_{i\max,j,k} a_{i\max-1,j,k} + \hat{x}_{2,j,k} a_{1,j,k} - \hat{x}_{1,j,k} a_{2,j,k} \right) \end{aligned} \tag{6.13}$$

Neglecting the boundary effect yields

$$\begin{aligned} \sum_{j=2}^{j\max-1} \sum_{k=2}^{k\max-1} \sum_{i=2}^{i\max-1} \hat{x}_{i,j,k} \left(a_{i+1,j,k} - a_{i-1,j,k} \right) &= \sum_{j=2}^{j\max-1} \sum_{k=2}^{k\max-1} \sum_{i=2}^{i\max-1} \left(\hat{x}_{i-1,j,k} - \hat{x}_{i+1,j,k} \right) a_{i,j,k} \\ &= -2\Delta h \sum_{i=2}^{i\max-1} \sum_{j=2}^{j\max-1} \sum_{k=2}^{k\max-1} a_{i,j,k} \end{aligned} \tag{6.14}$$

Similarly it can be derived that

$$\begin{aligned} \sum_{k=2}^{k\max-1} \sum_{i=2}^{i\max-1} \sum_{j=2}^{j\max-1} \hat{x}_{i,j,k} \left(b_{i,j+1,k} - b_{i,j-1,k} \right) &= -2\Delta h \sum_{i=2}^{i\max-1} \sum_{j=2}^{j\max-1} \sum_{k=2}^{k\max-1} b_{i,j,k} \\ \sum_{i=2}^{i\max-1} \sum_{j=2}^{j\max-1} \sum_{k=2}^{k\max-1} \hat{x}_{i,j,k} \left(c_{i,j,k+1} - c_{i,j,k-1} \right) &= -2\Delta h \sum_{i=2}^{i\max-1} \sum_{j=2}^{j\max-1} \sum_{k=2}^{k\max-1} c_{i,j,k} \end{aligned} \tag{6.15}$$

Substituting (6.14) and (6.15) into (6.12) yields

$$\sum_{\Omega} \hat{x}\nabla_c \cdot \vec{A} = -\sum_{i=2}^{i\max-1}\sum_{j=2}^{j\max-1}\sum_{k=2}^{k\max-1}(a_{i,j,k} + b_{i,j,k} + c_{i,j,k}) = -\sum_{\Omega} \vec{A}\cdot\vec{I} \tag{6.16}$$

The equation governing a convecting scalar field with confinement term added was derived in 2.1.3 (equation (2.17)):

$$\frac{\partial \phi}{\partial t} = -\nabla_d \cdot (\vec{q}\phi) + \mu \nabla_d{}^2 \phi - \varepsilon \nabla_d{}^2 \Phi \tag{6.17}$$

The corresponding difference equation using central spatial difference formulae can be written as

$$\phi^{n+1} = \phi^n - \Delta t \nabla_c \cdot (\vec{q}^n \phi^n) + \Delta t\left(\mu \nabla_c{}^2 \phi^n - \varepsilon \nabla_c{}^2 \Phi^n\right) \tag{6.18}$$

Multiplying both side of the above equation by $\hat{x}$ and sum over the whole computational grid yields

$$\sum_{\Omega} \hat{x}\phi^{n+1} = \sum_{\Omega} \hat{x}\phi^n - \Delta t \sum_{\Omega} \hat{x}\nabla_c \cdot (\vec{q}^n \phi^n) + \Delta t \sum_{\Omega} \hat{x}\left(\mu \nabla_c{}^2 \phi^n - \varepsilon \nabla_c{}^2 \Phi^n\right) \tag{6.19}$$

According to (6.1), the two terms involving second derivatives on the right hand sides of equation (6.19) vanish, which gives

$$\sum_{\Omega} \hat{x}\phi^{n+1} = \sum_{\Omega} \hat{x}\phi^n - \Delta t \sum_{\Omega} \hat{x}\nabla_c \cdot (\vec{q}^n \phi^n) \tag{6.20}$$

Define the sum of the scalar as

$$< \psi >= \sum_{\Omega} \phi \tag{6.21}$$

which is constant in this case if neglecting the boundary effect, and the centroid of the scalar field as

$$< \hat{X} >^n = \frac{\sum_{\Omega} \hat{x}\phi^n}{< \psi >} \tag{6.22}$$

Also define the weighted mean velocity as

$$< Q >^n = \frac{\sum_{\Omega} \left(\vec{q}^n \phi^n\right) \cdot \vec{I}}{< \psi >} \tag{6.23}$$

Dividing both side of equation (6.20) by $< \psi >$ gives

$$\frac{\sum_{\Omega} \hat{x}\phi^{n+1}}{< \psi >} = \frac{\sum_{\Omega} \hat{x}\phi^{n}}{< \psi >} - \Delta t \frac{\sum_{\Omega} \hat{x}\nabla_c \cdot (\vec{q}^{\,n}\phi^{n})}{< \psi >} \tag{6.24}$$

Applying (6.10), (6.22) and (6.23) to (6.24) yields

$$< \hat{X} >^{n+1} = < \hat{X} >^{n} + \Delta t < Q >^{n} \tag{6.25}$$

which is the equation governing the centroid motion of the convecting scalar field.

Vita

Lesong Wang was born in Hong-Lake City, Hubei Province of China on September 14, 1972. He was raised in Bai-Yu village of Hong-Lake City and went to local grade school in 1978. He went to junior high school at Shi-Matou middle school in 1983. After graduating from Hong-Lake No. 1 High School in 1990, he went to the Beijing University of Aeronautics and Astronautics in China. From there he received a B.S. in Mechanical Engineering in 1994 and a M.S. in Mechanical Engineering in 1997. In early 1998 he came to the United States to pursue his Ph. D degree at the University of Tennessee Space Institute. Lesong got his Doctoral degree in December 2003.

Lesong is currently working for Flow Analysis Inc. in Tullahoma, TN.